Exploring oligo(*p*-phenylenevinylene) gelators as sensors and stimuli responsive materials

Thesis Submitted to the
Cochin University of Science and Technology in Partial Fulfillment of the Requirements for the Degree of

DOCTOR OF PHILOSOPHY
in Chemistry under the Faculty of Science

By

Krishnan Kartha K.

Under the Supervision of
Dr. A. Ajayaghosh

Photosciences and Photonics
Chemical Sciences and Technology Division
CSIR-National Institute for Interdisciplinary Science and Technology (CSIR-NIIST), Trivandrum 695 019, Kerala

January 2014

DECLARATION

I hereby declare that the matter embodied in the thesis entitled "**Exploring oligo(*p*-phenylenevinylene) gelators as sensors and stimuli responsive materials**" is the result of investigations carried out by me at the Photosciences and Photonics Section, Chemical Sciences and Technology Division of the CSIR-National Institute for Interdisciplinary Science and Technology (CSIR-NIIST), Trivandrum, under the supervision of Dr. A. Ajayaghosh and the same has not been submitted elsewhere for a degree.

In keeping with the general practice of reporting scientific observations, due acknowledgement has been made wherever the work described is based on the findings of other investigators.

(Krishnan Kartha K.)

(Formerly Regional Research Laboratory)

Council of Scientific & Industrial Research (CSIR)
Industrial Estate P.O., Trivandrum - 695 019
Kerala, INDIA

ISO 9001 REGISTERED
MGMT. SYS. RvA C024
DNV Certification B.V., The Netherlands

Dr. A. Ajayaghosh FASc., FNASc., FNA.
CSIR Outstanding Scientist (Director Level)
Chemical Sciences and Technology Division
Dean, Chemical Sciences, AcSIR

Tel: 91-471-2515 306
Fax: +91-471-2491 712
E-mail: ajayaghosh62@gmail.com
ajayaghosh@niist.res.in

January 08, 2014

CERTIFICATE

This is to certify that the work embodied in the thesis entitled "**Exploring oligo(*p*-phenylenevinylene) gelators as sensors and stimuli responsive materials**" has been carried out by **Mr. Krishnan Kartha K.** under my supervision at the Photosciences and Photonics Section, Chemical Sciences and Technology Division of the CSIR-National Institute for Interdisciplinary Science and Technology (CSIR-NIIST), Trivandrum and the same has not been submitted elsewhere for a degree. All the relevant corrections, modifications and recommendations suggested by the audience and the doctoral committee members during the pre-synopsis seminar of **Mr. Krishnan Kartha K.** have been incorporated in the thesis.

(A. Ajayaghosh)
Thesis Supervisor

ACKNOWLEDGEMENTS

I am extremely grateful to Dr. A. Ajayaghosh, my thesis supervisor, for suggesting the research problem and for his valuable guidance, support and encouragement, leading to the successful completion of this work.

I would like to express my sincere gratitude to Prof. M. V. George for his constant support and inspiration during the tenure of this work.

I wish to thank Dr. Suresh Das, Director, CSIR-National Institute for Interdisciplinary Science and Technology for providing me the necessary facilities for carrying out the work.

I sincerely thank Dr. D. Ramaiah, Dr. K. R. Gopidas, Dr. K. George Thomas, Dr. Narayanan Unni, Dr. Biswapriya Deb, Dr. Joshy Joseph, Dr. Yoosaf K., and Dr. Karunakaran V. scientists of the Photosciences and Photonics, Chemical Sciences and Technology Division, for all the help and support extended to me.

I am extremely thankful to Dr. Santhosh S. Babu, Dr. Vakayil K. Praveen, Dr. C. Vijayakumar, Dr. Bijitha Balan and Mrs. Archana Santhosh for their help, support and encouragement.

I wish to thank Dr. Masayuki Takeuchi, Dr. Takashi Nakanishi, Dr. Kazunori Sugiyasu and Dr. Sochiro Ogi for the help rendered during my research stays at the National Institute for Materials Science (NIMS), Tsukuba, Japan.

I deeply express my sincere thanks to Dr. K. K. Mohammed Yusuff and Dr. S. Prathapan, CUSAT and Dr. Mrinal Pai, BARC for their kind support at the initial stage of my research career.

I thank all the members of the Photosciences and Photonics and in particular, Dr. S. Mahesh, Dr. S. Sreejith, Dr. S. Srinivasan, Dr. K. P. Divya, Dr. S. Prasanthkumar, Dr. Anesh G., Mr. Thirumalai K., Mr. Anees P., Mr. Sandeep A., Mr. Vishnu S., Mr. Sandeep C., Mr. Vedanarayan B., Mr. Rahul Dev M., Ms. Divya Susan Philips, Mr. Samrat Ghosh, Mr. Sudheesh K. V., Mr. Arindam Mal, Mr. Hifsudeen M., Mr. Satyajit Das, Dr. Rakesh K. M. and members of other divisions of NIIST for their help and support. I would like to thank Dr. J. D. Sudha, Mr. Robert Philip, Mr. P. Gurusamy, Mr. Chandrakanth C. K, Mr. Kiran M., Mr. C. Chandran, Ms. Viji, Ms. Soumini, Mr. Adarsh and Mr. Kiran J. S. for technical assistance and general help.

I sincerely thank Dr. R. V. Omkumar, RGCB, Trivandrum for CLSM imaging and HEMRL, DRDO, Pune for providing TNT.

I express my sincere thanks to all my friends for their love, care and support at different stages of my life.

I owe a lot to my family members, who encouraged and helped me at every stage of my personal and academic life, and longed to see this achievement come true.

I sincerely thank the Department of Science and Technology (DST), DST-JSPS, CSIR and NIMS for the financial support.

Krishnan Kartha K.

PREFACE

Gelation provides a unique medium, which often induces organization of molecules resulting in the modulation of their optical, morphological and electronic properties thereby opening a new world of fascinating materials with interesting physical properties at nano- meso- and macroscopic levels. Supramolecular gels based on linear π-systems have attracted much attention due to their inherent optical and electronic properties which find application in organic electronics, light harvesting and sensing. They exhibit reversible properties due to the dynamic nature of non-covalent forces. As a result, studies on such soft materials are currently a topic of great interest. Recently, researchers are actively involved in the development of sensors and stimuli-responsive materials based on self-assembled π-systems, which are also called smart materials.

The present thesis is divided into four chapters. In the first chapter, an overview of the recent developments on stimuli-responsive materials based on π-gelators and assemblies, their properties and applications is given. Attention has been paid to discuss the self-assembled π-gelators reported as sensors, multi-

stimuli responsive and mechanoresponsive materials. Finally, the origin, objectives and the approach of the present thesis entitled "**Exploring oligo(*p*-phenylenevinylene) gelators as sensors and stimuli responsive materials**" are given.

The second chapter describes a fluorescent oligo(*p*-phenylenevinylene) (**OPV**) organogelator which exhibits excellent detection capability for nitroaromatics in the gel form. The gel when coated on disposable paper strips detects nitroaromatics including 2,4,6-trinitrotoluene (TNT) at a record attogram (ag, 10^{-18} g) level (~12 ag/cm^2) with a detection limit of 0.23 ppq. The gelator molecule (**OPVPF**) is not efficient for the sensing of TNT in the solution state, whereas, in the xerogel state, high sensitivity has been achieved. The efficient fluorescence quenching of **OPVPF** xerogel coated filter paper by extremely small amount of TNT could be explained by a faster exciton diffusion mechanism as described earlier in the case of conjugated polymers. This is a simple and low-cost method for the detection of TNT on surfaces or in aqueous solutions in contact mode, taking advantage of the unique molecular packing of an organogelator and the associated photophysical properties.

The third chapter of the thesis describes the design, synthesis and hierarchical self-assembly of an amide functionalized **OPV** derivatives (**OPV-PY** and **OPV-BZ**) containing pyridine and benzene as the end substituent. The main focus of this chapter is the multi-stimuli responsive gelation and morphological properties of **OPV-PY**. The molecule **OPV-PY** was unable to form gel independently in common organic solvents except pyridine. However, two component gels could be prepared by the co-assembly of **OPV-PY** with trifluoroacetic acid (TFA) and Ag^+ ion in $CHCl_3$. The presence of pyridine unit enables the protonation of **OPV-PY** with TFA which facilitates the formation of hydrogen bonded assembly which is reversible by the addition of an organic base. A metallosupramolecular assembly with Ag^+ ion leading to the gel formation has been observed for **OPV-PY**. The multi-stimuli responsive self-assembly and gelation properties were studied in detail by monitoring the changes in the photophysical properties as well as from the morphological analyses.

The role of supramolecular chirality in the design of a mechanochromic gelator is described in the last chapter of the thesis. Herein, we illustrate the design and synthesis of an amide

functionalized chiral **OPV** derivative (**OPV-C**) and its mechanochromic behaviour. The effect of aggregation on optical and chiroptical properties in solution, gel, xerogel and solid states were studied in detail. The chiral derivative (**OPV-C**) was much sensitive to shearing when compared to the achiral derivative (**OPV-A**), which revealed that the bottom-up self-assembly pathway has a key role in designing stimuli responsive materials. An isothermally self-reversible fluorescent **OPV-C** film was prepared to understand the complex pathways of the self-assembly and the excited state processes in detail.

In summary, we have used different **OPV** gelators as sensor and stimuli responsive materials and studied their self-assembly and photophysical properties in detail. The brick-wall type arrangement by **OPVPF** allows an entrapment of TNT into the self-assembled **OPV**s and subsequent excited state energy migration assisted electron transfer enables a quenching of fluorescence. In the case of **OPV-PY**, the presence of pyridine facilitates a multi-stimuli responsive gelation and morphological transition of **OPV**s. Supramolecular chirality of the self-assembled **OPV-C** was used for the design of a mechanochromic gelator. Thus, in this work we have

used a rational approach to structurally modify OPV backbone, resulting in a few stimuli responsive organogelators.

Note: *The abbreviation of various compounds given here corresponds to those given under the respective chapters.*

CONTENTS

Chapter 1

Stimuli Responsive Materials Based on Self-Assembled π-Systems and Gels: An Overview

1.1. Abstract

Soft materials made up of π-systems, through non-covalent interactions are extremely sensitive to surrounding media. They exhibit reversible properties due to the dynamic nature of the non-covalent forces. As a result, such soft materials are of great interest in chemistry, biology and material science. Chromophores based assemblies and gels are of particular interest due to their inherent optical and electronic properties which find application in organic electronics, light harvesting and sensing. Gelation is a convenient approach to the organization of molecules, resulting in the modulation of their optical, morphological and electronic properties. A recent interest in chromophores based assemblies and gels are due to their stimuli responsive properties. In this chapter, an overview of the recent developments in stimuli-responsive materials based on π-gels and assemblies, their properties and applications are described. Finally, the origin, objective and the approach to the present thesis are discussed.

1.2. Introduction

Supramolecular chemistry exploits intermolecular non-covalent interaction between molecules to form different architectures with interesting properties.[1] Certain molecules self-assemble in appropriate solvents to form soft non-flowing solid masses called supramolecular gels.[2] They have received considerable attention as a mean of creating "smart" materials.[3] Supramolecular gels are held together by multiple weak forces between molecules which are dynamic in nature and hence they are stimuli-responsive and tunable form of soft matter.[4] The optical and morphological properties of these soft materials eventually depend on how molecules are packed in the aggregates, rather than being an intrinsic property of the material. It is of particular interest to organize the chromophores in a regular array to improve the optical and electronic properties. Due to the reversible optical and electronic properties, linear π-system based gelators (π-gelators) have attracted much attention.[2b,5] Such materials are expected to have applications as sensors for biologically and environmentally relevant analytes, as security labels and in organic electronics. The reversible modulation of excited state properties such as fluorescence of π-gels has been exploited for sensing various analytes including explosives.[6]

1.3. Fluorescent probes based on self-assembled π-systems

Design of chemosensors based on fluorescent molecules has been a subject of great interest to chemists. A measurable signal of the sensor in response to an analyte of interest is the key requirement. Among diverse methods, the most common signal transduction schemes utilize optical or electrical properties. To produce a functional sensor, a highly sensitive optical transduction method such as fluorescence is of great advantage where the analyte binding produces a reduction (turn-off), enhancement (turn-on), or wavelength shift in the emission. In the past few years, fluorescent conjugated polymers have been employed extensively as sensing materials.[7] Recently, molecular assemblies of π-systems have been found efficient in the sensing of analytes.[8]

In 2002, Park *et al.* have reported a new class of fluorescent organic nanoparticles (FONs) derived from 1-Cyano-*trans*-1,2-bis-(4'-methylbiphenyl)-ethylene (**1**).[9] A strongly enhanced emission and on/off fluorescence switching in response to organic vapors were reported for these FONs. Aggregation induced enhanced emission (AIEE) of nanoparticles of compound **1** in water (Figure 1.1b) was ascribed to the synergetic effect of planarization and J-aggregation. The formation of nanoparticles was characterized with FE-SEM measurements (Figure 1.1c). Later, a few high-performance fluorescent probes for organic vapors using the AIEE fluorophores, **1** and 4,4'-bis-((2-((4-(3,5-bitolyl)phenyl)phenyl)-2-cyano)-transethenyl)-*trans*-stilbene (**2**) have been reported. Exposure of **1** and **2** to

volatile organic compounds showed reversible on/off fluorescence and dual color fluorescence switching with a rapid response. The real time vapor sensing was followed by using a TLC plate absorbed with nanoparticles as shown in Figure 1.1d. These reversible switching behaviors were recognized as the changes to the molecular conformation and intermolecular interactions in the sensor molecules by the penetration of the analyte molecules.

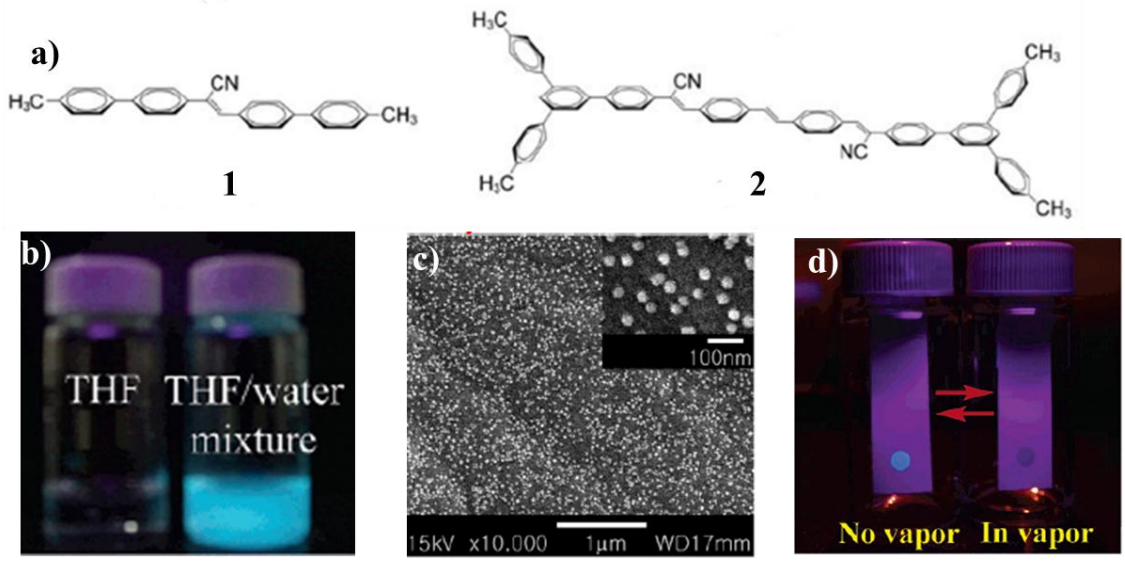

Figure 1.1. (a) Chemical structures of **1** and **2**. (b) Fluorescence emission of **1** (2×10^{-5} mol L^{-1}) in THF (left) and THF/water mixture (80% water) (right) under the UV light (365 nm). (c) FE-SEM images of nanoparticles derived from **1**. (d) On/off fluorescence switching of nanoparticles derived from **1** on the TLC plate in the absence of vapor (left) and in the presence of dichloromethane vapor (right).

Nanostructured, one-dimensional (1D) morphologies have significant role in developing efficient analyte sensors. Recent research suggests that π-π stacking is

an effective way to obtain 1D nanowire structures from rigid aromatic molecules. For example, perylene tetracarboxylic diimides (PTCDIs), a class of *n*-type semiconductor and arylene ethynylene macrocycles, a class of *p*-type semiconductor, were employed for the fabrication of 1-D nanowires.[6] One-dimensional self-assembly of π-systems usually exhibits uniaxial optical properties along the π-π stacking direction as shown in Figure 1.2a. Uniaxial optical properties consistent with 1D molecular stacking were proved by Zang *et al.* with consecutive rotating microscopy imaging of a nanobelt fabricated from PTCDI molecules (Figure 1.2b).[10] The anisotropic birefringence was maximum under crossed polarization only when PTCDI nanobelt was 45° to the direction of the polarizer. The birefringence of the nanobelt became minimal at a position parallel to the polarizer. Orientation of molecules which determines the transition dipole moment of the molecular assembly was further investigated with a polarized emission at single nanowire level using a Near-field Scanning Optical Microscope (NSOM) (Figure 1.2c). Depending on the polarizer angle with respect to the orientation of nanobelt, the emission intensity changed when a plane polarizer was placed before the emission detector. The emission was weakened when the polarizer was closely kept in a position perpendicular to the long-axis of the belt (Figure 1.2d), while at a position parallel to the nanobelt, the emission was enhanced (Figure 1.2e). By rotating the emission polarizer from 0° to 180°, the emission intensity changes with respect to the relative angle between the polarizer and the long-axis of the belt

which indicated a tilted molecular stacking along the long axis of the nanobelt (Figure 1.2f).

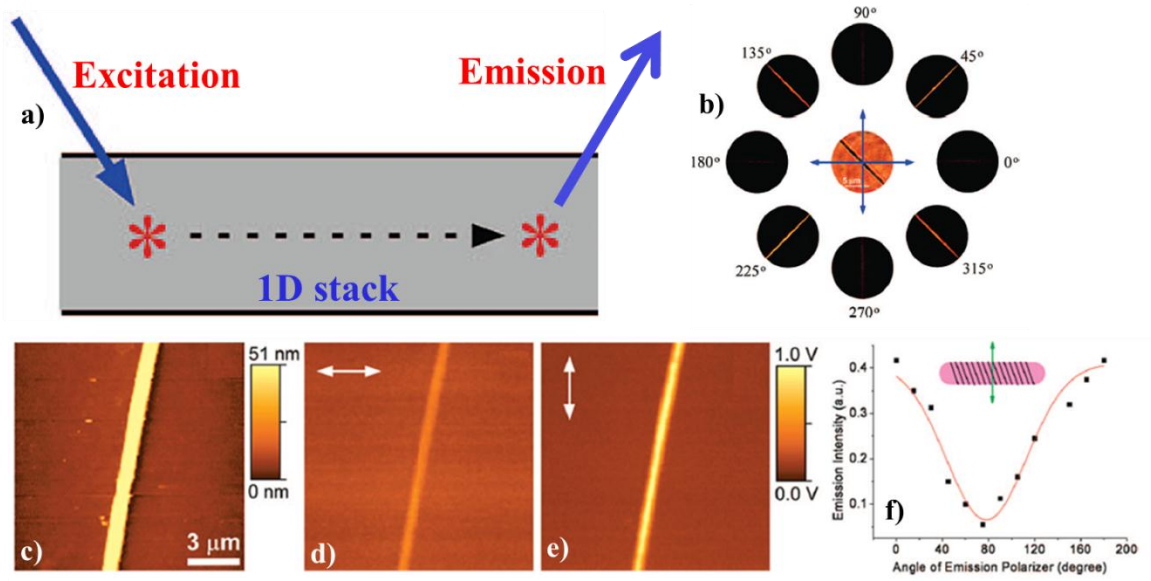

Figure 1.2. (a) A schematic diagram showing the uniaxial migration of exciton. (b) Single nanobelt under cross-polarized microscope: consecutive rotation of the sample showed alternate appearance of birefringence as the nanobelt was aligned at 45° to the polarizer. (c) NSOM topography image of a nanobelt assembled from propoxyethyl-PTCDI with belt thickness of about 50 nm. NSOM emission images collected (by PMT) after a polarizer was placed at horizontal (d) and vertical (e) positions. (f) Emission intensity of a single nanobelt depending on the angle between the polarizer and the long axis of the nanobelt.

Moore *et al.* reported amplified fluorescence quenching of 1D nanofibers upon adsorption of a quencher like 2,4,6-trinitrotoluene (TNT). The long range π-π overlap assisted enhanced exciton migration through 1-D structure and subsequent electron transfer enabled an amplified quenching.[11] In this work, authors have

fabricated an efficient sensor film from the alkoxycarbonyl-substituted, carbazole-cornered, arylene-ethynylenetetracycle (**3**) (Figure 1.3a). The presence of carbazole groups increase the electron donating ability of the molecule and thus efficient fluorescence quenching was observed upon exposure to electron deficient explosives. The shape persistent molecular structure of **3** in combination with the networks formed by interdigitated fibers produced a multi-scale porosity, making it an ideal sensing material for probing oxidative gaseous molecules. The porous film morphology was confirmed using TEM analysis. Micrometer long nanofibers fabricated *via* surface casting technique were used for sensing 2,4-dinitrotoluene (DNT) and TNT. The fluorescence of the film was slowly recovered by exposure to air for a few days or quickly recovered by exposure to the vapor of hydrazine, a strong reducing reagent capable of reducing the oxidized defects within the film.

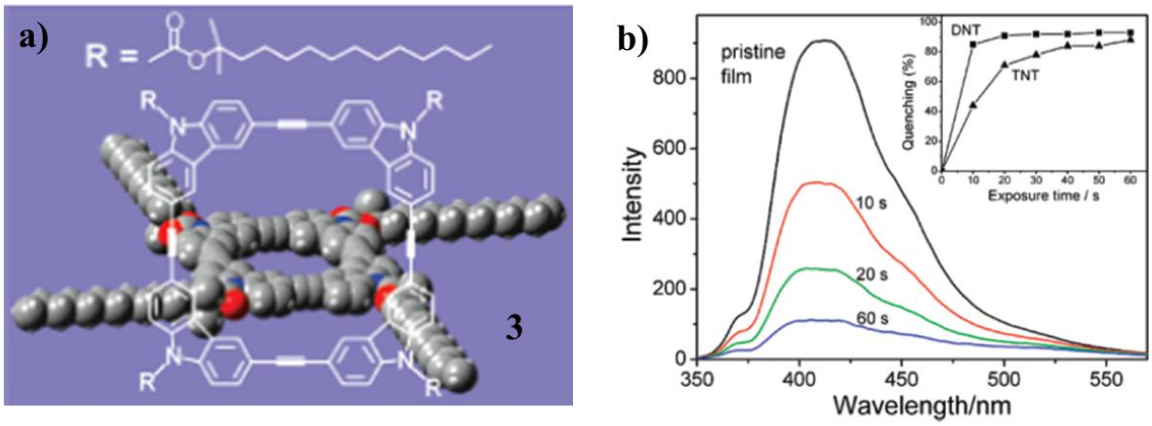

Figure 1.3. (a) Chemical structure of **3**. (b) Fluorescence spectra of a 90 nm thick film of **3** upon exposure to saturated vapor of TNT (5 ppb) at different times.

Films fabricated from such materials have revealed high efficiency in the detection of explosive vapors (Figure 1.3b), probably due to the extended 1D molecular stacking *via* intermolecular stacking and intrinsic nanoporous morphology formed within the film. The former facilitates efficient exciton migration, while the latter favors adsorption and diffusion of gaseous analytes within the film. A combination of these two characteristics allows efficient fluorescence quenching of the film by gaseous quenchers.

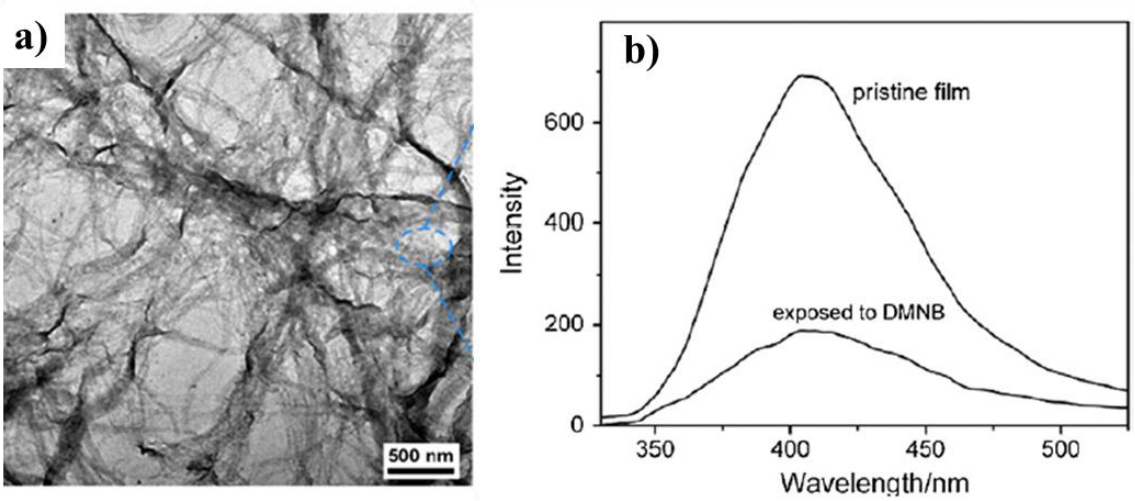

Figure 1.4. (a) A TEM image showing the nanofibril structure of a thin film cast on silicon oxide grids from solution of **3** in THF. (b) Fluorescence spectra of a 90 nm thick nanofibril film made up from **3** before and after exposure to the DMNB vapor (2.7 ppm) for 2 min.

Fluorescence sensing materials fabricated from the molecule **3** was found highly efficient in the detection of 2,3-Dimethyl-2,3-dinitrobutane (DMNB).[12] The fluorescence of a 90 nm thick nanofibril film spin-casted from a tetrahydrofuran

(THF) solution of **3** (Figure 1.4a), upon exposure to the saturated vapor of DMNB (2.7 ppm) was quenched about 73% (Figure 1.4b). Exposing the film to hydrazine for 2 h followed by blowing of nitrogen to remove the hydrazine condensation, retains the fluorescence intensity of the pristine film. The fluorescence quenching observed was due to the electron transfer from the excited state of **3** to DMNB.

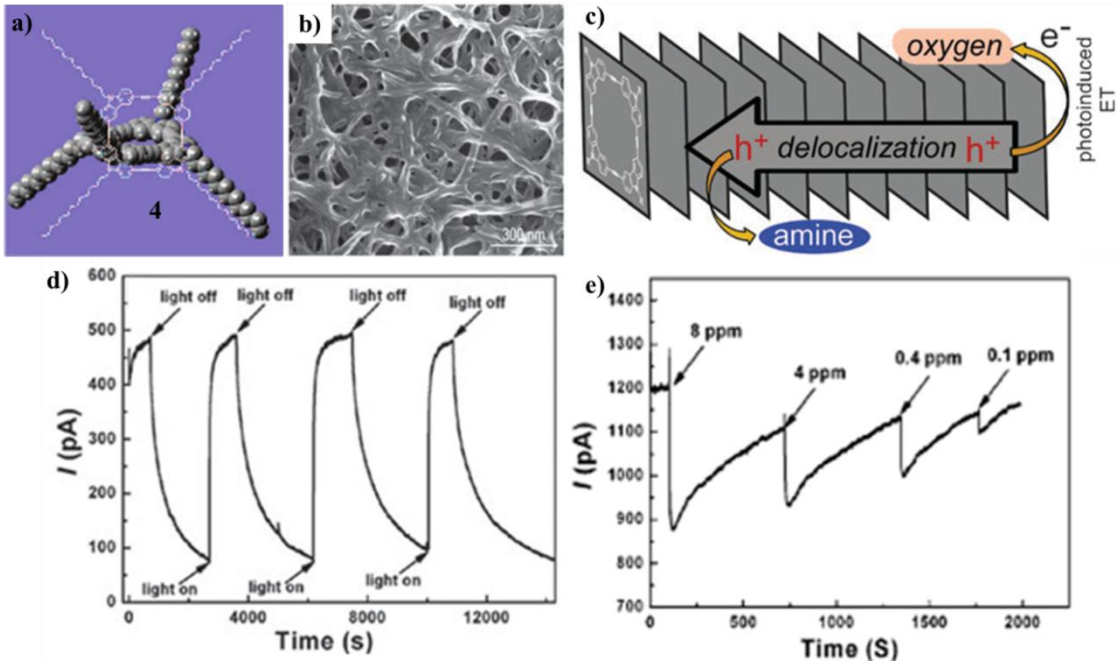

Figure 1.5. (a) Chemical structure of **4**. (b) SEM image of entangled nanofibers of **4** deposited on glass. (c) A schematic illustration showing the enhancement of conductivity through photodoping and the decrease in conductivity due to hole depletion by surface adsorbed amines. (d) Photocurrent (at 10 V) in response to turning on and off the irradiation. (e) Photocurrent change of nanofibers upon exposure to aniline vapor at various pressures.

Zang *et al.* demonstrated that active photodoping of *p*-type organic nanofibers assembled from an alkyl-substituted, carbazole-cornered, arylene-ethylene tetracyclic macromolecule (**4,** Figure 1.5a) yielded high photoconductivity and demonstrated sensing of amine vapor.[13] The SEM images of the nanofibers made-up of **4** through a simple solution-based self-assembly are ca. 20–50 nm in diameter and several micrometres in length (Figure 1.5b). The extended 1D molecular arrangement is clearly observed by the d-spacing (3.8 Å) as shown in the XRD pattern which corresponds to a regular π–π stacking distance. The strong π–π interaction is also consistent with the new absorption band emerged at longer wavelength as measured for the nanofibers in comparison to the molecular solution of **4**. The nanofibers showed a high conductivity upon irradiation with white light under ambient condition, whereas negligible current was observed in the dark (Figure 1.5c). The high photoconductivity observed is likely correlated to the presence of oxygen, which can usually help increase the concentration of holes for *p*-type organic materials. The photoresponse observed for aniline was much higher than that observed for other organic vapors. The change in photocurrent upon exposure to common organic vapors could be recovered completely within 30 s. In comparison, the recovery of photocurrent after exposure to aniline vapor was in the time range of 10 min or longer, which is recognized as a strong binding between amine and the positively charged nanofiber. Slower recovery of current thus detected for aniline was used as a signature for selective detection of amines

against the common organic vapors (Figure 1.5d, e).

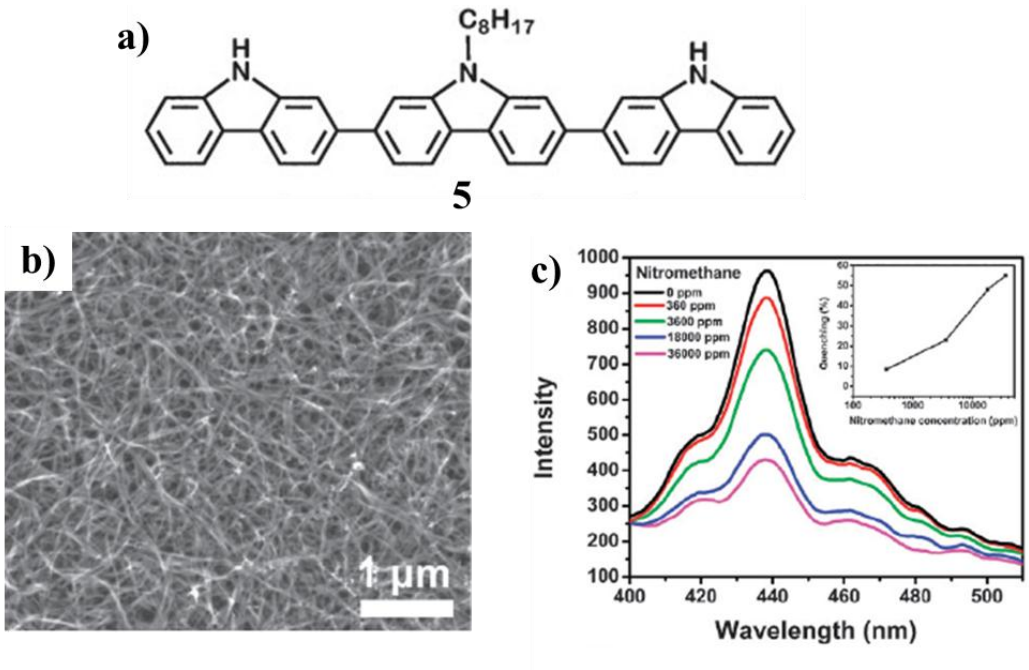

Figure 1.6. (a) Chemical structure of a 2,7-linked carbazole trimer **5**. (b) SEM image of nanofibrils deposited on a silicon substrate. (c) Fluorescence spectra of the nanofibril film upon exposure to various concentrations of nitromethane vapor. The inset shows the vapor concentration dependent quenching.

Zang and co-workers have reported an easy synthesis of a 2,7-linked carbazole trimer (**5**, Figure 1.6a) and preparation of nanofibril structures of **5** *via* self-assembly approach.[14] The film thus fabricated exhibits efficient, fast fluorescent sensing for nitroaliphatic explosives (e.g., nitromethane) which remain difficult to detect due to their high volatility when compared with nitroaromatic explosives (e.g., TNT, DNT) and low chemical binding to many sensory materials. SEM

image of the nanofibrils fabricated from the carbazole trimer deposited on a silicon substrate showed a high aspect ratio, with diameter of only ca. 30 nm and length of several microns. The deposited nanofibrils formed a nanoporous film consisting of entangled fibril networks as shown in Figure 1.6b. Increase in the vapor pressure of nitromethane resulted in fluorescence quenching, reaching 55% under the saturated vapor of 36,000 ppm. Upon blowing at 1800 ppm (5% dilution from the saturated pressure), a significant fluorescence quenching (11%) was observed (Figure 1.6c).

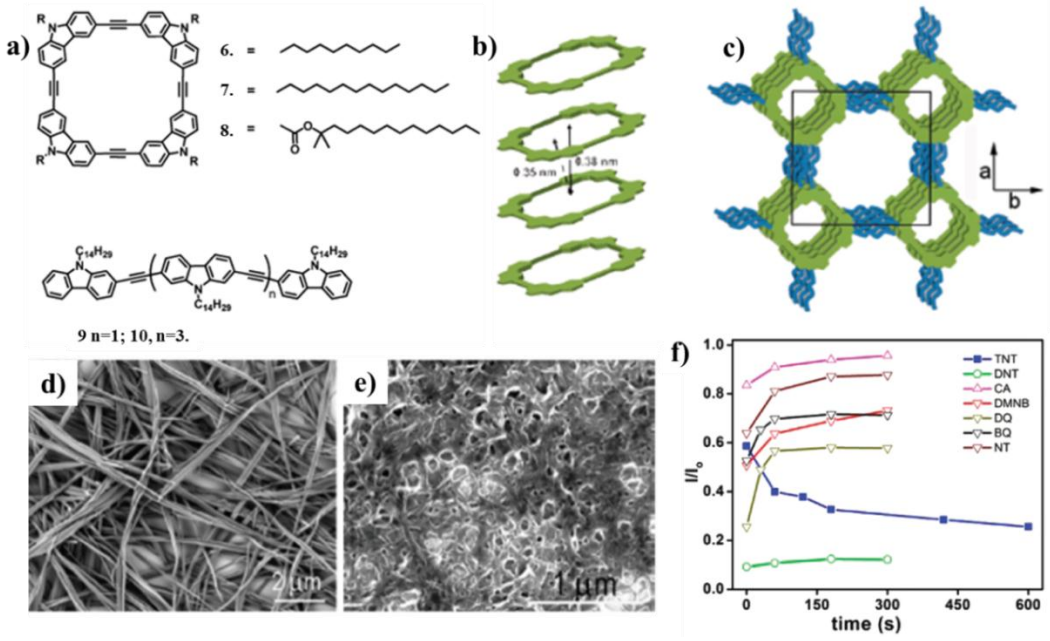

Figure 1.7. (a) Chemical structures of **6**-**10**. (b,c) Modeling of tubular or nanoporous packing of **6** and the rectangular lattice. (d,e) SEM images of nanoporous nanofibers fabricated from **6** and **7**, respectively. (f) Post exposure fluorescence quenching measured over nanoporous nanofibers from **8**.

The carbazole-based tetracycles (TC) **6−10** facilitate the formation of nanoporous nanofibers *via* self-assembly process under low-temperature conditions (Figure 1.7).[15] Upon exposure to explosive vapors, the emission of the nanoporous nanofibers of **6** was quenched. Upon reopening the nanofibers to clean air, further quenching was observed in fluorescence, which was ascribed to the further diffusion of trapped TNT vapors. No such post-exposure fluorescence quenching was observed for other nitroaromatics; rather the fluorescence emission was recovered to certain extents. This may be due to diffusion controlled process within the porous structure for the post-exposure quenching observed with TNT. Similar behavior was observed for the nanoporous fibers fabricated from **7** and 8, in which the nanoporous fibers of **8** exhibited much weaker interaction with oxygen, thereby enabling the high intake of TNT (Figure 1.7f). Nanoporous fibers showed an enhanced selectivity towards TNT as enabled by the post-exposure fluorescence quenching. The quenched fluorescence of nanoporous nanofibers of **7** remained almost unchanged after immersion in the saturated vapor of hydrazine for 1 min followed by drying in a stream of nitrogen. However, the fluorescence of the nanofibers made from **9** and **10** was restored to over 90% under the same recovery conditions. The porosity caused by entangled piling of nanofibers prepared by spin-casting technique exhibited no post-exposure fluorescence quenching.

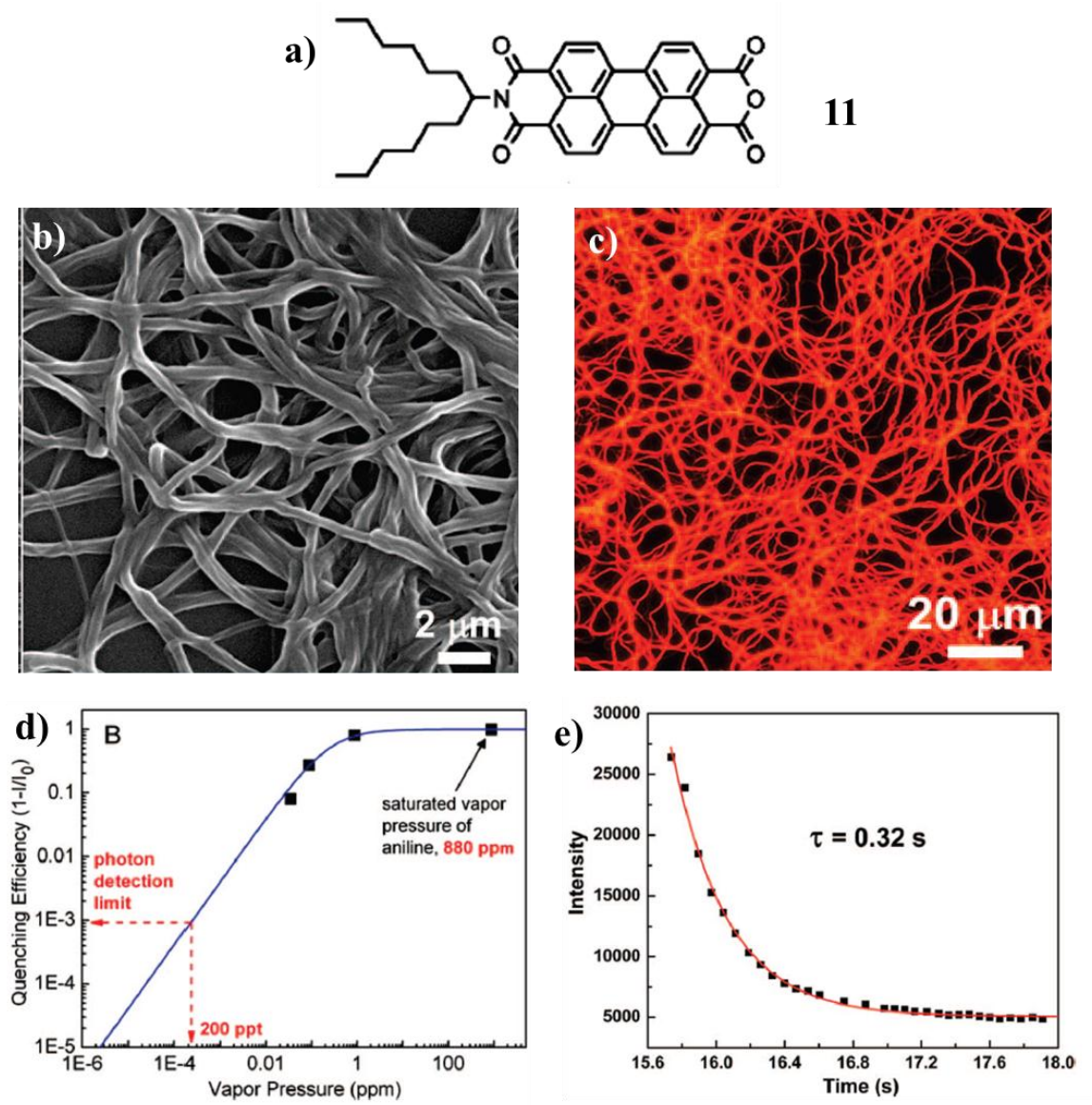

Figure 1.8. (a) Chemical structure of **11.** (b) SEM image of a nanofibril film deposited on a glass slide. (c) Fluorescence optical microscopy image of a nanofibril film. (d) Fluorescence quenching efficiency (1 - I/I_0) as a function of the vapor pressure of aniline. (e) Time-course of fluorescence quenching of a nanofibril film upon blowing over with saturated vapor of aniline (880 ppm), indicating a response time of about 0.32 s.

Followed by Moore's design strategy of sensors based on self-assembled organic materials, Zang *et al.* fabricated nanofibers from a strongly fluorescent *n*-type organic semiconductor material and employed in efficient fluorescent sensing of gaseous amines.[16] The perylene molecule **11** (Figure 1.8a) provides a good balance between the molecular stacking and the fluorescence yield, thus made the material suitable for sensing. The average diameter of the nanofibers determined by SEM was ~350 nm. The extended 1D molecular arrangement obtained for **11** is likely dominated by the π-π interaction between the perylene backbones in cooperation with the hydrophobic interactions between the side chains in appropriate size (Figure 1.8b). Red fluorescence of nanofibers (Figure 1.8c) with quantum yield of ~15% showed quenching on exposure to aniline vapors. Increased surface area for enhanced adsorption of gaseous analytes provided by the porous film enabled convenient diffusion of guest molecules across the film matrix. Such a porous and emissive nanofiber was efficient in probing gaseous molecules with both high sensitivity and fast time response (Figure 1.8d). Upon exposure to the saturated vapor of aniline (880 ppm), the fluorescence of the nanofibril film was suddenly quenched by almost 100%. The emission intensity of the film monitored upon exposing to a saturated vapor of aniline (880 ppm) showed a decay lifetime of only 0.32 s (Figure 1.8e). Such an efficient quenching observed was explained with a photoinduced electron transfer process with the favorable energy difference between HOMO of aniline and **11**. Further, the

pristine films generated from **11** with thinner fibers possessed increased porosity facilitating the cross-film diffusion of gaseous species, thus enhancing the efficiency of the amine vapor sensing.[17]

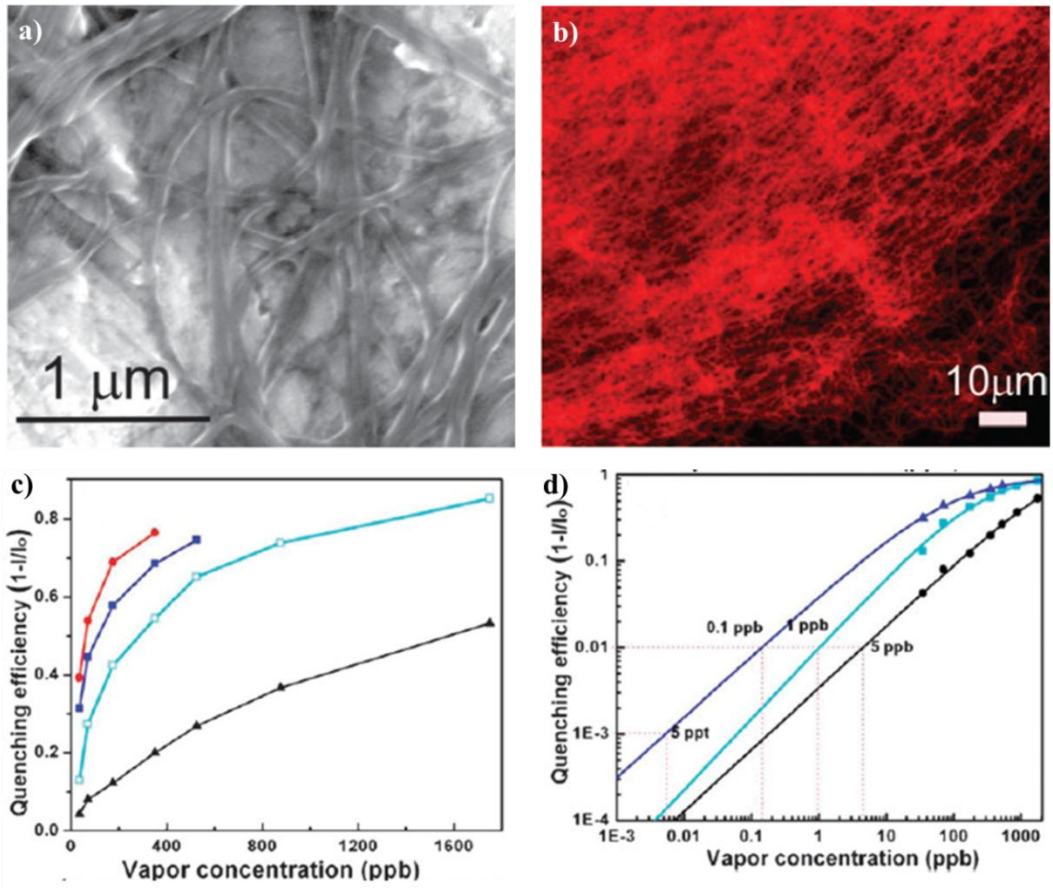

Figure 1.9. (a) SEM image, (b) fluorescence optical microscopy image and (c) fluorescence quenching efficiency (1 - I/I0) as a function of the vapor concentration of aniline in the nanofibers deposited on a glass slide with various amount of fibril materials (cyan: 0.35 mg; blue: 0.15 mg; red: 0.1 mg) as well as a film fabricated from the large fibers (black: 0.35 mg). (d) Fitting the three sets of data with the Langmuir equation aiming to predict the detection limit based on the common photon detection threshold of PMT.

A SEM image of the nanofibers exhibited relatively uniform size and shape with diameter ranging from 30 to 50 nm (Figure 1.9a). The same intermolecular stacking structure of the ultrathin nanofiber also yielded the same fluorescence quantum yield as that of the larger fibers (Figure 1.9b , ca. 15%), which enables the application of the molecules in fluorescence sensing. As described earlier, the one-dimensional confined exciton diffusion favors the enhancement in sensing *via* intermolecular hoping along the long axis of nanofibers. Interestingly, superior quenching percentage was observed under the same vapor pressure for the film fabricated with fewer amounts of nanofibers. Under the vapor pressure of amine vapor, 35 ppb, 31% of fluorescence quenching was detected for the film deposited from 0.15 mg nanofibers, whereas only 13% of fluorescence quenching was obtained for the film deposited from 0.35 mg nanofibers (Figure 1.9 c,d). Thus, the sensing efficiency can be enhanced by reducing the amount of the nanofibers used in the film.

Well-defined ultrathin nanoribbons have been fabricated from amphiphilic electron donor-acceptor (D-A) perylene tetracarboxylic diimide derivatives (Figure 1.10a).[18] Photoinduced intramolecular charge separation between the D and A moieties resulted in photocurrent generation which was further improved by controlling the intramolecular charge separation to match the subsequent intermolecular charge transport along the π-π stack. Among the three building blocks, molecule **12** was selected as a reference to prove the mechanism of

photocurrent generation while molecules **13** and 1**4** were selected for comparative investigation. The ultrathin nanoribbons have been observed with a SEM analysis (Figure 1.10b-d).

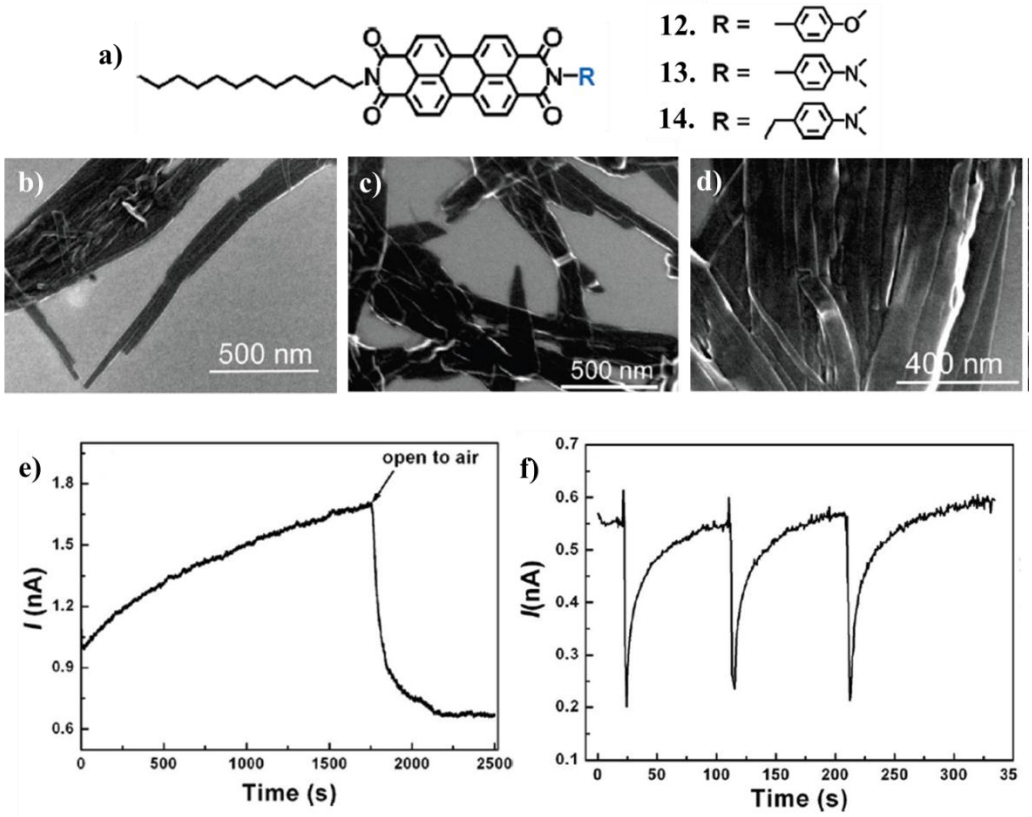

Figure 1.10. (a) Chemical structures of **12**-**14**. (b-d) SEM images showing the nanoribbons fabricated from molecules **12**, **13**, and **14**, respectively. (e) Photocurrent change (at 10 V) with time upon argon blowing (monitored after 5 min of blowing) and when open to air measured over the nanoribbons of **14**. (f) Photocurrent measured over the nanoribbons fabricated from **14** in response to the open-air blowing of saturated vapor of nitromethane.

Upon continuous blowing of argon to the nanoribbons of **14**, the photocurrent gradually increased (Figure 1.10e), reaches a plateau, indicating the establishment

of surface exchange equilibrium with argon. Shutting down the blow of argon quickly dropped the photocurrent to a constant value, reflecting the rapid saturation with the adsorption of oxygen. Several nitro-based explosives with varying vapor pressures were employed to prove the concept of the electrical sensing of vapors that depends on the photocurrent modulation. For *e.g.* upon exposure to the vapor of nitromethane over the nanoribbons, a sharp decrease in the photocurrent was observed. It also showed excellent reversibility in the sensing with a quick recovery of the original photocurrent upon stopping the blowing of nitromethane (Figure 1.10f).

Triphenylamine functionalized bis(dioxaborine)carbazole derivatives (**15-17**, Figure 1.11a) having low-dimensional nanostructures with different morphologies have been fabricated by Lu and co-workers.[19] Re-precipitation of **15** from tetrahydrofuran/hexane yielded 1D single-crystalline nanowires, where 1D nanofibers based on **17** were prepared *via* organogelation process, and amorphous nanoparticles were prepared from **16**. The mesh-like film obtained from the **17**-based gel shows faster fluorescent response and higher sensitivity than the nanoparticle (**16**) and nanowire (**15**) based films (Figure 1.11b-d). Exposing to the saturated vapor of aniline (880 ppm), the fluorescence of the film based on the nanofibers of **17** was rapidly quenched by about 90% (Figure 1.11e). The response time is 0.67 s for the quenching process, whereas it is 2.46 s for the nanoparticle-based film of **16**. The organogel fibers of **17** showed high selectivity and

sensitivity towards aniline vapor with a detection limit of 8.6 ppm. Upon exposure to the saturated aniline vapor for 15 s, 90% and 80% fluorescence quenching was observed for nanofibers and nanoparticles, respectively. However, nanowires showed only 37% fluorescence quenching after exposure to the saturated aniline vapor for 200 s. The supramolecular nanofibers mainly fabricated by gelation process, saturate and fill the entire volume on the film and the entangled piling of such fibers increases the porosity.

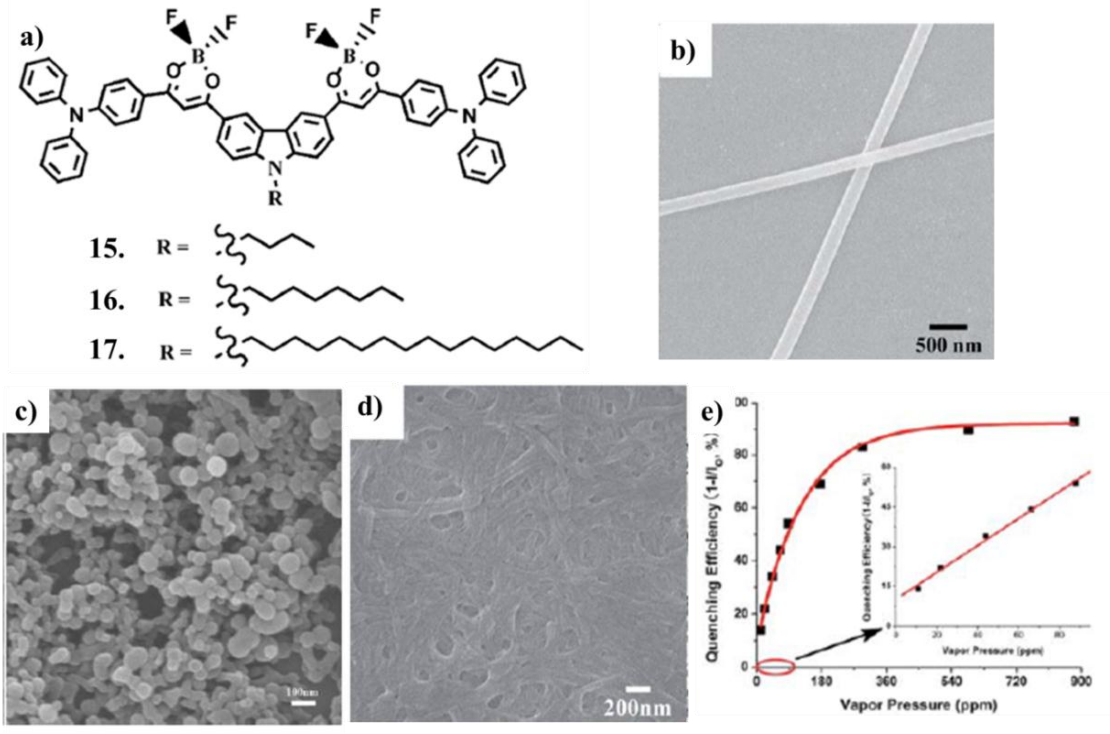

Figure 1.11. (a) Chemical structures of **15**-**17**. SEM images of (b) nanowires derived from **15**, (c) nanoparticles based on **16** and (d) 1D nanofibers based on **17**. (e) The concentration-dependent fluorescence quenching efficiency of the film based on nanofibers of **17** exposed to the vapor of aniline for 5 s.

Takeuchi *et al.* reported an enhancement in efficiency for self-assembled fibers fabricated from a binaphthyl functionalized with donor–acceptor substituted stilbenes (**18**, Scheme 1.1).[20] The molecule forms an ill-defined structure in chloroform, whereas in toluene-chloroform mixture (3:1), it self-assembles resulting in the formation of entangled network of fibers. The bright yellowish-green fluorescence of the pristine film comprised of such fibrillar network showed about 91% fluorescence quenching on exposure to saturated DNT vapors for 10 min, whereas the film of the same molecule drop cast from chloroform showed just 12% fluorescence quenching under identical conditions. This work demonstrates the application of self-assembly for the enhancement of functional properties of organic molecules to make them suitable as analyte sensors.

Mukherjee *et al.* reported a new type of supramolecular fluorescence sensor from a π-electron rich fluorophore for the detection of trace amount of nitroaromatic explosives. A π-electron rich supramolecular polymer, 9,10-bis(1,3-dicarboxylicphenyl-5-ethynyl)anthracene (**19**) and its discrete analogues (**20** and **21**) were used for selective detection of nitroaromatic explosives such as TNT and picric acid (PA) both in solution as well as in thin-film.[21] Amplification of optical signal caused by long range exciton communication along supramolecular chain formed by strong intermolecular interaction by adjacent molecules of **19** results in high sensitivity of **19** for the electron deficient quencher. The overall quenching efficiency/sensitivity of the analogous discrete systems (**20** and **21**) in the solid

state is lower due to the absence of polymeric arrangement *via* H-bonding when compared to supramolecular chain of **19** in the film state.

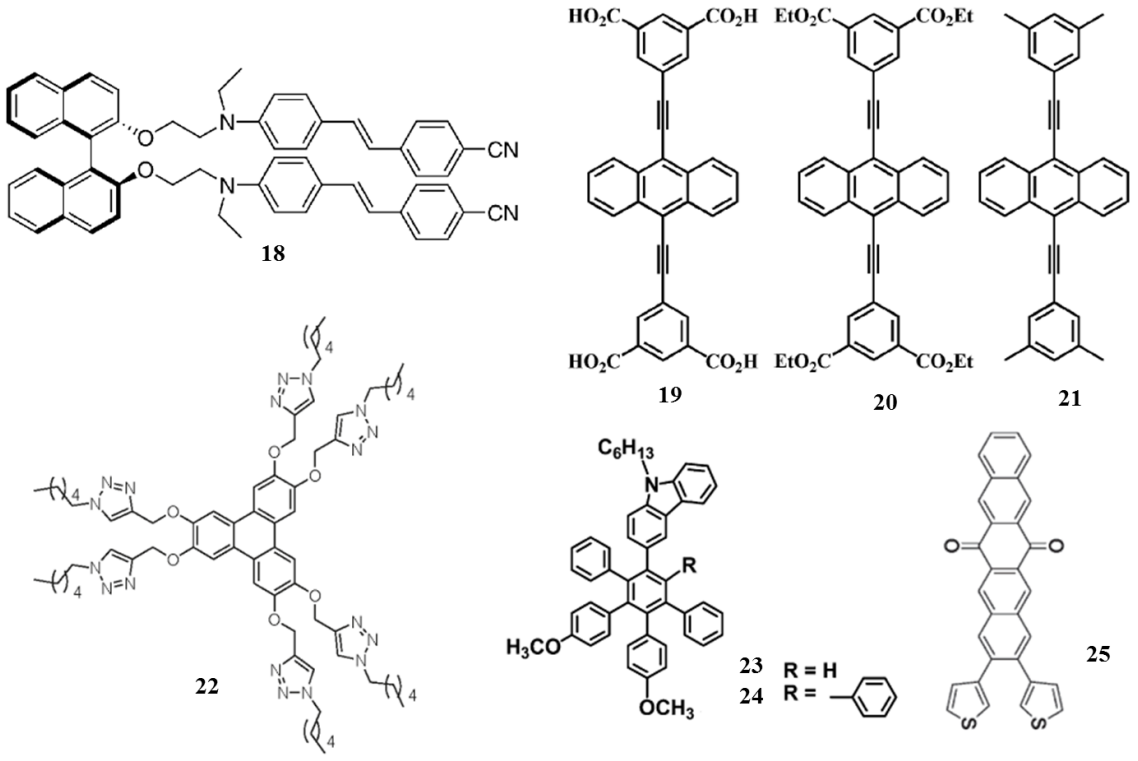

Scheme 1.1. Molecular structures of different stimuli responsive π-systems.

Bhalla and co-workers have synthesized the triphenylene derivative **22**, which forms supramolecular aggregates in bulk as well as in solution phases, using "click" chemistry. In bulk phase at high temperature, long-range stacking of columns were observed which leads to the formation of stable and ordered columnar mesophase. Electron rich derivative **22** works as an efficient and sensitive fluorescent sensor for nitroaromatic explosives. These authors have developed different π-systems (**22-25**, Scheme 1.1) for sensing explosives in the vapor phase, solid state and aqueous media.[22]

1.4. Stimuli responsive π-gelators

Organogels derived from molecules with more than one aromatic π-unit either fused or conjugated are called "π-gels" which are soft, non-flowing materials.[2b] Recent interest in soft materials based on gel chemistry has led to the design of a variety of π-gelators which attracted the attention of interdisciplinary scientists. This is because π-conjugated molecules are extensively used in organic electronic devices such as, light emitting devices (LEDs), field effect transistors (FETs) and photovoltaic devices (PVDs).[23] Solvent polarity and temperature are the crucial factors for maintaining the balance between gelator-solvent and gelator-gelator interactions. The role of solvent is crucial in the nucleation and growth processes of the self-assembly and gelation since it assist/hinder the non-covalent interaction between the gelator molecules. By effective self-assembly and gelation, optical, morphological and electronic properties of π-gelators can be significantly modulated.[2a,24] Depending on the associated groups or functional property of the π-system, π-gels respond to various stimuli such as temperature, light, electric field, metal ions, ultrasound, pH and/or a combination of these.[25] Multi-responsive (more than dual-responsive) organogels and assemblies are a new class of fascinating materials since their properties can be tuned with more than two external triggers.

1.4.1. Multistimuli responsive organogelators

In 2002, Pozzo *et al.* demonstrated the multistimuli responsive organogelator 3,3-diphenyl-*3H*-naphtho[2,1-b]pyran covalently linked to sodium *N*-acyl-11-aminoundecanoate.[26] Addition of sodium hydroxide to DMF and DMSO solution of the gelator resulted in the formation of homogeneous solutions of neutral carboxylic species which are reversibly transformed into gels. This approach establishes a new route towards the creation of nanosized architectures which could also be reversibly influenced upon irradiation and protonation. Gels become colored and then begin to flow upon irradiation using a 366 nm lamp. When irradiation stops, the color gradually disappears to yield a viscous solution which does not revert spontaneously into a gel. Gelation was simply achieved upon heating and then cooling.

Rowan and co-workers introduced the use of reversible metal-ligand interactions to build metallo-supramolecular gel like systems which are responsive to diverse stimuli.[27] The tridentate ligand, bis(2,6-bis(1-methylbenzimidazolyl)-4-hydroxypyridine) (**26**), used as a potential ligand for the construction of larger aggregates. The use of bis-ligand functionalized compound **26** as the monomer unit in conjunction with either Co(II) or Zn(II) ions as the linear chain extension binding units, and La(III) or Eu(III) ions as the cross-linking components resulted in the formation of four possible metallo-supramolecular gel materials **26**:Co/La, **26**:Zn/La, **26**:Co/Eu, and **26**:Zn/Eu (Figure 1.12a). At 100 °C, the orange color of

these materials persists in solution, suggesting that it is the La/ligand interactions which are being thermally broken. Such materials were also mechanoresponsive, exhibiting a thixotropic (shear-thinning) behavior. Shaking of 1:Zn/La result in the formation of a free-flowing liquid, which upon standing for ca. 20 s results in the reformation of the gel like material (Figure 1.12b,c).

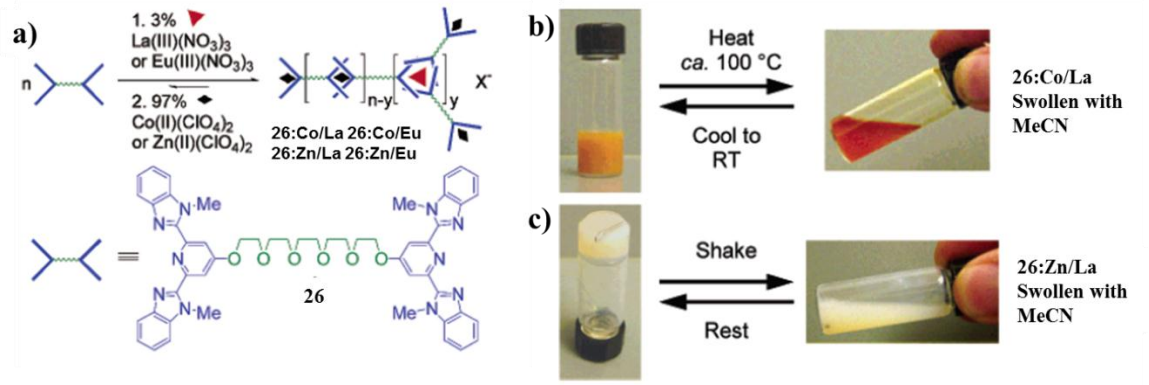

Figure 1.12. (a) Schematic representation of the formation of a metallosupramolecular gel like material using a combination of lanthanoid and transition ions mixed with monomer **26.** (b)The thermoresponsive nature of **26**:Co/La and (c) the mechanoresponsive nature of the thixotropic **26**:Zn/La system.

Fang *et al.* reported a cholesterol-appended ferrocene derivative, a supergelator and responsive to various stimuli such as redox, mechanical, thermal and ultrasound (Figure 1.13).[28] The molecule was designed in such a way that carbonyl amide groups were intentionally introduced into the linker structures in order to give the ferrocene derivatives some hydrogen-bond formation sites and to enhance their aggregation ability and thereby leading to the formation of extended

structures. Compound **27** forms gel in cyclohexane and CCl_4 at room temperature and the critical gelation concentration (CGC) for cyclohexane is only 0.09 wt % and hence falls into the category of super-gelators. However, the compound **28** requires distinctly higher concentration (2.5%, w/v) and longer time to gelate cyclohexane when compared to **27**. The length and structure of the spacer connecting the cholesterol entity and ferrocene residue is crucial for the gelation abilities of these compounds. Increasing the length of the spacer results (**28** and **29**) in a complete loss of the gelation ability.

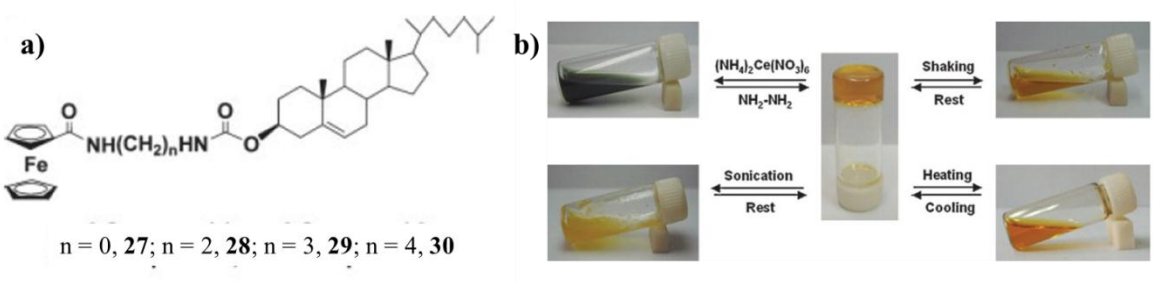

Figure 1.13. (a) Structure of the cholesterol-appended ferrocene derivatives **27**-**30** (left). (b) Reversible sol–gel phase transition of the gel of **27**/cyclohexane triggered by chemical redox reaction, shear stress, sonication, and temperature.

A change in the oxidation state of the central ion of ferrocenyl residue causes a disturbance on the interaction of adjacent ferrocenyl moieties. Subsequent damage to the intermolecular hydrogen bonding interaction will affect the supramolecular structures of the aggregates resulting in breaking of gel. The sol-gel phase transition induced by chemical oxidation and reduction of the ferrocenyl moiety

was confirmed by parallel experiments, in which NH_4NO_3 and $Ce(NO_3)_3$ were used instead of $(NH_4)_2Ce(NO_3)_6$ and no changes were observed during the time scale of the experiment. Immediate sol–gel phase transition can be induced by shaking the gel vigorously. Resting the solution resulted in gelation again. Ultrasonic treatment is another effective way to trigger the phase transition of gels.

Zhang and co-workers have developed a multistimuli responsive organogel from a low molecular organogelator appended with electroactive tetrathiafulvalene (TTF) and photoresponsive azobenzene groups (**31**) (Figure 1.14).[29] The sol-gel transition for the organogels of **31** was reversibly tuned by manipulating the redox state of the TTF group. It is known that the TTF group can be reversibly transformed to the corresponding radical cation ($TTF^{\bullet+}$) either chemically or electrochemically. When one equiv. of $Fe(ClO_4)_3$ was carefully placed above the gel of **31** in CH_2Cl_2/CH_3OH (3/1, v/v), the gel gradually destroyed within 10 min, leading to a dark green suspension. When excess ascorbic acid was added to reduce $TTF^{\bullet+}$ to the neutral TTF, the dark green solution became an orange solution instantly. On further heating and cooling, the gel phase was regenerated (Figure 1.14b). The molecule **31** gelate the CH_2Cl_2/CH_3OH mixture (3/1, v/v) containing Bu_4NPF_6 (0.1 M). The gel was converted to the dark green solution by applying an oxidation potential of 0.75 V (vs Ag/AgCl) for 90 s. When a reduction potential of -0.20 V (vs Ag/AgCl) was sequentially applied for 140 s, the solution changed to orange with a small amount of precipitate. Subsequent heating and

further cooling result in gel formation (Figure 1.14c). The organogel of **31** in CH_2Cl_2/CH_3OH (3/1, v/v, 8.0 mg/mL) in an NMR tube was slowly collapsed and converted into solution after UV (365 nm) light irradiation for 1 h at room temperature. Further exposure of solution to a visible light (λ >460 nm) irradiation for 2 h followed by keeping in dark at 5 °C for 18 h, resulted in the regeneration of the orange-yellow gel (Figure 1.14d). The fibrous xerogel formation was observed with SEM analysis (Figure 1.14e).

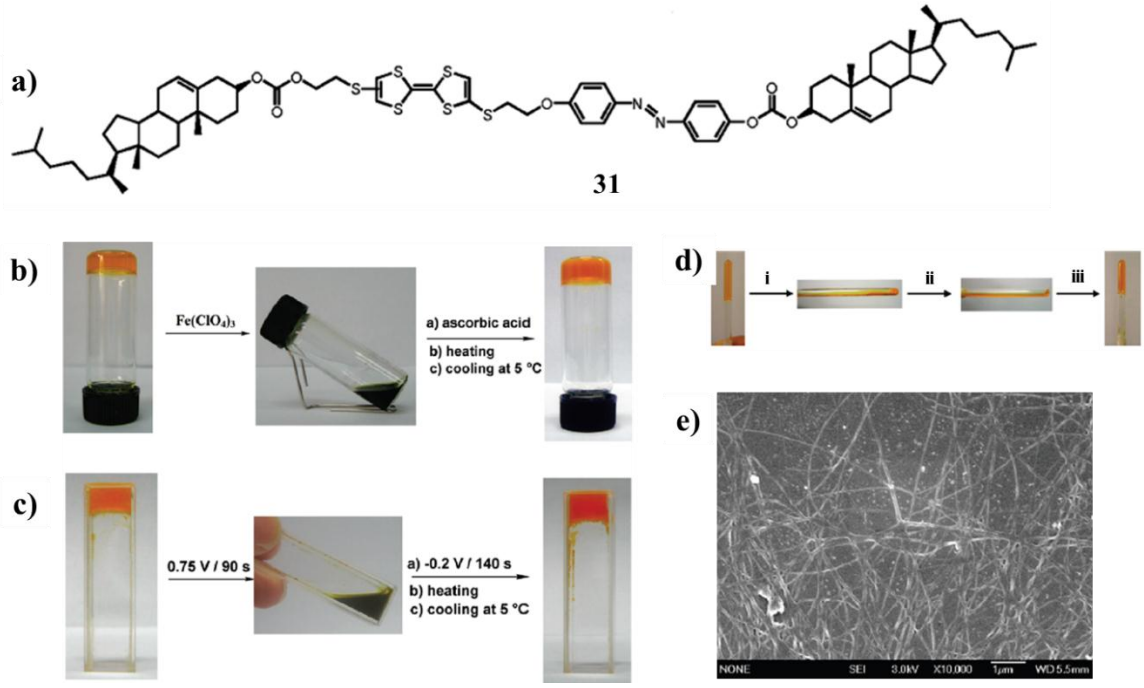

Figure 1.14. (a) Chemical structure of **31**. Reversible tuning of the gel formation of **31** (8.0 mg/mL) in CH_2Cl_2/CH_3OH (3/1, v/v) (b) by chemical oxidation and reduction and (c) by sequential electrochemical oxidation and reduction (d) by UV light irradiation for 30 min (i); 1 h (ii); further visible light irradiation for 2 h and then darkness at 5 °C for 18 h (iii). (e) SEM image of the gel **31**.

A class of efficient low-molecular-weight gelators composed of 2-substituted anthraquinone and hydrazide subunit were synthesized (Figure 1.15a) and the structure property relationships with respect to their gelation abilities in organic solvents were investigated by Chen and co-workers.[30] These gels show thermo-reversible gel-to-sol transition that occurs by self-assembly and dis-assembly processes, respectively (Figure 1.15b,c). The SEM pictures of the dried sample exhibited a three-dimensional network in toluene and ethyl acetate. The electron micrographs showed the transformations in the morphology of the same gelator in different solvents (Figure 1.15d-g). It is also observed that the gelation of some compounds (**32b-e**) could not occur in polar solvents by heating and cooling but form stable gels during the cooling process in the presence of ultrasound which remarkably change the morphology of the assembly in pyridine. The morphology of the precipitate and xerogel of **32c** were strongly dependent upon the solvents and external ultrasound stimuli. The precipitate of **32c** from pyridine gives flower-like spherical structures with an approximate diameter 20-40 mm, whereas the xerogel from pyridine under ultrasound gives rod shaped fibrillar network of approximate width 0.5-1.5 mm and approximate length of 10-15 mm. Moreover, the reversible gel to sol phase transition was achieved by adding trifluoroacetic acid (TFA) and triethyl amine (TEA). The transparent gel of **32c** in toluene was converted into fluid solution by the addition of 10 equiv. of TFA and the solution was further changed into gel upon the addition of 12 equiv. of TEA. It has been

realized that TFA intercalates the intermolecular hydrogen bonding and thus breaks the gel.

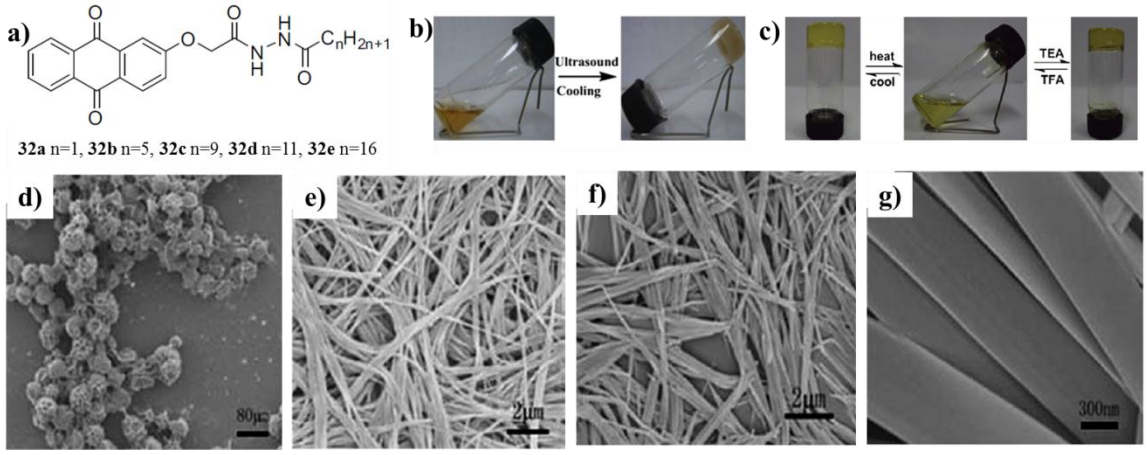

Figure 1.15. (a) The chemical structures of the low-molecular-weight gelators **32**a-e. (b) Ultrasound induced gelation in pyridine and (c) reversible gel to sol phase transition by heating-cooling and adding TFA/TEA of **32c**. (d) SEM images of **32**c precipitates from pyridine, (e) xerogel from pyridine under ultrasound, (f) precipitates of **32**c from DMF and (g) xerogel from DMF under ultrasound.

A new dendritic gelator **33** with photoresponsive azobenzene groups exhibited reversible sol-gel phase transition in response to external stimuli including temperature, sonication, light and shear-stress (Figure 1.16b-d).[31] Stable organogels were formed in most organic solvents through heating-cooling processes. A dense fiber like morphology for **33** in different organic solvents was observed by SEM and TEM (Figure 1.16e-g). Gels were formed upon ultrasonic treatment in some polar solvents, such as 2-methoxyethanol, 2-ethoxyethanol, acetone, ethyl acetate and mixture of anisole/hexane. An orange suspension instead

of a stable gel was observed when a hot solution of the gelator in 2-methoxyethanol was cooled to room temperature.

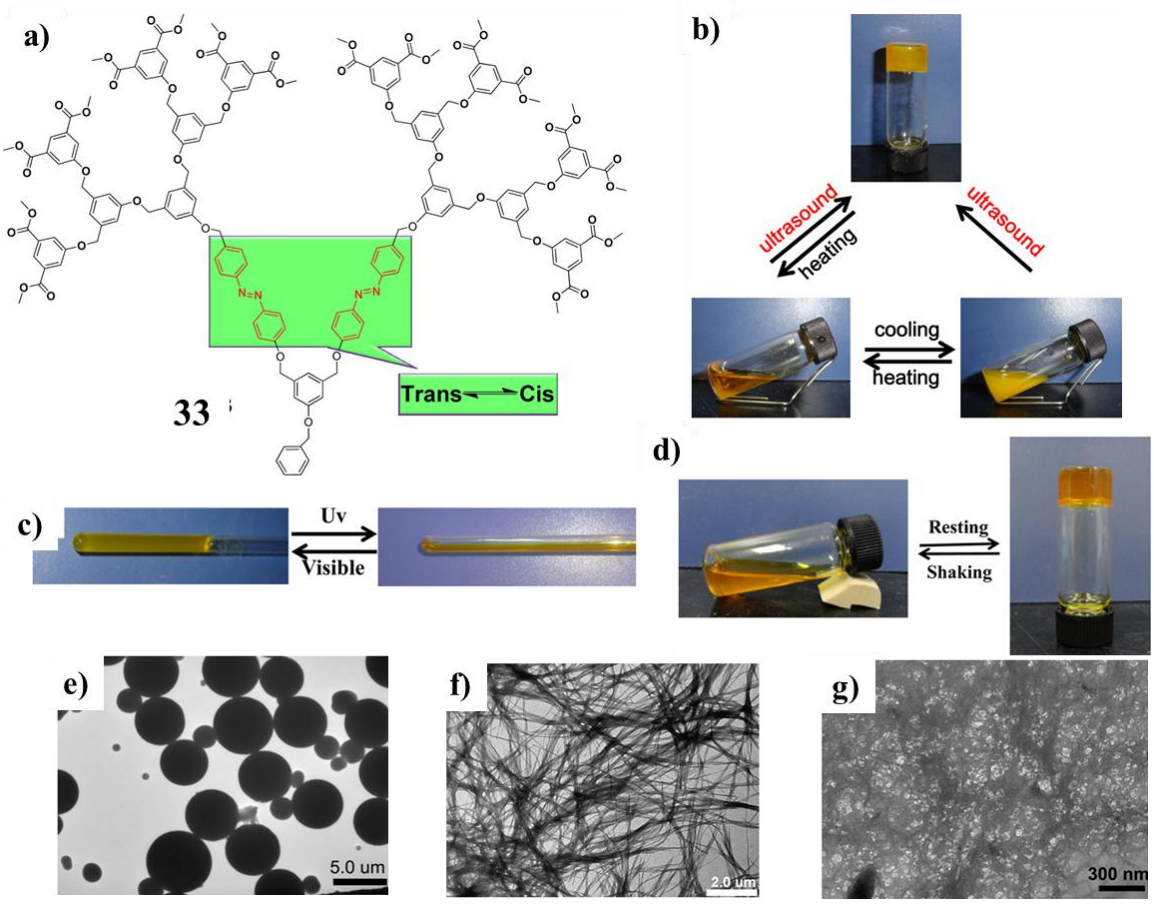

Figure 1.16. (a) Chemical structure of the dendritic organogelator **33**. (b) Reversible sol−gel phase transition of the gel of **33**/ 2-methoxyethanol triggered by sonication. Photographs of the gels of **33** in toluene (0.67 wt %) (c) before and after UV irradiation (365 nm) for 20 min and (d) showing thixotropic behavior. TEM images of **33** (e) before and (f) after sonication. (g) SEM image of the xerogel of **33** after drying from the gel state.

However, when the suspension or its hot solution was submitted to sonication

for a few minutes, a shining gel was formed rapidly. In addition to temperature and sonication, the gel-sol phase transition was responsive to light also. Upon UV irradiation, the stable orange gels were found to collapse gradually and finally turned into solution. Also, gel regeneration was achieved by the subsequent irradiation with visible light. These dendritic gels from most of the tested organic solvents were thixotropic also. Upon vigorous shaking, the transparent gel of **33** in toluene was changed into a clear sol. Upon resting, the gel regenerated rapidly. These prominent features of the dendritic organogelator **33** impart the qualities of an excellent soft material with promising potential applications. Ning and co-workers have synthesized a new low molecular-weight gelator, **34** (Figure 1.17a), composed of a hydrazone group, an azobenzene unit, and a 3,4,5-trialkoxybenzoic acid moiety, which can respond to multistimuli by perturbing the hydrogen-bonding and amphiphilic properties.[32] Organogel formed by heating-cooling of **34** in DMF was analyzed with SEM (Figure 1.17b,c). On the one hand, the hydrazone group introduced into the gelator **34** offered a convenient way to modulate the sol–gel transformation by adding anions to disturb the hydrogen bonds (Figure 1.17d). On the other hand, the azobenzene unit in the gelator structure was also receptive to trigger the gel–sol transition, attributing to the alternation of the amphiphilic properties of the gelator through complexation/decomplexation with α-CD as a result of photoisomerization of the azobenzene group (Figure 1.17e).

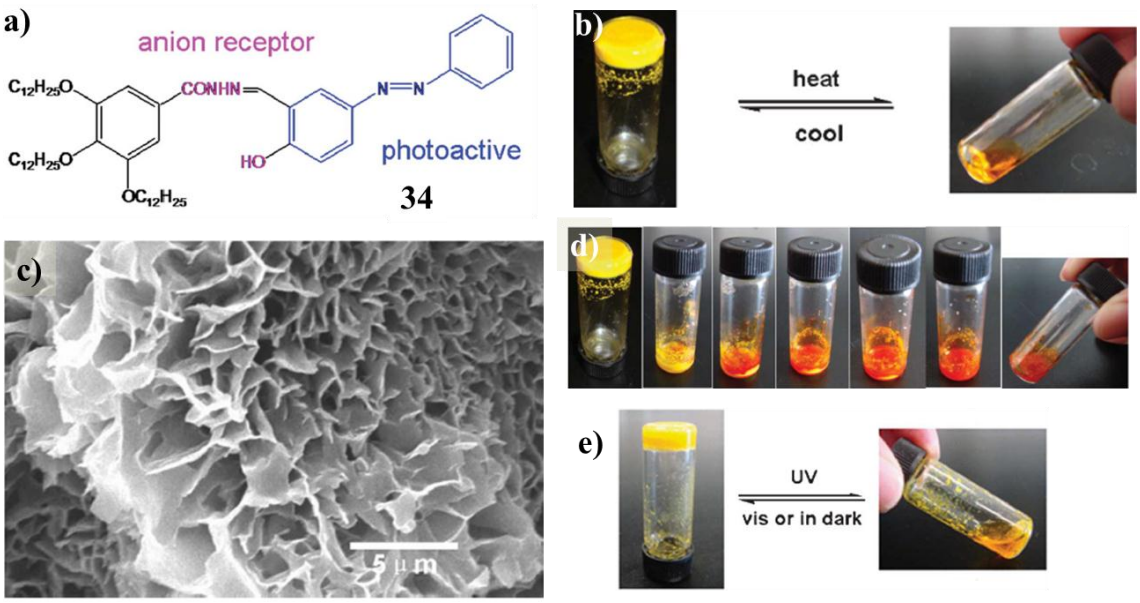

Figure 1.17. (a) Chemical structure of **34**. (b) Organogel formed by heating-cooling of **34** in DMF. (c) SEM image of the xerogel **34**. (d) Organogels formed from a solution of **34** in DMF after addition of solid tetrabutylammonium phosphate salt (1 eqv.) at different time intervals from 0 to 10 min. (e) Organogel formed from a solution of 1% **34** with α-CD in DMF in the dark or vis irradiation.

Wang and co-workers have reported a CF_3-substituted benzothiadiazole-cored phenylenevinylene fluorophore (**35**) with pronounced multistimuli-responsive fluorescence behavior.[33] When a hot solution of the compound **35** in DMF was left at room temperature for over 0.5 h, some organic fibers were gradually formed in the solution, suggesting that compound **35** has the ability to form assembly due to non-covalent intermolecular interactions (Figure 1.18). Interestingly, after the DMF solution was quickly cooled to room temperature in the water bath followed by sonication (0.45 W/cm^2, 40 kHz, 30 s), the homogeneous solution turned into an opaque viscous state and formed a stable organogel. Self-assembled

microstructures of the compound **35** showed thermo-induced fluorescence variation accompanied with fluorescence switching from green to orange. The treatment of the microrods at 220 °C for 10 min resulted in remarkable fluorescence transition from green (550 nm) to orange (592 nm).

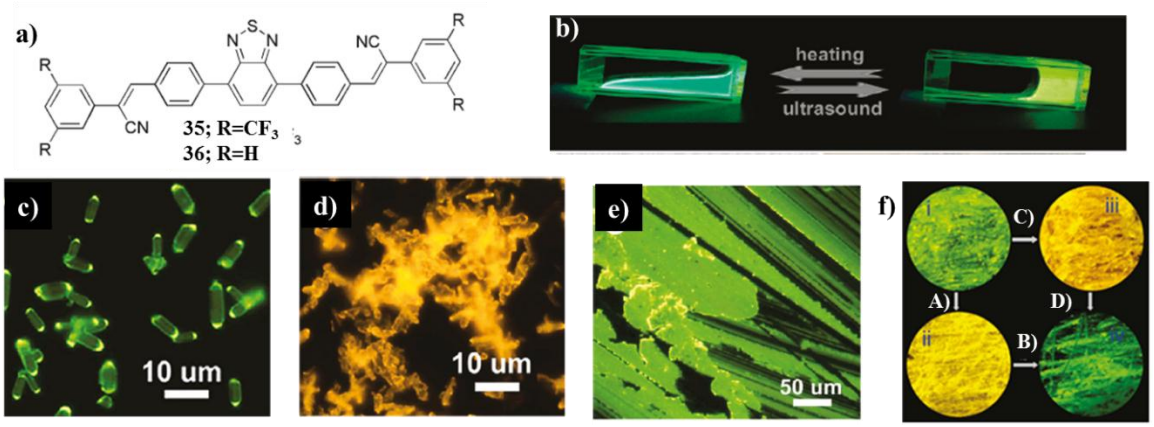

Figure 1.18. (a) Chemical structures of **35** and **36**. (b) Stimuli-responsive gelation properties of compound **35** in DMF solution upon heating and ultrasound treatments. Fluorescent microscopy images: (c) microrods, (d) heated microrods, (e) microsolids upon grinding. (f) Vapochromism of the ground sample under different organic vapors (excited at 365 nm): (A) ether (1 min or even longer), (B) THF (0.5 h), (C) THF (1 min), and (D) THF (0.5 h).

Recrystallization of the compound **35** from a mixture of chloroform and petroleum ether (1:1, v/v) or vacuum sublimation resulted in an orange powder with bright orange luminescence. Interestingly, grinding with a spatula or pestle, changed the sample into a yellow solid with a green fluorescence. The ground sample recovered its original orange color and luminescence by heating at about

100 °C for 1 min. Vapochromism was observed in this system and organic vapors could result in fluorescence changes between orange and green. After exposure of the ground solid to a saturated ether vapor for about 1 min or even longer, the fluorescence changed from green to orange. Exposing this in-situ-formed orange sample to THF vapor for over 0.5 h generated an intense green emissive powder. Exposure of the ground solid to THF vapor for about 1 min resulted in an orange fluorescence and the color of the formed orange sample further converted to green when exposed for longer time.

1.5. Mechanochromic π-assemblies

Mechanochromic luminescent materials change their emission colors (spectra) when appropriate mechanical forces (such as grinding, crushing, rubbing, or extrusion) are applied.[34] Many examples are known about mechanochromic chromophores covalently incorporated into polymer matrices.[35] These include polydiacetylenes, poly(urethane-diacetylene) segmented copolymers and poly(methyl acrylate) with spiropyran motifs covalently linked in the middle of the chain.[36] Other substances that exhibit significant color changes with mechanical forces include azobenzenes and cyano-substituted oligo(*p*-phenylenevinylene) (OPV) chromophores when incorporated into polyurethanes or polyesters.[37] Weder *et al.* reported that self-assembled dyes dispersed in a polymer matrix upon deformation transform into monomeric species.[38] Dispersing a certain

concentration of OPV derivatives with cyano groups which generally form excimers *via* a melt-processing method in a linear low-density polyethylene (LLDPE) matrix yielded a deformation sensitive polymer blend (OPV/LLDPE). Several other chromophore-polymer blends were reported after the first report on a mechanochromic system by Weder, that include poly(propylene) (PP) blend films with stilbene derivatives, poly(phenyleneethynylene) derivatives and perylene derivatives. Preparation, properties, mechanism, and possible application of such polymer blends have been well studied and documented in the literature.[39] Apart from the blending technique, the piezofluorochromic behavior can also be attained by switching the solid state molecular packing modes.[40] Tang *et al.* have reported that aggregation-induced emission (AIE) materials are more efficient emitters in the aggregated state than in the dissolved form.[41] The mechanofluorochromism of such AIE compounds were first reported by Park *et al.* in 2010.[42] The structural relationship between the aggregation-induced emission compounds and mechanofluorochromism is recognized based on recent results.

In the case of non-AIE based mechanochromic materials, an ordered state with relatively good emission is required for mechanofluorochromism. The first report of such a mechanofluorochromic compound is by Araki *et al.* with a pyrene-based dye (**37a**) containing four hexyl amide groups at the *para* position of the phenyl units.[43] A strong blue luminescence was exhibited by a white powder that was precipitated out by the addition of methanol to a chloroform solution of the dye.

Upon pressing with a spatula, the white powder with blue emission (B-form) transformed into a yellowish solid with a strong greenish emission (G-form). The green emissive solid on precipitation with chloroform-methanol mixture yielded the white powder again. The blue emission could be recovered back by heating the green emissive solid at above 112 °C (Figure 1.19). According to authors, the B-form was found stable with ordered hydrogen-bonding arrays which transformed to G-form, a metastable state, with random hydrogen bonding. Under applied pressure, the destruction of hydrogen bonding interactions occurred and the consequent mismatch in packing inhibited the formation of H-aggregates, thus facilitating the change in luminescent color.

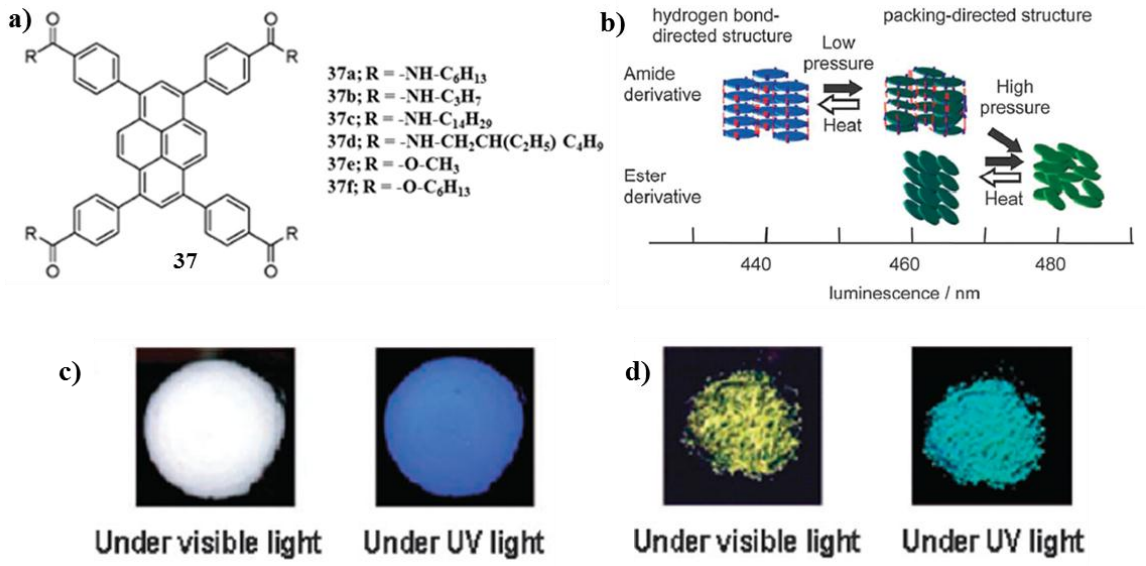

Figure 1.19. (a) Chemical structures of **37**a-f. (b) Schematic illustration of mechanochromic response of pyrene derivatives. Images of dye **37**a in B-form (c) and G-form (d) under visible light and UV light (365 nm).

Later, a few more dyes were reported by the same group in order to study the role of amide hydrogen bonds and side chains on mechanochromism. The effect of applied pressure on mechanochromism was observed, when the partially disrupted hydrogen bonds were below 9.8 MPa. Upon heating, the initial state could be restored. When pressure beyond 9.8 MPa was applied, excessive destruction of hydrogen bonds occurred and the reformation was not successful by the thermal process. The ester derivative **37f** required a higher pressure >9.8 MPa to bring a visible emission change from blue-green to green. Authors concluded that the presence of amide hydrogen bonds was essential for a sensitive and repeatable mechanofluorochromic response and that the excessive destruction of hydrogen bonds restricted the re-formation of the hydrogen bond-directed structure.[44] Subsequently, they checked the effect of alkyl chain length on the mechanochromism and they have concluded that the hexyl chain can be easily accommodated in the columnar phases, whereas the longer alkyl chains hamper the formation of such packing. Dyes with shorter alkyl chain length showed mechanochromism but the effect of thermal annealing was limited.

Later, Weder reported a series of oligo(*p*-phenylenevinylene) derivatives with mechanofluorochromic characteristics.[45] When compared to the polymer blends, the mechanochromic behavior in pure solid state of **38a-c** was small after pressing. When compressed, the blue-emitting crystalline powders of dyes **38a** and **38b** emitted a yellow color and thermal annealing of the compressed samples eased the

recovery of the original luminescent color. Followed by these reports, mechanofluorochromic behavior of the liquid crystalline dyes (**39**a and **39**b) was reported by Kato *et al.*[46] The yellow emission of the liquid crystalline states converted to blue-green for the pyrene derivative **39**a and to light blue for the anthracene derivative by mechanical shearing (Figure 1.20).

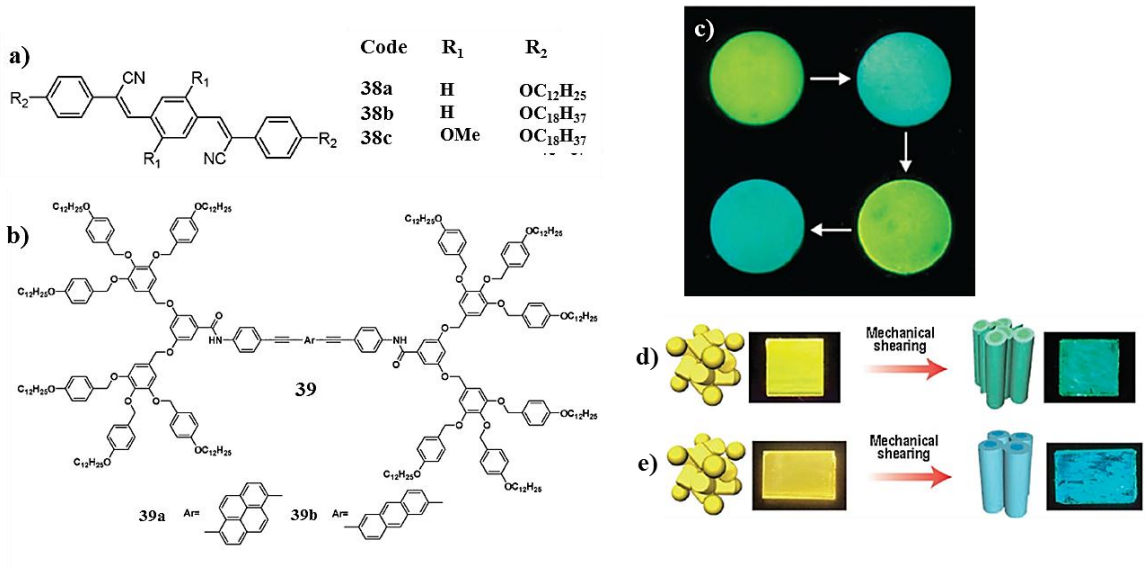

Figure 1.20. (a) Chemical structures of **38**a-c, (b) **39**a-b. (c) Mechanochromism of a dye **38**a–KBr mixture pressed for 1 min at 1500 psi. The change in luminescent color and molecular assemblies for the dyes (d) **39**a and (e) **39**b.

During recent years, a number of self-assembled dyes have been reported by different groups around the globe aiming towards pressure sensitive materials. Most of them have been found to possess mechanofluorochromic properties.[47] Such reported dyes (**40**-**51**), which possess mechanochromism are shown in Scheme 1.2. Harima *et al.* reported a series of heteropolycyclic donor-acceptor π-

conjugated (D-π-A) fluorescent dyes (**40a-l)**. The mechanofluorochromic property of these molecules decreased with increasing steric size of the substituent and with increasing electron accepting capability of the *para* substituted phenyl group.[48] Thus authors proved that dipole moment has a crucial role in developing mechanofluorochromic materials by designing such D-π-A fluorescent dye molecules.

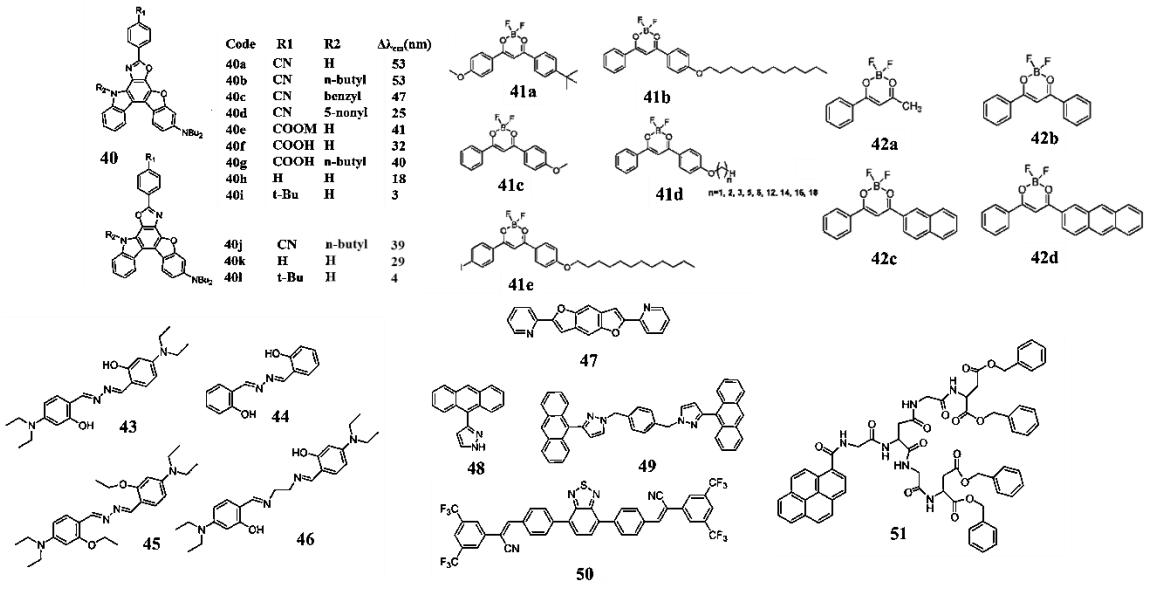

Scheme 1.2. Molecular structures of different mechanochromic dyes.

A dye containing boron diketonate (**41a**) reported by Fraser *et al.* possessed different emission colors depending on the crystal types and processing conditions.[49] When the crystals were crushed or the solid samples were smeared, the emission color was red-shifted significantly and the fluorescence spectrum was drastically broadened. The molecules **41b** and **41c,** apart from the difference in their alkyl substituents showed different mechanochromic properties (Scheme

1.2).[50] The molecules **41d** with different alkyl chain length showed mechanochromic luminescent properties except the one with short chain length C_n = 1. Molecules with longer chain ($n \geq 6$) were not returned to the original annealed emissive state even after months on quartz substrates. An iodo compound of the dye (**41e**) significantly exhibited a red-shift in fluorescence upon mechanical perturbation. When the solid film sample was smeared under air, the emission was quenched, however, it became orange under nitrogen atmosphere. This is ascribed to the possibility of the single excited state generation closer to the triple excited state by an increase in the coupling between the two states and subsequent induction on luminescence quenching. Fraser *et al.* have also studied the effect of arene substitution on mechanofluorochromism in a series of boron diketonate dyes (**42a-d**) with methyl, phenyl, naphthyl, and anthryl groups.[51] A red shift in the emission maximum was observed for the dye depending on the arene conjugation length. Interestingly, authors observed an effect of thickness on the recovery of emission after smearing. They found that the recovery of powder sample is slower when compared to an amorphous film of the same sample, which was considered as a sample thickness effect. Subsequently, they observed that thermal annealing was an important step in observing the mechanochromism of different samples. The lifetime values of smeared and amorphous samples were found similar since smearing generated an amorphous state.

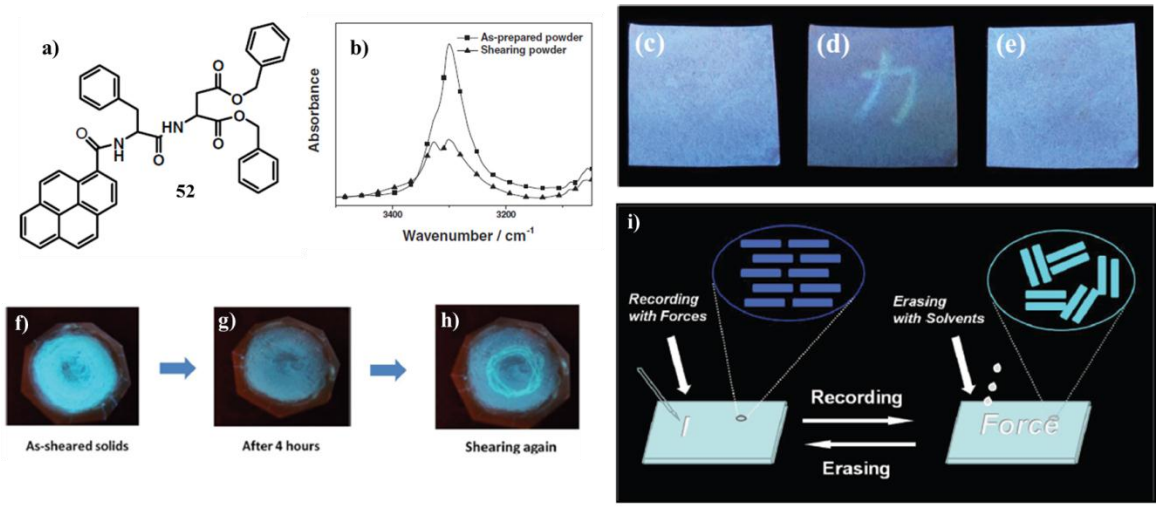

Figure 1.21. (a) Molecular structure of **52**. (b) FT-IR spectra of **52** in different states. (c) Fluorescent image of a suspension of **52** deposited on a filter paper. d) The Chinese character "force" was written on the paper. e) Pattern erased by adding CH_3OH on the paper and drying. (f-h) Images of **52** after shearing, after 4 h and after re-shearing at the center, respectively. (i) Illustrations of luminescent color variation from blue to bright green.

It has been noted that self-assembly has a pivotal role in making mechanofluorochromic materials. According to Fraser, formation and disappearance of aggregates might be the reason of variation in luminescence upon thermal annealing and smearing.[50,51] The driving force must be the thermally induced formation and mechanically induced destruction of aggregate. Such an example was reported by Jia *et al.* where a polypeptide-based dendron from glycine and aspartic acid with a pyrenyl group as the focal luminophore (dye **51,** Scheme 1.2) exhibited both reversible mechanofluorochromic and thermal dependent luminescent properties.[52] A dual-mode switching of fluorescence in the

condensed state was achieved in the molecular assembly of a dipeptide-based molecule by controlling the microstructure.[53] The emission band at 412 nm appeared for the as-prepared powder of **52** which was red-shifted to 484 nm after shearing with a spatula. The involvement of hydrogen bonding interactions in the transition of molecular arrangements was revealed by the Fourier transform infrared (FT-IR) spectra (Figure 1.21). The stretching vibration of the amide NH group absorption band at 3300 cm^{-1} was monitored for the as-prepared powder of **52** which indicated the existence of strong hydrogen bonding interactions. It significantly decreased and shifted to a higher wavenumber upon shearing. Based on such evidence, authors proved the force-induced disruption of hydrogen bonding and the variation of molecular packing of the dye **52**.

Tian and co-workers have reported another example of a piezochromic luminescence of the molecule **53**, which showed noticeably different emission in its three crystals.[54] The photoluminescence spectra showed a change in the molecular aggregation state in the powder form of **53** upon grinding or under external pressure leading to an enhanced intermolecular π–π interaction and thus induced the piezochromic luminescence (Figure 1.22). Such a pressure dependent luminescence switching of **53** was potentially used for application in pressure sensing materials as shown in Figure 1.22.

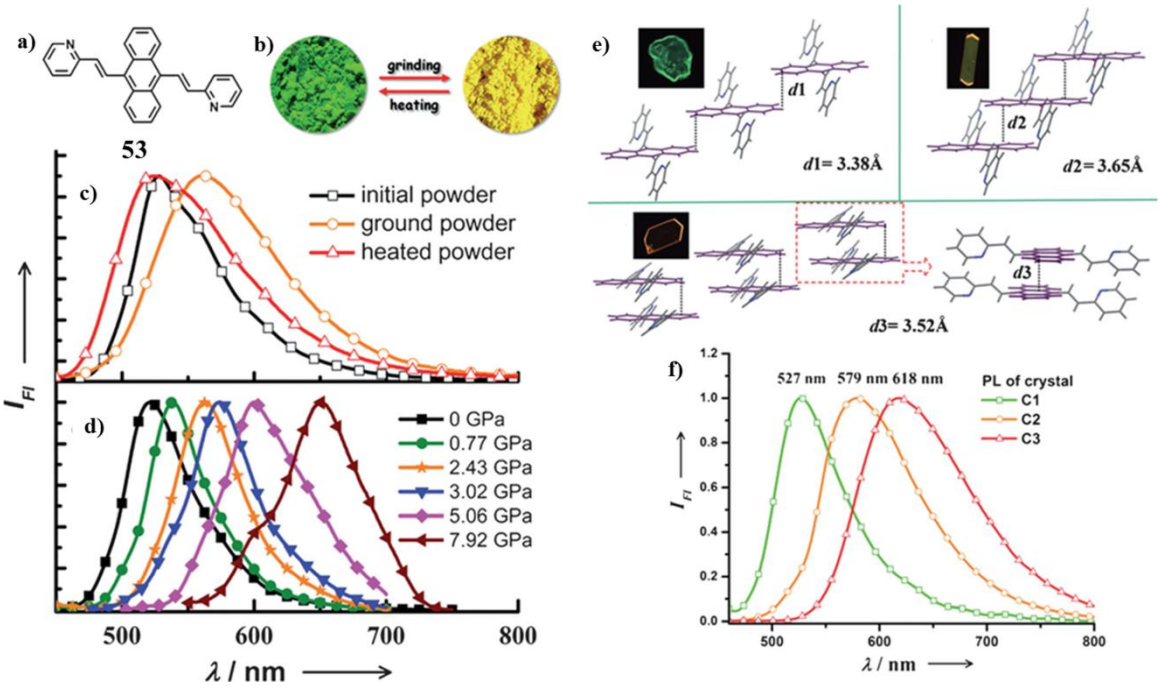

Figure 1.22. (a) Molecular structure of **53**. (b) Photographs of the ground powder and the heated powder under UV light (365 nm). (c) PL spectra of the initial, ground, and heated powders. (d) PL spectra of **53** (powder) under external pressure. (e) Stacking modes of the anthracene planes in adjacent **53** molecules in three single crystals. f) PL spectra of the three different crystals.

Most of the organic mechanofluorochromic materials described are based on the changes in the mode of packing of the molecule. Therefore, fluorescent molecules having assemblies that are easily amenable to changes in the molecular arrangements have great chance of being mechanochromic systems. In this context, chromophores based π-gelators are potential candidates as mechanochromic systems. However, not much research has gone in this direction.

1.6. Origin, objectives and approach to the thesis

As mentioned above, electronic properties of π-systems are sensitive to intermolecular interactions, particularly the way in which the chromophores are organized. **OPV**s are one of the extensively studied classes of molecules due to their interesting optoelectronic properties. Ajayaghosh and co-workers have reported a number of functionalized **OPV**s and their spontaneous self-assembly from nonpolar hydrocarbon solvents at low concentrations leading to gelation *via* the formation of entangled fiber network.[24h] **OPV** gelators exhibit significant red shift of the emission during the gelation. This property has been shown to be due to the efficient energy migration between aggregates of different energy levels. Therefore, **OPV** gels are very good energy donor scaffolds for energy transfer to a suitable acceptor. This hypothesis was proved by energy transfer from **OPV** gels to entrapped Rhodamine B as the acceptor.[55]

Guenet and co-workers carried out a series of experiments to understand the role of functional group and solvent in the gelation process of **OPV**s.[56] Such experiments detailed the dramatic effect of the solvent on the molecular structure and on the morphology of the organogels. These investigations revealed that the self-assembly of **OPV**-based gelators can be extremely sensitive to the chemical structure of the end groups located on the backbone. These end groups also play a decisive role in the morphology and the molecular level structure of **OPV**-based

organogelators. Ajayaghosh *et al.* demonstrated the influence of the length of the oligomer in a linear π-system on molecule–molecule and molecule-substrate interactions, which could influence the morphological features of the self-assembly.[57]

Even though modulation of optical, chiroptical and morphological features of **OPV** based gelators are studied well, these properties have not been properly exploited for any potential application. From the above mentioned studies on **OPV** self-assemblies and gels, we speculated that they are potential stimuli responsive materials. One of the main objective of the present thesis is to have a detailed investigation on the sensing and stimuli responsive behavior of fluorescent **OPV** gelators in solution, gel as well as in film states. For sensing purpose, we have chosen an **OPV** gelator with high solid state quantum yield and a unique molecular packing in the gel state.

Aggregation behavior and stimuli-responsive properties of various linear π-systems and their hybrid composites were reported by Ajayaghosh and co-workers.[2b] Organogelation of **OPV**s brings significant changes to the fluorescence properties, which are responsive towards temperature. In view of creating stimuli responsive materials, the design and synthesis of a variety of **OPV**s with appropriate structural variations were planned (Scheme 1.3). The structural design involves **OPV**s with N-H hydrogen bonding end groups and with long aliphatic hydrocarbon side chains. The presence of pyridine as the end functional group

provides additional functionality as a stimuli responsive gelator with multiple properties (Scheme 1.3a). The non-covalent interactions in benzene appended derivatives were expected to lead the formation of supramolecular assembly and gels in hydrocarbon solvent (Scheme 1.3b). Detailed studies on the film state properties were planned.

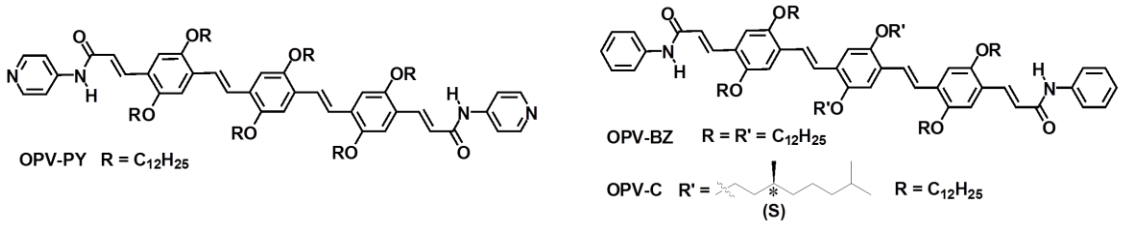

Scheme 1.3. Proposed molecular structures of **OPV**s.

It is also important to study the effect of chiral chain on the self-assembly, gelation and film state properties of such derivatives. Therefore, synthesis of **OPV** derivatives with chiral chain on either side of central benzene ring was planned. Finally, we wanted to address the stimuli responsive behavior of **OPV** assemblies at gel and film states. The present thesis is a detailed and systematic approach to the realization of the above objectives which are presented in different chapters.

1.7. References

(1) (a) Lehn, J. M. *Science* **1993**, *260*, 1762; (b) Lehn, J. M. *Science* **2002**, *295*, 2400.

(2) (a) Kartha, K. K.; Mukhopadhyay, R. D.; Ajayaghosh, A. *Chimia* **2013**, *67*, 51; (b) Ajayaghosh, A.; Praveen, V. K. *Acc. Chem. Res.* **2007**, *40*, 644.

(3) (a) Wang, Y. J.; Tang, L. M.; Yu, J. *Progress in Chemistry* **2009**, *21*, 1312; (b) Dawn, A.; Shiraki, T.; Haraguchi, S.; Tamaru, S.; Shinkai, S. *Chem. Asian J.* **2011**, *6*, 266.

(4) (a) Steed, J. W. *Chem. Commun.* **2011**, *47*, 1379; (b) Piepenbrock, M. O. M.; Lloyd, G. O.; Clarke, N.; Steed, J. W. *Chem. Rev.* **2010**, *110*, 1960.

(5) Ajayaghosh, A.; Praveen, V. K.; Vijayakumar, C. *Chem. Soc. Rev.* **2008**, *37*, 109.

(6) Zang, L.; Che, Y. K.; Moore, J. S. *Acc. Chem. Res.* **2008**, *41*, 1596.

(7) Thomas, S. W.; Joly, G. D.; Swager, T. M. *Chem. Rev.* **2007**, *107*, 1339.

(8) Palmer, L. C.; Stupp, S. I. *Acc. Chem. Res.* **2008**, *41*, 1674.

(9) An, B. K.; Kwon, S. K.; Jung, S. D.; Park, S. Y. *J. Am. Chem. Soc.* **2002**, *124*, 14410.

(10) Datar, A.; Balakrishnan, K.; Yang, X. M.; Zuo, X. B.; Huang, J. L.; Oitker, R.; Yen, M.; Zhao, J. C.; Tiede, D. M.; Zang, L. *J. Phys. Chem. B* **2006**, *110*, 12327.

(11) Naddo, T.; Che, Y. K.; Zhang, W.; Balakrishnan, K.; Yang, X. M.; Yen, M.; Zhao, J. C.; Moore, J. S.; Zang, L. *J. Am. Chem. Soc.* **2007**, *129*, 6978.

(12) Naddo, T.; Yang, X. M.; Moore, J. S.; Zang, L. *Sens. Actuators, B* **2008**, *134*, 287.

(13) Che, Y. K.; Yang, X. M.; Zhang, Z. X.; Zuo, J. M.; Moore, J. S.; Zang, L. *Chem. Commun.* **2010**, *46*, 4127.

(14) Zhang, C. Y.; Che, Y. K.; Yang, X. M.; Bunes, B. R.; Zang, L. *Chem. Commun.* **2010**, *46*, 5560.

(15) Che, Y. K.; Gross, D. E.; Huang, H. L.; Yang, D. J.; Yang, X. M.; Discekici, E.;

Xue, Z.; Zhao, H. J.; Moore, J. S.; Zang, L. *J. Am. Chem. Soc.* **2012**, *134*, 4978.

(16) Che, Y. K.; Yang, X. M.; Loser, S.; Zang, L. *Nano Lett.* **2008**, *8*, 2219.

(17) Che, Y. K.; Zang, L. *Chem. Commun.* **2009**, 5106.

(18) Che, Y. K.; Yang, X. M.; Liu, G. L.; Yu, C.; Ji, H. W.; Zuo, J. M.; Zhao, J. C.; Zang, L. *J. Am. Chem. Soc.* **2010**, *132*, 5743.

(19) Liu, X. L.; Zhang, X. F.; Lu, R.; Xue, P. C.; Xu, D. F.; Zhou, H. P. *J. Mater. Chem.* **2011**, *21*, 8756.

(20) Vijayakumar, C.; Tobin, G.; Schmitt, W.; Kim, M. J.; Takeuchi, M. *Chem. Commun.* **2010**, *46*, 874.

(21) Gole, B.; Shanmugaraju, S.; Bar, A. K.; Mukherjee, P. S. *Chem. Commun.* **2011**, *47*, 10046.

(22) (a) Bhalla, V.; Gupta, A.; Kumar, M. *Org. Lett.* **2012**, *14*, 3112; (b) Bhalla, V.; Singh, H.; Kumar, M.; Prasad, S. K. *Langmuir* **2011**, *27*, 15275; (c) Bhalla, V.; Gupta, A.; Kumar, M.; Rao, D. S. S.; Prasad, S. K. *Acs Appl. Mater. Inter.* **2013**, *5*, 672.

(23) Babu, S. S.; Prasanthkumar, S.; Ajayaghosh, A. *Angew. Chem. Int. Ed.* **2012**, *51*, 1766.

(24) (a) Ajayaghosh, A.; Praveen, V. K.; Vijayakumar, C.; George, S. J. *Angew. Chem. Int. Ed.* **2007**, *46*, 6260; (b) Ajayaghosh, A.; Varghese, R.; George, S. J.; Vijayakumar, C. *Angew. Chem. Int. Ed.* **2006**, *45*, 1141; (c) Ajayaghosh, A.; Varghese, R.; Mahesh, S.; Praveen, V. K. *Angew. Chem. Int. Ed.* **2006**, *45*, 7729; (d) Ajayaghosh, A.; Varghese, R.; Praveen, V. K.; Mahesh, S. *Angew. Chem. Int. Ed.* **2006**, *45*, 3261; (e) Ajayaghosh, A.; Vijayakumar, C.; Varghese, R.; George, S. J. *Angew. Chem. Int. Ed.* **2006**, *45*, 456; (f) George, S. J.; Ajayaghosh, A.; Jonkheijm, P.; Schenning, A. P. H. J.; Meijer, E. W.

Angew. Chem. Int. Ed. **2004**, *43*, 3422; (g) Babu, S. S.; Praveen, V. K.; Prasanthkumar, S.; Ajayaghosh, A. *Chem. -Eur. J.* **2008**, *14*, 9577; (h) George, S. J.; Ajayaghosh, A. *Chem. -Eur. J.* **2005**, *11*, 3217; (i) Yagai, S.; Aonuma, H.; Kikkawa, Y.; Kubota, S.; Karatsu, T.; Kitamura, A.; Mahesh, S.; Ajayaghosh, A. *Chem. -Eur. J.* **2010**, *16*, 8652.

(25) (a) Lloyd, G. O.; Steed, J. W. *Nat. Chem.* **2009**, *1*, 437; (b) Wang, S. H.; Dormidontova, E. E. *Soft Matter* **2010**, *6*, 1004; (c) Batabyal, S. K.; Leong, W. L.; Vittal, J. J. *Langmuir* **2010**, *26*, 7464; (d) Moriyama, M.; Mizoshita, N.; Yokota, T.; Kishimoto, K.; Kato, T. *Adv. Mater.* **2003**, *15*, 1335; (e) Mizoshita, N.; Hanabusa, K.; Kato, T. *Adv. Mater.* **1999**, *11*, 392.

(26) Ahmed, S. A.; Sallenave, X.; Fages, F.; Mieden-Gundert, G.; Muller, W. M.; Muller, U.; Vogtle, F.; Pozzo, J. L. *Langmuir* **2002**, *18*, 7096.

(27) Beck, J. B.; Rowan, S. J. *J. Am. Chem. Soc.* **2003**, *125*, 13922.

(28) Liu, J.; He, P. L.; Yan, J. L.; Fang, X. H.; Peng, J. X.; Liu, K. Q.; Fang, Y. *Adv. Mater.* **2008**, *20*, 2508.

(29) Wang, C.; Chen, Q.; Sun, F.; Zhang, D. Q.; Zhang, G. X.; Huang, Y. Y.; Zhao, R.; Zhu, D. B. *J. Am. Chem. Soc.* **2010**, *132*, 3092.

(30) Liu, J. W.; Ma, J. T.; Chen, C. F. *Tetrahedron* **2011**, *67*, 85.

(31) Liu, Z. X.; Feng, Y.; Yan, Z. C.; He, Y. M.; Liu, C. Y.; Fan, Q. H. *Chem. Mater.* **2012**, *24*, 3751.

(32) Chen, W. D.; Gong, W. T.; Ye, J. W.; Lin, Y.; Ning, G. L. *RSC Adv.* **2012**, *2*, 809.

(33) Dou, C. D.; Chen, D.; Iqbal, J.; Yuan, Y.; Zhang, H. Y.; Wang, Y. *Langmuir* **2011**, *27*, 6323.

(34) Carpick, R. W.; Sasaki, D. Y.; Burns, A. R. *Langmuir* **2000**, *16*, 1270.

(35) Roberts, D. R. T.; Holder, S. J. *J. Mater. Chem.* **2011**, *21*, 8256.

(36) (a) Pucci, A.; Ruggeri, G. *J Mater Chem* **2011**, *21*, 8282; (b) Weder, C. *Nature* **2009**, *459*, 45.

(37) Weder, C. *Chimia* **2009**, *63*, 758.

(38) Lowe, C.; Weder, C. *Adv. Mater.* **2002**, *14*, 1625.

(39) (a) Caruso, M. M.; Davis, D. A.; Shen, Q.; Odom, S. A.; Sottos, N. R.; White, S. R.; Moore, J. S. *Chem Rev* **2009**, *109*, 5755; (b) Ariga, K.; Mori, T.; Hill, J. P. *Adv. Mater.* **2012**, *24*, 158.

(40) Mutai, T.; Satou, H.; Araki, K. *Nat. Mater.* **2005**, *4*, 685.

(41) Luo, J. D.; Xie, Z. L.; Lam, J. W. Y.; Cheng, L.; Chen, H. Y.; Qiu, C. F.; Kwok, H. S.; Zhan, X. W.; Liu, Y. Q.; Zhu, D. B.; Tang, B. Z. *Chem. Commun.* **2001**, 1740.

(42) Yoon, S. J.; Chung, J. W.; Gierschner, J.; Kim, K. S.; Choi, M. G.; Kim, D.; Park, S. Y. *J. Am. Chem. Soc.* **2010**, *132*, 13675.

(43) Sagara, Y.; Mutai, T.; Yoshikawa, I.; Araki, K. *J. Am. Chem. Soc.* **2007**, *129*, 1520.

(44) Sase, M.; Yamaguchi, S.; Sagara, Y.; Yoshikawa, I.; Mutai, T.; Araki, K. *J. Mater. Chem.* **2011**, *21*, 8347.

(45) Kunzelman, J.; Kinami, M.; Crenshaw, B. R.; Protasiewicz, J. D.; Weder, C. *Adv. Mater.* **2008**, *20*, 119.

(46) Sagara, Y.; Yamane, S.; Mutai, T.; Araki, K.; Kato, T. *Adv. Funct. Mater.* **2009**, *19*, 1869.

(47) (a) Sheth, A. R.; Lubach, J. W.; Munson, E. J.; Muller, F. X.; Grant, D. J. W. *J. Am. Chem. Soc.* **2005**, *127*, 6641; (b) Shen, X. Y.; Wang, Y. J.; Zhao, E. G.; Yuan, W. Z.; Liu, Y.; Lu, P.; Qin, A. J.; Ma, Y. G.; Sun, J. Z.; Tang, B. Z. *J. Phys. Chem. C* **2013**, *117*,

7334; (c) Yamane, S.; Sagara, Y.; Mutai, T.; Araki, K.; Kato, T. *J. Mater. Chem. C* **2013**, *1*, 2648; (d) Yoon, S. J.; Park, S. *J. Mater. Chem.* **2011**, *21*, 8338; (e) Gong, Y. Y.; Tan, Y. Q.; Liu, J.; Lu, P.; Feng, C. F.; Yuan, W. Z.; Lu, Y. W.; Sun, J. Z.; He, G. F.; Zhang, Y. M. *Chem. Commun.* **2013**, *49*, 4009; (f) Sagara, Y.; Kato, T. *Nat. Chem.* **2009**, *1*, 605; (g) Chi, Z. G.; Zhang, X. Q.; Xu, B. J.; Zhou, X.; Ma, C. P.; Zhang, Y.; Liu, S. W.; Xu, J. R. *Chem. Soc. Rev.* **2012**, *41*, 3878.

(48) Ooyama, Y.; Harima, Y. *J. Mater. Chem.* **2011**, *21*, 8372.

(49) Zhang, G. Q.; Lu, J. W.; Sabat, M.; Fraser, C. L. *J. Am. Chem. Soc.* **2010**, *132*, 2160.

(50) Nguyen, N. D.; Zhang, G. Q.; Lu, J. W.; Sherman, A. E.; Fraser, C. L. *J. Mater. Chem.* **2011**, *21*, 8409.

(51) Liu, T. D.; Chien, A. D.; Lu, J. W.; Zhang, G. Q.; Fraser, C. L. *J. Mater. Chem.* **2011**, *21*, 8401.

(52) Teng, M. J.; Jia, X. R.; Chen, X. F.; Ma, Z. Y.; Wei, Y. *Chem. Commun.* **2011**, *47*, 6078.

(53) Teng, M. J.; Jia, X. R.; Yang, S.; Chen, X. F.; Wei, Y. *Adv. Mater.* **2012**, *24*, 1255.

(54) Dong, Y. J.; Xu, B.; Zhang, J. B.; Tan, X.; Wang, L. J.; Chen, J. L.; Lv, H. G.; Wen, S. P.; Li, B.; Ye, L.; Zou, B.; Tian, W. J. *Angew. Chem. Int. Ed.* **2012**, *51*, 10782.

(55) Ajayaghosh, A.; George, S. J.; Praveen, V. K. *Angew. Chem. Int. Ed.* **2003**, *42*, 332.

(56) Dasgupta, D.; Srinivasan, S.; Rochas, C.; Thierry, A.; Schroder, A.; Ajayaghosh, A.; Guenet, J. M. *Soft Matter* **2011**, *7*, 2797.

(57) Gopal, A.; Varghese, R.; Ajayaghosh, A. *Chem. Asian J.* **2012**, *7*, 2061.

Chapter 2

Attogram Sensing of Trinitrotoluene with a Self-Assembled Molecular Gelator

2.1. Abstract

Detection of explosives is of utmost importance due to the threat to human security as a result of illegal transport and terrorist activities. Trinitrotoluene (TNT) is a widely used explosive in landmines and military operations that contaminates the environment and groundwater, posing a threat to human health. Achieving the detection of explosives at a sub-femtogram level using a molecular sensor is a challenge. Herein we demonstrate that a fluorescent organogelator exhibits superior detection capability for TNT in the gel form when compared to that in the solution state. The gel when coated on disposable paper strips detects TNT at a record attogram (ag, 10^{-18} g) level (~12 ag/cm^2) with a detection limit of 0.23 ppq. This is a simple and low-cost method for the detection of TNT on surfaces or in aqueous solutions in a contact mode, taking advantage of the unique molecular packing of an organogelator and the associated photophysical properties.

2.2. Introduction

Trinitrotoluene (TNT) is a widely used military explosive, found in different explosive formulations posing threats to human life and the environment.[1] Therefore, detection of TNT has been a matter of great concern to scientists.[2] Even though a large number of reports are available, a simple approach to the detection of explosives at extremely low concentrations still remains a challenge.[1g,3] This is particularly true in the case of TNT, due to its relatively low vapor pressure when compared to other explosives.[4] Swager[5] and Trogler[6] independently have made pioneering contributions to the detection of TNT and RDX (Research Department Explosive, chemical name is Cyclotrimethylenetrinitramine). For example, fluorescent polymers containing bulky groups such as pentiptycene moiety (Scheme 1), developed by Swager and co-workers, were found to be highly efficient toward the vapor-phase detection of TNT.[7]

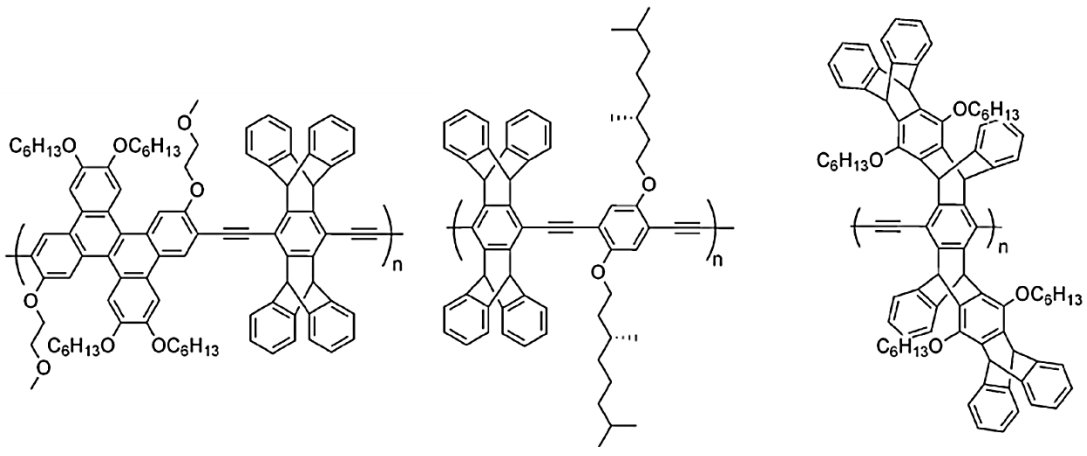

Scheme 1. Chemical structure of pentiptycene based fluorescent polymers.

In an apparently different way, Trogler and co-workers have achieved a sensitivity near picogram level in solid-phase sensing of explosives using metalloles (for *e.g.* polysilanes) as the fluorescent donors.[6c] Polysilanes are reported to exhibit high hole mobility and experience S–S* delocalization along Si–Si backbones which confine the conjugated electrons along the backbone. A few typical examples of polysilane used for detection of explosives are shown in Scheme 2.

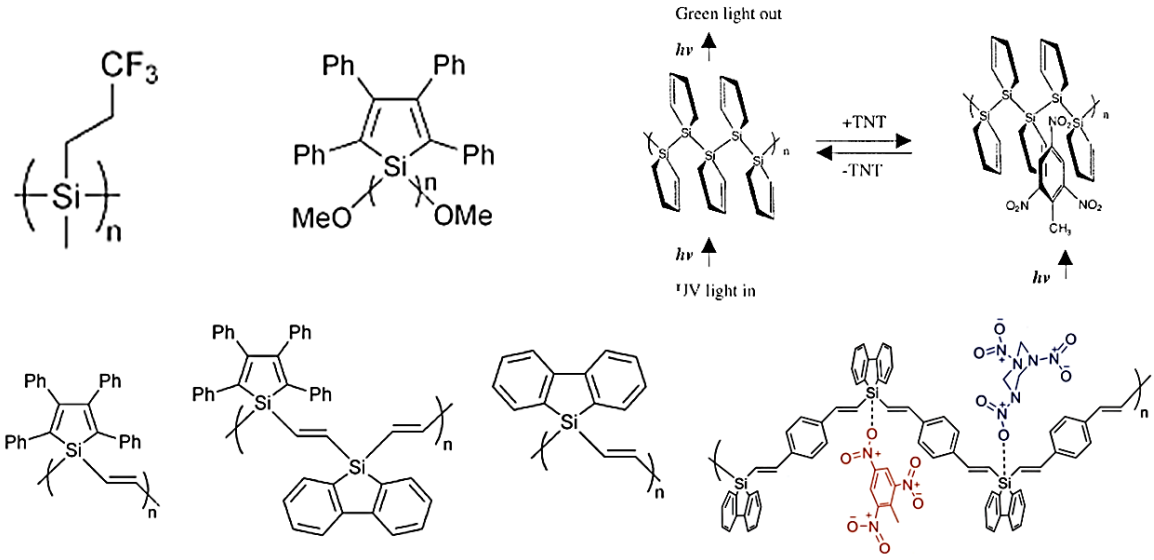

Scheme 2. Chemical structures of a fw polysilanes used as TNT sensors.

Subsequently, several strategies using quantum dots,[8] gold nanoparticles,[9] silver–gold alloy nanostructures,[10] metal-organic frameworks[11] and molecular imprinting with AuNPs[12] have been reported for the sensing of TNT. Recently, Engel *et al.* have reported a large array of chemically modified silicon nanowire-based field-effect transistors for the selective detection of TNT with

high sensitivity (Figure 2.1), in which the sensing demands a high-cost instrumental setup.[13]

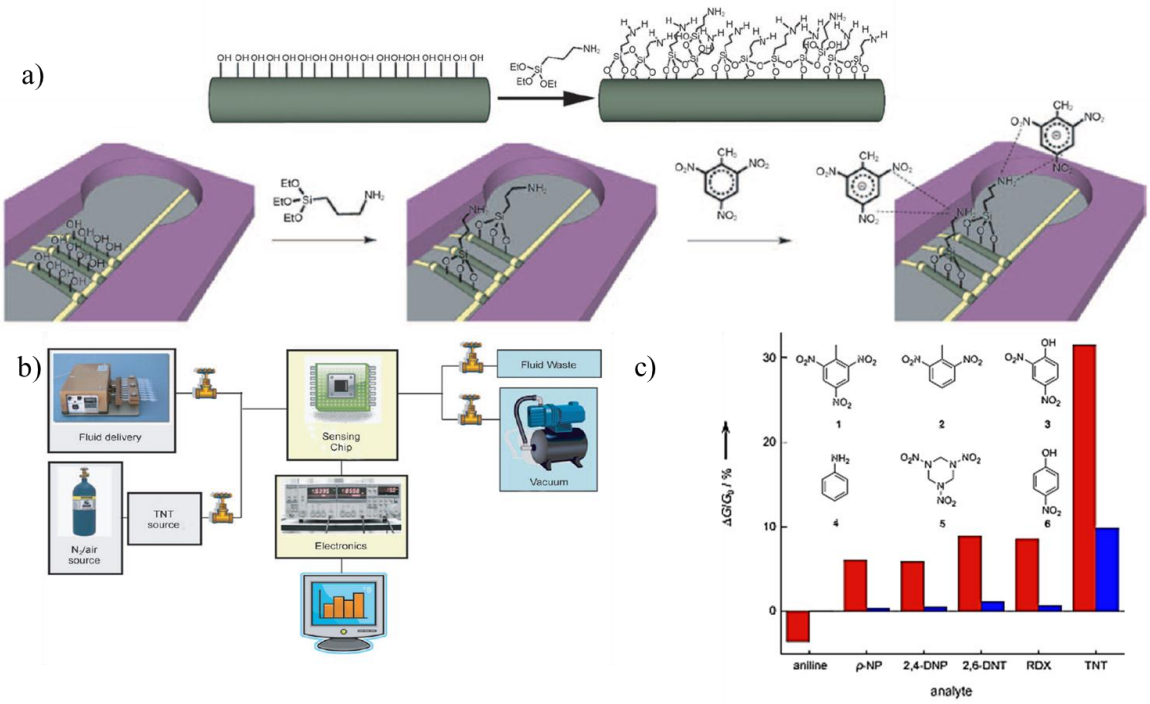

Figure 2.1. (a) Representation of 3-aminopropyltriethoxy silane (APTES) surface modification on a silicon nanowire device (top) and representation of TNT sensing (bottom). (b) Schematic representation of the setup for the fluid and gas sensing of explosives. (c) Response of an APTES-functionalized silicon nanowire device towards (red) 5 μM solutions and (blue) 5 nM solutions of: TNT (1), 2,6-DNT (2), 2,4-dinitrophenol (2,4-DNP, 3), aniline (4), RDX (5), and p-nitrophenol (*p*-NP, 6).

Self-assembled nanoarchitectures of π-conjugated molecules exhibit properties which are different from those of their individual building blocks.[14] Fluorescence is one such property that shows a significant response to the self-assembly phenomenon. For example, fluorescent molecules as a consequence of

self-assembly and gelation exhibit significant modulation in the emission color and intensity which is reversible with external inputs.[15] Therefore, fluorescent molecular assemblies and gels are useful candidates for the detection of various analytes.[16] In several cases, fluorescent nanofibers obtained by molecular self-assembly have been reported to be good sensing materials for the detection of nitroaromatic explosives due to the unique combination of porous structures with efficient exciton migration in the nanofibers as shown in Figure 2.2.[16a,16b]

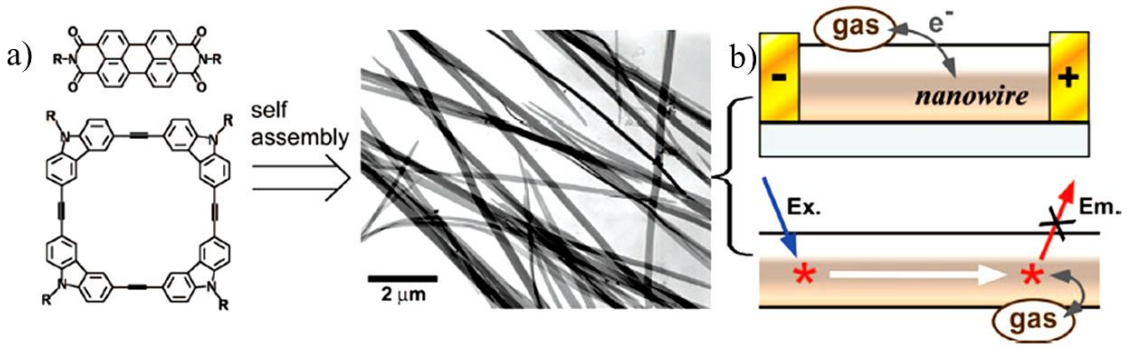

Figure 2.2. (a) One-dimensional fibers of donor-acceptor *π*-conjugated molecules. (b) Sensing mechanism of the detection of aromatic explosives.

However, detection of explosives at a sub-femtogram level using molecular self-assemblies and gels remains challenging. We speculated that fluorescent gel fibers exhibiting efficient exciton diffusion and capable of interacting with nitroaromatics may be useful as TNT sensors. With this viewpoint, we have examined several oligo(*p*-phenylenevinylene) (**OPV**)-based gelators[17] for the detection of TNT. An interesting feature of these gels is their efficient exciton

diffusion and energy transfer within the self-assembled aggregates which may be of relevance to the detection of various analytes.[18] However, none of these gelators (Scheme 3) showed considerable fluorescence quenching with TNT either in solution or in vapor state. Therefore, it was obvious that TNT was not able to interact with the gels, probably due to the close packing of the **OPV** molecules in the gel form leaving no room for the TNT molecules to be trapped inside.

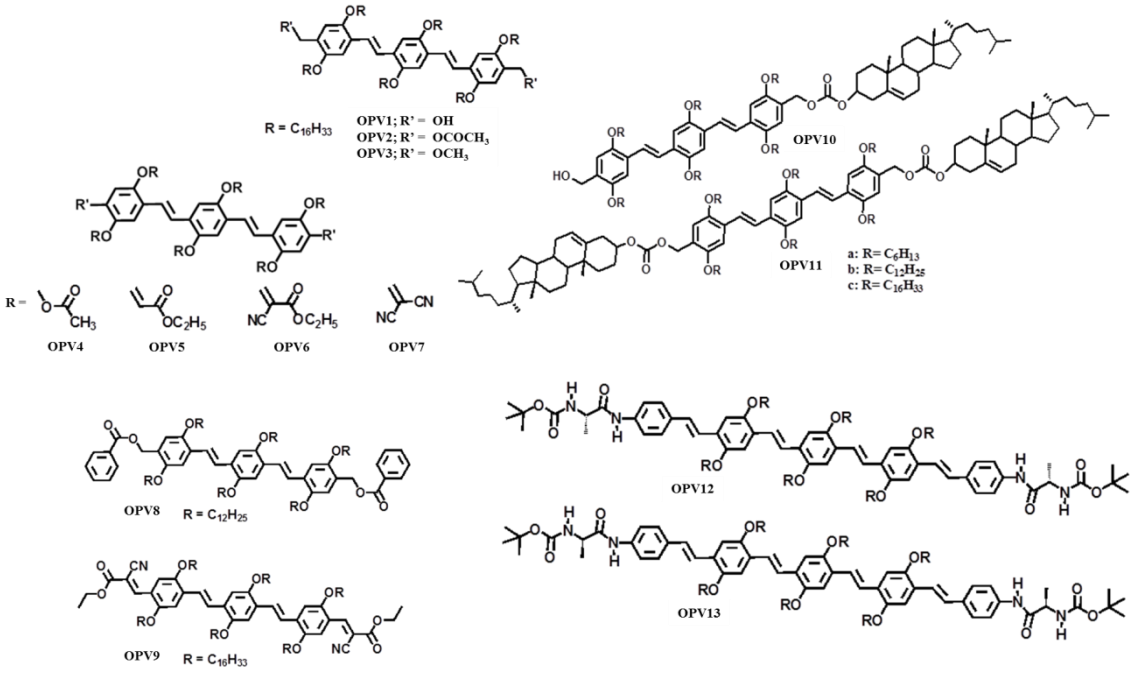

Scheme 3. Molecular structures of different **OPV**s.

Later, we focused our attention on a perfluoroarene-based gelator, **OPVPF**, which forms stable gels in nonpolar solvents at room temperature (critical gelation concentration value in *n*-hexane is 0.75 mM, 1.58 mg/mL), with a good

solid-state emission quantum yield of 63%.[19] The high solid state fluorescent quantum yield of **OPVPF** is due to the peculiar arene–perfluoroarene (ArH–ArF) interaction, whereas the other **OPV** derivatives most likely stacks via a lamellar type packing through cooperative hydrogen bonding, π-π stacking and van der Waals forces. In the latter case, the aryl units of **OPV** backbones might be coplanar and cofacial resulting the fluorescence quenching while in the former case the observed fluorescence enhancement is due to the slipping of aryl backbone because of the ArH–ArF interactions. There are several reports on organogels based on ArH–ArF interactions, mostly formed through a brickwall type of molecular packing.[20] We hypothesized that such a brickwall type molecular packing and the possible charge localization in **OPVPF** (as evident from the electron density distribution calculation using TITAN software, Figure 2.3) may facilitate strong interaction with electron-deficient aromatic molecules such as TNT. Surprisingly, **OPVPF** gel showed significant quenching of fluorescence in the presence of different nitroaromatic compounds in vapor state, which led us to a detailed investigation on the potential of the gelator for TNT detection.

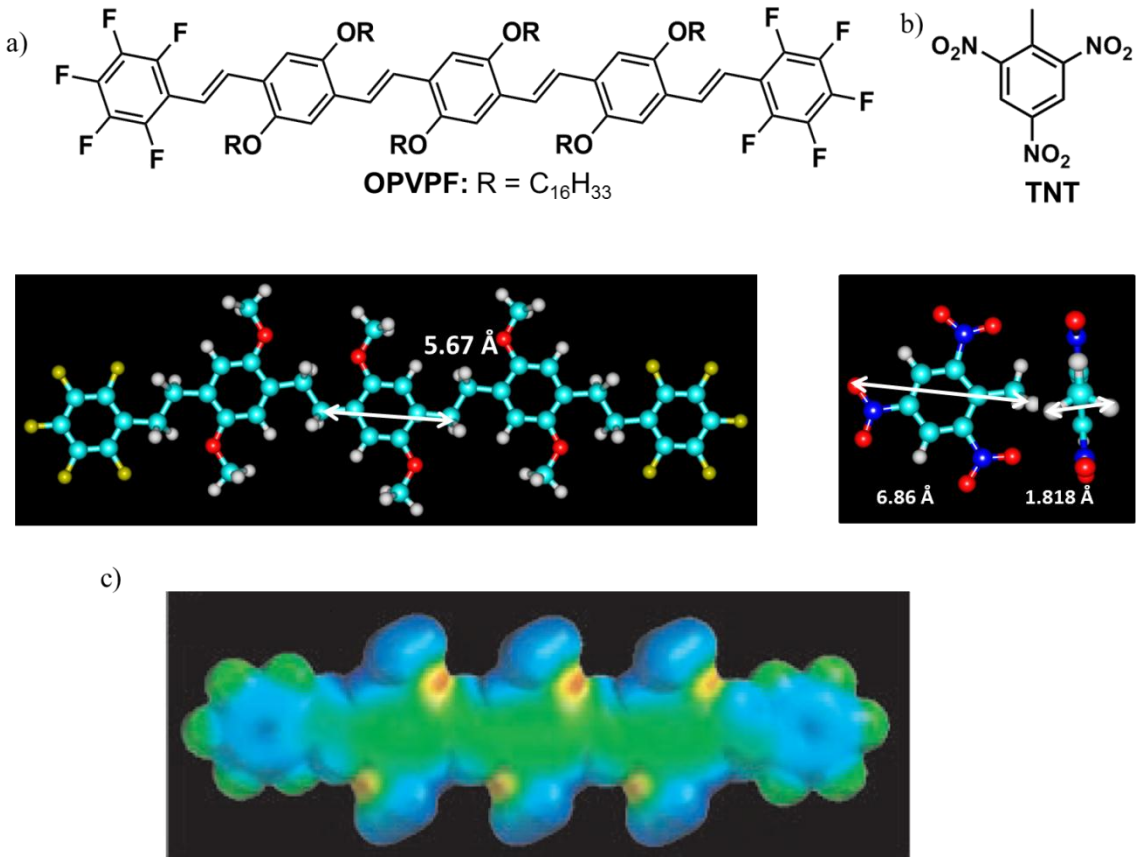

Figure 2.3. Molecular structures of (a) **OPVPF** and (b) TNT and the corresponding energy-minimized structures. (c) Electron-density distributions of **OPVPF** (calculated with TITAN software Wavefunction, Inc). In the computation experiments, the hexadecyloxy side chains in the **OPVPF** structure were replaced with methoxy groups.

2.3. Results and discussion

2.3.1. Self-assembly of oligo (*p*-phenylenevinylene) gelator (OPVPF)

In *n*-hexane solution, **OPVPF** exhibits a green fluorescence which upon gelation turns to yellow (Figure 2.4a,b). The yellow emission could be attributed to the formation of aggregates.[18c] A hot solution of the gel when dip-

coated on a filter paper and cooled to room temperature resulted in an yellow emission which further changes to an orange-red emission upon evacuating the solvent (Figure 2.4c). The orange emission of the paper-coated xerogel indicates the decrease of the fraction of monomers/lower order aggregates and increase in the higher order aggregates with reduced optical band gaps. The emission color is thermally reversible as observed by the shift in the color from orange-red to green upon heating the filter paper to 70 °C (Figure 2.4d) and vice versa upon cooling to room temperature. The corresponding emission spectra of the molecules in monomer, gel and film states are shown in Figure 2.4e.

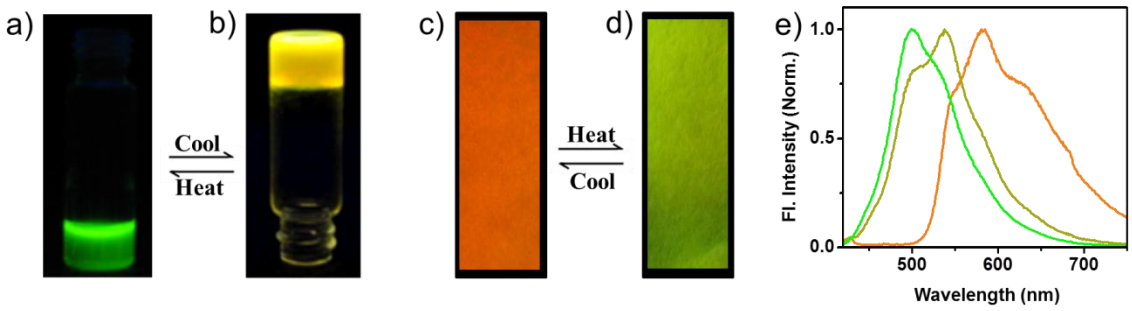

Figure 2.4. Photographs of (a) *n*-hexane solution and (b) *n*-hexane gel of **OPVPF**. (c,d) Reversible emission color change of the filter paper coated with xerogel upon heating to 70 °C and cooling to room temperature. (e) Normalized emission spectra in solution (green line), gel (olive line), and film (orange line) states (λ_{ex} = 400 nm).

Scanning electron microscopy (SEM) images of the filter paper before and after coating with the gel are shown in Figure 2.5. The SEM image of the filter

paper before coating with the gel showed the characteristic micrometer-sized fibers. However, the filter paper coated with the gel showed entangled fibers (100−200 nm) of the **OPVPF** molecules (Figure 2.5). We prepared several samples of **OPVPF** solutions, gels and the xerogel-coated filter papers to study their fluorescence response with different nitroaromatic compounds and the details are discussed.

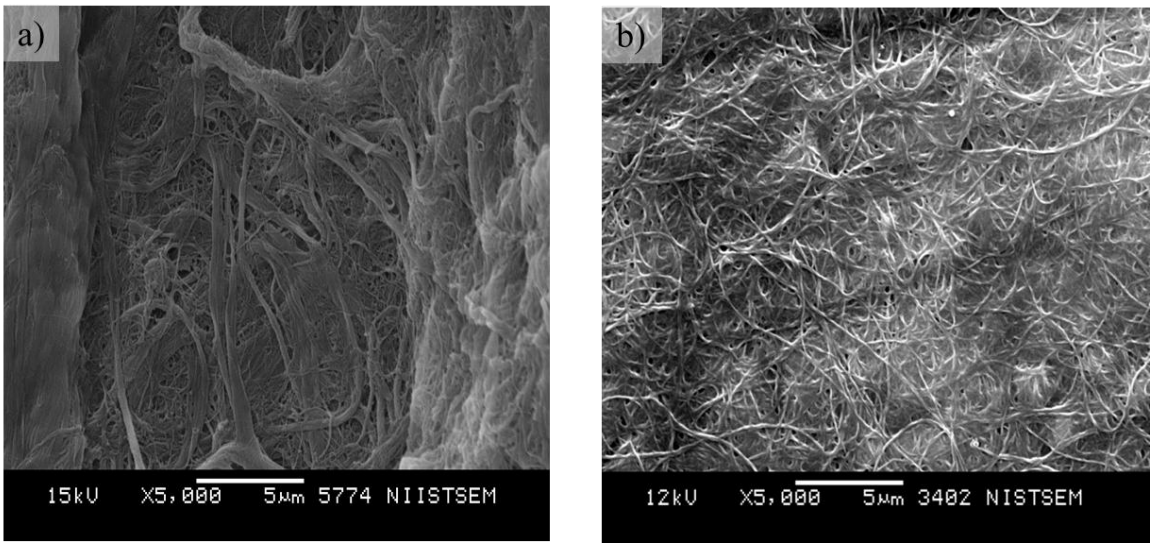

Figure 2.5. SEM images of a Whatman filter paper (a) before and (b) after coating with the **OPVPF** gel.

2.3.2. Solution and vapor-phase sensing of explosives using OPVPF

Our first attempt was to study the fluorescence changes of **OPVPF** in solution upon addition of TNT. The response of **OPVPF** (1×10^{-4} M) in chloroform against TNT was observed as a weak fluorescence quenching (Figure 2.6a).

This observation implies that TNT is not an efficient quencher for **OPVPF** in the isotropic solution state and hence is not suitable for the detection of TNT. Having seen the effect in solution, we decided to test the fluorescence response of the gel state with TNT. A definite amount of *n*-hexane gel (50 μL, 1×10^{-3} M) was dropped on a glass slide (0.5 cm diameter) and dried under vacuum. The xerogel-coated glass slide was placed in a vial containing TNT at room temperature. The emission spectra were measured by using a front-face technique after exposing the film for specific intervals.

Surprisingly, significant quenching of the fluorescence was observed (Figure 2.6b) upon exposure to TNT vapors (as per literature reports, the vapor pressure of TNT at 20 °C is ~10 ng/L or 1 ppb).[13] Nearly 20 ± 5% quenching was noticed within 5 s of exposure (Figure 2.6b, inset), indicating a fast response time and detection limit between ppb and ppt concentration levels. In order to understand the excited-state behavior of the **OPVPF** gel, the fluorescence lifetime decay profiles before and after exposure to TNT were recorded. These data of **OPVPF** xerogel (λ_{ex} = 440 nm) exhibited a biexponential character with lifetimes of 1.47 ns (14.4%) and 2.12 ns (85.6%) when monitored at 600 nm. Upon exposure to TNT vapor for 20 sec, a fast biexponential decay with time constants of 0.28 ns (68.3%) and 1.4 ns (31.7%) was observed (Figure 2.4c). The decrease in the average lifetime can be attributed to the interaction of TNT with the self-assembled xerogel fibrils.

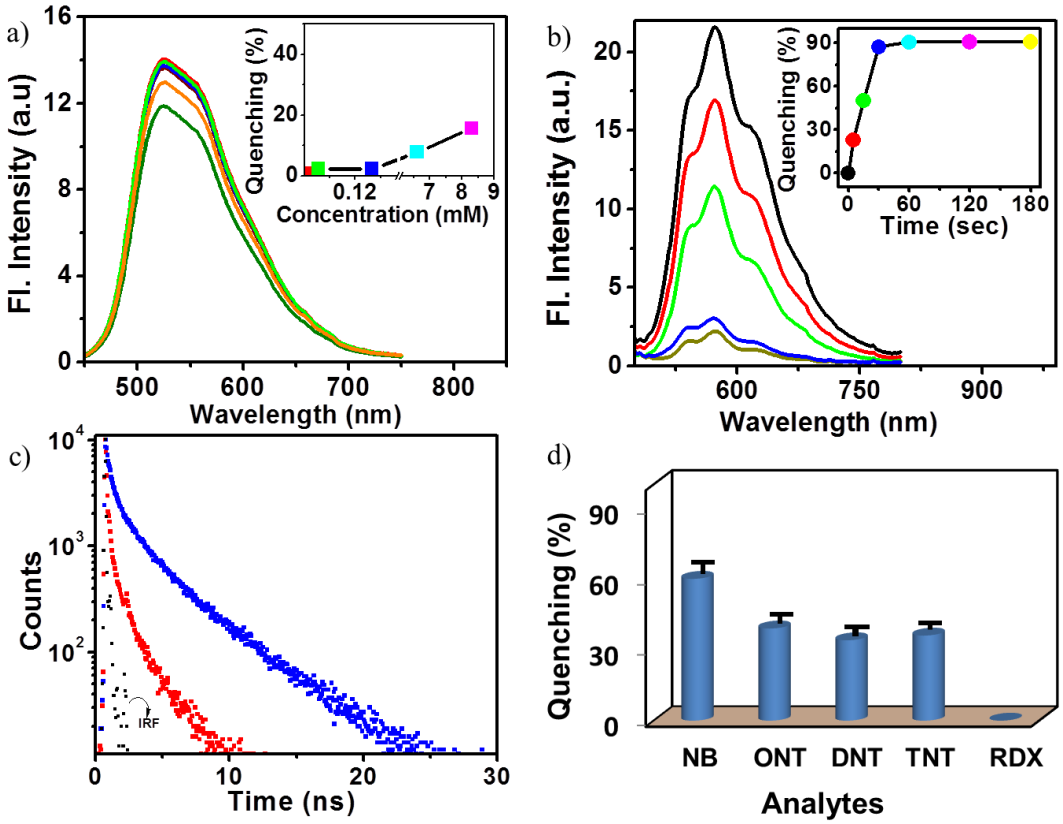

Figure 2.6. (a) Emission spectra of **OPVPF** in chloroform (1×10^{-4} M) upon addition of different amounts of TNT. Inset: Plot of quenching (%) at 525 nm vs concentration of TNT (λ_{ex} = 400 nm). (b) Time dependent fluorescence quenching of **OPVPF** xerogel upon TNT vapor exposure. Inset: Plot of fluorescence quenching (%) at 580 nm vs time in seconds. (c) Lifetime decay profiles (λ_{ex} = 440 nm, monitored at 600 nm) of **OPVPF** xerogel before (blue circles) and after (red circles) exposure to TNT vapors for 10 s at room temperature. (d) Comparison of the fluorescence quenching efficiency of **OPVPF** xerogel upon exposure to saturated vapors of different analytes for 10 s in a closed chamber (λ_{ex} = 450 nm; error bar = 5%).

A comparison of the response of gel fibrils against nitrobenzene (NB), o-nitrotoluene (ONT), 2,4-dinitrotoluene (DNT), and TNT on 10 s exposure is

shown in Figure 2.6d. About 90 ± 5% quenching was observed within 40 s of exposure for these different nitroaromatics. In order to test the specificity of the gelator for the detection of nitroaromatics, we have studied the effect of RDX, which is a non-aromatic explosive. Interestingly, the xerogel did not show any fluorescence response when exposed to RDX vapors.(Figure 2.6d).

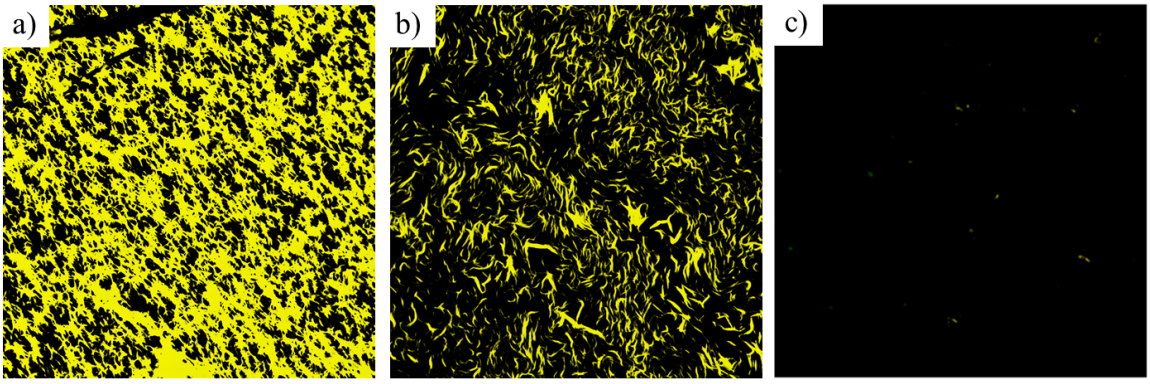

Figure 2.7. CLSM images of the **OPVPF** gel on glass slides (a) before and (b) 20 and (c) 40 s after exposure to saturated vapors of TNT (~1 ppb) in a closed chamber (λ_{ex} = 438 nm, λ_{em} = 450−550 nm, 10x magnification).

Confocal laser scanning microscopy (CLSM) images of **OPVPF** gel obtained from *n*-hexane before and after exposure to TNT vapors are shown in Figure 2.7. After 20 s of exposure to TNT, about 60% of the fluorescence was quenched, and after 40 s, almost complete quenching was observed. These results reveal that **OPVPF** fluorescence is more responsive to the gel phase when compared to the solution state. Since 5% quenching of the fluorescence is sufficient to detect an analyte, the gel is suitable for the sensing of explosives in

the native state. The relatively low response of TNT vapors to the gel fluorescence could be attributed to the low equilibrium vapor pressure of TNT (5.6×10^{-6} Torr at 25 °C) when compared to NB (0.15 Torr at 20 °C).[1b]

2.3.3. Contact mode detection of TNT

While vapor-phase detection of TNT is extremely important to sense the proximity of explosive devices, a simple method for the on-site instant detection of TNT contamination on surfaces and specimens is equally important. Similar is the case of monitoring of TNT contamination in potable water. Therefore, we decided to test the viability of a contact-mode testing approach using xerogel-coated disposable paper strips which will be of relevance to the on-site instant detection of TNT. It is known that explosive particles can contaminate the human body, clothing, and other materials in the surroundings during preparation and packaging of explosive devices or during an explosion.[1c,1d] In such cases, contact mode is appropriate to check for residual contamination by an explosive chemical. For this purpose, test strips were prepared by transferring **OPVPF** gel fibers onto a Whatman filter paper by dip-coating a hot solution of the gel, followed by drying under vacuum and cutting the dried filter paper into pieces. The contact-mode response to TNT by the filter paper strips was tested by placing TNT crystals over a test strip for 5 s, resulting in black spots upon illumination with a UV lamp (Figure 2.8a,c).

The same experiment was repeated with RDX, and no spots corresponding to fluorescence quenching were found (Figure 2.8b,d).

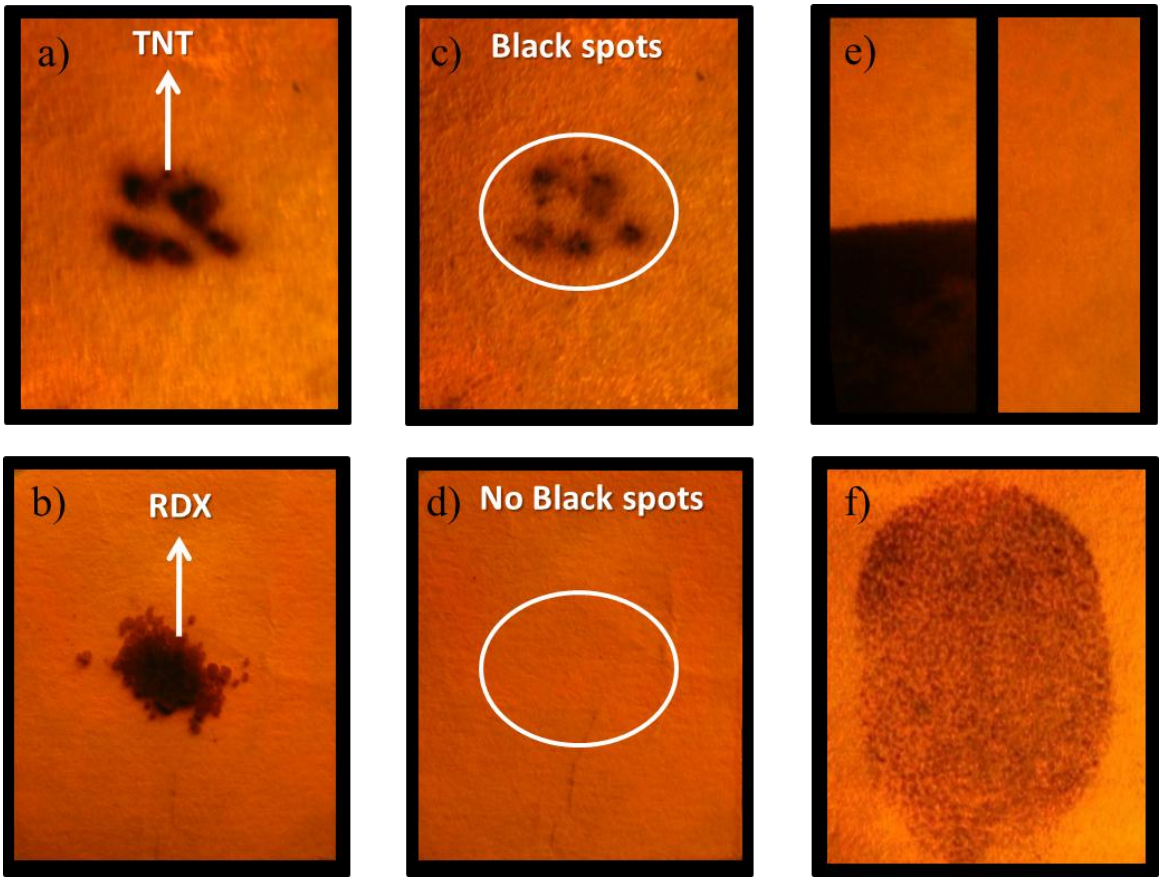

Figure 2.8. Photographs of **OPVPF**-coated test strips under different experimental conditions. (a) TNT and (b) RDX crystals on top. (c,d) Corresponding photographs upon removal of the crystals after 5 s. (e) After dipping into solutions of TNT (left) and RDX (right) in acetonitrile (1×10^{-3} M). (f) Thumb impression after rubbing with TNT crystals. All photographs were taken under 365 nm UV illumination.

In addition, the test strips were dipped into acetonitrile solutions of TNT and RDX and the fluorescence quenching was observed only in the case of TNT

(Figure 2.8e). In another experiment, a human thumb was rubbed with TNT (caution: no direct contact, use a glove!), and then the TNT particles were brushed off, followed by pressing the thumb against a test strip. The fingerprint of the thumb could be seen as quenched luminescence when illuminated with UV light (Figure 2.8f). As a control experiment, the thumb (gloved) which was not contaminated with TNT was pressed on the test strip, and no fingerprint was seen. These images illustrate the utility of the gel-coated test strips for the on-site instant visualization of trace residues of TNT present on a specimen. Detection of extremely small amounts of TNT on different substrates or from debris of explosions could be better performed by extraction with a suitable solvent and then dilution to a required volume followed by spot-testing using the paper strips. To test this possibility, aqueous solutions of different analytes (acetonitrile:water, 0.5:9.5 v/v) were prepared, and 10 μL of each solution was placed on the paper test strips to give a spot area of ~0.2 cm^2 (aqueous condition was preferred to avoid any possible leaching of the gelator from the test strip).

The visual fluorescence response of different nitroaromatics at different concentrations by contact mode detection on filter paper test strips is shown in Figure 2.9a.The minimum amount of TNT detectable by the naked eye was as low as 10 μL of 1×10^{-15} M solution, thereby registering a detection limit of 0.227 parts per quadrillion (ppq).

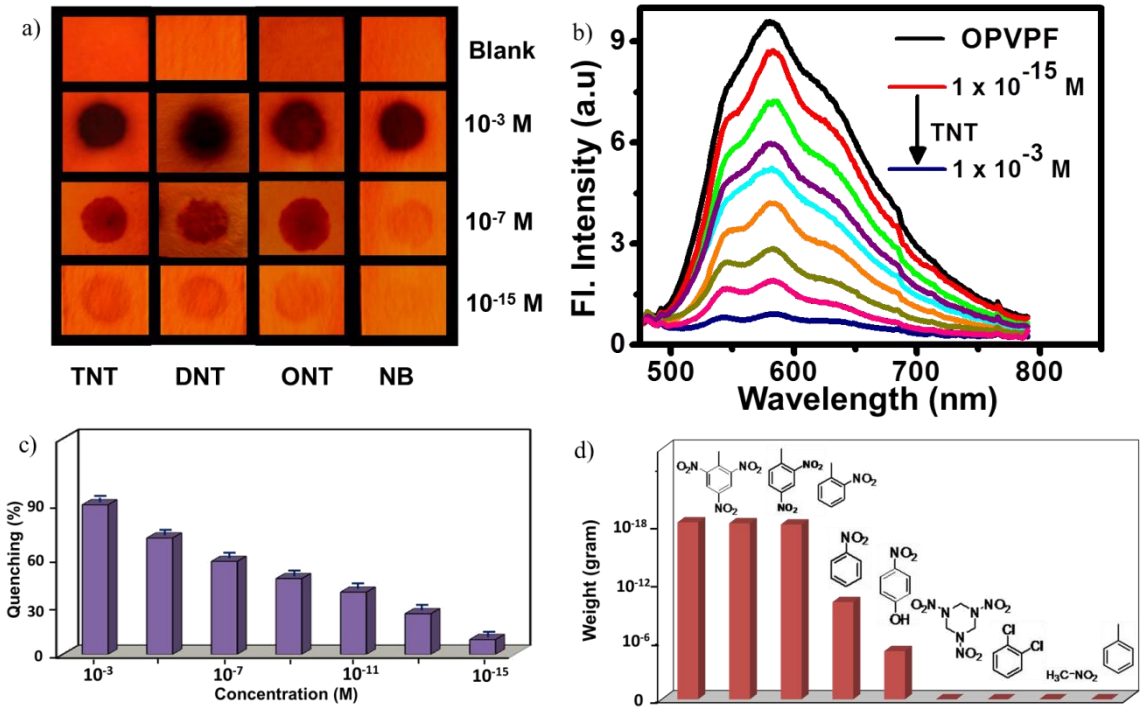

Figure 2.9. (a) Photograph of the fluorescence quenching of **OPVPF** coated test strips by nitroaromatics on contact mode (10 μL of the analyte with a spot area of ~0.2 cm^2) when viewed under 365 nm UV illumination. (b) Emission spectral change (λ_{ex} = 450 nm) of the test strips against concentration of added TNT (10 μL, 1 × 10^{-15} – 1 × 10^{-3} M). (c) Plot of the emission at 580 nm (%) of the test strips against concentration of added TNT in acetonitrile:water (0.5:9.5, 10 μL, 1 × 10^{-15} – 1 × 10^{-3} M). (d) Contact-mode detection of the lowest amount of different analytes by the emission quenching of the test strip. In all experiments, a front-face technique was used to record the emission from the test strips.

The fluorescence spectral changes of the test strips on contact with TNT for a wide range of concentration is shown in Figure 2.9b, and the corresponding fluorescence quenching (%) at 580 nm is shown in Figure 2.9c. A comparison

of the minimum detectable amounts of the analytes estimated from the fluorescence quenching indicates that nonaromatic explosives and aromatic compounds without nitro groups are not sensed by the test strips (Figure 2.9d).

	System	Sensitivity	Journal
1.	Silicon Nanowire	Attomolar	*Angew. Chem. Int. Ed.* **2010**, *49*, 6830 –6835.
2.	Ag–DNA nanostructure	Femtomolar	*J. Mater. Chem.*, **2009**, *19*, 6849–6856.
3.	Imprinted AuNPs	10 Femtomolar	*J. Am. Chem. Soc.* **2009**, *131*, 7368–7378.
4.	Au Nanoparticles	Picomolar level	*Angew. Chem. Int. Ed.* **2008**, *47*, 8601 –8604.
5.	Pentiptycene polymer thin film	Femtogram	*MRS Bull.* **2002**, *27*, 446-450.
6.	Poly(4-vinylpyridine) thin film	0.95 ppb and 3fg	*Adv. Funct. Mater.* **2010**, *20,* 1144–1151.
7.	Silafluorene–fluorene-conjugated copolymers	1 Picogram/cm^{-2}	*J. Mater. Chem.,* **2008**, *18*, 3143–3156.
8.	Phosphole Oxide	10 ng cm^{-2}	*Applied materials & interfaces,* **2009,** *7,* 1379–1382.
9.	Organic nanofibrils - carbazole trimer	5 ppb	*Chem. Commun.,* **2010**, *46,* 5560–5562.
10.	Fluorescent Nanofibril Film	5 ppb	*J. Am. Chem. Soc.* **2007**, *129,* 6978-6979.
11.	1,4-Diarylpentiptycenes	7.70 ppb	*Org. Lett.* **2008**, *10*, 3681-3684.
12.	Alligned Single-Walled Carbon Nanotube	8 ppb	*Adv. Mater.* **2010**, *22,* 1900–1904.
13.	ZnO nanowire	60ppb	*Adv. Mater.* **2010**, *22,* 1900–1904.

Table 2.1. A comparative chart of the detection limit of different organic molecules/polymers for TNT.

Fluorescence quenching could be visually detected upto a level of 1.37×10^{-18} g (ONT), 1.82×10^{-18} g (DNT), 2.27×10^{-18} g (TNT), and 1.23×10^{-10} g (NB) using the test strips when 10 μL of the analyte was spotted with a spread

area of ~0.2 cm^2. From these data, the detection limit of TNT is calculated as ~12 ag/cm^2, which is much lower than the values previously achieved using a surface detection method (Table 2.1). [6c,8c,8d] Thus, for TNT, DNT, and ONT, the limit of detection up to a record attogram level with sensitivity in the range of ppq could be achieved by using **OPVPF** gel fibers.

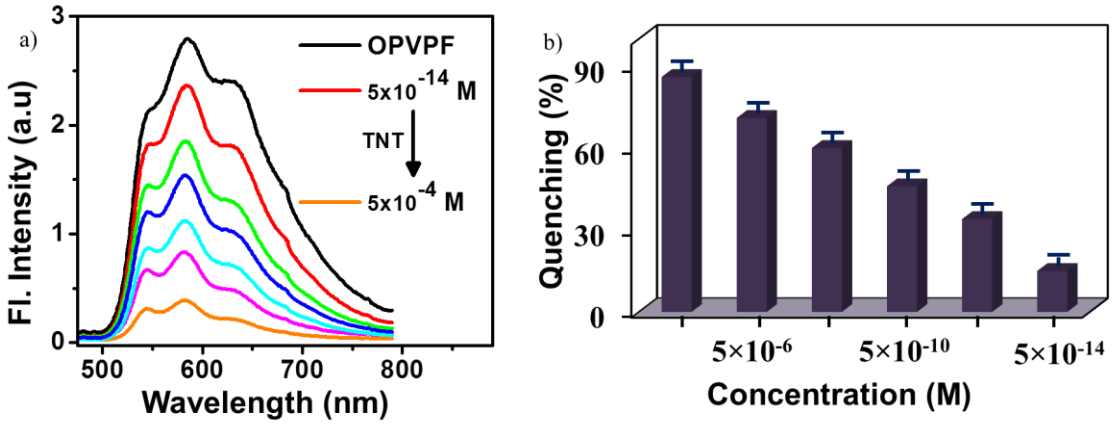

Figure 2.10. (a) Emission spectral change (λ_{ex} = 450 nm) of the **OPVPF** coated test strips with added amount of TNT in potable water (10 μL, 5 × 10^{-14} – 5 × 10^{-4} M). (b) Corresponding % quenching of fluorescence at 580 nm.

Nitroaromatic compounds are environmental contaminants that pollute soil and groundwater after military operations.[21] The amount of TNT above 2 ppb in drinking water can be toxic and carcinogenic.[1c,1d] The intake of TNT may cause liver damage, gastritis, aplastic anemia, cyanosis, and dermatitis.[22] Hence, the detection of nitroaromatics, particularly TNT, in potable water for low-level contamination is of great relevance.[21,23] With this objective, aqueous solutions

of TNT were prepared, and 10 μL aliquots of each of these solutions were placed on the paper test strips, covering an area of ~0.2 cm^2. The fluorescence spectral change upon addition of the test samples is shown in Figure 2.10a, and the corresponding quenching (%) bar diagram is shown in Figure 2.10b. The lowest amount of TNT in potable water detectable by the naked eye on filter paper strips is $5 \times 10^{-14} - 1 \times 10^{-15}$ M, which corresponds to a sensitivity in the range of 11.4−0.23 ppq.

2.3.4. X-ray diffraction studies

To get an insight on the mode of interaction and molecular packing, X-ray diffraction (XRD) analysis of **OPVPF** gel before and after exposure to TNT was performed (Figure 2.11). The XRD pattern before exposure to TNT (Figure 2.11a) indicates a brickwall-type arrangement of the molecules, which is in analogy to the previous reports.[19-20] For example, the crystal XRD data of a bis(pentafluorostyryl)stilbene derivative shows a brickwall-type assembly in which each brick is situated over the gap between the bricks in the row below.[20a] In a similar situation, each of the terminal fluorinated aromatic rings of **OPVPF** is sandwiched between the central aromatic rings of the neighboring **OPVPF** molecules, and vice versa. By considering XRD analysis as well as previous reports on the crystal packing of fluorinated distyryl derivatives, it could be assumed that the molecules are involved in C−F···H−C interactions in

addition to the face-to-face π-stacking (Figure 2.12).

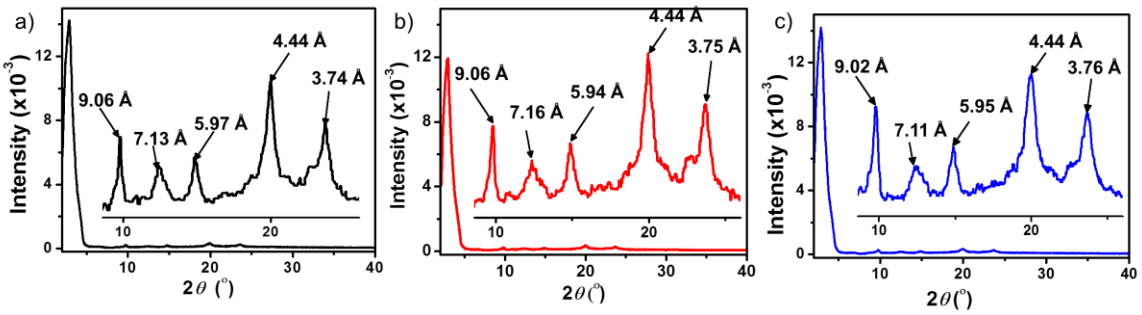

Figure 2.11. XRD patterns of the xerogel of **OPVPF** (a) before, (b) after TNT vapor exposure and (c) after TNT contact-mode exposure in water. Insets show the 2θ values of the zoomed region between 8.6 and 26°.

The peak corresponding to a d-spacing of 3.74 Å could be the π-stacking distance between two **OPVPF** molecules. The d-spacing of 7.13 Å corresponds to the distance between the alternate (top and bottom) **OPVPF**. The diffraction peak corresponding to 5.97 Å could be the end-to-end distance between two **OPVPF** molecules. The d-spacings of ~9.0 and ~4.4 Å may correspond to the packing distances of the alkyl side chains in the brickwall-type assembly. The xerogel-coated glass plate after exposure to saturated TNT vapors exhibited almost identical XRD patterns (Figure 2.11b). A similar experiment was conducted with dried xerogel after dipping in TNT solution in water (5×10^{-14} M) (Figure 2.11c). In this case also, only negligible changes were observed in the diffraction peaks, indicating that the **OPVPF** packing is not considerably disturbed either by TNT vapors or by the solvent. This is further confirmed by

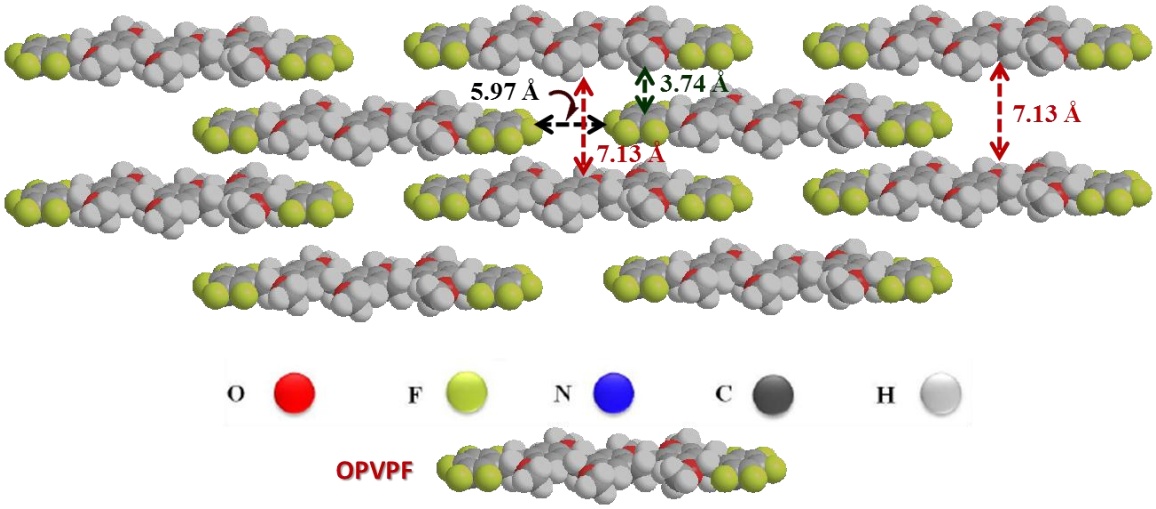

Figure 2.12. Proposed molecular packing of **OPVPF** xerogel.

the film-state absorption and reflection spectra of the gelator before and after contact with TNT solutions (Figure 2.13), which did not show any visible change. This observation also indicates that there is no ground-state charge transfer between **OPVPF** and TNT. Therefore, we conclude that the TNT molecules are trapped inside the interstitial space of the **OPVPF** molecules without changing the overall brickwall-type molecular packing, and the observed fluorescence quenching is due to excited-state processes.

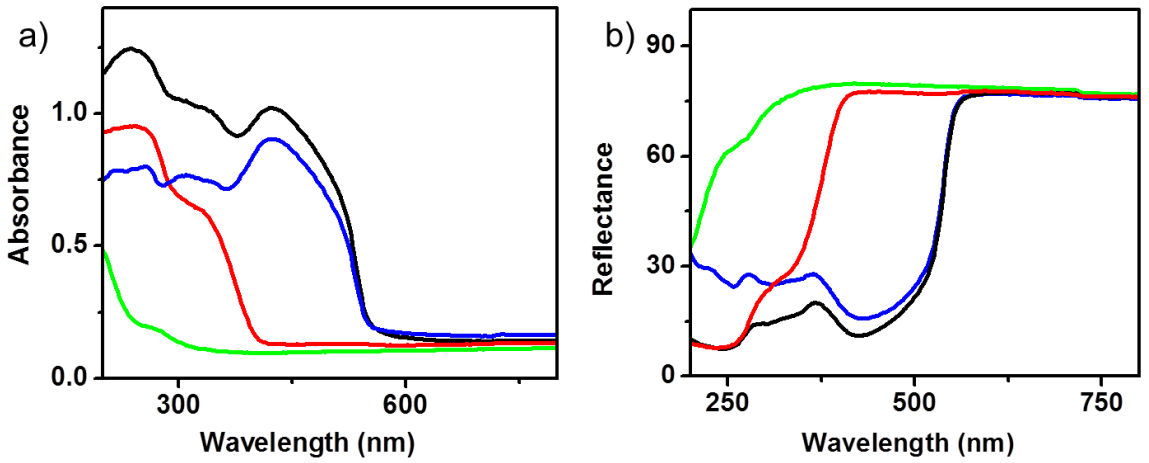

Figure 2.13. (a) Absorption and (b) reflectance spectra of **OPVPF** xerogel on filter paper before (—), after (—) the addition of TNT, TNT alone on filter paper (—) and blank filter paper (—).

2.3.5. Mechanism of sensing

Based on the above observations, a plausible mechanism of the fluorescence quenching with TNT in the xerogel state is depicted in Figure 2.14. The gel fiber bundles of **OPVPF** are comprised of nanosized fibrils, which in turn are formed by self-assembled aggregates having different energy levels. Each aggregate is formed by the brickwall-type arrangement of **OPVPF** with interstitial free space within the aggregates with a vertical distance of ~7.13 Å and a horizontal distance of 5.97 Å, as shown in Figure 8. Since the calculated maximum molecular length of TNT (between the methyl group and the oppositely placed nitro group) is ~6.86 Å (Figure 2.14), it can fit vertically into the free space through electrostatic interaction with **OPVPF** (Figure 2.14).

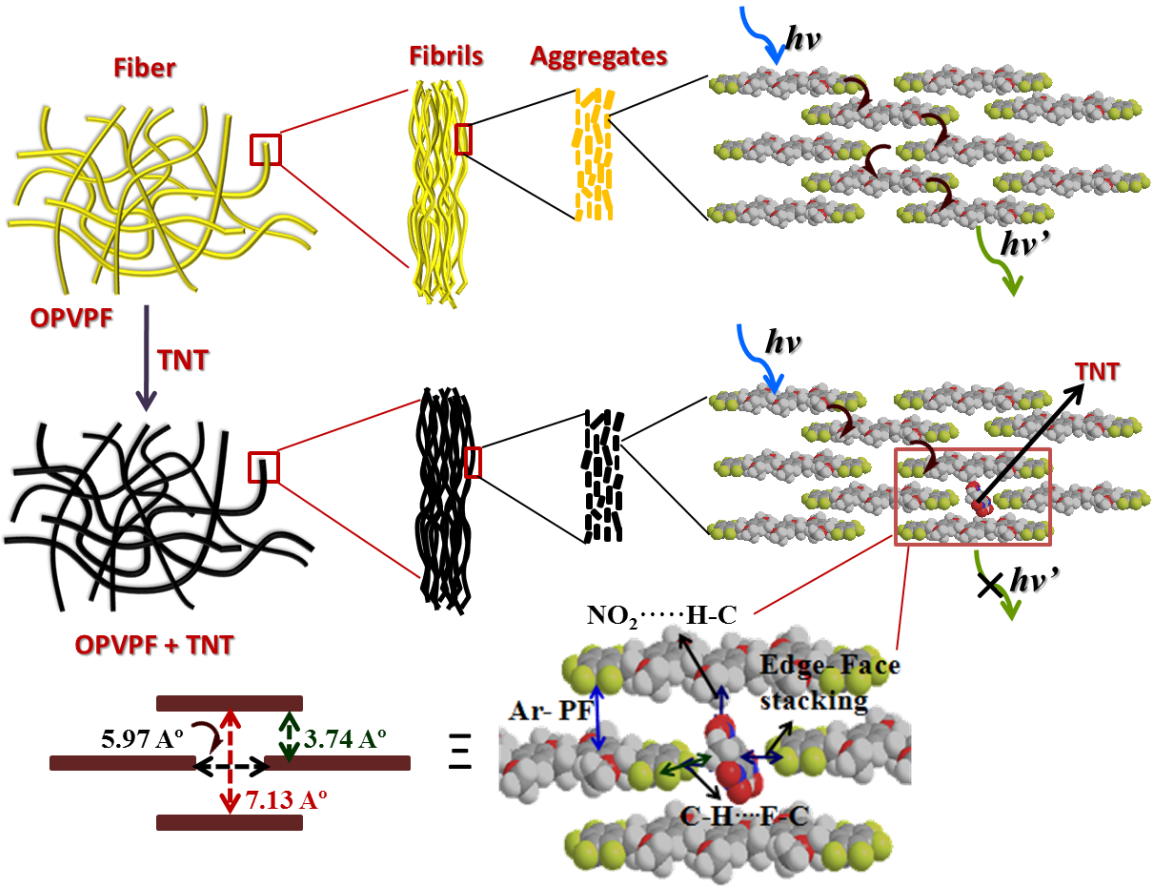

Figure 2.14. A schematic illustration of the fluorescence quenching mechanism of **OPVPF** xerogel fibers in the presence of attogram levels of TNT. The bottom right picture shows various noncovalent interactions, and the bottom left picture shows the approximate distance between neighboring **OPVPF** in a brickwall-type arrangement.

Thus, the possible edge-to-face π-stacking between the electron-deficient aromatic core of TNT and the electron-rich perfluoroarene moieties of **OPVPF** favors the formation of a tight complex. Such an interaction may be further assisted by the hydrogen bonding between the nitro groups in TNT and the hydrogen atoms in the **OPVPF** backbone. Similarly, hydrogen bonding is also

possible between the hydrogen atoms in the methyl group of TNT and the fluorine atoms of the **OPVPF**. Due to the cooperative interaction of the above weak forces, whenever the xerogel fibers are in contact with a TNT molecule, it gets entrapped and acts as a fluorescence trap.

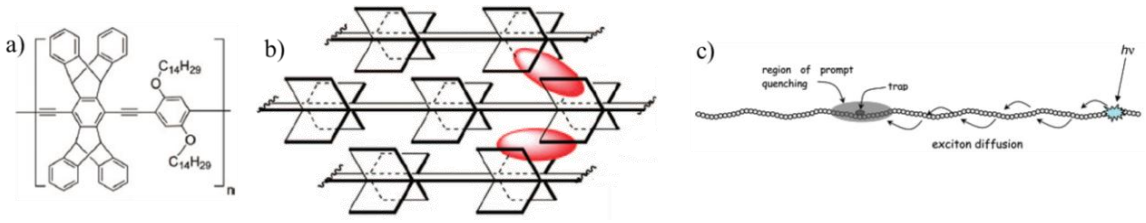

Figure 2.15. (a) Pentiptycene-derived phenyleneethynylene polymer. (b) Schematic picture of polymer porosity for analyte binding. (c) Exciton diffusion mechanism by conjugated organic polymer.

In addition, there is the possibility of TNT molecules getting trapped between the interstitial sites of the elementary fibrils of the xerogel due to the exposed pentafluoro aryl moieties. The efficient fluorescence quenching of **OPVPF** xerogel coated filter paper by an extremely small amount of TNT could be explained by a faster exciton diffusion mechanism, as described earlier by Swager and co-workers as in the case of conjugated polymers (Figure 2.15).[24] It is known that excitation energy migration is possible in **OPV** based assemblies. To study such phenomenon in the present system, wavelength dependent decay profiles were collected in the gel state (Figure 2.16a). The fluorescence decay collected at 520 nm was bi-exponential and decays were faster at higher

wavelengths. With increasing emission wavelength, the decay becomes slower and exhibited a tri-exponential decay with the formation of a rising component in the initial time scale (Figure 2.16a; inset). The initial rise in the decay profile indicates the population build-up of the excited states of higher order aggregates via energy migration from lower order aggregates.

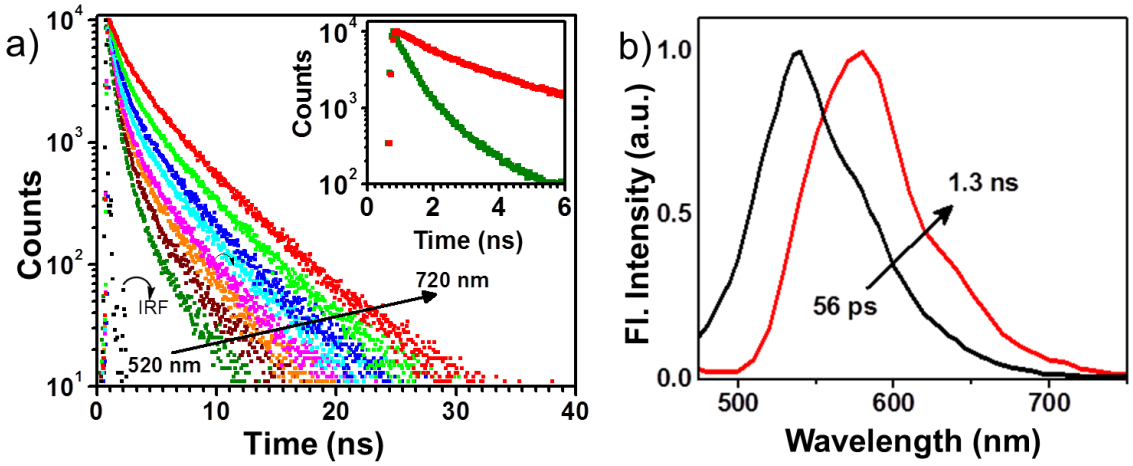

Figure 2.16. (a) Wavelength-dependent fluorescence lifetime decay monitored between 520 and 720 nm (λ_{ex} = 440 nm). The inset shows the lifetime decay profiles monitored at 520 nm (green circles) and at 720 nm (red circles), showing a growth corresponding to the excitation of the lower energy aggregates at the initial time scales. IRF = instrument response function. (b) Time-resolved emission spectra **OPVPF** xerogel at 56 ps (—) and 1.3 ns (—) after excitation at 440 nm at 20 ºC.

Time-resolved emission studies (TRES) of the xerogel indicated a dynamic red shift of the emission spectra from 540 to 580 nm when collected after 56 ps and 1.3 ns, respectively. This observation reveals the possibility of fast

excitation energy migration within the self-assembled nanostructure (Figure 2.16b).[19] These data indicate that the self-assembled gelator favors exciton hoping via intermolecular electronic coupling, thereby facilitating long-range exciton diffusion in the xerogel state. Thus, the fast excitation energy diffusion within the fibrils and between the fibrils facilitates efficient fluorescence quenching by possible energy-transfer and electron-transfer mechanisms, even with extremely low quantities of the quencher, resulting in attogram level detection.

In the case of Föster-type energy transfer, a single quencher molecule can cover approximately a distance of 1−10 nm. However, in the case of **OPVPF** xerogel fibers, due to efficient excitation energy migration, a single quencher molecule in principle may cover a longer distance than the normal Föster distance, making the quenching more efficient. Thus, when a 10 μL volume of 1 $\times$ 10^{-15} M TNT solution is spotted on the filter paper test trip covering an area of ~0.2 cm^2, 2.27 ag of the TNT present can get entrapped and distributed at different locations, which will be sufficient to have a detectable fluorescence quenching of the spotted area, giving a detection limit of ~12 ag/cm^2. In the solution, since the gelator molecules are in the isotropic state, such a mechanism is not feasible, and hence the sensitivity is extremely low for TNT, as observed. The weak fluorescence quenching with nonaromatic and poorly electron-deficient aromatic compounds indicates that the binding strength of the

analyte with the gelator is crucial for the low-level detection.

2.4. Conclusions

In conclusion, the attogram level detection of TNT using a self-assembled fluorescent gelator has been demonstrated. The gelator molecule (**OPVPF**) is not efficient for the sensing of TNT in the solution state, whereas in the xerogel state high sensitivity has been achieved. This finding highlights the unique capability of the self-assembled fibrous structures as new materials over the individual molecules for a specific application. While the sensitivity to TNT in the vapor phase was in the ppt range, the detection level was in the ppq range in the contact mode. The attogram detection level with high sensitivity achieved using disposable filter paper-based test strips allows a simple and low-cost protocol for the on-site instant detection of TNT on contaminated specimens, as well as monitoring of TNT contamination in groundwater, which has great relevance to human health and safety.

2.5. Experimental section

General procedures: Unless otherwise stated, all materials and reagents were purchased from commercial suppliers. The solvents and reagents were purified and dried by standard methods prior to use. **OPVPF** was synthesized as per our previous report.[19] TNT and RDX were obtained from High Energy Materials

Research Laboratory, Pune, and recrystallized from ethanol.

Spectral measurements: The absorption or reflection spectra were recorded on a Shimadzu UV−vis recording spectrophotometer UV-2100 with $BaSO_4$ as standard. The emission spectra were recorded on a SPEX-Flourolog F112X spectrofluorimeter using a front face sample holder.

Lifetime measurements: Fluorescence lifetimes were measured using an IBH (FluoroCube) time-correlated picosecond single photon counting (TCSPC) system. Solutions were excited with a pulsed diode laser (<100 ps pulse duration) at a wavelength of 440 nm (NanoLED-10) with a repetition rate of 1 MHz. The detection system consists of a microchannel plate photomultiplier (5000U-09B, Hamamatsu) with a 38.6 ps response time coupled to a monochromator (5000M) and TCSPC electronics (DataStation Hub including Hub-NL, NanoLED controller and preinstalled Fluorescence Measurement and Analysis Studio (FMAS) software). The fluorescence lifetime values were determined by deconvoluting the instrument response function with biexponential decay using DAS6 decay analysis software. The quality of the fit has been judged by the fitting parameters such as χ^2 (<1.2) as well as the visual inspection of the residuals. All measurements were carried out using a front face sample holder (5000U-04).

Fluorescence quantum yield measurements: Fluorescence quantum yield of the gel-coated filter paper was measured using a calibrated integrating sphere in a SPEX Fluorolog spectrofluorimeter. A Xe-arc lamp was used to excite the sample placed in the sphere, with 450 nm as the excitation wavelength. Absolute fluorescence quantum yield was calculated on the basis of the de Mello method[25] using the equation

$$\phi_{PL} = [E_i(\lambda) - (1 - A)E_0(\lambda)]/L_e(\lambda)A \qquad (1)$$

In equation 1

$$A = [L_0(\lambda) - L_i(\lambda)]/L_0(\lambda) \qquad (2)$$

where $E_i(\lambda)$ and $E_0(\lambda)$ are respectively the integrated luminescence as a result of direct excitation of sample and secondary excitation. A is the absorbance of the sample calculated using eq 2. $L_i(\lambda)$ is the integrated excitation when the sample is directly excited, $L_0(\lambda)$ is the integrated excitation when the excitation light first hits the sphere and reflects to the sample, and $L_e(\lambda)$ is the integrated excitation profile for an empty sphere.

Scanning electron microscopy: SEM images were taken on a JEOL 5600 LV scanning electron microscope with an accelerating voltage of 12−15 kV after sputtering with gold.

Confocal laser scanning microscopy: CLSM images were recorded on a Leica-DMIR2 Optical Microscope using UV light (438 nm) as the excitation

source, and the emission was collected between 450 to 550 nm with 10x magnification. Samples were prepared by drop-casting *n*-hexane solution on a glass slide followed by slow evaporation.

X-ray diffraction: *n*-Hexane gel of **OPVPF** (5 mg/mL) was transferred to a glass plate, and the prepared film was kept a day for slow evaporation of the solvent and finally dried under vacuum. The same xerogel-coated glass plate was exposed to saturated TNT vapor in a clossed vessel for 5 min, and immediately after exposure, the diffraction pattern was recorded. A similar experiment was conducted with the dried xerogel after dipping in TNT solution in water (5×10^{-14} M). The X-ray diffractograms of the samples before and after exposure to TNT were recorded on a Phillips diffractometer using Ni-filtered Cu Kα radiation.

Preparation of filter paper test strips: Filter paper (5 cm × 2 cm) test strips were prepared by coating the melted **OPVPF** *n*-hexane gel (1×10^{-3} M) followed by removal of solvent under vacuum at room temperature. The dip-coating of the hot solution above CGC allowed the spontaneous self-assembly of the gelator on the filter paper. The gel-coated filter papers were then cut into 10 pieces (1 cm × 1 cm) to get the test strips and used for the detection of explosives.

Contact mode visual detection of TNT: Aqueous samples were prepared by dissolving TNT in acetonitrile:water (0.5:9.5) mixture. The solutions were spotted onto the test strips at the desired concentration level using a glass microsyringe. A solvent blank was spotted near to the spot of each explosive. In order to ensure consistent analysis, all depositions were prepared from a 10 μL volume, thereby producing a spot area of ~0.2 cm^2. After solvent evaporation, the filter paper was illuminated with 365 nm UV light. The dark spots were identified by an independent observer, and each set of experiments was repeated three times for consistency. The detection limits were calculated from the lowest concentration of the explosive that enabled an independent observer to detect the quenching visually.

Quantitative detection of TNT by emission quenching: The required analyte solutions of various concentrations ($1 \times 10^{-15} - 1 \times 10^{-3}$ M) were added to each strip, and the solvents were allowed to evaporate. The film was placed in such a way that the excitation beam falls on the spot where TNT is added. Emission was collected by a front face technique using a film sample holder. Emission of a blank sample was monitored by the addition of solvent alone.

Detection of TNT in potable water: A stock solution (5×10^{-4} M) was prepared by dissolving TNT in potable water by overnight stirring at room temperature (0.114 mg/mL). This solution was diluted to different

concentrations and used as the test samples. The test samples (10 μL) were transfered to the test strips, and the fluorescence quenching was monitored under 365 nm illumination by an independent observer. The minimum detection level of TNT was qualitatively judged by the naked eye detectable fluorescence quenching on the test strip and quantitatively determined by measuring the fluorescence quenching (%) using the front face technique.

2.6. References

(1) (a) Fainberg, A. *Science* **1992**, *255*, 1531; (b) Yinon, J. *Forensic and Environmental Detection of Explosives*; John Wiley & Sons Ltd., 1999; (c) Albert, K. J.; Lewis, N. S.; Schauer, C. L.; Sotzing, G. A.; Stitzel, S. E.; Vaid, T. P.; Walt, D. R. *Chem. Rev.* **2000**, *100*, 2595; (d) Kim, T. H.; Lee, B. Y.; Jaworski, J.; Yokoyama, K.; Chung, W. J.; Wang, E.; Hong, S.; Majumdar, A.; Lee, S. W. *Acs Nano* **2011**, *5*, 2824; (e) Pinnaduwage, L. A.; Gehl, A.; Hedden, D. L.; Muralidharan, G.; Thundat, T.; Lareau, R. T.; Sulchek, T.; Manning, L.; Rogers, B.; Jones, M.; Adams, J. D. *Nature* **2003**, *425*, 474; (f) Moore, D. S. *Rev. Sci. Instrum.* **2004**, *75*, 2499; (g) Salinas, Y.; Martinez-Manez, R.; Marcos, M. D.; Sancenon, F.; Costero, A. M.; Parra, M.; Gil, S. *Chem. Soc. Rev.* **2012**, *41*, 1261.

(2) (a) Trogler, W. C. *In NATO ASI Workshop, Electronic Noses & Sensors for the Detection of Explosives*; Kluwer Academic Publishers: Netherlands., 2004; (b) Czarnik, A. W. *Nature* **1998**, *394*, 417; (c) Oxley, J. C.; Smith, J. L.; Resende, E.; Pearce, E. *J. Forensic Sci.* **2003**, *48*, 742; (d) Singh, S. *J. Hazard. Mater.* **2007**, *144*, 15.

(3) Germain, M. E.; Knapp, M. J. *Chem. Soc. Rev.* **2009**, *38*, 2543.

(4) (a) Howard, P. H.; Meylan, W. M. *Handbook of Physical Properties of Organic Chemicals*; CRC Press: Boca Raton, FL, 1997; (b) Pushkarsky, M. B.; Dunayevskiy, I. G.; Prasanna, M.; Tsekoun, A. G.; Go, R.; Patel, C. K. N. *Proc. Natl. Acad. Sci. USA* **2006**, *103*, 19630.

(5) (a) Linnen, G.; Kobrin, P. H.; Seabury, C.; Harker, A. B.; McGill, R. A.; Houser, E. J.; Chung, R.; Weber, R.; Swager, T. *Detection and Remediation Technologies for Mines and Mine like Targets Iv, Pts 1 and 2* **1999**, *3710*, 328; (b) Rose, A.; Zhu, Z. G.; Madigan, C. F.; Swager, T. M.; Bulovic, V. *Nature* **2005**, *434*, 876; (c) Swager, T. M. *Electronic Noses & Sensors for the Detection of Explosives* **2004**, *159*, 29; (d) Cumming, C. J.; Aker, C.; Fisher, M.; Fox, M.; la Grone, M. J.; Reust, D.; Rockley, M. G.; Swager, T. M.; Towers, E.; Williams, V. *Ieee Transactions on Geoscience and Remote Sensing* **2001**, *39*, 1119; (e) Narayanan, A.; Varnavski, O. P.; Swager, T. M.; Goodson, T. *J. Phys. Chem. C* **2008**, *112*, 881.

(6) (a) Toal, S. J.; Trogler, W. C. *J. Mater. Chem.* **2006**, *16*, 2871; (b) Sohn, H.; Sailor, M. J.; Magde, D.; Trogler, W. C. *J. Am. Chem. Soc.* **2003**, *125*, 3821; (c) Sanchez, J. C.; Trogler, W. C. *J. Mater. Chem.* **2008**, *18*, 3143.

(7) Swager, T. M.; Wosnick, J. H. *MRS Bull.* **2002**, *27*, 446.

(8) (a) Goldman, E. R.; Medintz, I. L.; Whitley, J. L.; Hayhurst, A.; Clapp, A. R.; Uyeda, H. T.; Deschamps, J. R.; Lassman, M. E.; Mattoussi, H. *J. Am. Chem. Soc.* **2005**, *127*, 6744; (b) Stringer, R. C.; Gangopadhyay, S.; Grant, S. A. *Advanced Environmental, Chemical, and Biological Sensing Technologies Vii* **2010**, *7673*; (c) Freeman, R.; Finder, T.; Bahshi, L.; Gill, R.; Willner, I. *Adv. Mater.* **2012**, *24*, 6416; (d) Zhang, K.; Zhou, H.

B.; Mei, Q. S.; Wang, S. H.; Guan, G. J.; Liu, R. Y.; Zhang, J.; Zhang, Z. P. *J. Am. Chem. Soc.* **2011**, *133*, 8424.

(9) Dasary, S. S. R.; Singh, A. K.; Senapati, D.; Yu, H. T.; Ray, P. C. *J. Am. Chem. Soc.* **2009**, *131*, 13806.

(10) (a) Jerez Rozo, J. I.; del Rocio Balaguera, M.; Cabanzo, A.; de la Cruz Montoya, E.; Hernandez-Rivera, S. P. *Sensors, and Command, Control, Communications, and Intelligence (C31)Technologies for Homeland Security and Homeland Defense V* **2006**, *6201*, G2012; (b) Yang, L. B.; Chen, G. Y.; Wang, J.; Wang, T. T.; Li, M. Q.; Liu, J. H. *J. Mater. Chem.* **2009**, *19*, 6849.

(11) (a) Lan, A. J.; Li, K. H.; Wu, H. H.; Olson, D. H.; Emge, T. J.; Ki, W.; Hong, M. C.; Li, J. *Angew. Chem. Int. Ed.* **2009**, *48*, 2334; (b) Nagarkar, S. S.; Joarder, B.; Chaudhari, A. K.; Mukherjee, S.; Ghosh, S. K. *Angew. Chem. Int. Ed.* **2013**, *52*, 2881; (c) Gole, B.; Bar, A. K.; Mukherjee, P. S. *Chem. Commun.* **2011**, *47*, 12137; (d) Xu, H.; Liu, F.; Cui, Y. J.; Chen, B. L.; Qian, G. D. *Chem. Commun.* **2011**, *47*, 3153; (e) Sun, L. B.; Xing, H. Z.; Xu, J.; Liang, Z. Q.; Yu, J. H.; Xu, R. R. *Dalt. Trans.* **2013**, *42*, 5508; (f) Zhou, X. H.; Li, H. H.; Xiao, H. P.; Li, L.; Zhao, Q.; Yang, T.; Zuo, J. L.; Huang, W. *Dalt. Trans.* **2013**, *42*, 5718; (g) Xue, Y. S.; He, Y. B.; Zhou, L.; Chen, F. J.; Xu, Y.; Du, H. B.; You, X. Z.; Chen, B. L. *J. Mater. Chem. A* **2013**, *1*, 4525; (h) Pramanik, S.; Zheng, C.; Zhang, X.; Emge, T. J.; Li, J. *J. Am. Chem. Soc.* **2011**, *133*, 4153; (i) Li, R.; Yuan, Y. P.; Qiu, L. G.; Zhang, W.; Zhu, J. F. *Small* **2012**, *8*, 225.

(12) (a) Riskin, M.; Tel-Vered, R.; Bourenko, T.; Granot, E.; Willner, I. *J. Am. Chem. Soc.* **2008**, *130*, 9726; (b) Riskin, M.; Tel-Vered, R.; Lioubashevski, O.; Willner, I. *J. Am. Chem. Soc.* **2009**, *131*, 7368.

(13) Engel, Y.; Elnathan, R.; Pevzner, A.; Davidi, G.; Flaxer, E.; Patolsky, F. *Angew. Chem. Int. Ed.* **2010**, *49*, 6830.

(14) (a) Ajayaghosh, A.; Praveen, V. K. *Acc. Chem. Res.* **2007**, *40*, 644; (b) Ajayaghosh, A.; Praveen, V. K.; Vijayakumar, C. *Chem. Soc. Rev.* **2008**, *37*, 109; (c) Ariga, K.; Hill, J. P.; Lee, M. V.; Vinu, A.; Charvet, R.; Acharya, S. *Sci. Tech. Adv. Mater.* **2008**, *9*; (d) Babu, S. S.; Kartha, K. K.; Ajayaghosh, A. *J. Phys. Chem. Lett.* **2010**, *1*, 3413; (e) Kim, H. J.; Kim, T.; Lee, M. *Acc. Chem. Res.* **2011**, *44*, 72.

(15) (a) Vijayakumar, C.; Praveen, V. K.; Ajayaghosh, A. *Adv. Mater.* **2009**, *21*, 2059; (b) Ajayaghosh, A.; Praveen, V. K.; Srinivasan, S.; Varghese, R. *Adv. Mater.* **2007**, *19*, 411; (c) Ajayaghosh, A.; Vijayakumar, C.; Varghese, R.; George, S. J. *Angew. Chem. Int. Ed.* **2006**, *45*, 456; (d) Ajayaghosh, A.; Vijayakumar, C.; Praveen, V. K.; Babu, S. S.; Varghese, R. *J. Am. Chem. Soc.* **2006**, *128*, 7174; (e) Srinivasan, S.; Babu, P. A.; Mahesh, S.; Ajayaghosh, A. *J. Am. Chem. Soc.* **2009**, *131*, 15122.

(16) (a) Naddo, T.; Che, Y. K.; Zhang, W.; Balakrishnan, K.; Yang, X. M.; Yen, M.; Zhao, J. C.; Moore, J. S.; Zang, L. *J. Am. Chem. Soc.* **2007**, *129*, 6978; (b) Zang, L.; Che, Y. K.; Moore, J. S. *Acc. Chem. Res.* **2008**, *41*, 1596; (c) Zyryanov, G. V.; Palacios, M. A.; Anzenbacher, P. *Org. Lett.* **2008**, *10*, 3681; (d) Vijayakumar, C.; Tobin, G.; Schmitt, W.; Kim, M. J.; Takeuchi, M. *Chem. Commun.* **2010**, *46*, 874; (e) Gole, B.; Shanmugaraju, S.; Bar, A. K.; Mukherjee, P. S. *Chem. Commun.* **2011**, *47*, 10046; (f) Bhalla, V.; Gupta, A.; Kumar, M. *Org. Lett.* **2012**, *14*, 3112; (g) Kumar, M.; Vij, V.; Bhalla, V. *Langmuir* **2012**, *28*, 12417; (h) Bhalla, V.; Pramanik, S.; Kumar, M. *Chem. Commun.* **2013**, *49*, 895.

(17) (a) Babu, S. S.; Mahesh, S.; Kartha, K. K.; Ajayaghosh, A. *Chem. Asian J.* **2009**, *4*, 824; (b) George, S. J.; Ajayaghosh, A. *Chem. -Eur. J.* **2005**, *11*, 3217; (c) Ajayaghosh, A.; George, S. J. *J. Am. Chem. Soc.* **2001**, *123*, 5148.

(18) (a) Vijayakumar, C.; Praveen, V. K.; Kartha, K. K.; Ajayaghosh, A. *Phys. Chem. Chem. Phys.* **2011**, *13*, 4942; (b) Ajayaghosh, A.; George, S. J.; Praveen, V. K. *Angew. Chem. Int. Ed.* **2003**, *42*, 332; (c) Praveen, V. K.; George, S. J.; Varghese, R.; Vijayakumar, C.; Ajayaghosh, A. *J. Am. Chem. Soc.* **2006**, *128*, 7542.

(19) Babu, S. S.; Praveen, V. K.; Prasanthkumar, S.; Ajayaghosh, A. *Chem. -Eur. J.* **2008**, *14*, 9577.

(20) (a) Feast, W. J.; Lovenich, P. W.; Puschmann, H.; Taliani, C. *Chem. Commun.* **2001**, 505; (b) Capelli, R.; Loi, M. A.; Taliani, C.; Hansen, H. B.; Murgia, M.; Ruani, G.; Muccini, M.; Lovenich, P. W.; Feast, W. J. *Synth. Met.* **2003**, *139*, 909; (c) Kilbinger, A. F. M.; Grubbs, R. H. *Angew. Chem. Int. Ed.* **2002**, *41*, 1563; (d) Borges, A. R.; Hyacinth, M.; Lum, M.; Dingle, C. M.; Hamilton, P. L.; Chruszcz, M.; Pu, L.; Sabat, M.; Caran, K. L. *Langmuir* **2008**, *24*, 7421; (e) Ryan, D. M.; Doran, T. M.; Nilsson, B. L. *Langmuir* **2011**, *27*, 11145.

(21) Sanchez, J. C.; DiPasquale, A. G.; Rheingold, A. L.; Trogler, W. C. *Chem. Mater.* **2007**, *19*, 6459.

(22) (a) Shriverlake, L. C.; Breslin, K. A.; Charles, P. T.; Conrad, D. W.; Golden, J. P.; Ligler, F. S. *Anal. Chem.* **1995**, *67*, 2431; (b) ShriverLake, L. C.; Donner, B. L.; Ligler, F. S. *Environ. Sci. Technol.* **1997**, *31*, 837; (c) Van Bergen, S. K.; Bakaltcheva, I. B.; Lundgren, J. S.; Shriver-Lake, L. C. *Environ. Sci. Technol.* **2000**, *34*, 704.

(23) Saxena, A.; Fujiki, M.; Rai, R.; Kwak, G. *Chem. Mater.* **2005**, *17*, 2181.

(24) (a) Bredas, J. L.; Cornil, J.; Heeger, A. J. *Adv. Mater.* **1996**, *8*, 447; (b) Tan, C. Y.; Alas, E.; Muller, J. G.; Pinto, M. R.; Kleiman, V. D.; Schanze, K. S. *J. Am. Chem. Soc.* **2004**, *126*, 13685.

(25) deMello, J. C.; Wittmann, H. F.; Friend, R. H. *Adv. Mater.* **1997**, *9*, 230.

Chapter 3

A Multi-Stimuli Responsive π-Gelator with Tunable Gelation and Morphological Properties

3.1. Abstract

*Amide functionalized **OPV** derivatives containing pyridine (**PY**) and benzene (**BZ**) groups as the end substituents were designed and synthesized. **OPV-PY** was able to form organogels independently in pyridine and toluene/tetrahydrofuran mixture (9.5:0.5) upon heating, followed by cooling. Since **OPV-PY** contains a pyridine unit, protonation with TFA facilitates the formation of hydrogen bonded assembly leading to gelation, which was reversible by the addition of an organic base. **OPV-PY** also forms a metallosupramolecular assembly with Ag^{+} ions resulting in organogel formation. Further, two component gels were prepared with different organic acids. Surprisingly, ultrasound induced gelation was observed for one of the pyridine-acid complex (**OPV-PY**-A1). The self-assembly, gelation and morphological properties were monitored using different spectroscopic and microscopic experimental techniques.*

3.2. Introduction

Supramolecular assembly of small molecules have been intensively studied in terms of fundamental interest and practical applications.[1] In this context, one dimensional (1-D) self-assembly of π-systems is of much importance in the creation of supramolecular architectures and as promising materials for nanodevices.[2] In certain cases, the self-assembly process of π-systems through different non-covalent interactions leads to the formation of organogels in different apolar solvents. Organogelators with urea and amide moieties, provides a better way of packing through unidirectional hydrogen bonds (Scheme 3.1).[3] Usually, sol to gel transtion of a gelator also could be achieved using a thermal stimuli. Recently, organogels with stimuli-responsive properties have been evolved as one of the fascinating class of functional materials.[4] Stimuli responsive systems are aslo known as smart materials because of their tunable properties. Most of these materials are responsive to an external stimulus such as temperature,[5] light,[6] sound[7] or a combination of these. Among the different classes, stimuli responsive gels are receiving much attention due to applications in various areas such as sensors,[2e,8] actuators,[9] drug delivery,[10] display devices[11] etc. Control of the sol-gel phase transition in a predictable fashion is important to the design of functional nanomaterials and nanodevices.[1d,2e] Even though, a number of stimuli responsive gels are known, reports pertaining to multiple stimuli responsive organogels are rare.[12] In

stimuli responsive systems containing ferrocene,[12e,13] tetrathiafulvalene,[14] pyridine,[3a,15] various external stimuli such as oxidizing and reducing reagents, metal ions, acids, ultrasound etc. are used to modulate gelation and morphological properties.

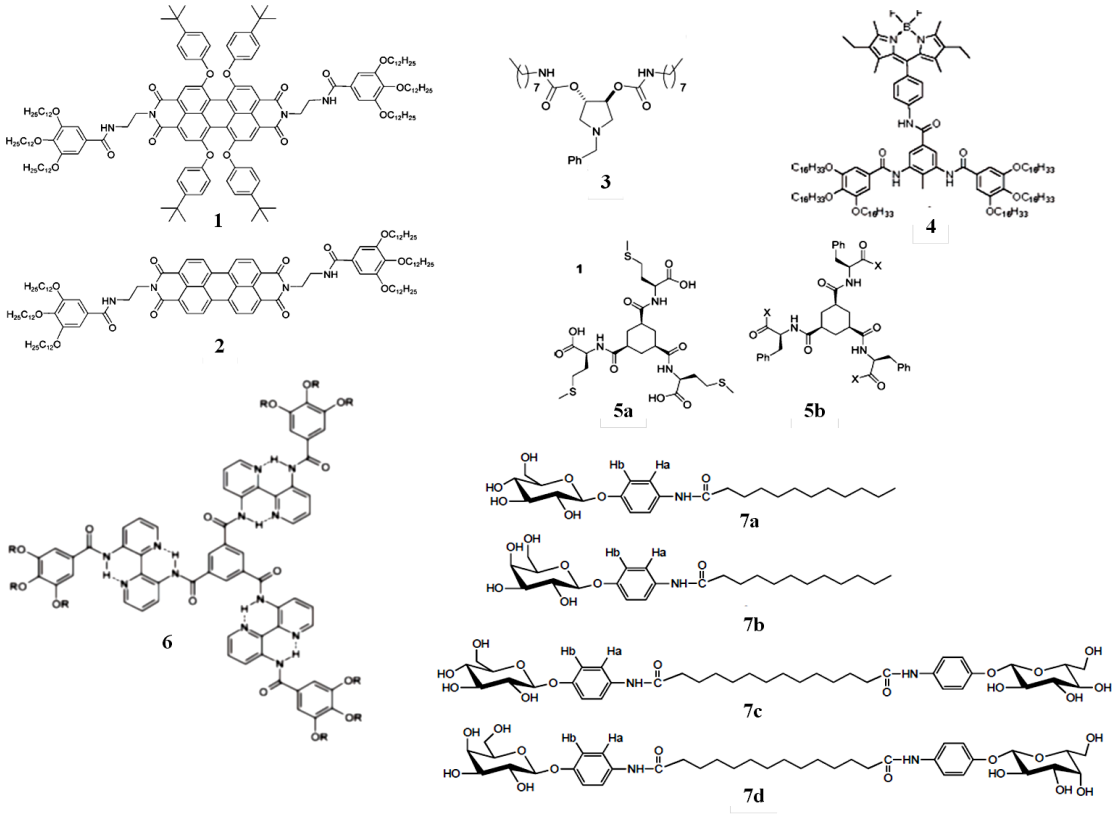

Scheme 3.1. Molecular strcutures of different amide derivatives.

Lee *et al.* reported reversible sol-gel interconversion of coordination polymers in aqueous media from a folded helical chain to an unfolded zig-zag conformation with counteranion exchange, driven by depolymerization or conformational change.[16] Gels reversibly transform into fluid solutions with

counteranion exchange of BF_4^- with a larger ion $C_2F_5CO_2^-$. Upon addition of one equivalent of $Bu_4N^+C_2F_5CO_2^-$ to the [Ag-**8**]BF_4 gel, it transforms rapidly into a fluid solution (Figure 3.1a).

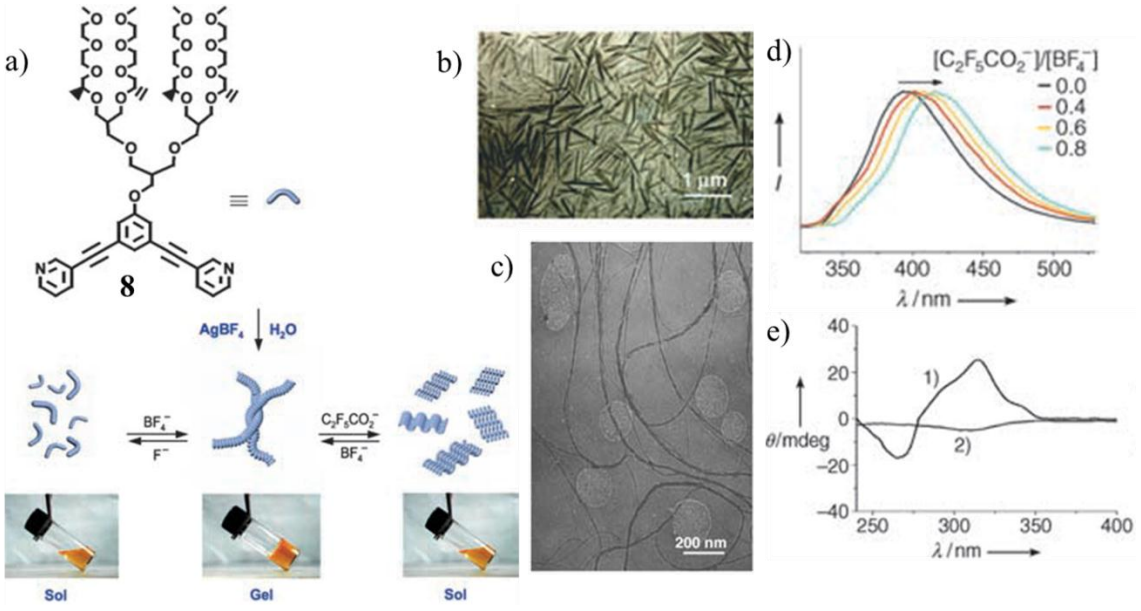

Figure 3.1. (a) Chemical structure of **8** and schematic representation of reversible polymerization and reversible conversion between folded and unfolded conformations of a coordination chain upon counteranion exchange. (b) TEM image of dried gel from [Ag-**8**]BF_4 in H_2O (0.3 wt%) stained with RuO_4. (c) TEM image of [Ag-**8**]$C_2F_5CO_2$ in H_2O (0.3 wt%) stained with RuO_4. (d) Fluorescence spectra of [Ag-**8**]BF_4 (5 wt%) with increasing amounts of $Bu_4N^+C_2F_5CO_2^-$. (e) Circular dichroism (CD) spectra of: [Ag-**8**]BF_4 (5 wt%); 1) before and 2) after the addition of 1 equivalent of $Bu_4N^+C_2F_5CO_2^-$.

Transmission electron microscopy (TEM) analysis of the gels revealed right-handed helical bundles of elongated fibers with diameters of 6–30 nm, leading

to the formation of an entangled fibrillar network (Figure 3.1b). In contrast to the gel of [Ag-**8**]BF_4, the TEM image of the homologous complex, [Ag-**8**]$C_2F_5CO_2$, showed discrete ribbon-like aggregates with a length of 0.7‑1.3 mm and width of 20‑40 nm (Figure 3.1c). The fluorescence spectrum of the gel of [Ag-**8**]BF_4 exhibited an emission maximum at 400 nm, indicating helix formation. Upon addition of upto 0.8 equivalent of $C_2F_5CO_2^-$ ions, the emission maximum gradually red-shifted (20 nm) with respect to that observed in the gel state (Figure 3.1d). The gels exhibited a significant cotton effect at the chromophore absorption region, which supported the presence of elongated helical aggregates in aqueous solution, whereas CD spectra of the [Ag-**8**]BF_4/$C_2F_5CO_2$ solution showed no cotton effect (Figure 3.1e).

The formation of coordination polymers based on Ag^+ ion complexed with pyridine ligands based on phenanthrene (Figure 3.2a) with a bent conformation and their dynamic self-assembly in aqueous solution were studied by Lee *et al.* (Figure 3.2b).[17] The CD spectra of the polymers showed strong signals over the absorption region, indicating the formation of a helical structure with a preferred handedness (Figure 3.2c). The evidence for the formation of helical structures were also provided by TEM experiments (Figure 3.2d). At high temperatures, absorption spectra of **10** was significantly red shifted (20 nm) with respect to that at lower temperatures, indicating that the coordination polymers adopt longer conjugation length (Figure 3.2e). The CD spectra, upon

heating, showed red-shifted signals and significant decrease in intensity, which were attributed to the diminished exciton coupling between aromatic stackings due to elongated conjugation length (Figure 3.2f).

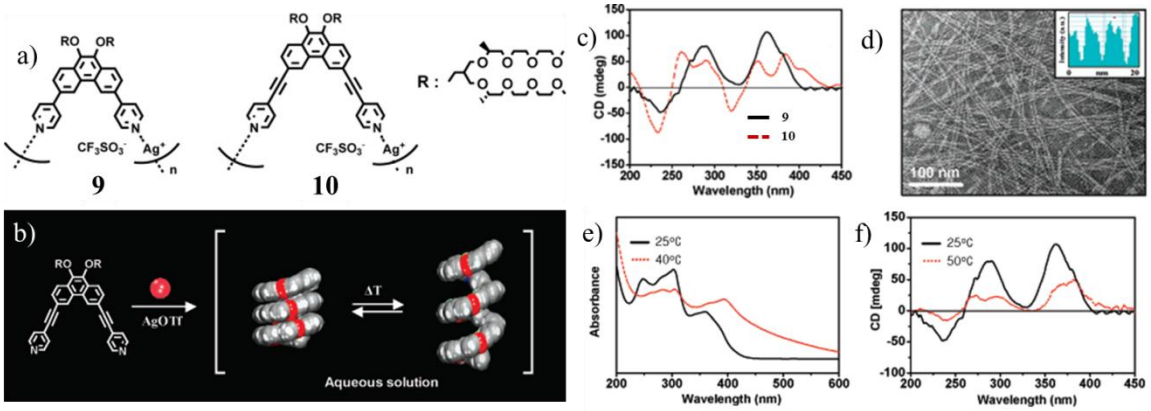

Figure 3.2. (a) Chemical structure of phenanthrene based ditopic bridging ligands **9** and **10**. (b) Schematic representation of a reversible helical spring. (c) CD spectra for **9** and **10** in aqueous solution (0.1 wt %) at 25 °C. (d) TEM image of **10** with density profile inset. UV/vis spectra (e) and CD spectra (f) of **10** (0.1 wt % aqueous solutions) with temperature variation.

A series of bis(pyridyl) acceptors were synthesized and the liquid crystalline (LC) and photophysical properties of their supramolecular structures, including H-bonded polymer networks and trimers (Figure 3.3), were explored by Lin *et al.*[18] The mesomorphic and photophysical properties of the H-bonded polymer networks and trimers were adjusted by tuning the composition of donor polymers and acceptor emitters in the complexes. In addition, the emission properties of the bis(pyridyl) acceptors were manipulated by their surrounding

nonphotoluminescent proton donors.

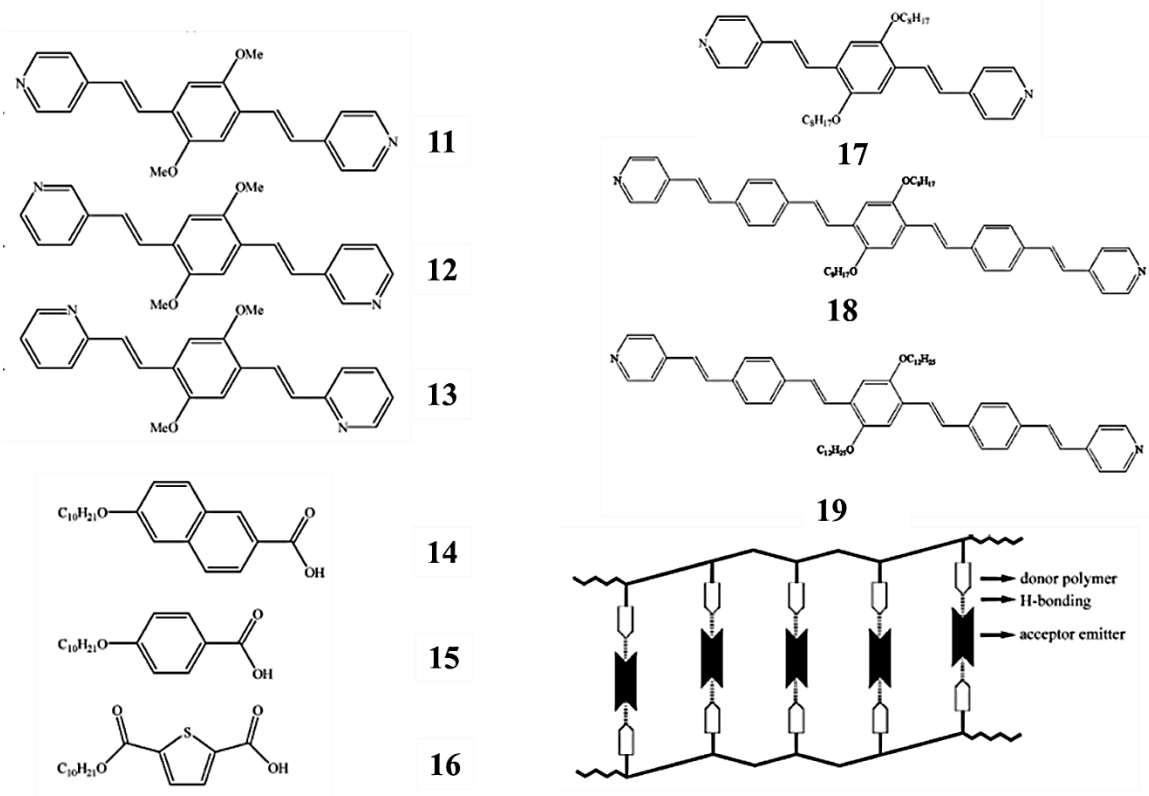

Figure 3.3. Chemical structures of bis(pyridyl) acceptors and donor polymers and the simplified schematic drawing of the idealized H-bonded polymer networks.

A highly fluorescent chiral transparent organogel was developed by Park *et al. via* a H-bond mediated supramolecular assembly of non-fluorescent and achiral CN-TFMBPPE and chiral L/D-tartaric acid (L-TA or D-TA) (Figure 3.4a).[19] The SEM image of the dried gel revealed a typical network structure of entangled and fibrillar aggregates (Figure 3.4b). As the H-bonded complex was generated (Figure 3.4c), a translucent partial gel with a characteristic absorption

and aggregation induced enhanced emission (AIEE) was slowly formed over a period of several hours.

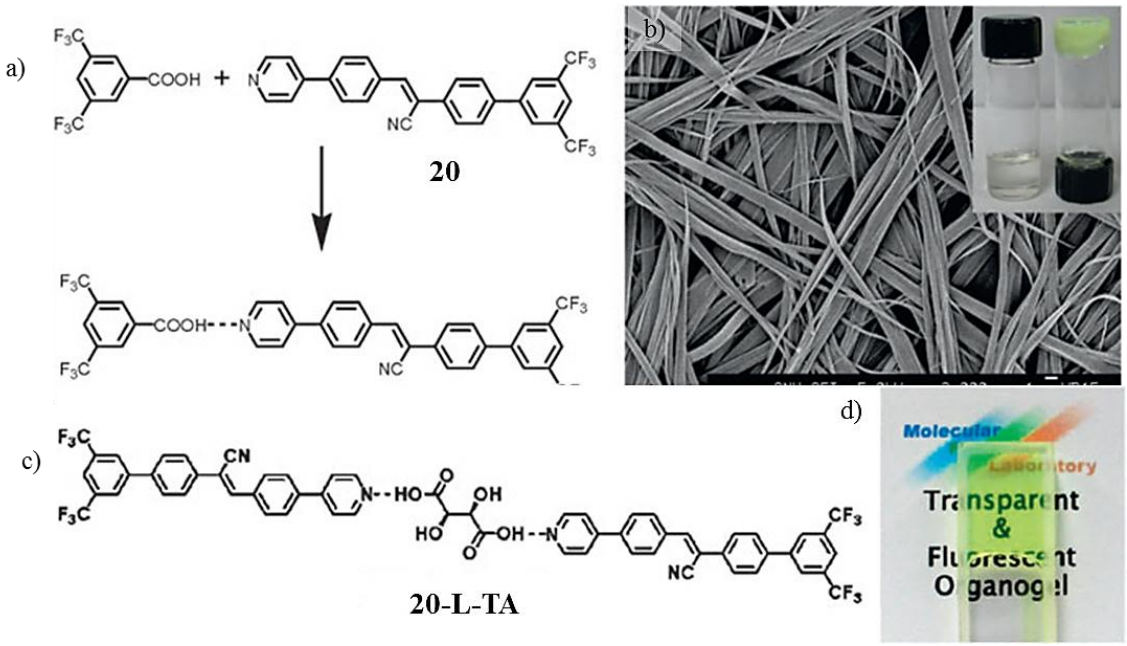

Figure 3.4. (a) Schematic representation of the hydrogen (H)-bonded complex between **20** and 3,5-bistrifluoromethyl benzoic acid (BA). (b) SEM image of a dried gel (partial) formed from the H-bonded complex between **20** (1 wt%, 1 equiv.) and BA (1 equiv.) in DCE. Inset displays photo images of the corresponding solution of **20** (left) and H-bonded complex gel (right) state. (c) H-bonded complex between **20** and L-TA, and (d) photo image of a transparent gel (L-TA complex gel (1 wt%) from **20** (1 wt%, 1 equiv.) and L-TA (0.5 equiv.) in DCE–THF (10 : 1).

Authors introduced L-TA to improve the gel stability as well as to induce chiral organization in this system. The formation of a transparent and highly fluorescent organogel accompanied by the characteristic appearance of a bright yellow color due to AIEE was observed (Figure 3.4d).

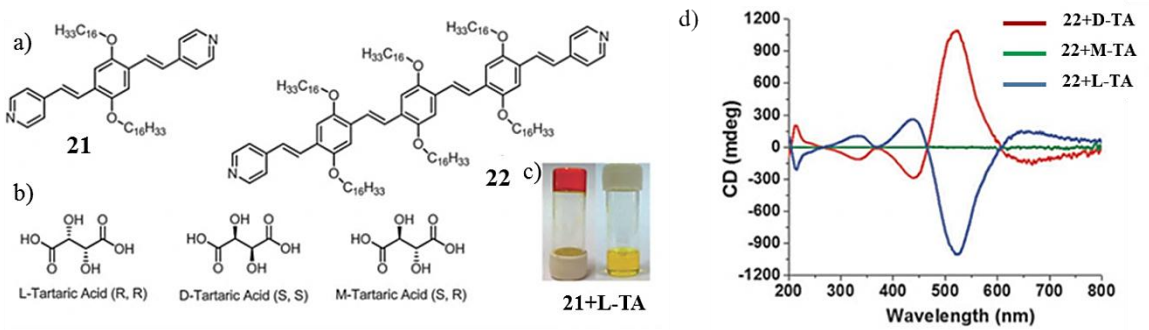

Figure 3.5. (a) Structures of the gelators **21** and **22** and (b) tartaric acids (TAs) used for the gelation studies. (c) Photographs showing sol and gel of **21**+L-TA. (d) Circular dichroism spectra of **22**+TA complexes.

Recently, Bhattacharya *et al.* reported the organogelation of new chromophoric pyridine-end capped oligo(*p*-phenylenevinylenes) (**OPV**s, **21** and **22**, Figure 3.5) in combination with isomeric tartaric acids viz. L-tartaric acid (L-TA) and D-tartaric acid (D-TA). Studies were carried out on chirality transcription in the supramolecular assembly *via J*-aggregate formation.[20] Red-shifts in the emission maxima were considered to be due to the protonation and *J*-aggregation induced by gel formation. Circular Dichroism (CD) spectral studies verified the chiral transcription abilities of the self-assembly of the isomeric TAs with the gelator **22** as shown in Figure 3.5.

In bottom-up self-assembly process, a large number of molecules interact each other to form nanostructures with more or less defined size and shape. Despite the above mentioned studies, controlling the reversible sol-gel processes, control over the aspect ratio of supramolecular architectures and

creation of different nanostructures from same building block etc. remain to be the challenging tasks for a supramolecular chemist.[21] In the present work, we synthesized the oligo(*p*-phenylenevinylene) derivatives, **OPV-PY** and **OPV-BZ** functionalized with pyridine and benzene groups, respectively, through an amide linkage (Scheme 3.2). We envisioned that the introduction of pyridine units at both ends of the **OPV** segment might form stimuli-responsive nanostructures, since pyridine units are known to interact specifically with acids and Ag^+ ions through reversible coordination bonds. An oligo(*p*-phenylenevinylene) derivative (**OPV-BZ**) functionalized with a benzene moiety through an amide linkage was prepared for comparitive studies.

3.3. Results and discussion

3.3.1. Syntheses of OPV-PY and OPV-BZ

OPV-PY and **OPV-BZ** were synthesized from the **OPV** bisacid (**OPV2**) as depicted in Scheme 3.2. For this purpose, the **OPV** bisester **(OPV1)** was synthesized according to a known procedure.[5e,22] **OPV1** on hydrolysis using **KOH** in methanol and tetrahydrofuran (THF) yielded the **OPV** bisacid (**OPV2**). The final reaction between **OPV2** and the amine derivative was conducted using the peptide coupling agent, 2-(1H-7-Azabenzotriazol-1-yl)-1,1,3,3-tetramethyl uranium hexafluorophosphate methaminium (HATU) in dichloromethane in the presence of *N*,*N*-diisopropylethylamine. 4-Amino pyridine and aniline were used

in the final coupling reaction for the preparation of **OPV-PY** and **OPV-BZ**, respectively (Scheme 3.2). These compounds were characterized by ^{1}H NMR, ^{13}C NMR, MALDI-TOF and FT-IR spectroscopic techniques.

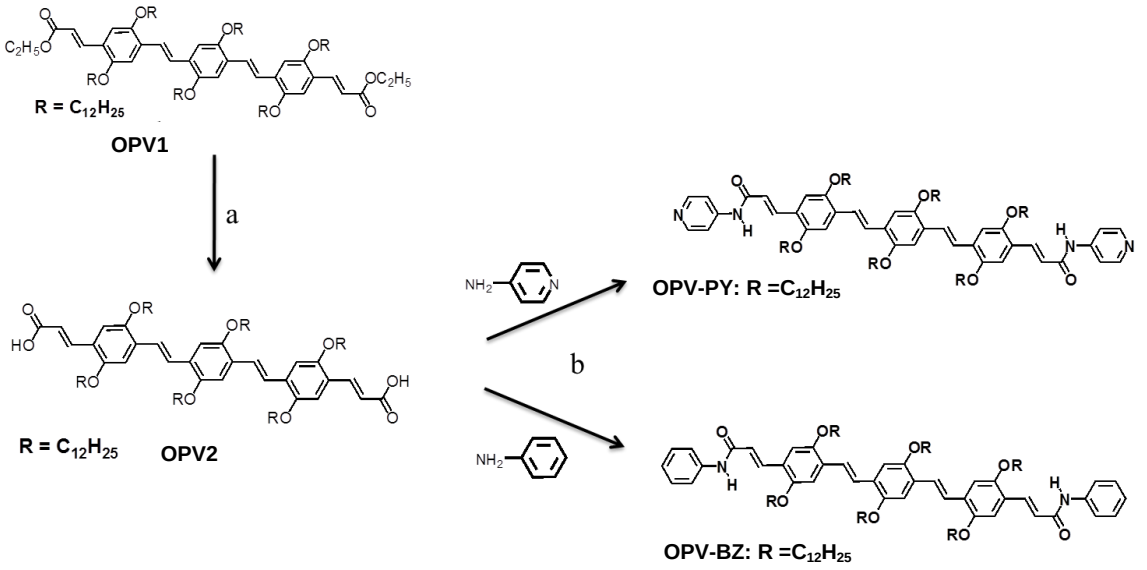

Scheme 3.2. Reagents and conditions: (a) KOH, Methanol/THF, 60 °C, 5 h, (95%); (b) HATU, N,N'- DiPEA, DCM, 0 °C – 25 °C, 6 h, (90%).

3.3.2. Aggregation properties of OPV-PY in different solvents

In THF, at a concentration of 5×10^{-5} M, both the amide derivatives were in the molecularly dissolved state. **OPV-PY** showed a strong π-π* electronic transition band around 450 nm and broad band with maxima around 520 and 550 nm in the absorption and emission spectra, respectively. The absence of the aggregate band at higher wavelength region in the absorption spectrum is an indication of the monomeric state in THF.

Solvent	λ_{abs} (nm)	λ_{ems} (nm)	Φ_f	τ (ns)
THF	448	520, 550	0.61	1.35
Pyridine	438	505, 540	0.25	0.79 (43%) 1.6 (57%)
$CHCl_3$	446	535, 560	0.35	0.69 (45%) 1.62 (55%)
Toluene	446	505, 540	0.30	0.88 (48%) 1.62 (52%)

Table 1. [a] Fluorescence quantum yields (±5% error) were determined using fluorescein as the standard (Φ_f = 0.99 in water). All measurements were carried out at a concentration of 5 × 10^{-5} M except for fluorescence quantum yield measurement for which the absorbance at the excitation wavelength (λ_{ex} = 440 nm) was adjusted to 0.1.

The absorption spectrum of **OPV-PY** in toluene (5 × 10^{-5} M) showed a shoulder band at around 530 nm and the emission spectrum showed significant quenching of intensity with further broadening of the band (Figure 3.6). Similarly, **OPV-PY** in $CHCl_3$ (5 × 10^{-5} M) showed an aggregation band at higher wavelength with a decrease in the intensity of the absorption. Aggregation of **OPV-PY** was also observed in pyridine (5 × 10^{-5} M) as

evidenced from the absorption and emission spectra (Figure 3.6). In THF, both compounds showed monoexponential decay with lifetime of 1.35 ns for **OPV-PY** and 1.4 ns for **OPV-BZ**. Details of the absorption and emission characteristics of **OPV-PY** in different solvents together with the quantum yields (Φ_f) and lifetimes (τ) are shown in Table 1.

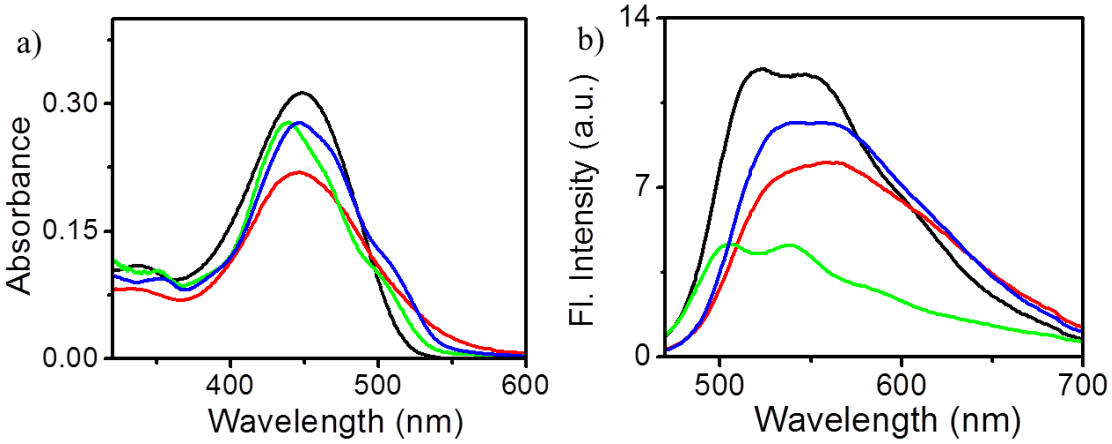

Figure 3.6. (a) Absorption and (b) emission spectra of **OPV-PY** in THF (black), pyridine (green) $CHCl_3$ (blue) and toluene (red) at a conc. of 5×10^{-5} M.

A small blue shift in absorption and emission maxima of **OPV-PY** in pyridine was observed when compared to **OPV-PY** in THF. However, there was no significant shift in the absorption and emission maxima both in toluene and $CHCl_3$. A shoulder band at higher wavelength was observed in the absorption spectrum for **OPV-PY** in these solvents except in THF which is an indication of aggregation. However, the blue shift of **OPV-PY** in pyridine indicates the formation of an assembly different from the **OPV-PY** assembly in toluene and

$CHCl_3$. The quenched but structured band in the emission spectrum of **OPV-PY** in pyridine may be due to the formation of an organized assembly when compared to that in toluene and $CHCl_3$.

In order to understand the difference in the packing of **OPV-PY** in different solvents, variable temperature (VT) experiments were performed in toluene and pyridine. In toluene, at 20 °C, the absorption spectrum of **OPV-PY** showed a shoulder band at 530 nm corresponding to aggregates, in addition to the π-π* transition band (λ_{max} = 440 nm). In contrast to other **OPV** amides, no considerable blue shift in the absorption maximum was observed for **OPV-PY** aggregates in toluene. At 70 °C, the shoulder band disappeared with an increase in the intensity of the π-π* transition band. Slightly red shifted emission maximum at 20 ℃ was observed for **OPV-PY** aggregates in toluene which showed an increase in the intensity with increase in temperature. In pyridine, at 20 ℃, the absorption spectrum of **OPV-PY** showed an aggregate band around 520 nm with a ~10 nm blue shift in the absorption maximum. Whereas the emission spectrum retained the structure but quenched due to aggregation. Disappearance of the aggregation band and subsequent enhancement in the absorption as well as emission maxima were observed for **OPV-PY** assembly in pyridine with an increase in temperature. Plots of the fraction of the aggregate (α) vs temperature in toluene and pyridine revealed that the melting transition temperature of **OPV-PY** aggregate is 54 ℃ in toluene, whereas in pyridine it is

decreased to 39 ℃ (Figure 3.7).

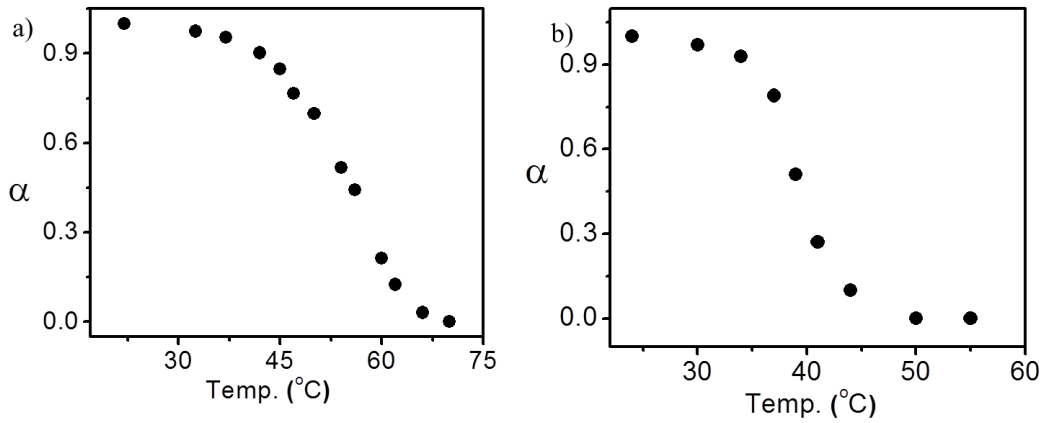

Figure 3.7. Plots of fraction of the aggregate (α) vs. temperature of **OPV-PY** in (a) toluene and (b) pyridine with a conc. of 5×10^{-5} M.

Since **OPV-PY** contains two pyridine units on both ends, modulation of the self-assembly of **OPV-PY** through protonation of the pyridine moiety using trifluoroacetic acid (TFA) has been achieved. As shown in Figure 3.8a, addition of TFA to the solution of **OPV-PY** in $CHCl_3$ (5×10^{-5} M) shifted the absorption maximum from 445 nm to 474 nm with decrease in the intensity ($CHCl_3$ was chosen because of the high solubility of TFA and metal salts). In addition, the emission was significantly quenched with a red shift of the maximum from 525 to 567 nm. Addition of excess of TFA induced further shift of the absorption maximum to 490 nm and the emission maximum to 610 nm (Figure 3.8a; inset). The aggregate band observed at higher wavelength in the absorption spectrum of **OPV-PY** (5×10^{-5} M) in the presence of TFA is an indication of the

formation of extended hierarchical assemblies.

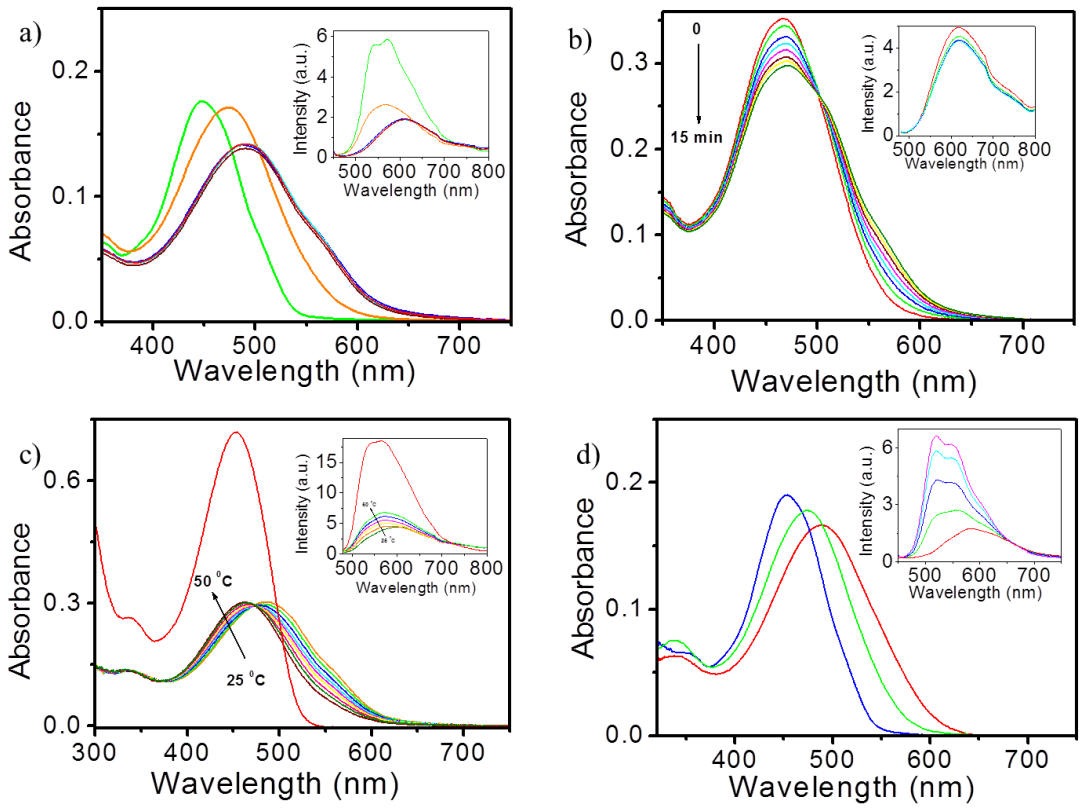

Figure 3.8. (a) Absorption spectral changes of **OPV-PY** in $CHCl_3$ (5×10^{-5} M) containing different concentrations of TFA. (b) Time dependent absorption changes of **OPV-PY** in $CHCl_3$ with 3 eq. of TFA. (c) Variable temperature absorption spectra of **OPV-PY** in $CHCl_3$ containing 3 eq. of TFA and addition of 3.2 equivalents of diisopropylethylamine (red trace). (d) Absorption spectral changes of **OPV-PY** in $CHCl_3$ (5×10^{-5} M) containing different concentrations of AgOTf; inset (right top) corresponding emission spectra.

Thus, **OPV-PY** functions as an acid sensitive gel in the presence of TFA in $CHCl_3$. Time dependent absorption spectra of **OPV-PY** in $CHCl_3$ in the presence of 3 equivalents of TFA have shown that, with increase in time, there

is a decrease in the absorbance (Figure 3.8b). Without much change in the intensity, the absorption maximum was blue shifted and the emission spectrum showed a slight increase in the intensity, once the temperature of **OPV-PY** in $CHCl_3$ in the presence of 3 equivalents of TFA changed from 25 °C to 50 °C (Figure 3.8c). Interestingly, addition of 3.2 equivalents of diisopropyethylamine (DiPEA) to such **OPV-PY**-TFA (1:3) complex resulted in the formation of monomer absorption and emission bands due to the deprotonation followed by the disassembly of the **OPV-PY** (Figure 3.8c; red trace). These observations suggest the control of aggregation through the addition of acid and base.

It is known that nitrogen atom of pyridine can coordinate with metal ions such as Ag^+, Zn^{2+}, Cd^{2+}, Mg^{2+} ions etc. Among these, the complexation between Ag^+ ions and pyridine is well studied. In order to understand the changes in the optical properties, **OPV-PY** in $CHCl_3$ (5×10^{-5} M) was titrated with silvertriflate (AgOTf) in $CHCl_3$. With increase in the concentration of Ag^+ ions, absorption and emission intensity were decreased and at 1:1 molar ratio, the absorption and emission maxima were red shifted with further decrease in the intensity (Figure 3.8d). Upon increasing the concentration of **OPV-PY** to 5×10^{-4} M, a stable gel in $CHCl_3$ was formed. This is attributed to the formation of an extended linear metallosupramolecular polymer in solution, growth of which may be assisted by the amide hydrogen bonding and π-stacking.

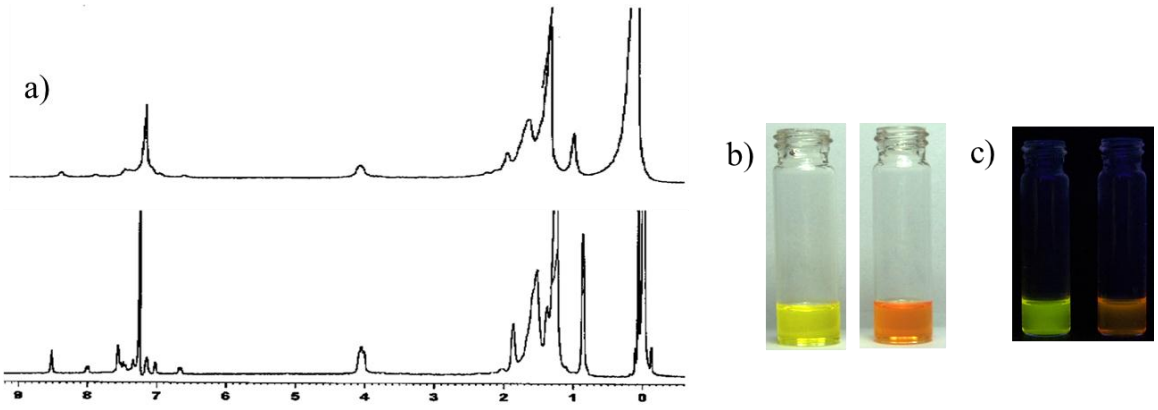

Figure 3.9. (a) ^{1}H NMR spectra of **OPV-PY** (1×10^{-4} M) in $CDCl_3$ before (bottom) and after (top) addition of 1eq. of TFA. (b,c) Photographs of **OPV-PY** (1×10^{-4} M) in $CHCl_3$ showing changes before (left) and after (right) the addition of TFA under normal and uv light, respectively.

Upon addition of TFA, a broadening was observed in the ^{1}H NMR spectrum in $CDCl_3$, which indicated the acid induced aggregation of **OPV-PY** (Figure 3.9a). This could be visualized directly from the photographs of the $CHCl_3$ solutions of **OPV-PY** before and after the addition of TFA as shown in Figure 3.9b. The greenish emission of the dissolved **OPV-PY** in $CHCl_3$ changed to an organge red emission upon addition of TFA which is evident from the photographs shown in Figure 3.9c.

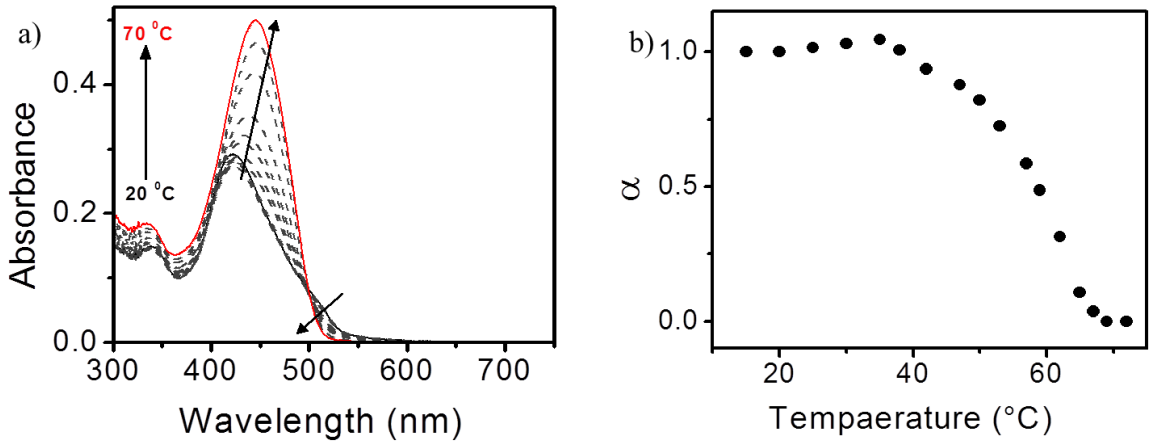

Figure 3.10. (a) Variable temperature absorption spectra and (b) plot of fraction of the aggregate (α) vs. temperature of the **OPV-BZ** in toluene at a conc. of 5 × 10^{-5} M.

To get insight into the effect of pyridine end functional group to the stimuli responsive self-assembly of the **OPV-PY**, a model derivative (**OPV-BZ**) with benzene units on either end was prepared. In toluene, the **OPV-BZ** showed a blue shift of the absorption maximum from 450 nm to 430 nm with the appearance of a shoulder band around 520 nm (5 × 10^{-5} M) corresponding to aggregation. Upon varying the temperature from 20 ℃ to 70 ℃, a decrease in the shoulder band with increase in the absorption maximum were noticed (Figure 3.10a). A plot of the fraction of aggregate vs. temperature for **OPV-BZ** in toluene showed a melting transition temperature of 59 ℃ (Figure 3.10b). No significant changes were observed in the absorption and emission spectra by the addition of excess TFA into a $CHCl_3$ solution (5 × 10^{-5} M) of the **OPV-BZ** (Figure 3.11). This observation emphasises the importance of the heteroatom

nitrogen in the **OPV-PY** to induce the stimuli responsive character. A reduction in the electron density of the pyridine ring, especially on nitrogen atom enhances aggregation and thereby gelation of the **OPV-PY**.

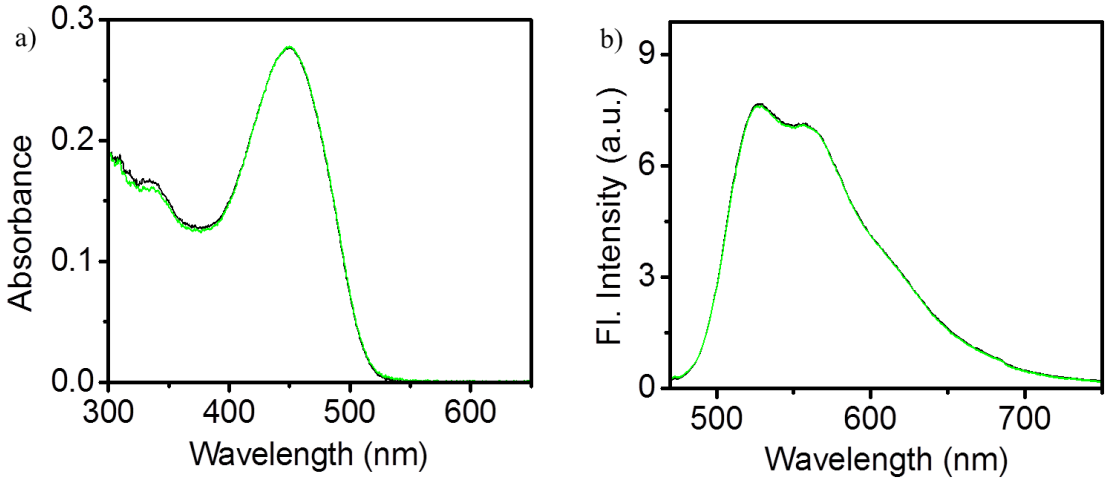

Figure 3.11. Absorption (a) and emission (b) spectra of the **OPV-BZ** in $CHCl_3$ (1×10^{-5} M, black) containing 3 equivalents of TFA (green).

Since the **OPV-PY** has two pyridine moieties on both ends, hydrogen bonded supramolecular polymers could be formed by the co-assembly with appropriate dicarboxylic acids. We have chosen a few organic acids for this purpose as shown in Scheme 3.3. Refluxing the **OPV-PY** with the appropriate acid in a 1:1 stoichiometry in THF for 2 h at 60 ℃ followed by the removal of the solvent resulted in the formation of supramolecular complexes. These compexes in $CHCl_3$ formed stable gels upon heating and cooling, whereas precipitation occured in toluene. Surprisingly, the precipitate of **OPV-PY**-[4,4'-(nonane-1,9-

diylbis(oxy))bis(3,5-dimethoxybenzoic acid)] (**OPV**-**PY**-A1) complex formed a weak gel in toluene upon ultrasound sonication.

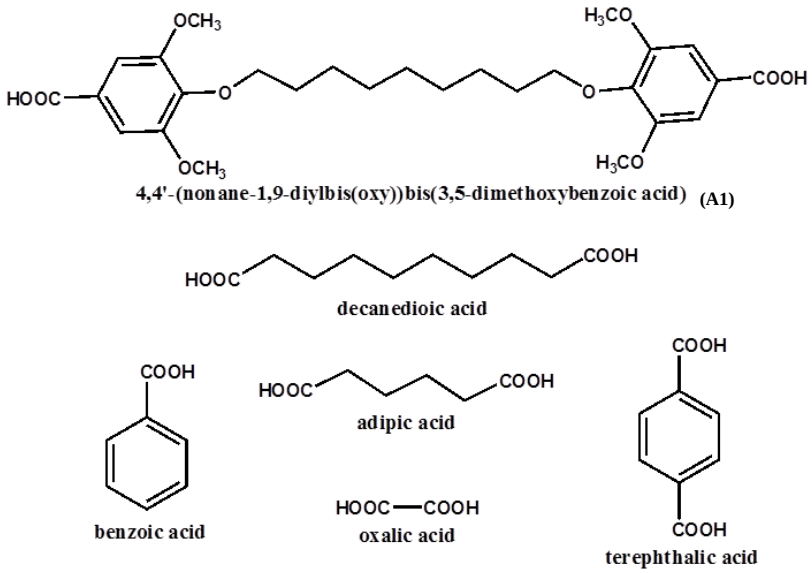

Scheme 3.3. Chemical structures of different acids used for complexation with **OPV**-**PY**.

Among the different acids tested (Scheme 3.3), the acid A1 showed best results. Variable temperature absorption and emission studies revealed the details of the nature of the aggregation of the **OPV**-**PY**-A1 complex (Figure 3.12). At 20 °C, the absorption spectrum showed a shoulder band at 530 nm in addition to the π-π* transition band (λ_{max} = 450 nm). As the temperature is increased to 70 °C, the shoulder band started disappearing with an increase in the intensity of the π-π* transition band. A plot of the fraction of aggregates (α) vs. temperature obtained from the variable temperature absorption studies showed a melting transition temperature (T_m) of 59.5 ℃. At 25 °C, the emission

spectrum was red shifted with relatively less emission intensity. At 70 °C, the emission maximum was shifted towards a shorter wavelength with an increase in the intensity. Similar observations were monitored for the VT-UV and VT-emission studies of other **OPV-PY**-acid complexes also.

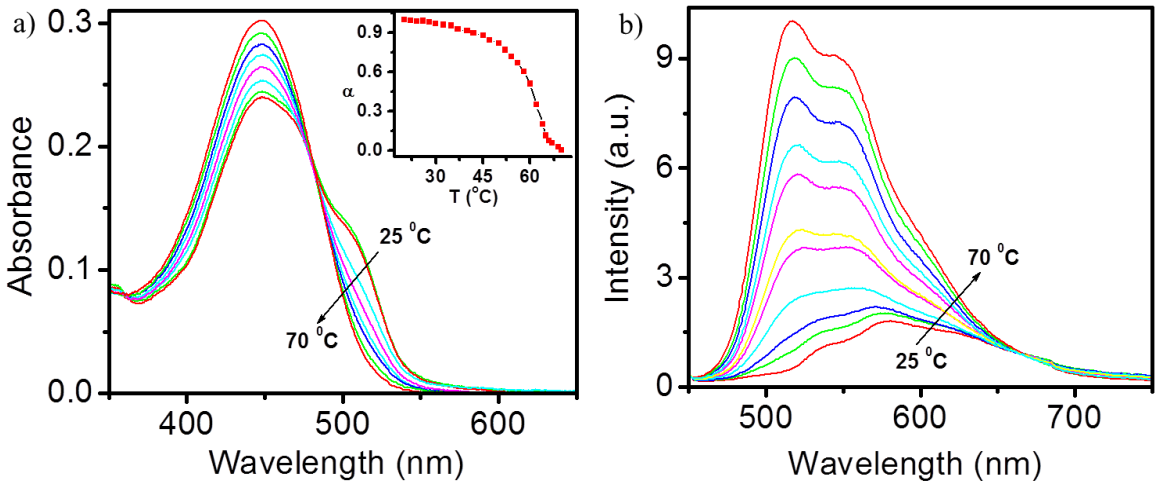

Figure 3.12. Variable Temperature (a) absorption (inset; a plot of fraction of aggregate (α) vs. temperature) and (b) emission spectra of **OPV-PY**-A1 in $CHCl_3$ at a conc. of 5×10^{-5} M.

3.3.3. Gelation studies

Detailed gelation studies have shown that the **OPV-PY** aggregates formed in toluene could not hold the solvent molecules to form a stable gel, instead precipitation from the solution occurs. However, in pyridine, the **OPV-PY** aggregates were able to hold the solvent molecules to form a weak gel. The precipitation in toluene can be attributed to the formation of a random self-assembly through hydrogen bonding between the amide N-H and the N atom of

the pyridine ring in toluene. [23] Thus, the precipitation in toluene must be due to the aggregation of the **OPV-PY**, resulting in the formation of aggregates via a combination of intermolecular hydrogen bonding (NH-pyridyl and NH-O=C), π-π stacking and van der Waals forces. The blue shift in the absorption maximum in pyridine indicates an H-type aggregate formation. In such cases, the pyridine group of the **OPV-PY** might be stabilized by the solvent itself, thus providing a one-dimensional assembly via the amide hydrogen bonding. These observations specify the fact that the aggregation modes of the **OPV-PY** in toluene and pyridine are significantly diverse due to the difference in the solvent assistance. The key role of solvents on self-assembly process is well known, which suggest that solvent structure plays an important role in stabilizing the aggregates and subsequent formation of bundles and gels.[24] Interestingly, upon addition of 5% THF followed by heating-cooling of the **OPV-PY** aggregates in toluene provided an yellow transparent gel. Further increase in the THF:toluene ratio reduced the gel stability, indicating that the presence of small amount of THF might stabilize the pyridine part (polarity of THF is greater than toluene) of the gelator to provide a gel similar to the **OPV-PY** assembly in pyridine. Similar to **OPV-PY**, **OPV-PY**-A1 complex in toluene also exhibited precipitation from the solution. Sonication of the precipitate for a few seconds resulted in the formation of a gel. As described

earlier, **OPV-PY**-TFA, **OPV-PY**-Ag^+ and **OPV-PY**-A1 also form gels upon heating, followed by cooling the $CHCl_3$ solution.

Solute	Wt (mg/ml)	Wt (Wt %)	Wt (mM)
OPV-PY (95%Toluene/5%THF)	2.53	0.17	1.5
OPV-PY (Pyridine)	3.27	0.22	1.95
OPV-PY-Ag^+ (1:1 in $CHCl_3$)	4.30	0.30	2.83
OPV-PY-TFA (1:1 in $CHCl_3$)	4.75	0.32	2.92
OPV-PY-A1 (1:1 in $CHCl_3$)	5.48	0.38	3.27
OPV-PY-A1 (1:1 in Toluene)	5.30	0.36	3.15
OPV-BZ (Toluene)	2.62	0.13	0.45

Table 2. Critical gelation concentration of gels derived from **OPV-PY** and **OPV-BZ**.

The critical gel concentration (CGC) and stability of gels were measured by the 'inversion tube method'.[2f] Gel melting temperature (T_{gel}) was determined by the 'dropping ball method' for gels derived from **OPV-BZ** and **OPV-PY** (Table 2.). **OPV-BZ** gel in toluene showed maximum thermal stability when compared to other gels. CGC of the **OPV-BZ** gel was 0.45 mM which was lower when compared to the CGC of all other gels, such as, the **OPV-PY** gel in pyridine

(1.95 mM), in toluene/THF (1.5 mM), the **OPV-PY**-Ag^{+} gel (2.83 mM), the **OPV-PY**-TFA gel (2.92 mM), the **OPV-PY**-A1 (3.27 mM) gel in $CHCl_3$ and the **OPV-PY**-A1 (3.15 mM) gel in toluene. Comparison of the thermal stability of gels showed that at 60 ℃ the **OPV-BZ** gel was stable, whereas the **OPV-PY** gel starts melting at around 55 ℃ (Figure 3.13a,b). The two component gels were thermally less stable when compared to the parent **OPV-PY** gels. Photographs corresponding to the sol-gel transition of the **OPV-PY** alone is shown in Figure 3.13c.

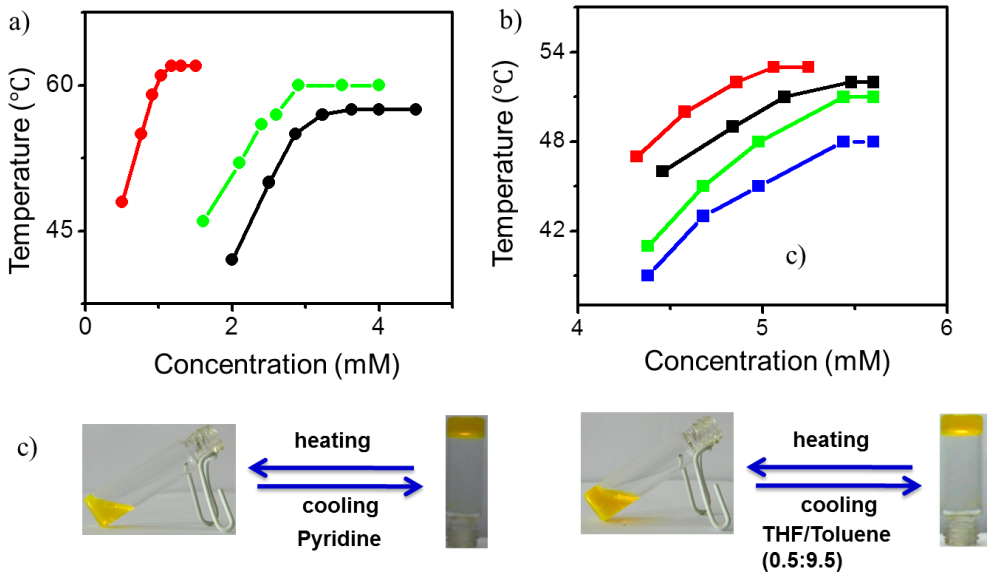

Figure 3.13. (a) T_{gel} plot of **OPV-BZ** gel in toluene (●), **OPV-PY** gel in toluene-THF mixture (9.5:0.5) (●) and pyridine (●). (b) Two component gels, **OPV-PY**-TFA (■), **OPV-PY**-Ag^{+} (■), **OPV-PY**-A1 (■) in $CHCl_3$ and **OPV-PY**-A1 in toluene (■). (c) Sol-gel transition of **OPV-PY** (5×10^{-3} M) in pyridine (left) and toluene/THF (9.5:0.5) (right) .

The overall multi-stimuli responsive behaviour of **OPV-PY** is summarized with photographs corresponding to the sol-gel transition as in Figure 3.14. Upon addition of different stimuli, like, Ag^{+} ion, TFA and A1 to a concentrated $CHCl_3$ solution of **OPV-PY**, gelation was observed after heating followed by cooling as described earlier. Subsequently a two-component gel was derived from a hot toluene solution of **OPV-PY-A1** upon sonication for few minutes. Thus, the molecule **OPV-PY** can be termed as multi-stimuli responsive gelator.

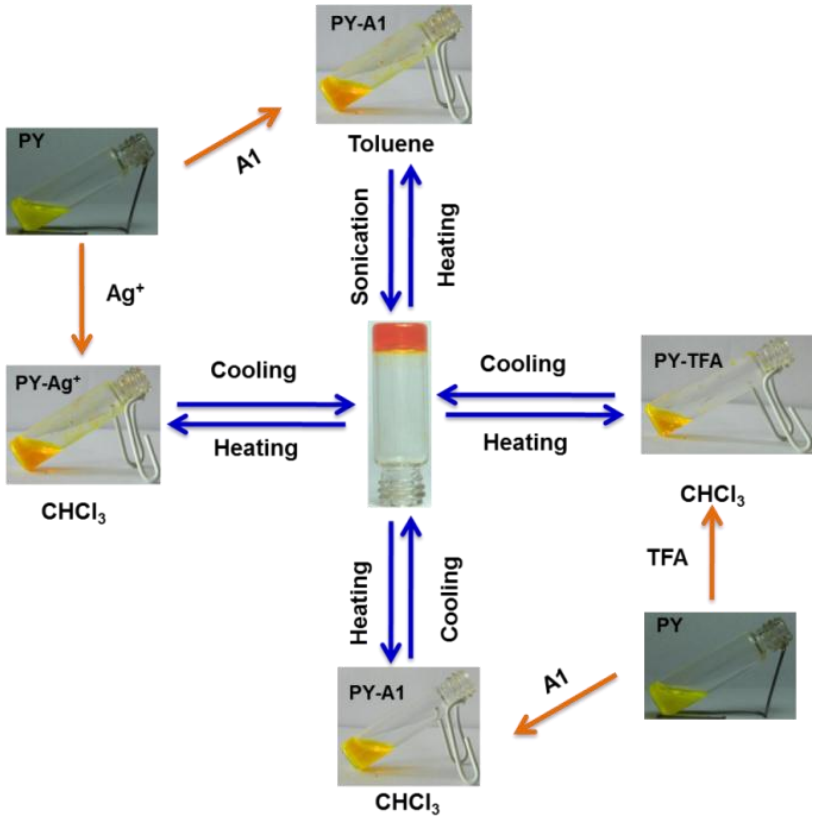

Figure 3.14. Multi-stimuli responsive sol-gel transition of 1:1 two component gels of **OPV-PY** (5 × 10^{-3} M) with TFA, Ag^{+} ions and A1 in different solvents.

3.3.4. FT-IR studies

FT-IR measurements of the **OPV-PY** gel in pyridine and the two component **OPV-PY** gels in $CHCl_3$ revealed the presence of amide hydrogen bonding in the xerogel state. In solid **OPV-PY,** the N-H stretching band appeared at 3315 cm^{-1}, whereas in THF solution it was at 3420 cm^{-1}. In pyridine, the N-H stretching frequency band appeared at 3325 cm^{-1}, whereas in toluene it appeared as a broad band around 3100-3500 cm^{-1}. In the case of $CHCl_3$ gels of **OPV-PY**-TFA and **OPV-PY**-Ag^+, the N-H stretching band was observed at 3300, 3280 cm^{-1}, respectively (Figure 3.15). Similarly, significant changes were observed for the carbonyl (C=O) stretching frequency of all these samples (Figure 3.15). In toluene solution of **OPV-PY**, C=O stretching frequency was observed at 1720 cm^{-1} and in the solid **OPV-PY** it was at 1670 cm^{-1}. Aggregate from toluene showed a band at 1670 cm^{-1} and for xerogel from pyridine it appeared at around 1675 cm^{-1}. Two component xerogels of **OPV-PY** with TFA and Ag^+ ions showed a stretching band around 1670 cm^{-1} which supported the formation of amide hydrogen bonding leading to the formation of gels. Overall, amide hydrogen bonding was observed for all the samples derived from **OPV-PY**, except in $CHCl_3$. Significant shift was observed for N-H and C=O stretching frequency of the **OPV-PY** xerogels when compared to the **OPV-PY** assemblies from toluene indicating diverse assembly formation of **OPV-PY** in different solvents.

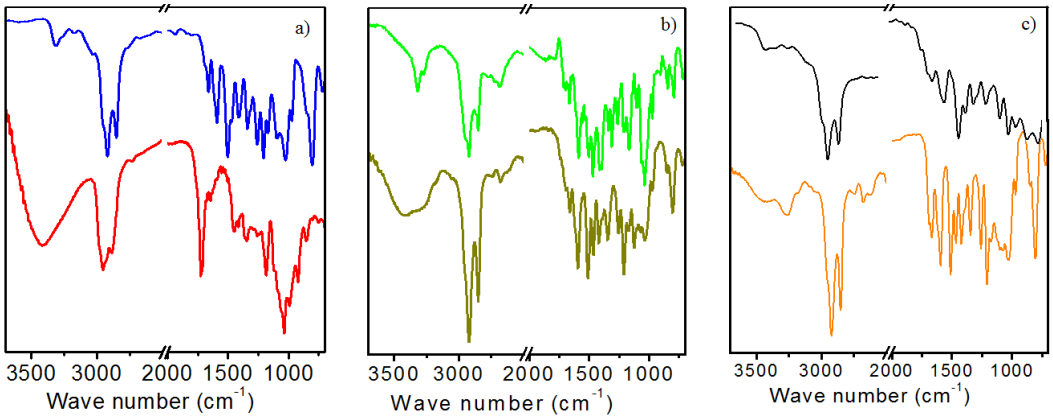

Figure 3.15 FT-IR spectra of **OPV-PY** (a) as prepared solid (blue) and $CHCl_3$ solution (red), (b) aggregates from pyridine (green) and toluene (yellow), (c) two-component xerogel of **OPV-PY**-TFA (orange) and **OPV-PY**-Ag^+ (black).

The effect of sonication on gelation was monitored with FT-IR studies as shown in Figure 3.16. IR spectrum of the **OPV-PY**-A1 complex showed peaks at 3317 cm^{-1} for N-H stretching, 1690 cm^{-1} for acid C=O stretching, 1664 cm^{-1} for amide I band and 1562 cm^{-1} for amide II band. These bands confirmed the formation of the complex between **OPV-PY** and A1 in the solid state. When dissolved in toluene, the IR spectrum of **OPV-PY**-A1 showed shift towards a higher wavenumber as 3495 cm^{-1} for N-H stretching, 1741 cm^{-1} for acid C=O stretching, 1668 cm^{-1} for amide I band and 1591 cm^{-1} for amide II band. Upon sonication, these values were shifted to 3331 cm^{-1} for N-H stretching, 1691 cm^{-1} for acid C=O stretching, 1662 cm^{-1} for amide I band and 1565 cm^{-1} for amide II band. It was observed that upon dissolution in toluene, **OPV-PY**-A1 complex precipitates out from the solution which might be due to the formation of

random aggregates. Upon sonication, the respective FT-IR peaks were shifted to lower wavenumber, indicating the formation of a hydrogen bonded assembly through acid-pyridine interaction along with amide hydrogen bonding.

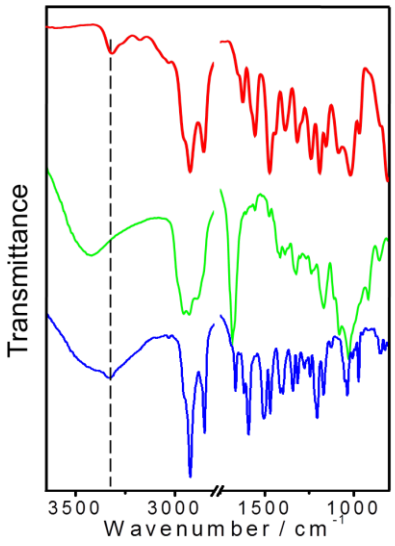

Figure 3.16. FT-IR spectra of **OPV-PY** as prepared solid (red) and **OPV-PY**-A1 complex before (green) and after sonication (blue).

3.3.5. Morphological investigation by microscopic studies

Morphological features of the **OPV-PY** gels and assemblies were studied using Atomic Force Microscopy (AFM), Scanning Electron Microscopy (SEM) and Transmission Electron Microscopy (TEM). **OPV-PY** assemblies from different solvents, such as toluene, $CHCl_3$ and pyridine (5×10^{-5} M) were observed by AFM and TEM. The AFM images revealed the formation of short fibers with 1-2 μm length, 0.3-0.7 μm width and 200-400 nm height for

assemblies from toluene (Figure 3.17a). The TEM image (Figure 3.17b) indicates that these structures are formed by the bundling of thin fibers. Elongated fibers were observed by AFM with height less than 10 nm and several micrometer length for the **OPV-PY** assemblies from pyridine (Figure 3.17c). TEM image also shows formation of such elongated fibers (Figure 3.17d). However, the morphological feature of the assemblies obtained from $CHCl_3$ was different from those obtained from toluene and pyridine. In this case short rods of 1-2 µm length, 0.2-0.5 µm width and 5-10 nm height was formed as also seen in the TEM image (Figure 3.17e and f, respectively).

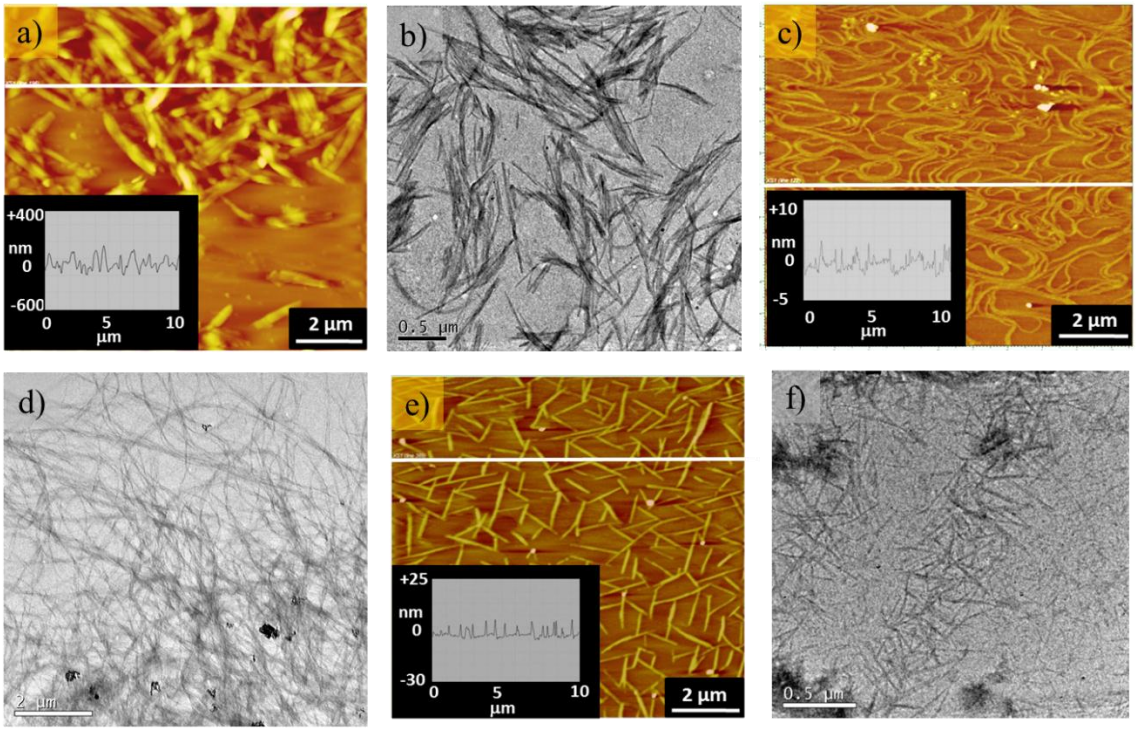

Figure 3.17. AFM (a,c,e) and TEM (b,d,f) images of **OPV-PY** assemblies (5×10^{-5} M) from toluene (a,b) pyridine (c,d) and $CHCl_3$ (e,f).

In the presence of TFA, the needle like short fibers of **OPV-PY** changed into flexible fibrous network having few micrometers in length, 0.2-0.3 µm width and 30-50 nm height (Figure 3.18a). Similarly, a 1:1 complex of **OPV-PY** and Ag^+ ions in $CHCl_3$ (5×10^{-5} M) showed the presence of interconnected fibrous structures with a few micrometers in length, 0.2-0.3 µm width and 20-60 nm height which are densely packed in large areas (Figure 3.18b). Similar obsevation was noticed for **OPV-PY**-A1 complex (5×10^{-5} M) from $CHCl_3$ as shown in Figure 3.18c. This was further proved with the TEM images as shown in Figure 3.18d-f.

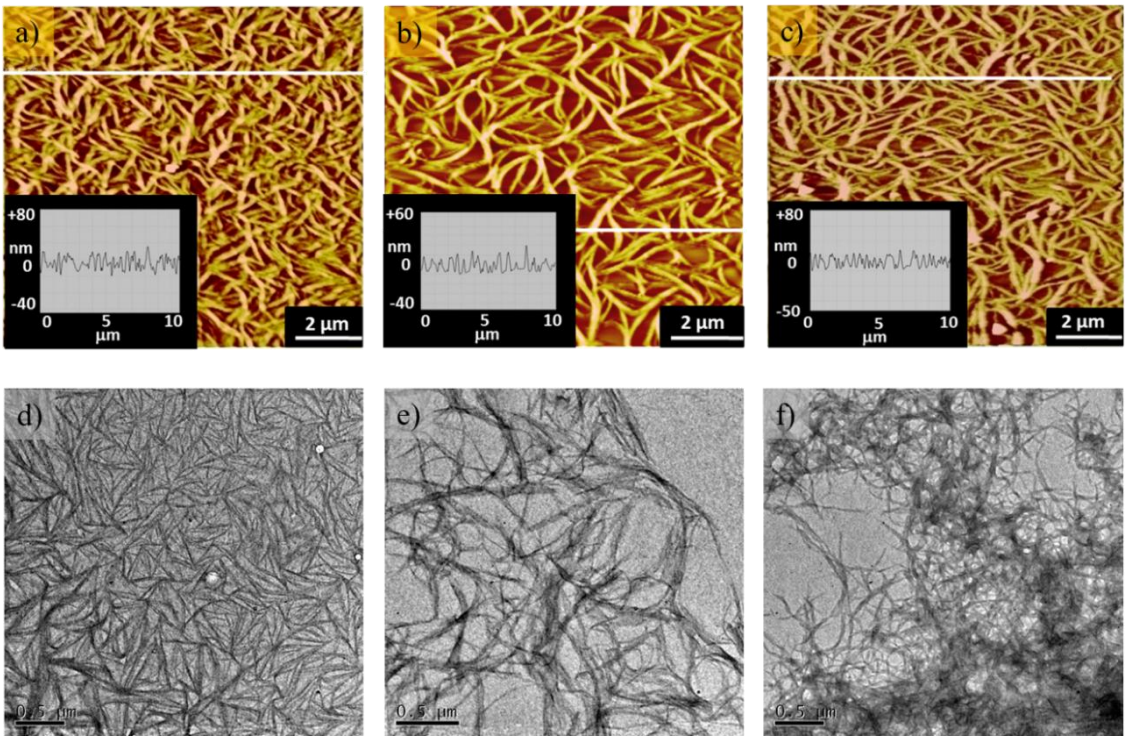

Figure 3.18. AFM (top) and TEM (bottom) images of **OPV-PY**-TFA (a,d), **OPV-PY**-Ag^+ (b,e), **OPV-PY**-A1 (c,f) from $CHCl_3$ (5×10^{-5} M).

OPV-PY-A1 assemblies from toluene comprised of ill-defined aggregates as well as fibers (Figure 3.19a). Upon sonication for few minutes, entangled fibers with a height of 15-40 nm and several micrometers length were observed as shown in Figure 3.19b. This is further confirmed with TEM analysis (Figure 3.19d,e). Stimuli-responsive variation of self-assemblies and formation of well-defined nanoarchitectures from ill-defined strctures are known in literature.[7h] Modulation of dense fibrous network to large fibers and narrow tapes by sequential self-organization upon metal coordination of a bis(urea)dipyridyl derivative was also reported elsewhere.[25] The aggregates of **OPV-PY** formed in toluene was changed into entangled fibers in presence of ultrasound, which must be due to the reorganization process caused by sonication. The AFM and TEM images of samples from a toluene solution (5×10^{-5} M) provided the morphological information about **OPV-BZ** fibrillar structures (Figure 3.19 c,f). Fibers with several micrometers in length, 0.2-0.5 μm width and 10-20 nm height were observed from AFM image as shown in Figure 3.19c. Such a fibrous structure was further characterised with TEM which showed flexible thin nanowires with several micrometers in length (Figure 3.19f).

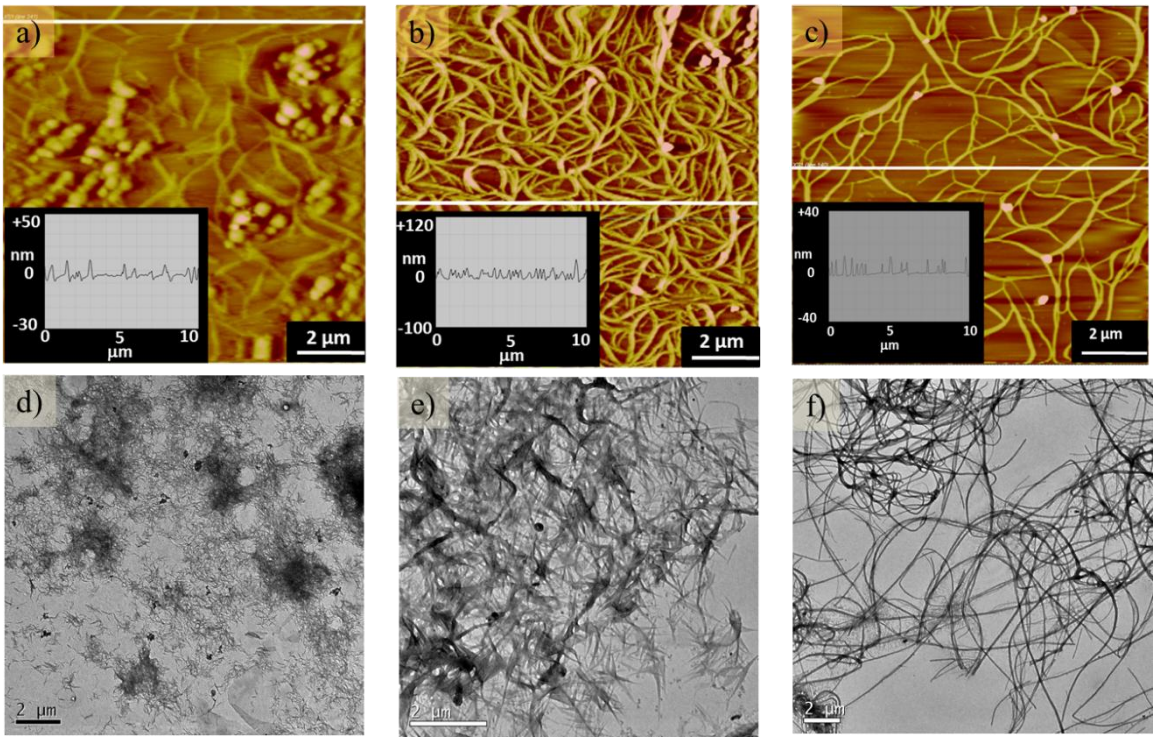

Figure 3.19. AFM (top) and TEM (bottom) images of **OPV-PY**-A1 before (a, d) and after (b, e) ultrasound sonication (5×10^{-5} M). (c, f) **OPV-BZ** from toluene (5×10^{-5} M).

OPV-PY assemblies showed a change in the morphology upon addition of different external stimuli, which reflects in the gelation properties also. Gelation occurs when the sovent molecules get entrapped in defined architectures such as elongated fibers. As described earlier, external stimuli plays a crucial role in extending the self-assembly from short fibers to long entangled networks. The SEM pictures of **OPV-BZ** and **OPV-PY** gelators (Figure 3.20a-d) confirm the important role of fibrous structures to hold the solvent molecules. In these cases, large bundles of fibers comprising of several coiled and entangled fibers were observed. Such an elongated fiber formation

was absent in the case **OPV-PY** in toluene and $CHCl_3$ which might be the reason for precipitaion of aggregates rather than gelation. SEM analysis of **OPV-PY**-A1 complex showed the formation of fibers and clusters together (Figure 3.20e). Upon sonication, the amount of cluster formation largely reduced and subsequent growth of network of fibers was observed (Figure 3.20f).

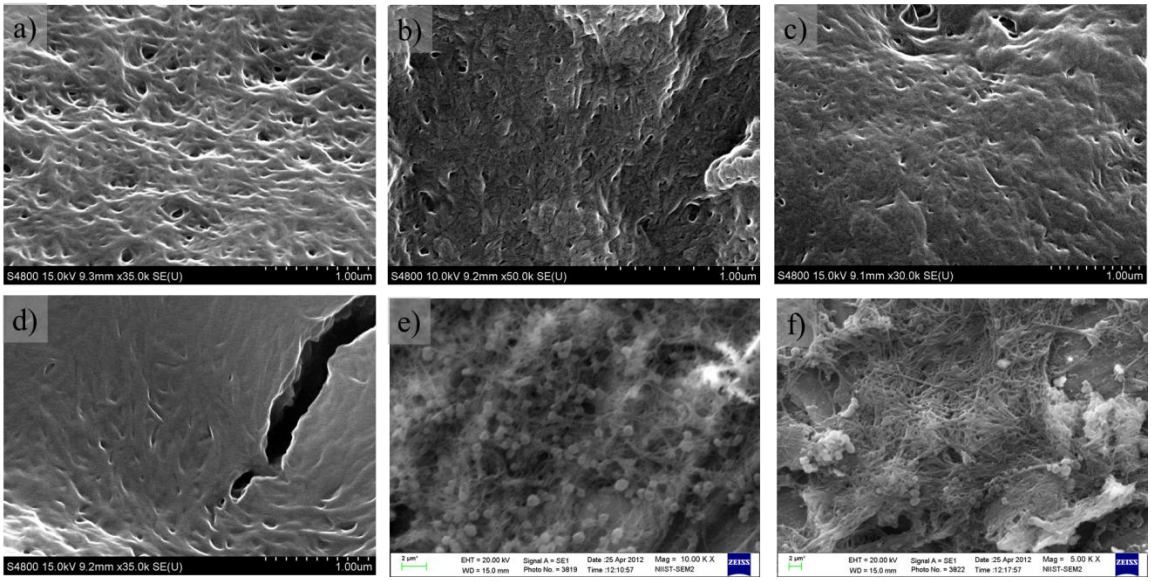

Figure 3.20. Xerogel SEM images of **OPV-BZ** from toluene (a), **OPV-PY** from pyridine (b), **OPV-PY**-Ag^+ (c) and **OPV-PY**-TFA (d) from $CHCl_3$, **OPV-PY**-A1 complex from toluene before (e) and after (f) sonication at a conc. of 1×10^{-3} M.

3.3.6. X-ray diffraction (XRD) studies

The packing of the gelator molecules in the self-assembled gels were investigated through XRD analysis of the xerogels and aggregates. XRD of

OPV-PY and **OPV-BZ** from pyridine and toluene, respectively, exhibited a long range ordering of the molecules, as shown in Figure 3.21. A characteristic peak corresponding to π-π stacking distance was absent in the diffraction pattern of **OPV-PY** aggregates, whereas in the case of **OPV-BZ** xerogel, the π-stacking distance was observed at 3.76 Å. The strong band around 4.5 Å corresponds to a layer by layer assembly of the alkyl chains. The absence of higher order reflections and the presence of broad reflection in the wide angle region point out a low degree of ordering in the case of **OPV-PY** assembly. The peaks were more predominant in the XRD of **OPV-BZ** xerogel, indicating a strong assembly formation when compared to **OPV-PY**.

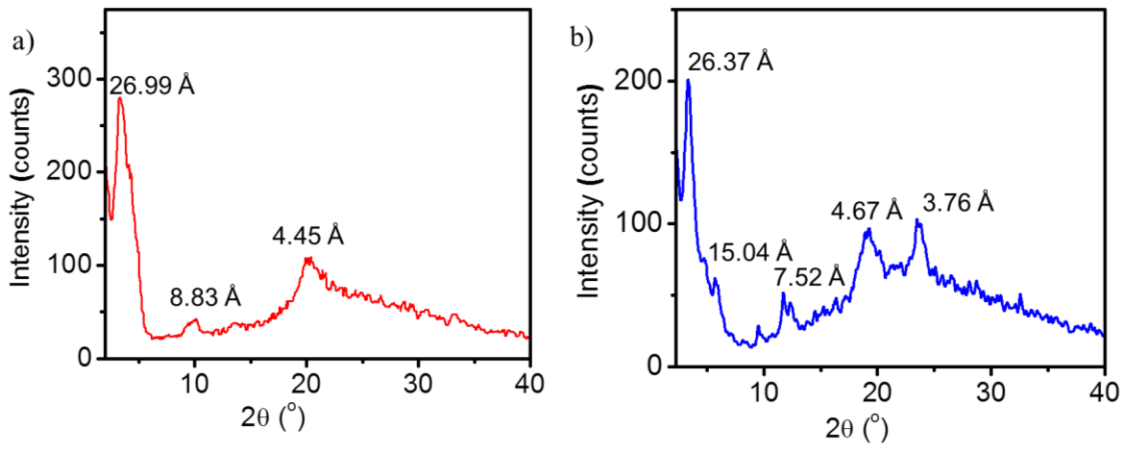

Figure 3.21. XRD of **OPV-PY** xerogel from pyridine (a) and **OPV-BZ** xerogel from toluene (b).

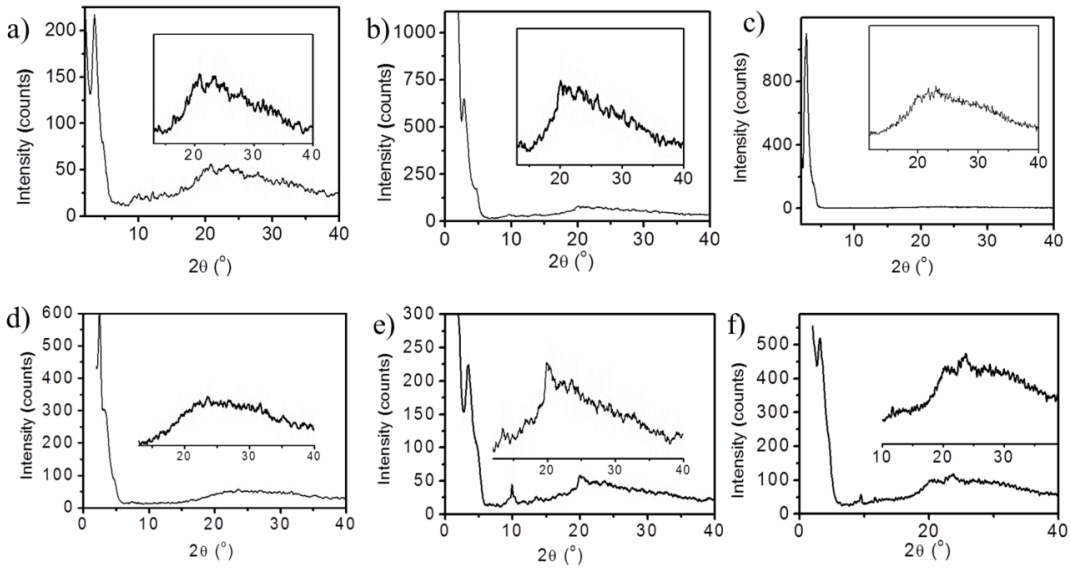

Figure 3.22. XRD of (a) **OPV**-**PY**-Ag^+ aggregates, (b) **OPV**-**PY**-TFA aggregates and (c) **OPV**-**PY** aggregates from toluene. XRD of **OPV**-**PY**-A1 from toluene before (d), after (e) sonication and (f) from $CHCl_3$ after heating-cooling.

In the case of the **OPV**-**PY** xerogel, the d-spacings at 4.42, and 3.89 Å indicate π-stacking. Similarly, in the presence of TFA, peaks with d-spacing were observed at 4.28 and 3.81 Å and in the presence of silver ions, peaks were observed at 4.43 and 3.75 Å (Figure 3.22a-c). In general, the diffraction peak with d-spacing value of around 28 Å corresponds to the side-wise packing of the alkyl side chains of the **OPV**s in the same plane. The xerogel XRD profile of **OPV**-**PY**-A1 complex from toluene before sonication showed a very broad peak with a weak signal at 3.64 Å, whereas after sonication two peaks were observed at 4.45 and 3.72 Å (Figure 3.22d,e). Xerogel XRD profile of **OPV**-**PY**-A1 complex in $CHCl_3$ showed a peak around 4.4 and 3.7 Å indicating a

more ordered assembly formation (Figure 3.22f). This observation indicates that **OPV-PY**-A1 complex in $CHCl_3$ self-organizes in a better fashion when compared to that in toluene. Upon sonication, the less defined assembly must be organizing into a better fashion. Thus, it can be concluded that, the **OPV-PY** assemblies are responsive towards diverse stimuli and the mode of packing can be controlled through changing the solvent or applying various stimuli.

The above studies provided information about the stimuli responsive gelation of **OPV-PY** and **OPV-BZ**. The short fibers of **OPV-PY** were formed in the aggregated state and no significant changes were observed for the short fibers even at high concentration of **OPV-PY**. The aspect ratio of such short fiber was increased in presence of diverse stimuli such as acids or metal ions. The photophysical and morphological experiments indicate that the gelation process was initiated *via* a growth mechanism as shown in Scheme 3.4. Morphological and X-ray diffraction data suggest that gelation occurs via the extension of self-assembly, which resulted in the formation of gels exhibiting pronounced stability and stimuli responsive behavior. Moreover, a comparative study between **OPV-PY** and **OPV-BZ** revealed the crucial role of the pyridine moiety in gelation and morphology, which made **OPV-PY** as an interesting multistimuli responsive gelator.

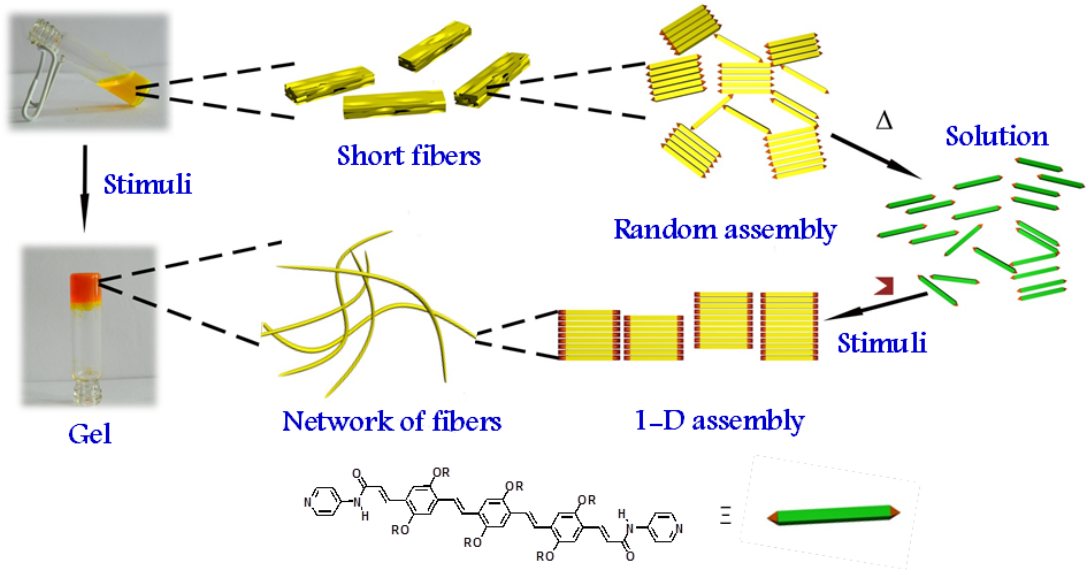

Scheme 3.4. A schematic representation of the stimuli responsive behaviour of **OPV-PY**.

3.4. Conclusions

In conclusion, we have designed and synthesized an amide functionalized OPV derivative **OPV-PY** containing pyridine as the end substituent. **OPV-PY** alone does not favour gelation in common non-polar solvents rather it forms a gel in pyridine through 1-D amide hydrogen bonding. Two component gels were prepared by the co-assembly of **OPV-PY** with TFA, Ag^+ ions and an organic acid (A1). The protonation of **OPV-PY** with TFA facilitated the formation of hydrogen bonded self-assembly which was reversible by the addition of an organic base. **OPV-PY** formed metallosupramolecular assemblies with Ag^+ ions leading to the gel formation. Ultrasound induced gelation was observed for **OPV-PY**-A1 complex in toluene.

The self-assembly, gelation and morphological features were monitored by photophysical and morphological analyses, which revealed the multi-stimuli responsive behaviour of **OPV-PY** assembly. Thus, **OPV-PY** has been labelled as a versatile molecular building block that forms multistimuli responsive self-assemblies and organogels.

3.5. Experimental section

3.5. 1. General

Unless otherwise stated, all starting materials and reagents were purchased from commercial suppliers and used without further purification. The solvents were purified and dried by standard methods prior to use. All melting points were determined on a Mel-Temp-II melting point apparatus. ^{1}H and ^{13}C NMR spectra were measured on a 500 MHz Bruker Avance DPX spectrometer. FT-IR spectra were recorded on a Shimadzu Nicolet Impact 400D Infrared spectrophotometer.

3.5. 2. Synthesis and characterization

3.5. 2.1. Synthesis of the OPV bis-acid (OPV2)

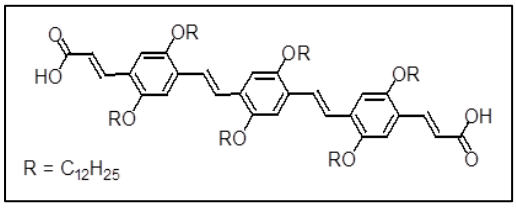

KOH (~10 mg, 0.85 mmol) in methanol (20 mL) was added to a solution of **OPV1** (260 mg, 0.17 mmol) in distilled THF (20 mL) (Scheme 3.2). The reaction mixture was then refluxed for 4 h. After checking

the completion of reaction by TLC, the solvent was evaporated under reduced pressure. The resulting suspension was poured into water, extracted with $CHCl_3$ and trifluoroacetic acid was added to adjust the pH around 2. The $CHCl_3$ layer was washed with water several times. Removal of the solvent gave **OPV2** in ~90 % yield;

mp: 120 ± 2℃. FT-IR (KBr) ν_{max} : 801, 856, 1031, 1097, 1203, 1261, 1420, 1466, 1500,1593, 1619, 1687, 2849, 2924, 3423 cm^{-1}; ^1H NMR (500 MHz, $CDCl_3$) δ (ppm): 0.85-0.87 (m, 18H, -CH_3), 1.1-1.8 (m, 120H, - CH_2-), 4.03-4.08 (m, 12H, -OCH_2), 6.52-6.55 (d, J = 15Hz, 2H, vinylic), 7.06-7.18 (m, 6H, aromatic), 7.48-7.50 (q, J = 10 Hz, 4H, aromatic), 8.09-8.12(d, J = 15 Hz , 2H, vinylic) ppm. ^{13}C NMR: 14.1, 14.2, 22.7, 25.9, 29.3, 29.6, 31.8, 61.4, 69.1, 81.4, 114.8, 116.0, 116.2, 125.6, 141.6, 145.7, 166.4, 171.2. MALDI-TOF mass: M_w = 1528.38, found: 1528.77.

3.5. 2.2. Synthesis of (2E,2'E)-3,3'-(4,4'-(1E,1'E)-2,2'-(2,5-bis(dodecyloxy)-1,4-phenylene)bis(ethene-2,1-diyl)bis(2,5-bis(dodecyloxy)-4,1-phenylene))bis(*N*-(pyridin-4-yl)acrylamide) (OPV-PY).

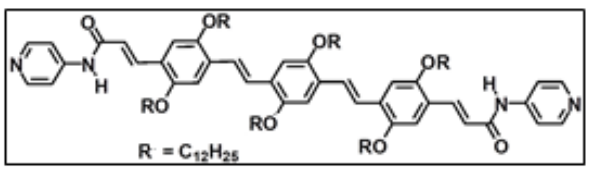

The **OPV2** (150 mg, 0.09 mmol) and 4-aminopyridine (370 mg, 0.39 mmol) were stirred in dichloromethane (50 mL) in the presence of *N*,*N*'-diisopropylethylamine (70 µL, 0.4 mmol) at 0 ^oC and

HATU (150 mg, 0.4 mmol) was added to the reaction mixture. Reaction was continued for 8 h at room temperature. The reaction mixture was extracted with dichloromethane and washed several times with water, dried over anhydrous sodium sulphate and the solvent was removed under reduced pressure. Purification by column chromatography (hexane/$CHCl_3$, 1:9) over silica gel (230-400 mesh) gave **OPV-PY** as a dark red solid in 61 % yield, mp: 165 ± 2°C; FT-IR (KBr) ν_{max}: 535, 718, 790, 846, 975, 1031, 1169, 1207, 1240, 1281, 1314, 1345, 1410, 1465, 1505, 1585, 1658, 2854, 2927, 3336 cm^{-1}; ^1H NMR (500 MHz, $CDCl_3$) δ (ppm): 0.85-0.89 (m, 18H, $-CH_3$), 1.25-1.7 (m, 150H, $-CH_2-$), 3.9-4.1 (m, 12H, $-OCH_2$), 6.62-6.65 (d, J = 15 Hz, 2H, vinylic), 7.04-7.6(m,18H, aromatic), 7.96-7.98 (d, J = 10 Hz, 2H, vinylic) ppm; ^{13}C NMR (125 MHz, $CDCl_3$) δ (ppm): 14.2, 22.7, 25.9, 29.3, 29.6, 31.6, 69.0, 109.2, 114.8, 116.1, 118.8, 125.2, 140.2, 143.1, 145.3, 150.3, 155.6 165.8. MALDI-TOF mass: Mw = 1680.58, found: 1680.82.

3.5. 2.3. Synthesis of (2E,2'E)-3,3'-(4,4'-(1E,1'E)-2,2'-(2,5-bis(dodecyloxy)-1,4-phenylene)bis(ethene-2,1-diyl)bis(2,5-bis(dodecyloxy)-4,1-phenylene))bis(*N*-phenylacrylamide) (OPV-BZ).

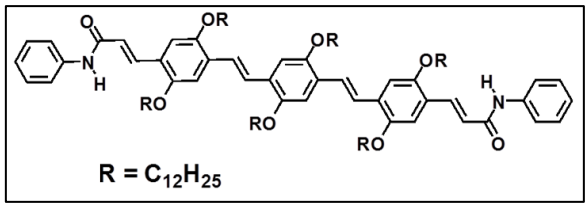

The **OPV2** (150 mg, 0.09 mmol) and aniline (370 mg, 0.4 mmol) were stirred in dichloromethane (50 mL) in the presence of *N*,*N*'-diisopropylethylamine (70 µL, 0.4 mmol) at 0 °C and HATU

(150 mg, 0.4 mmol) was added to the reaction mixture. Reaction was continued to stir for 8 h at room temperature. The reaction mixture was extracted with dichloromethane and washed several times with water, dried over anhydrous sodium sulphate and the solvent was removed under reduced pressure. Purification by column chromatography (hexane/$CHCl_3$, 1:9) over silica gel (230-400 mesh) gave **OPV-BZ** as a dark red solid in 61 % yield, mp: 156 ± 2 ℃; FT-IR (KBr) ν_{max} ; 3260, 3052, 2925, 2845, 1655, 1615, 1598, 1530, 1514, 1498, 1470, 1440, 1416, 1387, 1348, 1251, 1209, 1072, 1009, 962, 849, 755, 720, 695, 602, 549, 509, 479 cm^{-1}. ^1H NMR (500 MHz, $CDCl_3$) δ (ppm): 0.85-0.89(m, 18H, $-CH_3$), 1.25-1.7 (m, 120H, $-CH_2-$), 3.9-4.1 (m, 12H, $-OCH_2$), 6.65-6.69 (d, J = 20 Hz, 2H, vinylic), 7.04-7.6(m,18H, aromatic), 7.97-8.0 (d, J = 15 Hz, 2H, vinylic) ppm; ^{13}C NMR (125 MHz, $CDCl_3$) δ (ppm): 14.2, 22.7, 25.9, 29.3, 29.6, 31.6, 69.0, 109.2, 114.8, 116.1, 118.8, 121.5, 128.2, 130.4, 140.2, 143.1, 145.3, 150.3, 155.6 165.8. MALDI-TOF MS: M_w = 1622.50, found: 1623.72.

3.5.3. Description of instrumental techniques

Description of electronic spectral measurements, fluorescence lifetime measurements, scanning electron microscopy (SEM) and X-ray diffraction (XRD) studies is given in section 2.5, Chapter 2.

Gelation: The gelation studies were carried out as per reported procedures.[5e,26] A typical procedure for gelation studies is as follows: A weighed amount of the

compound in an appropriate solvent was placed in a glass vial of 1 cm diameter, which was sealed and heated until the compound was dissolved. The solution was then allowed to cool to room temperature. The gel formation was confirmed by the failure of the content to flow by inverting the glass vial. Repeated heating and cooling confirmed the thermal reversibility of the gelation. The critical gelator concentration (CGC) was determined from the minimum amount of the gelator required for the formation of a stable gel at room temperature.

Gel melting temperature (T_{gel}) determination: The thermotropic behavior of the gels formed by **OPV**s in different solvents was investigated by the dropping ball method.[2f,27] In the dropping ball method, a steel ball (~100 mg) was placed on the top of a 1 mL volume of the gel in a sealed glass vial. Then the gels were slowly heated, while the position of the ball on the top of the gel was continuously observed, until the gel no longer bears the ball. The temperature at which the ball reaches the bottom of the vial was taken as the sol-gel phase transition temperature (T_{gel}).

Transmission electron microscopy (TEM): TEM measurements were carried out using FEI (TECNAI G^2 30 S-TWIN) with an accelerating voltage of 100 kV. Samples were prepared by drop casting of decane solutions of **OPV**s on to carbon coated copper grids at the required concentrations at ambient conditions. The solvent was removed under vacuum. TEM images were obtained without staining.

Atomic force microscopy (AFM): Atomic Force Microscopy images were recorded under ambient conditions using a NTEGRA (NT-MDT) operating with a tapping mode regime. Micro-fabricated TiN cantilever tips (NSG10) with a resonance frequency of 299 kHz and a spring constant of 20-80 Nm^{-1} were used. AFM section analysis was done offline. Samples for the imaging were prepared by drop casting the solution on freshly cleaved mica surface at the required concentrations at ambient conditions.

3.6. References:

(1) (a) Ajayaghosh, A.; Praveen, V. K. *Acc. Chem. Res.* **2007**, *40*, 644; (b) George, M.; Weiss, R. G. *Acc. Chem. Res.* **2006**, *39*, 489; (c) Abdallah, D. J.; Weiss, R. G. *Adv. Mater.* **2000**, *12*, 1237; (d) Babu, S. S.; Prasanthkumar, S.; Ajayaghosh, A. *Angew. Chem. Int. Ed.* **2012**, *51*, 1766; (e) Hirst, A. R.; Escuder, B.; Miravet, J. F.; Smith, D. K. *Angew. Chem. Int. Ed.* **2008**, *47*, 8002; (f) Terech, P.; Weiss, R. G. *Chem. Rev.* **1997**, *97*, 3133; (g) Ajayaghosh, A.; Praveen, V. K.; Vijayakumar, C. *Chem. Soc. Rev.* **2008**, *37*, 109.

(2) (a) Wicklein, A.; Ghosh, S.; Sommer, M.; Wurthner, F.; Thelakkat, M. *Acs Nano* **2009**, *3*, 1107; (b) Mukhopadhyay, P.; Fujita, N.; Takada, A.; Kishida, T.; Shirakawa, M.; Shinkai, S. *Angew. Chem. Int. Ed.* **2010**, *49*, 6338; (c) Schenning, A. P. H. J.; Meijer, E. W. *Chem. Commun.* **2005**, 3245; (d) Hu, L. F.; Chen, M.; Fang, X. S.; Wu, L. M. *Chem. Soc. Rev.* **2012**, *41*, 1350; (e) Kartha, K. K.; Mukhopadhyay, R. D.; Ajayaghosh, A. *Chimia* **2013**, *67*, 51; (f) Prasanthkumar, S.; Gopal, A.; Ajayaghosh, A. *J. Am. Chem. Soc.* **2010**, *132*, 13206; (g) Prasanthkumar, S.; Saeki, A.; Seki, S.; Ajayaghosh, A. *J. Am. Chem. Soc.* **2010**, *132*, 8866.

(3) (a) Yabuuchi, K.; Marfo-Owusu, E.; Kato, T. *Org. Biomol. Chem.* **2003**, *1*, 3464; (b) Shirakawa, M.; Kawano, S.; Fujita, N.; Sada, K.; Shinkai, S. *J. Org. Chem.* **2003**, *68*, 5037; (c) Pratihar, P.; Ghosh, S.; Stepanenko, V.; Patwardhan, S.; Grozema, F. C.; Siebbeles, L. D. A.; Wurthner, F. *Beilstein J. Org. Chem.* **2010**, *6*, 1070; (d) Schoonbeek, F. S.; van Esch, J. H.; Hulst, R.; Kellogg, R. M.; Feringa, B. L. *Chem. -Eur. J.* **2000**, *6*, 2633; (e) Wang, F.; Gillissen, M. A. J.; Stals, P. J. M.; Palmans, A. R. A.; Meijer, E. W. *Chem. -Eur. J.* **2012**, *18*, 11761; (f) Rondeau-Gagne, S.; Neabo, J. R.; Desroches, M.; Cantin, K.; Soldera, A.; Morin, J. F. *J. Mater. Chem. C* **2013**, *1*, 2680; (g) Yamanaka, M.; Nakamura, T.; Nakagawa, T.; Itagaki, H. *Tetrahedron Lett.* **2007**, *48*, 8990; (h) Yagai, S.; Kubota, S.; Iwashima, T.; Kishikawa, K.; Nakanishi, T.; Karatsu, T.; Kitamura, A. *Chem. -Eur. J.* **2008**, *14*, 5246.

(4) (a) Sangeetha, N. M.; Maitra, U. *Chem. Soc. Rev.* **2005**, *34*, 821; (b) Xue, P. C.; Sun, J. B.; Xu, Q. X.; Lu, R.; Takafuji, M.; Ihara, H. *Org. Biomol. Chem.* **2013**, *11*, 1840; (c) Ishi-i, T.; Shinkai, S. *Top. Curr. Chem.* **2005**, *258*, 119.

(5) (a) Dumur, F.; Contal, E.; Wantz, G.; Phan, T. N. T.; Bertin, D.; Gigmes, D. *Chem. -Eur. J.* **2013**, *19*, 1373; (b) Huang, Y. Q.; Liao, F. L.; Zheng, W. R.; Liu, X. L.; Wu, X. J.; Hong, X. L.; Tsang, S. C. *Langmuir* **2010**, *26*, 3106; (c) Chung, J. W.; An, B. K.; Park, S. Y. *Chem. Mater.* **2008**, *20*, 6750; (d) Manna, S.; Saha, A.; Nandi, A. K. *Chem. Commun.* **2006**, 4285; (e) George, S. J.; Ajayaghosh, A. *Chem. -Eur. J.* **2005**, *11*, 3217.

(6) (a) Kitahara, T.; Fujita, N.; Shinkai, S. *Chem. Lett.* **2008**, *37*, 912; (b) Kim, J. H.; Seo, M.; Kim, Y. J.; Kim, S. Y. *Langmuir* **2009**, *25*, 1761; (c) Rajaganesh, R.; Gopal, A.; Das, T. M.; Ajayaghosh, A. *Org. Lett.* **2012**, *14*, 748; (d) Sugiyasu, K.; Fujita, N.; Shinkai, S. *Angew. Chem. Int. Ed.* **2004**, *43*, 1229.

(7) (a) Wu, J. C.; Yi, T.; Xia, Q.; Zou, Y.; Liu, F.; Dong, H.; Shu, T. M.; Li, F. Y.; Huang, C. H. *Chem. -Eur. J.* **2009**, *15*, 6234; (b) Afrasiabi, R.; Kraatz, H. B. *Chem. -Eur. J.* **2013**, *19*, 1769; (c) Zhang, M. M.; Meng, L. Y.; Cao, X. H.; Jiang, M. J.; Yi, T. *Soft Matter* **2012**, *8*, 4494; (d) Romeo, H. E.; Fanovich, M. A.; Williams, R. J. J.; Matejka, L.; Plestil, J.; Brus, J. *Macromol. Chem. Phys.* **2009**, *210*, 172; (e) Wu, J. C.; Yi, T.; Shu, T. M.; Yu, M. X.; Zhou, Z. G.; Xu, M.; Zhou, Y. F.; Zhang, H. J.; Han, J. T.; Li, F. Y.; Huang, C. H. *Angew. Chem. Int. Ed.* **2008**, *47*, 1063; (f) Isozaki, K.; Takaya, H.; Naota, T. *Angew. Chem. Int. Ed.* **2007**, *46*, 2855; (g) Cravotto, G.; Cintas, P. *Chem. Soc. Rev.* **2009**, *38*, 2684; (h) Yu, X. D.; Liu, Q. A.; Wu, J. C.; Zhang, M. M.; Cao, X. H.; Zhang, S.; Wang, Q.; Chen, L. M.; Yi, T. *Chem. -Eur. J.* **2010**, *16*, 9099.

(8) (a) Zhang, Y. P.; Jiang, S. M. *Org. Biomol. Chem.* **2012**, *10*, 6973; (b) Chen, J.; Wu, W. W.; Mcneil, A. J. *Chem. Commun.* **2012**, *48*, 7310; (c) Choi, M. M. F.; Shuang, S. M. *Analyst* **2000**, *125*, 301.

(9) (a) Liu, W. G.; Zhang, J. R.; Yao, K. D. *J. Appl. Polym. Sci.* **2002**, *86*, 259; (b) Furukawa, H.; Yoshikawa, M.; Yamada, K.; Watanabe, T.; Hidema, R.; Horie, K. *Active and Passive Smart Structures and Integrated Systems 2012* **2012**, *8341*; (c) Yu, C. J.; Duan, Z.; Yuan, P. X.; Li, Y. H.; Su, Y. W.; Zhang, X.; Pan, Y. P.; Dai, L. L.; Nuzzo, R. G.; Huang, Y. G.; Jiang, H. Q.; Rogers, J. A. *Adv. Mater.* **2013**, *25*, 1541; (d) Ghamsari, A. K.; Jin, Y. Y.; Woldesenbet, E. *Smart Mater. Struct.* **2012**, *21*; (e) Harada, S.; Hidema, R.; Furukawa, H. *Active and Passive Smart Structures and Integrated Systems 2012* **2012**, *8341*.

(10) (a) Xiao, S. Z.; Zou, Y.; Yu, M. X.; Yi, T.; Zhou, Y. F.; Li, F. Y.; Huang, C. H. *Chem. Commun.* **2007**, 4758; (b) Khan, M. K.; Sundararajan, P. *Chem. -Eur. J.* **2011**, *17*,

1184; (c) Svobodova, H.; Noponen, V.; Kolehmainen, E.; Sievanen, E. *RSC Adv.* **2012**, *2*, 4985.

(11) (a) Kuang, G. C.; Jia, X. R.; Teng, M. J.; Chen, E. Q.; Li, W. S.; Ji, Y. *Chem. Mater.* **2012**, *24*, 71; (b) Mizoshita, N.; Kutsuna, T.; Hanabusa, K.; Kato, T. *Liquid Crystals Iv* **2000**, *4107*, 108; (c) Bruning, M.; Kreplak, L.; Leopoldseder, S.; Muller, S. A.; Ringler, P.; Duchesne, L.; Fernig, D. G.; Engel, A.; Ucurum-Fotiadis, Z.; Mayans, O. *Nano Lett.* **2010**, *10*, 4533.

(12) (a) Liu, Z. X.; Feng, Y.; Yan, Z. C.; He, Y. M.; Liu, C. Y.; Fan, Q. H. *Chem. Mater.* **2012**, *24*, 3751; (b) Wang, C.; Chen, Q.; Sun, F.; Zhang, D. Q.; Zhang, G. X.; Huang, Y. Y.; Zhao, R.; Zhu, D. B. *J. Am. Chem. Soc.* **2010**, *132*, 3092; (c) Chen, W. D.; Gong, W. T.; Ye, J. W.; Lin, Y.; Ning, G. L. *RSC Adv.* **2012**, *2*, 809; (d) Liu, J. W.; Ma, J. T.; Chen, C. F. *Tetrahedron* **2011**, *67*, 85; (e) Liu, J.; He, P. L.; Yan, J. L.; Fang, X. H.; Peng, J. X.; Liu, K. Q.; Fang, Y. *Adv. Mater.* **2008**, *20*, 2508; (f) Liu, J.; Feng, Y.; Liu, Z. X.; Yan, Z. C.; He, Y. M.; Liu, C. Y.; Fan, Q. H. *Chem. Asian J.* **2013**, *8*, 572; (g) Dong, S. Y.; Zheng, B.; Xu, D. H.; Yan, X. Z.; Zhang, M. M.; Huang, F. H. *Adv. Mater.* **2012**, *24*, 3191.

(13) Tsuchiya, K.; Orihara, Y.; Kondo, Y.; Yoshino, N.; Ohkubo, T.; Sakai, H.; Abe, M. *J. Am. Chem. Soc.* **2004**, *126*, 12282.

(14) (a) Salle, M.; Canevet, D.; Balandier, J. Y.; Lyskawa, J.; Trippe, G.; Goeb, S.; Le Derf, F. *Phosphorus Sulfur and Silicon and the Related Elements* **2011**, *186*, 1153; (b) Tatewaki, Y.; Hatanaka, T.; Tsunashima, R.; Nakamura, T.; Kimura, M.; Shirai, H. *Chemistry-an Asian Journal* **2009**, *4*, 1474; (c) Danila, I.; Riobe, F.; Puigmarti-Luis, J.; del Pino, A. P.; Wallis, J. D.; Amabilino, D. B.; Avarvari, N. *J. Mater. Chem.* **2009**, *19*,

4495; (d) Taboada, E.; Feldborg, L. N.; del Pino, A. P.; Roig, A.; Amabilino, D. B.; Puigmarti-Luis, J. *Soft Matter* **2011**, *7*, 2755.

(15) (a) Duan, P. F.; Zhu, X. F.; Liu, M. H. *Chem. Commun.* **2011**, *47*, 5569; (b) Arai, S.; Imazu, K.; Kusuda, S.; Yoshihama, I.; Tonegawa, M.; Nishimura, Y.; Kitahara, K.; Oishi, S.; Takemura, T. *Chem. Lett.* **2006**, *35*, 634; (c) Yabuuchi, K.; Kato, T. *Mol. Cryst. Liq. Cryst.* **2005**, *441*, 261.

(16) Kim, H. J.; Lee, J. H.; Lee, M. *Angew. Chem. Int. Ed.* **2005**, *44*, 5810.

(17) Kim, H. J.; Lee, E.; Park, H. S.; Lee, M. *J. Am. Chem. Soc.* **2007**, *129*, 10994.

(18) Lin, H. C.; Tsai, C. M.; Huang, G. H.; Tao, Y. T. *Macromolecules* **2006**, *39*, 557.

(19) Seo, J.; Chung, J. W.; Jo, E. H.; Park, S. Y. *Chem. Commun.* **2008**, 2794.

(20) Samanta, S. K.; Bhattacharya, S. *Chem. Commun.* **2013**, *49*, 1425.

(21) (a) Kim, H. J.; Kim, T.; Lee, M. *Acc. Chem. Res.* **2011**, *44*, 72; (b) Shin, S.; Lim, S.; Kim, Y.; Kim, T.; Choi, T. L.; Lee, M. *J. Am. Chem. Soc.* **2013**, *135*, 2156; (c) Kim, Y.; Kim, T.; Lee, M. *Polymer Chemistry* **2013**, *4*, 1300; (d) Ajayaghosh, A.; Varghese, R.; Praveen, V. K.; Mahesh, S. *Angew. Chem. Int. Ed.* **2006**, *45*, 3261; (e) Ajayaghosh, A.; Varghese, R.; Mahesh, S.; Praveen, V. K. *Angew. Chem. Int. Ed.* **2006**, *45*, 7729.

(22) Ajayaghosh, A.; Praveen, V. K.; Srinivasan, S.; Varghese, R. *Adv. Mater.* **2007**, *19*, 411.

(23) (a) Reddy, L. S.; Srinivas, B.; Venu, R. V.; Ashwini, N. *Cryst. Growth Des.* **2006**, *6*; (b) Byrne, P.; Turner, D. R.; Lloyd, G. O.; Clarke, N.; Steed, J. W. *Cryst. Growth Des.* **2008**, *8*, 3335.

(24) (a) Dasgupta, D.; Thierry, A.; Rochas, C.; Ajayaghosh, A.; Guenet, J. M. *Soft Matter* **2012**, *8*, 8714; (b) Jonkheijm, P.; van der Schoot, P.; Schenning, A. P. H. J.; Meijer, E. W. *Science* **2006**, *313*, 80.

(25) Applegarth, L.; Clark, N.; Richardson, A.; Parker, A.; Radosavljevic-Evans, I.; Goeta, A.; Howard, J.; Steed, J. *Chem. Commun.* **2005**, 5423.

(26) Ajayaghosh, A.; George, S. J. *J. Am. Chem. Soc.* **2001**, *123*, 5148.

(27) Murata, K.; Aoki, M.; Suzuki, T.; Harada, T.; Kawabata, H.; Komori, T.; Ohseto, F.; Ueda, K.; Shinkai, S. *J. Am. Chem. Soc.* **1994**, *116*, 6664.

Chapter 4

An Unprecedented Role of Supramolecular Chirality in the Design of a Mechanochromic Chiral π-Gelator

4.1. Abstract

*In this chapter, we describe the design, synthesis and mechano responsive properties of an amide functionalized chiral oligo(p-phenylenevinylene) derivative (**OPV-C**). One dimensional helical nanostructures were successfully created from this system. Further, the effect of aggregation on optical and chiroptical properties in solution, film, gel, xerogel and solid states were studied in detail. This molecule was able to show mechanochromic luminescence by shear induced alteration of molecular packing. The achiral derivative (**OPV-A**) was less sensitive to shearing when compared to the chiral derivative (**OPV-C**), which revealed the key role of supramolecular chirality in the mechanoresponsive properties of self-assembled systems. Further, an isothermally self-reversible fluorescent **OPV-C** film was fabricated to understand the complex pathways of the self-assembly and the excited state processes in detail.*

4.2. Introduction

The solid state optical switching of supramolecular functional materials in response to external stimuli has drawn immense attention and has been intensively studied during the past one decade.[1] The phenomenon of change in optical properties by applying mechanical stimuli (e.g. stretching, shearing, grinding and pressing) is known as mechanochromism (Figure 4.1). Such systems which respond to mechanical stimuli are generally known as mechanochromic materials, also known as piezochromic or tribochromic materials. Mechanochromic materials are fascinating because the stimuli used is an external force/pressure which is easy to handle.[2] These materials are widely used in sensors, memory chips, and as security inks. There are enormous literature reports describing the transformation of monomeric to dimeric/excimeric forms which cause changes in luminescence.[3] It is well known that effective packing *via* π-overlap in the condensed phase can significantly change the luminescence.[4] The mechanically induced changes in the molecular packing and subsequent fluorescence changes continue to inspire chemists to look for new and improved systems. An equally important region to be explored is the fluorescence self-switching of such materials, which has immense application in the area of secret documentation and imaging.[5]

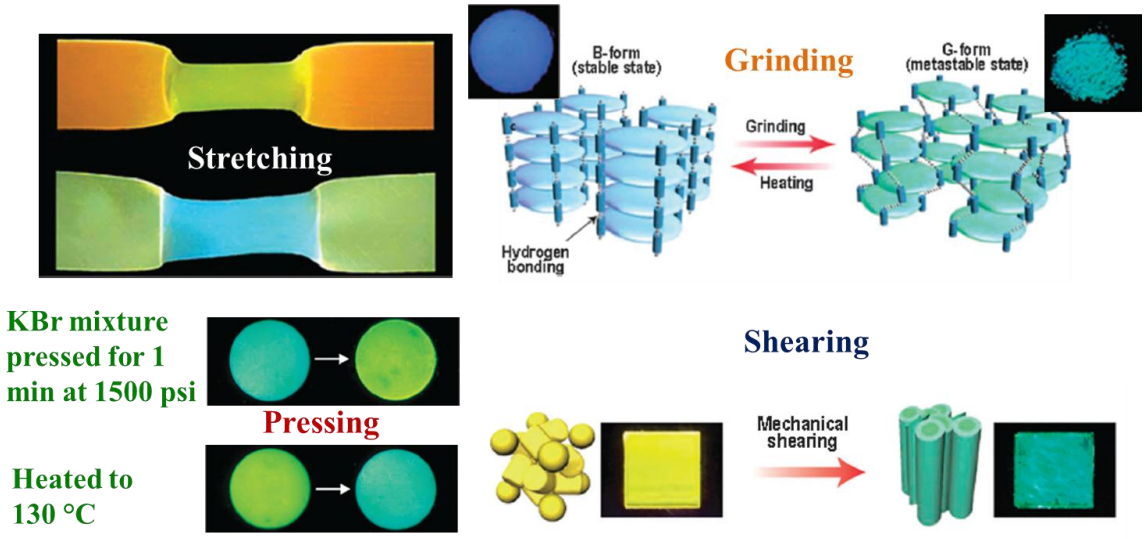

Figure 4.1. Images showing the changes in emission associated with different types of mechanical stimuli.

Linear π-systems are known to be a class of materials that can be used to make smart piezo-, vapo- and thermochromic luminescent assemblies.[2,6] Luminescent excimer forming π-systems dispersed into different thermoplastic and elastomeric polymer matrices are also reported by Weder *et al.* (Figure 4.2a).[6a] They have demonstrated that solid-state tensile deformation can lead to substantial changes in the emission *via* the formation of monomers and excimers upon stretching as shown in Figure 4.2b. The influence of temperature on the emission characteristics of the blend was monitored and the transformation of a red emission to a pure green emission was observed upon annealing the blend at 95 °C for 5 min (Figure 4.2c).

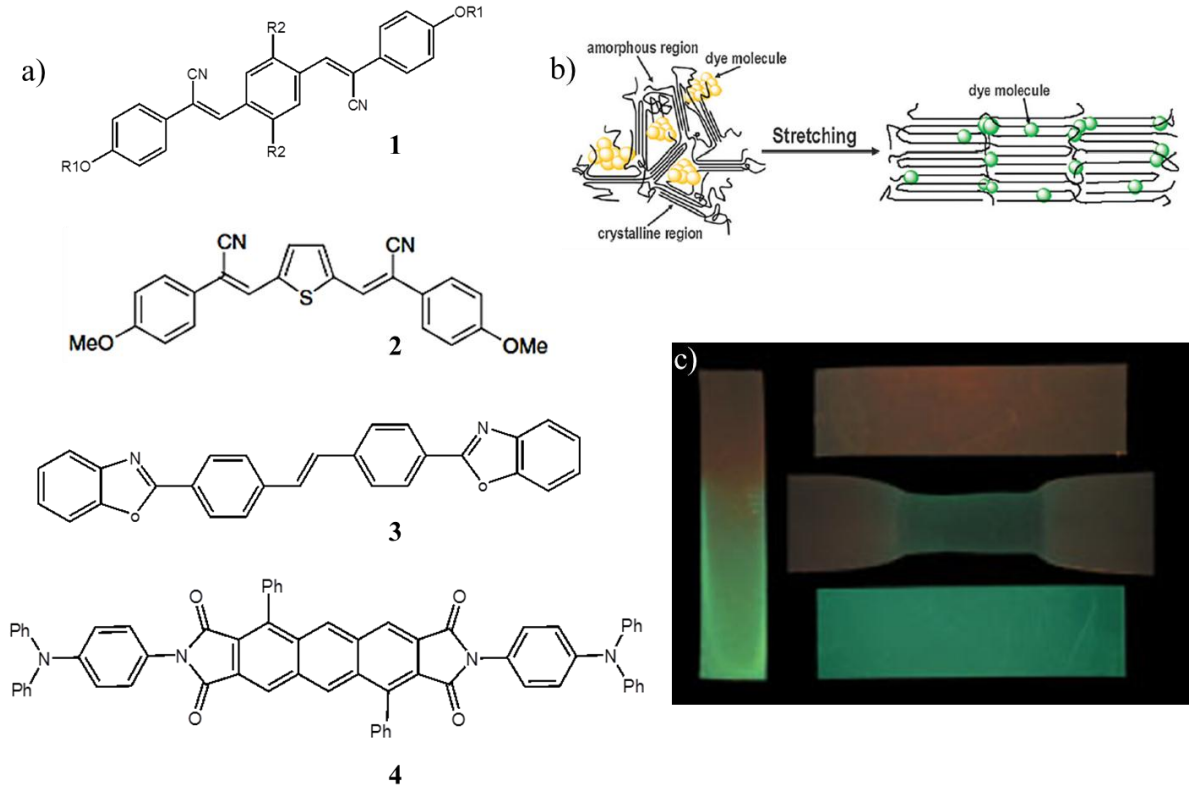

Figure 4.2. (a) Chemical structures of linear mechanochromic π-systems **1**-**4**. (b) Schematic representation of dye molecules incorporated into a polymer matrix in an aggregated fashion (left) and in a molecularly dispersed state (right). (c) Images of linear low-density polyethylene film comprising of **1** in the molecularly dissolved (green) and the aggregated forms (red), the bi-colored sample have been mechanically deformed (centre) and exposed to a temperature gradiant (left).

Tuning the optical and chiroptical features of π-gels and assemblies by applying mechanical stimuli is still a challenging area of research. Recently, Wang *et al*. reported a multistimuli responsive molecular gelator (Figure 4.3a) showing a transformation from green to orange luminescence upon applying mechanical stimuli (Figure 4.3b,c).[6b] A fluorescence microscope and field emission scanning

electronic microscope (FE-SEM) were used to study the morphologies of the fibers and xerogel (Figure 4.3d,e). A hot DMF solution of **5** upon cooling to room temperature and sonication for a few minutes resulted in the formation of a stable organogel as shown in Figure 4.3f.

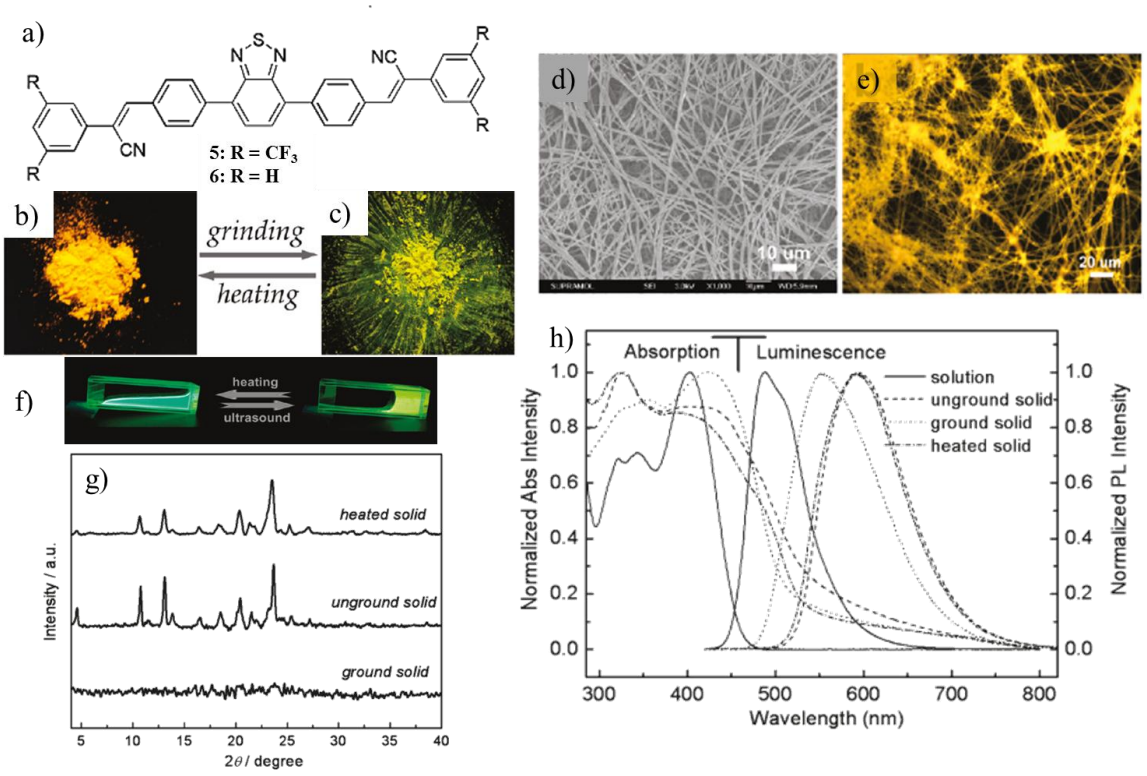

Figure 4.3. (a) Chemical structures of the molecular gelators **5** and **6**. (b,c) Stimuli-responsive behavior of the compound **5** upon grinding and heating. (d,e) FE-SEM and fluorescent microscopy images of the assembled structures of **5**. (f) Photographs showing stimuli-responsive gelation properties of the compound **5** in DMF solution upon heating and ultrasound treatments (under UV light, λ = 365 nm). (g) PXRD profiles of the compound **5** at different solid phases. h) UV-vis absorption (left) and emission (right) profiles of the solution, unground, ground, and heated solids of **5**.

The XRD patterns of the green and the orange solids showed different diffraction patterns (Figure 4.3g), suggesting that two kinds of molecular-packing modes exist in the green and orange crystalline microstructures. The dilute chloroform solution (1×10^{-5} M) of **5** exhibited an absorption maximum at 402 nm and intense fluorescence at 488 nm. The ground sample displayed an absorption maximum at 422 nm and green fluorescence at 545 nm. The heated sample exhibited a broad absorption band below 540 nm, an intense band at 323 nm and a shoulder at 430 nm. The unground solid and heated sample exhibited an orange emission at around 591 nm (Figure 4.3h). Even though a few reports are there in the literature on organogels showing mechanochromic response there is no report on isothermally reversible fluorescence of a mechanochromic organogelator to date.

Disruption of molecular packing upon mechanical stimulation and repairing *via* heating or solvent exposure of mechanoresponsive materials is a known phenomenon. Creation of such materials by tuning the molecular packing is continued to be an interesting area of research. Amide functionality is found to be an important tool for making such mechano-stimuli responsive systems (Figure 4.4a).[7] The presence of amide hydrogen bonds provides sensitivity and reproducibility to the mechanofluorochromic response. An excessive destruction of hydrogen bonds restrict the re-formation of the hydrogen bond-directed structure (Figure 4.4h).

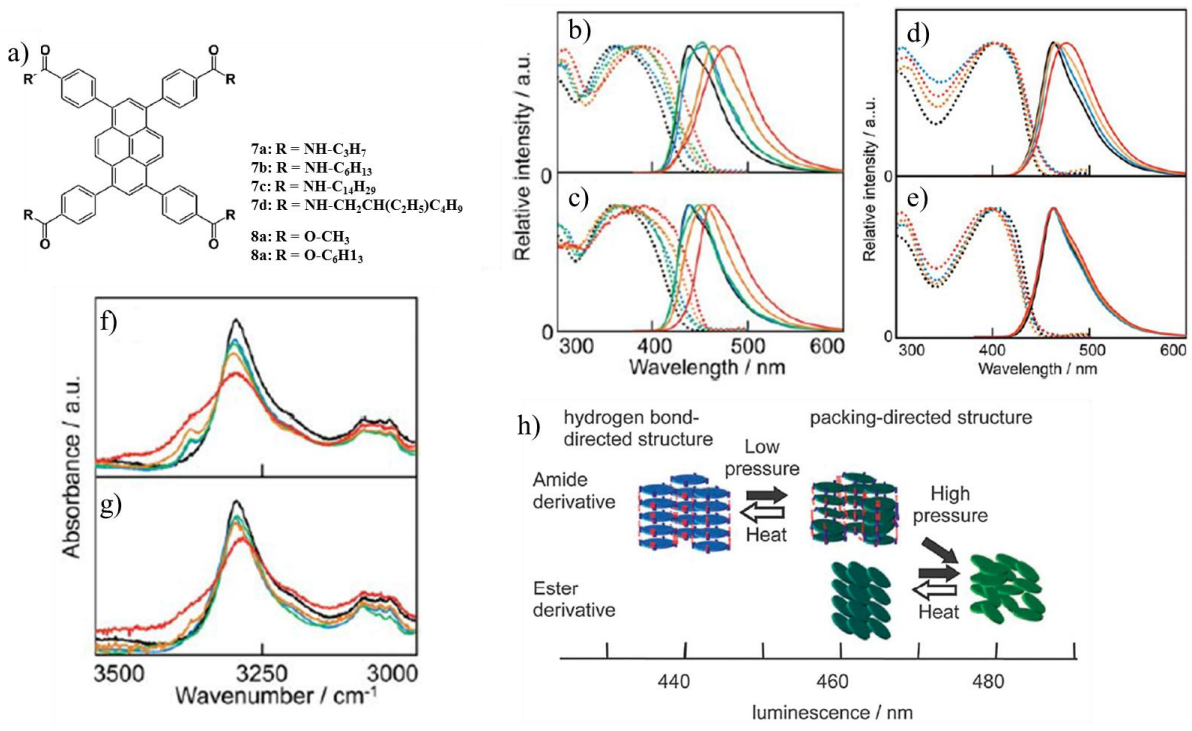

Figure 4.4. (a) Chemical structures of amide and ester derivatives of 1,3,6,8-tetraphenylpyrene (**TPPy**). Solid-state absorption (dotted line) and fluorescence (solid line) spectra after application of preset pressures (b for **7b** and d for **8b**) and subsequent heating (c for **7b** and e for **8b**). ν_{N-H} peaks in IR spectra of **7b** after application of preset pressures and subsequent heating (f, g respectively). Applied pressures are 2.0 (blue), 3.9 (green), 5.9 (orange) and 9.8 MPa (red). (h) Schematic illustration of piezochromic response of **TPPy** derivatives.

Earlier studies have shown that oligo(*p*-phenylenevinylene)s (**OPV**s) functionalised with different groups self-assembled to form one dimensional architectures such as tapes, fibers etc. leading to the gelation in non-polar solvents (Figure 4.5a).[8] Incorporation of chiral handle on **OPV** resulted in the formation of

a relatively weak gel comprising of helical fibers as described in our previous reports (Figure 4.5b).[9] Self-assembly of the oligo(*p*-phenyleneethynylene) derivatives (**OPE**s) having the same kind of end functional group and alkyl side chains as that of **OPV**, displayed different self-assembly pathways leading to vescicles and gels (Figure 4.5c,d).[10] These observation showed thermally reversible sol-gel process of self-assembled linear π-systems.

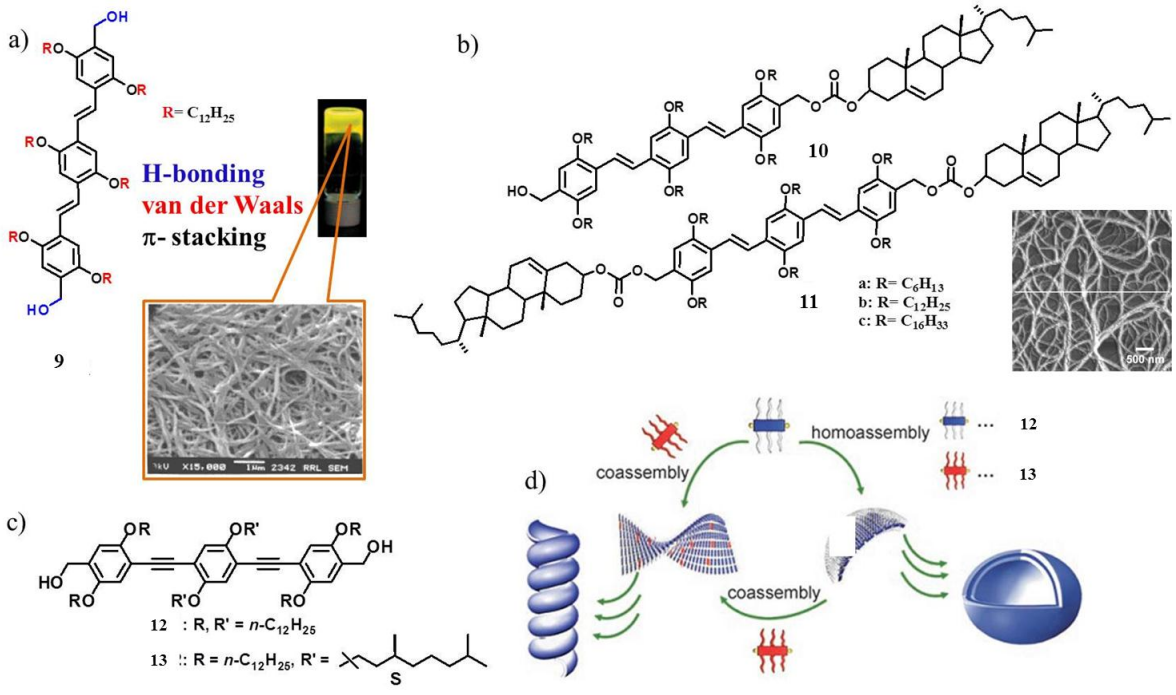

Figure 4.5. (a) Chemical structure, photograph and SEM image of the *n*-decane gel of **9**. (b) Chemical structures of the cholesterol-based **OPV** gelators **10** and **11** (inset; AFM image of **11**). (c) Chemical structures of the **OPE** based gelators, **12** and **13**. (d) Schematic representation of homo- and co-assembly of the **OPE** gelators, **12** and **13**.

Such assemblies and gels were thermoresponsive in general and photoresponsive when the moieties such as azobenzene was incorporated with the chromophore backbone (Figure 4.6).[11] Organic supramolecular nanorods of an azobenzene incorporated π-system has been reported.[11d] Self-assembled nanorod formation and and disassemby by irradiation under light of appropriate wavelengths was monitored using TEM (Figure 4.6a). Photoisomerization of azobenzene has been used to design a phase-selective low-molecular weight photoswitchable sugar hybrid gelator that selectively gelates aromatic solvents. The trans form of the molecule with long-range self-assembly leads to an entangled network structure that forms a gel in aromatic solvents.[11b] After UV irradiation, the bundled fibers disassembled to give short globular aggregates leading to gel breaking (Figure 4.6b). **OPE** gelators functionalized with photochromic azo moieties have been reported to undergo helicity inversion when irradiated at the aggregate melting temperature (Figure 4.6c).[11a] In this report, it has been shown that the handedness of a photoresponsive supramolecular object can be biased with the action of light and heat, without changing the inherent molecular chirality of the individual building blocks. Stimuli responsive morphological and fluorescence modulation of such assemblies has been carried out intensively in the solution and gel states, however, such variation of assemblies on film state is not yet well understood.

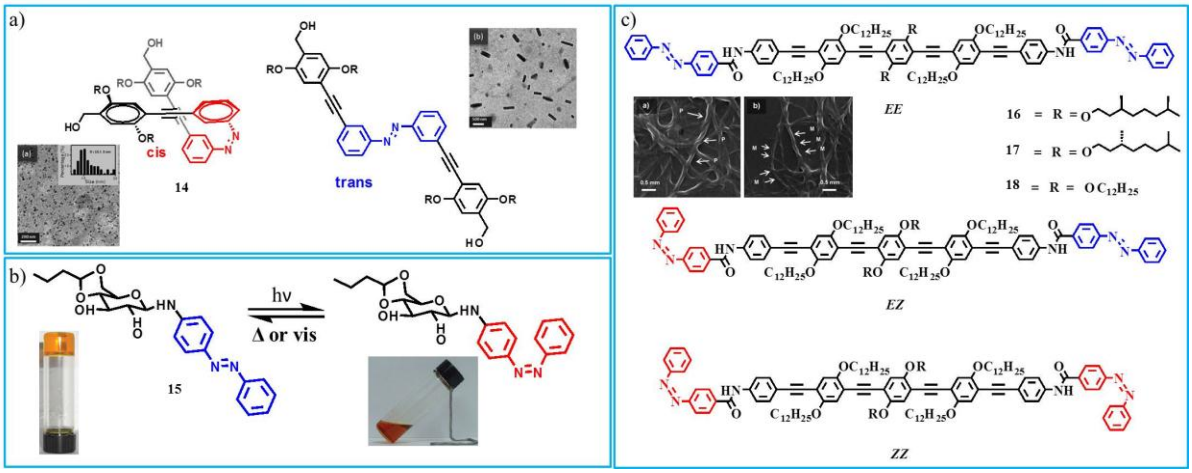

Figure 4.6. (a) Chemical structures of the trans and cis isomers of the photoresponsive π-gelator **14** and TEM images of nanodots (a; left bottom) and nanorod (a; right top). (b) Cis-trans isomerisation of **15** and the corresponding photographs showing photoresponsive sol-gel transition. (c) Chemical structures of **16**-**18**, SEM images of **17** before (left) and after (right) photoisomerization and chemical structures of EZ and ZZ isomers of **17**.

Supramolecular chirality of π-systems is a well studied phenomenon. A significant number of helical structures were used to probe the complex pathways of self-assembly of π-systems.[9a,10a,12] Stimuli responsive supramolecular chirality has been studied earlier, particularly the symmetry breaking/reversal of macroscopic chirality.[11a,13] Even though chiral molecules have been widely used for understanding the self-assembly pathways of supramolecular helicity, it is least exploited in the area of mechanochromism.

In the present study, excellent self-recoverable mechanochromic switching has been observed for an oligo(*p*-phenylenevinylene) chiral π-gelator (**OPV-C**). An

unprecedented role of supramolecular chirality in probing the pathways of mechanochromism and subsequent recovery process has been revealed. The self-reversible or self-repairing process was found to be mutable either by changing the concentration of the parent solution from which the film was prepared or the temperature at which recovery process occurs. A detailed study in solution, gel and solid phase were carried out to understand the pathways of mechanofluorochromism of the **OPV-C** gelator.

4.3. Results and discussion

4.3.1. Syntheses of OPV-C and OPV-A

OPV-C and **OPV-A** (abbreviated as **OPV-BZ** in the previous chapter) were synthesized from **OPV** bisacid as depicted in Scheme 4.1. For this purpose, an **OPV** bisester was synthesized according to a known procedure.[14] The reaction between the **OPV** bisacid and aniline was conducted using the peptide coupling agent HATU in dichloromethane in the presence of diisopropylethylamine.

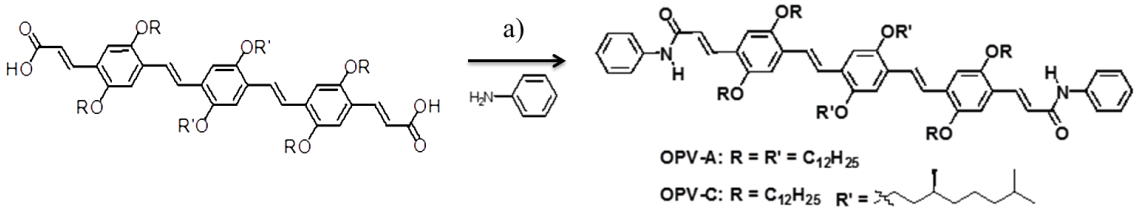

Scheme 4.1. Reagents and conditions: a) HATU, *N*,*N*-Diisopropylethylamine, 0 °C- 25 °C, 12 h, DCM.

4.3.2. Aggregation properties of OPV-C and OPV-A in solution

The details of the absorption and emission characteristics of **OPV-A** and **OPV-C** in $CHCl_3$ and *n*-decane are given in Table 4.1.

Compound	Solvent	λ_{abs} (nm)	λ_{ems} (nm)	log ε	Φ_f	τ (ns)
OPV-C	$CHCl_3$	450	530, 560	4.46	0.61	1.38
	n-decane	436	530, 570	4.33	0.25	0.7 (40%) 1.5 (60%)
OPV-A	$CHCl_3$	450	530, 560	4.45	0.58	1.4
	n-decane	432	535, 570	4.42	0.17	0.6 (58%) 1.44 (42%)

Table 4.1. Optical parameters of **OPV-A** and **OPV-C** in $CHCl_3$ and *n*-decane. [Fluorescence quantum yields (±5 % error) were determined using Fluorescein (Φ_r = 0.79 in 0.1M NaOH). All measurements were carried out at a concentration of 1 × 10^{-5} M except fluorescence quantum yield measurement, where the absorbance at the excitation wavelength (λ_{ex}= 440 nm) was adjusted at 0.1].

The data revealed that both **OPV** derivatives exist in the molecularly dissolved state in $CHCl_3$, whereas they exist as aggregates in *n*-decane. There is no significant difference between these two derivatives in solution state either in

$CHCl_3$ or in *n*-decane. A blue shift in absorption maximum and a small red shift in emission maximum indicates that these derivatives prefer a pseudo H-type packing in *n*-decane.[15] In the case of lifetime measurements, a monoexponential decay in $CHCl_3$ and a biexponential decay in *n*-decane were observed. Fluorescence quantum yields of **OPV-A** and **OPV-C** were decreased from 0.58 and 0.61 in $CHCl_3$ to 0.17 and 0.25 in *n*-decane, respectively.

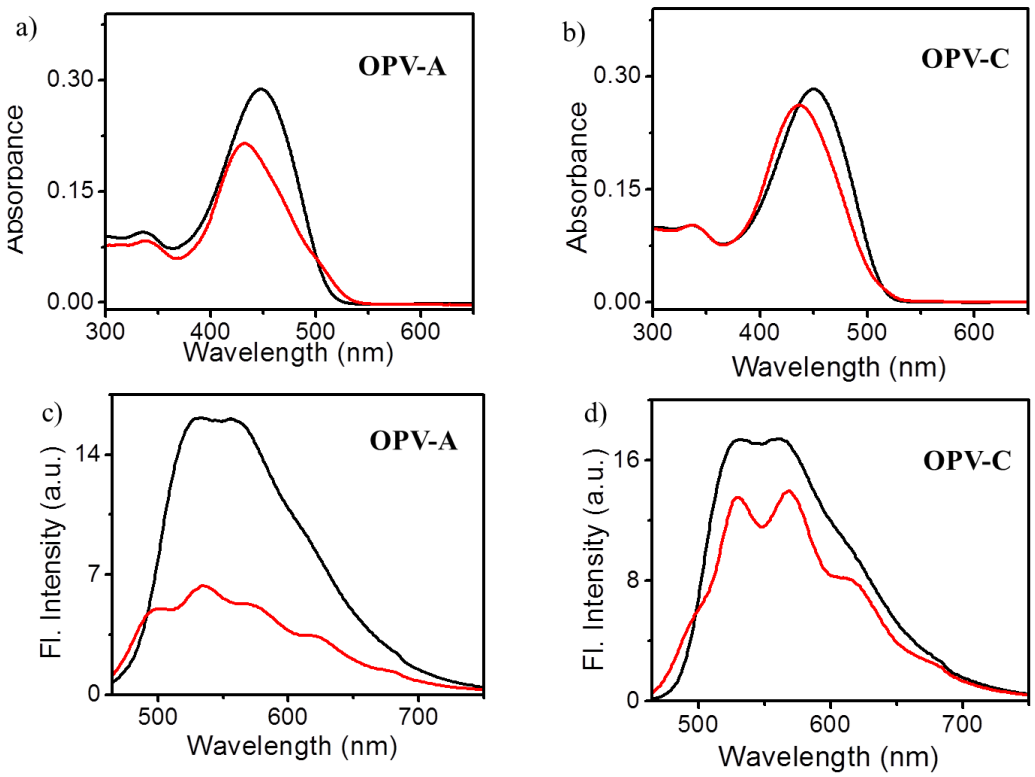

Figure 4.7. Absorption (a,b) and emission (c,d) spectra of **OPV-A** and **OPV-C** in chloroform (black) and *n*-decane (red) (conc. - 1×10^{-5} M, l = 1 cm, λ = 450 nm).

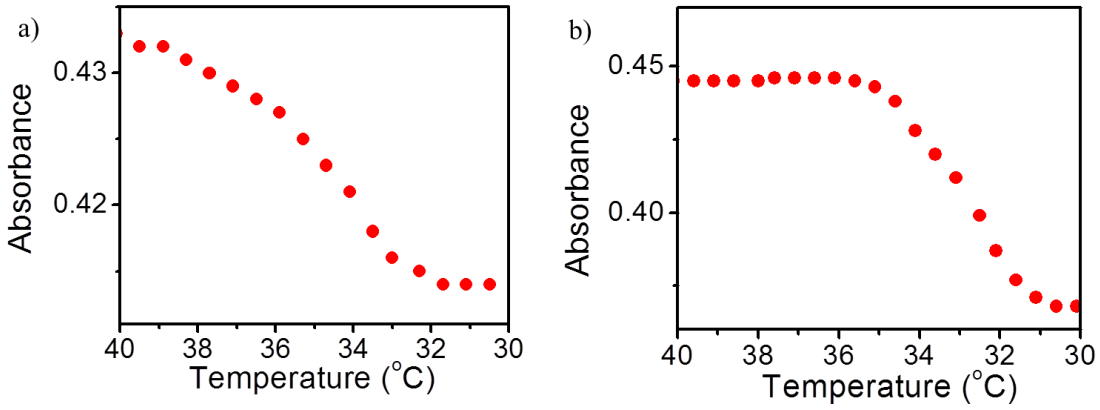

Figure 4.8. Plots of the absorbance vs temperature of (a) **OPV-A** and (b) **OPV-C** in *n*-decane (conc. - 5 × 10^{-5} M, *l* = 1 cm, *λ* = 450 nm).

Absorption spectra of **OPV-A** in $CHCl_3$ (1 × 10^{-5} M) showed a λ_{max} at 450 nm, whereas in *n*-decane (1 × 10^{-5} M) it exhibited a broad absorption band with maximum at 450 nm and a shoulder around 520 nm (Figure 4.7a). Quenching in absorption as well as emission can be ascribed to the aggregation of **OPV**s. However, **OPV-C** showed less quenching of absorption in *n*-decane when compared to that of **OPV-A** at the same concentration (1 × 10^{-5} M) (Figure 4.7b). This may be due to the high solubility of **OPV-C** owing to the presence of chiral chains. Broad emission spectra was observed for both **OPV-A** and **OPV-C** with maxima at 530 and 560 nm in $CHCl_3$ (1 × 10^{-5} M). In *n*-decane, quenching of emission with broadening was observed for both derivatives. The emission bands appeared around 500 nm and 620 nm as shown in Figure 4.7c,d can be ascribed to the formation of aggregates. Around 40% and 10% quenching of absorption and

emission was observed for **OPV-A** and **OPV-C**, respectively. This observation can be ascribed to a strong self-assembly behaviour of **OPV-A** when compared to that of **OPV-C** in *n*-decane due to the difference in solubility offered by the different alkyl chains.

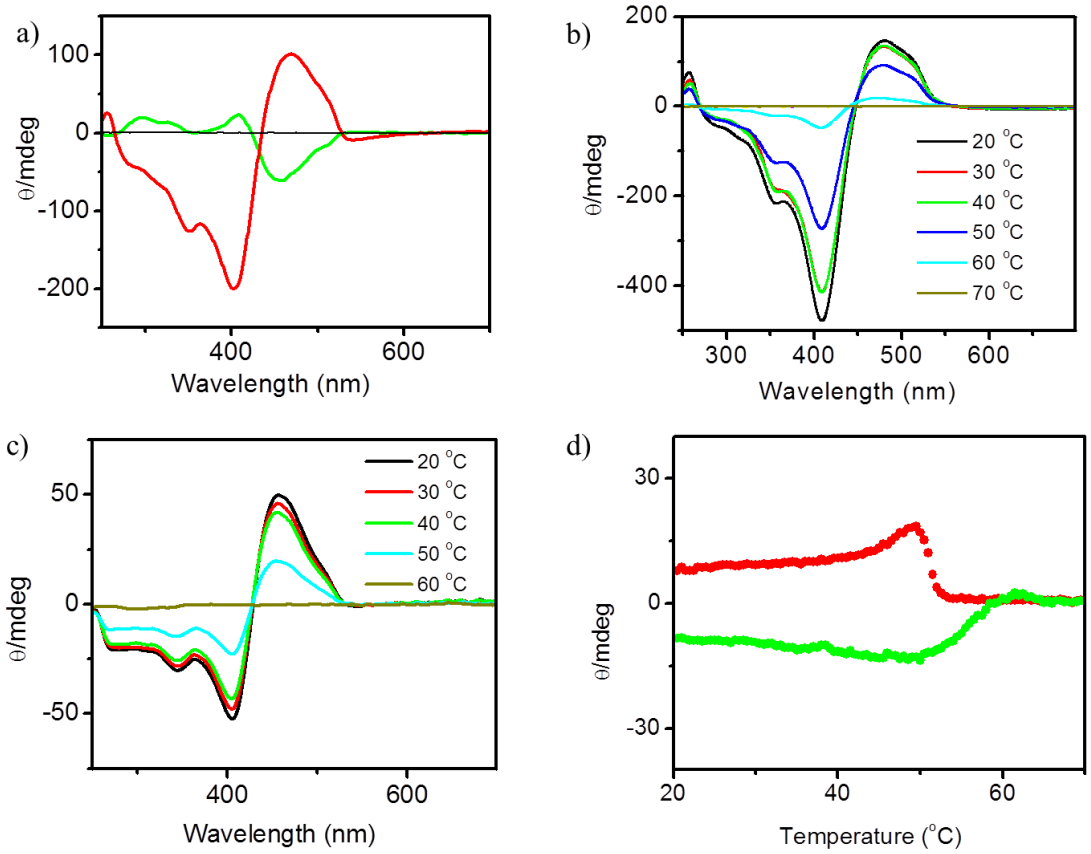

Figure 4.9. (a) CD spectra of **OPV-C** with fast (red) and slow (green) cooling rate. CD spectra of **OPV-C** at different temperature; heating mode (b) and cooling mode (c). (d) VT-CD measurements with slow (●) and fast (●) cooling rate, monitored at 500 nm. All solutions were prepared in *n*-decane with a conc. of 5×10^{-5} M.

Thermal stability of the aggregates has been monitored using variable temperature absorption and emission spectral changes. It has been observed that with increase in temperature, the aggregates start breaking and the solution finally become isotropic solution. Variable temperature (VT)-UV study revealed the significant role of the chiral chain in the thermal stability of **OPV-C** when compared to that of **OPV-A** in *n*-decane. The cooling curve of both derivatives in *n*-decane at a conc. of 5×10^{-5} M is shown in Figure 4.8, which revealed the aggregation of **OPV-A** and **OPV-C** at around 40 ℃ and 35 ℃, respectively.

Circular Dichroism (CD) studies were performed to follow supramolecular orgnization of the **OPV** derivatives. CD measurements of **OPV-A** and **OPV-C** in $CHCl_3$ upto a concentration of 1×10^{-3} M did not show any detectable Cotton effect because both these derivatives must be in their molecularly dissolved form. However, a hot isotropic solution upon cooling gave an exciton-coupled bisignate CD signal for **OPV-C** in *n*-decane (5×10^{-5} M), which revealed the formation of supramolecular helical assemblies. Interestingly, it has been observed that the formation of right handed and left handed helical assemblies can be controlled by changing the cooling rate. A hot solution of **OPV-C** in *n*-decane (5×10^{-5} M), when cooled to 0 ℃ by dipping in ice-salt bath yielded a bisignate CD signal with a positive cotton effect followed by a negative one. However, the same hot solution cooled by keeping at room temperature for few hours showed a reversal of the CD signal (Figure 4.9a). VT-CD measurement of **OPV-C** in *n*-decane (5 ×

10^{-5} M) revealed a decrease in the intensity of the CD signal upon increasing the temperature to 60 °C. At higher temperature, the supramolecular helical assembly collapses to the isotropic state with no CD signal as shown in Figure 4.9b. The bisignate CD spectra can be recovered by cooling the hot solution to lower temperature as shown in Figure 4.9c. Effect of the heating-cooling rate was studied with a VT-CD measurements as shown in Figure 4.9d. Upon cooling the isotropic solution of **OPV-C** in *n*-decane with a rate of 1 °C/min, a left handed assembly formation was observed, whereas a right handed assembly was formed upon changing the rate to 10 °C/min. This is confirmed by monitoring the CD signal at 500 nm of a *n*-decane solution of **OPV-C** (conc. 5×10^{-5} M) with different heating-cooling rate (Figure 4.9d). **OPV-A** was CD silent in *n*-decane which is a characteristic signature of an achiral assembly.

4.3.3. Gelation studies of OPV-C and OPV-A

Even though **OPV-A** and **OPV-C** form organogels in various non-polar solvents, significant differences in the gelation ability could be observed. The critical gelator concentration of **OPV-A** and **OPV-C** in different solvents was calculated and it was found that **OPV-A** is a strong gelator when compared to **OPV-C**, indicating the crucial role of alkyl chains in the gelation ability (Table 4.2).

Solvent	Decane	Hexane	Cyclohexane	Benzene	Toluene	Chloroform	THF
OPVA	0.25	3.26	1.60	1.60	0.13	Soluble	Soluble
OPVC	1.35	5.50	3.46	1.84	1.58	Soluble	Soluble

Table 4.2. Critical Gelator Conc. (CGC) of **OPV-A** and **OPV-C** in various organic solvents (in mM).

The viscoelastic nature of the *n*-decane gels of **OPV**s was monitored by rheological studies as shown in Figure 4.10. The frequency sweep experiments indicated that the storage modulus (G′) and loss modulus (G′′) are independent of the oscillation frequency. The G′ value was nearly an order of magnitude higher than G′′ showing that the gels were elastically stronger. The G′ value, which is a measure of resistance to elastic deformation was high for **OPV-A** indicating the high viscoelastic nature when compared to **OPV-C** gel.

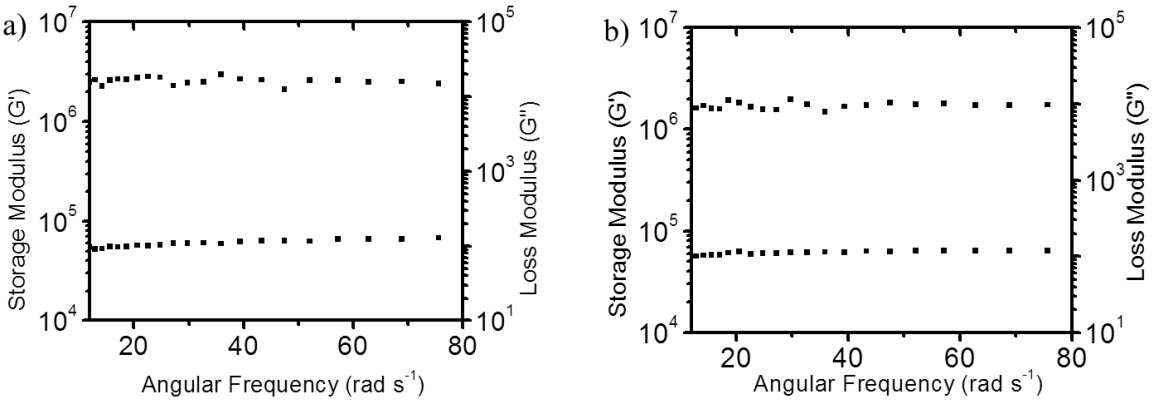

Figure 4.10. Rheolgical data of (a) **OPV-A** and (b) **OPV-C** gels in *n*-decane.

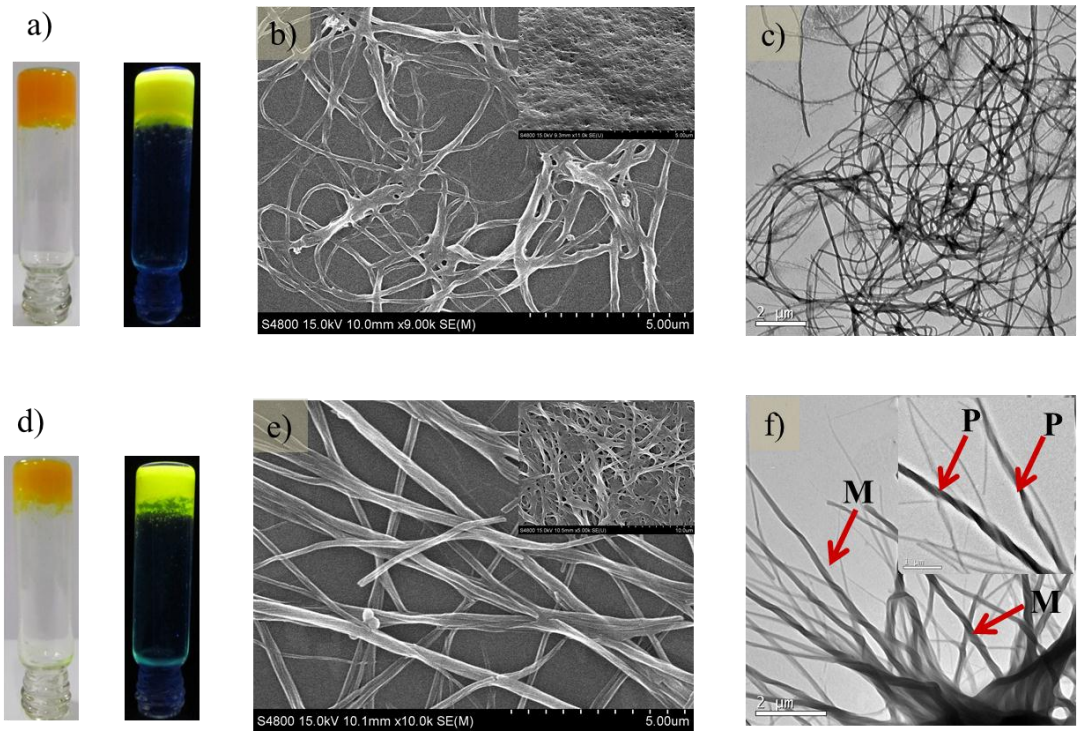

Figure 4.11. Photographs under ambient (left) and UV (right) light, FE-SEM and TEM images of **OPV-A** (a,b,c respectively) and **OPV-C** (d,e,f respectively) (Solutions were prepared by heating a 1×10^{-5} M *n*-decane solution and subsequent cooling at room temperature). Inset of b and e; FE-SEM images of **OPV-A** and **OPV-C** gels, respectively and inset of f; TEM image of P (right handed) helix.

Gel formation in *n*-decane must be due to the entrapment of solvent in fibrous network. Both these derivatives were able to show stable yellow emissive gels at room temperature (23 ℃) (Figure 4.11a, d). Morphological analysis of **OPV-A** and **OPV-C** were monitored using FE-SEM as shown in Figure 4.11 b and e, respectively. Entangled fibrous network formation was observed for xerogel and aggregates from dilute solutions of *n*-decane. Further, the flexible wire formation

was confirmed by TEM (prepared from curresponding gels) analysis as shown in Figure 4.11c (for **OPV-A**) and Figure 4.11f (for **OPV-C**), respectively. Both M (left) (Figure 4.11e) and P (right) (Figure 4.11e; inset) handed supramolecular helices were observed in TEM analysis. Thus, it can be concluded that both the molecules were able to form entangled fibrillar network in *n*-decane resulting in the gel formation.

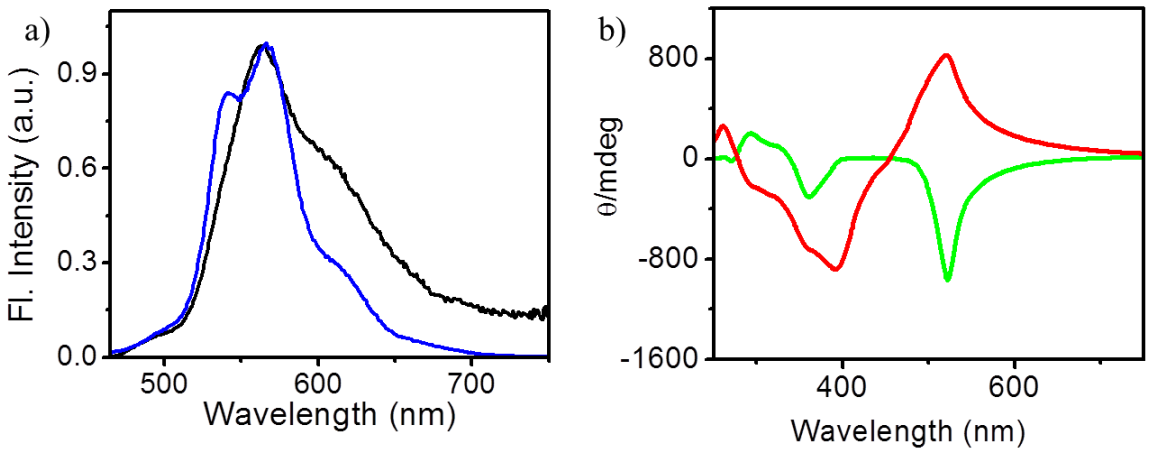

Figure 4.12. (a) Fluorescence spectra of **OPV-A** (black) and **OPV-C** (blue) gel in *n*-decane. (b) CD spectra of **OPV-C** with different cooling rate, fast (red) and slow (green).

Significant differences in the emission and CD characteristics were observed for these **OPV**s in the gel state. The emission spectrum of **OPV-A** gel showed a peak with a maximum at 570 nm with a strong shoulder band around 620 nm. However, **OPV-C** showed peaks at 570 nm and 620 nm similar to **OPV-A** and an extra band appeared at around 535 nm (Figure 4.12a). Supramolecular organization of **OPV-C** leads to a high intense CD signal in *n*-decane as explained previously. Further,

an increase in the CD signal was observed for the **OPV-C** gel from *n*-decane. A reversal of the CD signal from the right to the left handed signature was observed by changing the cooling rate of the hot isotropic solution to the gel phase (Figure 4.12b).

4.3.4. Self-reversible mechanochromism by OPV-C

The film state fluorescence properties of **OPV-C** were measured and it was observed that **OPV-C** aggregate emission responds to mechanical stimuli (Figure 4.13a-c). The greenish yellow emissive film was prepared on a glass plate by drop casting *n*-decane solution and subsequent evacuation of solvent under vacuum (Figure 4.13a). Upon shearing/grinding, the greenish yellow emission turned to an orange emission (Figure 4.13b). Initial emission of film was recoverd rapidly upon keeping the film at room temperature for 5 min (Figure 4.13c). This is further supported with a fluorescent microscopic experiment as shown in Figure 4.13d-f. A greenish yellow fibrous network was observed for a film prepared on a glass plate by drop casting 5 μL of 1×10^{-3} M *n*-decane solution of **OPV-C**. Upon shearing, the fibrous structures were changed into an ill-defined structure with an orange emission. Initial emission was recovered by keeping the film at room temperature for a few minutes.

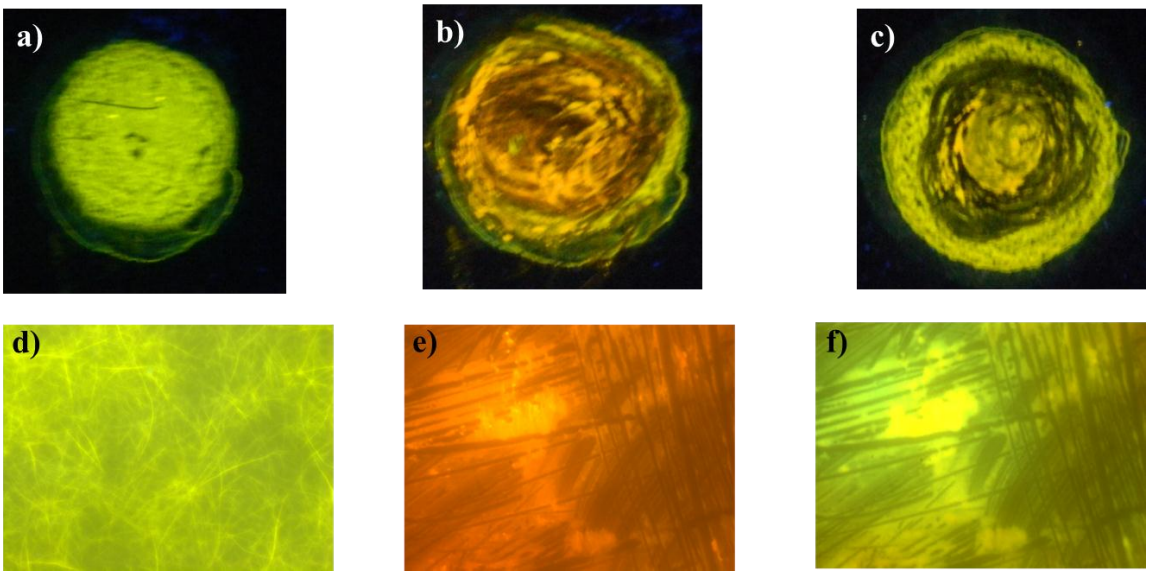

Figure 4.13. Photographs and optical microscopic images of as prepared (a,d), sheared (b,e) and self-recovered and (c,f) **OPV-C** film prepared from *n*-decane solution (1×10^{-3} M).

Initial fluorescence spectra of **OPV-C** film consist of three distinguishable peaks at 535, 570 and 620 nm. Significant reduction in the intensity of 535 nm band was observed upon grinding/shearing with a concomitant increase in the band at 620 nm resulting in an orange emission. Interestingly, the orange emission reverted back to initial greenish yellow emissive state isothermally without applying any stimuli (Figure 4.14a). Recording a time dependent emission spectra over a period of 30 min showed a quenching of emission. A normalized emission spectra of as prepared, sheared and recovered films were plotted as shown in Figure 4.14a;inset. Spectral features of the as prepared and the recovered films were similar, indicating an isothermal fluorescence recovery process. Recovery process of the film depends on the sample processing, especially on the

concentration of the solution. Araki *et al.* reported earlier that the sample thickness and processing has a major role in the packing as well as in the fluorescence switching.[7,16]

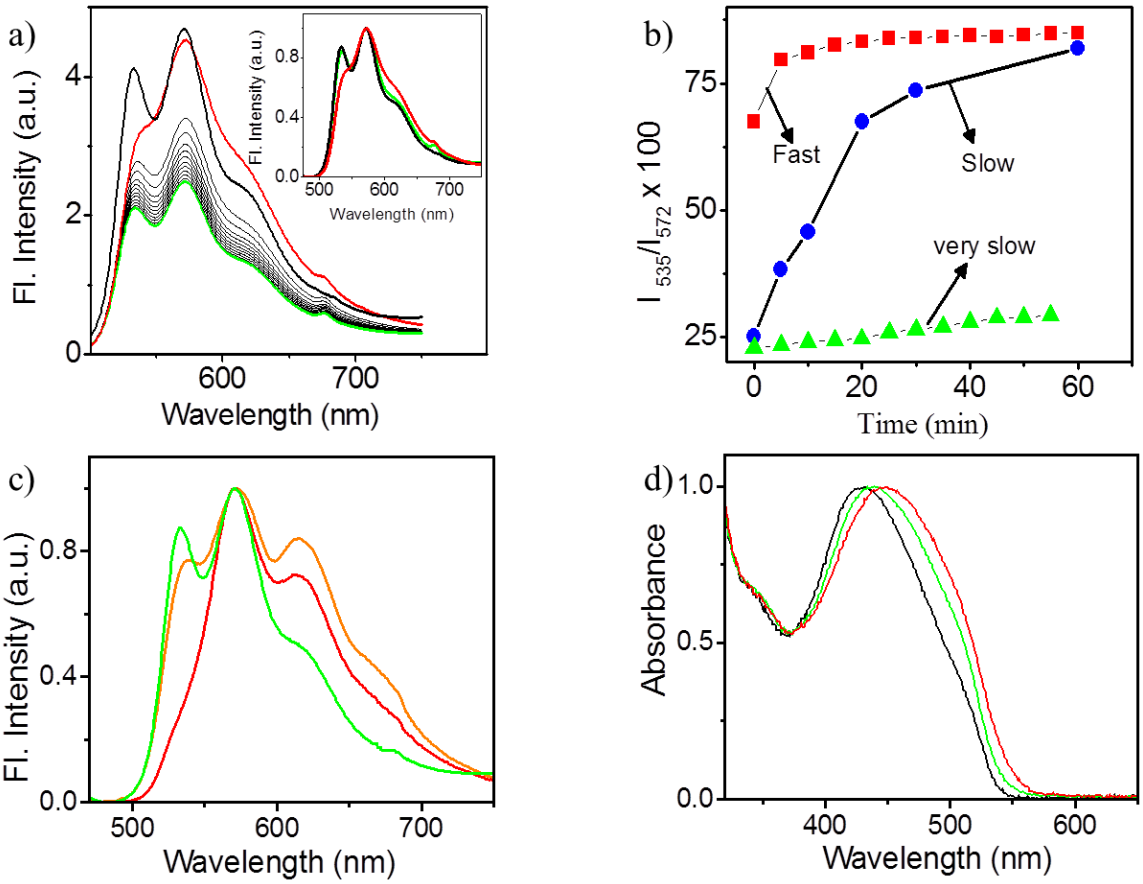

Figure 4.14. (a) Time dependent fluorescence spectra of **OPV-C** film after shearing (inset; normalised emission spectra of as prepared (black), sheared (red) and recovered (green). (b) Time dependent fluorescence plot of **OPV-C** film (red), xerogel (blue) and solid (green). (c) Normalized emission film (green), xerogel (yellow) and solid (red). (d) Film state absorption spectra of as prepared (black), sheared (red) and recovered (green).

Hence, we checked the effect of mechanical stimuli on **OPV-C** xerogel and

precipitated solid and compared with **OPV-C** film. All the samples responded to mechanical stimuli which was confirmed with the change in the emission. After shearing, it has been observed that the **OPV-C** film recovered faster when compared to the xerogel and the solid powder (Figure 4.14b). Similar to emission, mechanoresponsive absorption was observed for **OPV-C** aggregates, where shearing caused a 20 nm red-shift (430 nm – 450 nm). An isothermal recovery of absorption of the **OPV-C** film with time was observed with a 12 nm blue shift (450 nm – 438 nm) occurred while keeping (Figure 4.14d). Absorption maximum of the isotropic **OPV-C** solution in $CHCl_3$ was 450 nm and that of **OPV-C** aggregates in *n*-decane was 430 nm. Hence, it can be concluded as a mechanical perturbation and subsequent self-reorganization of **OPV-C** aggregates under isothermal condition.

OPV-A forms stronger aggregates when compared to **OPV-C** in *n*-decane, which is evident from gelation and VT-UV experiment as described earlier. These experiments revealed the effect of alkyl chain on self-assembly, gelation and fluorescence. We studied the mechanoresponsive behaviour of **OPV-A** aggregates which exhibited a red shift in fluorescence upon mechanical stimulation. However, the mechanochromic effect was not dynamic at room temperature as shown in Figure 4.15. Thus, it was obvious that the supramolecular helicity plays an important role in imparting the mechanoresponsive behaviour of **OPV-C**.

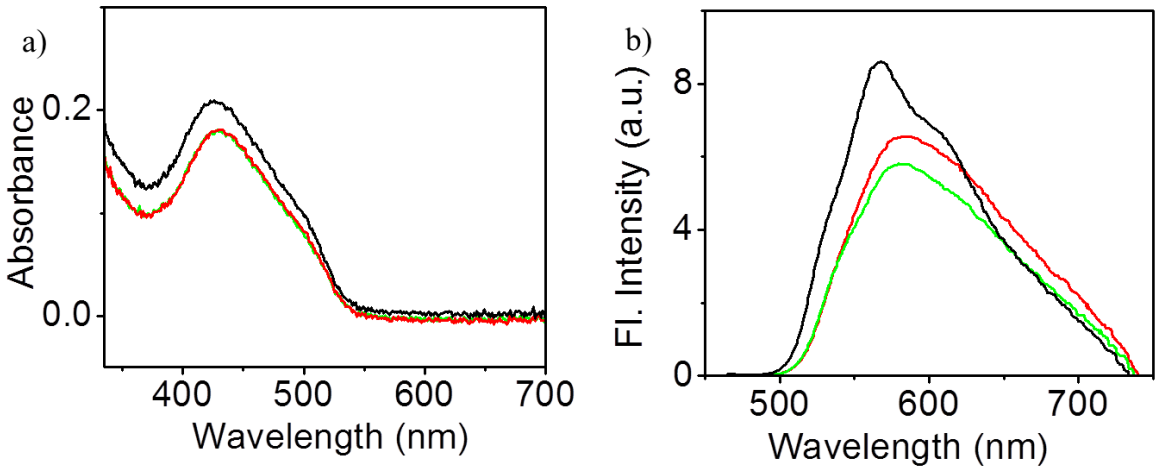

Figure 4.15. (a) Absoprtion and (b) emission spectra of as prepard (black), sheared (red) and aged (green) **OPV-A** aggregates.

4.3.5. Excited state processes associated with mechanochromism

To get more insight into the excited state processes during shearing and re-organization of the **OPV-C** aggregates, we performed fluorescence lifetime and time resolved emission (TRES) experiments. Lifetime decay analysis of as prepared (from *n*-decane solution, 5×10^{-4} M), sheared and recovered films were monitored and these were found to fit into a tri-exponential decay profile as shown in Table 4.3. Tri-exponential decay is an indication of **OPV-C** aggregates with different hierarchical orders with different size and HOMO–LUMO energy levels. Upon shearing, a decrease in the lifetime and a reduction in the relative intensity of shorter lifetime species were observed. Subsequently, an increase in the relative intensity of higher lifetime species was observed. This observation, independent of collection wavelength, is an indication of energy migration

process. The reduction of shorter lifetime species with a concomitant increase in the longer lifetime species can again be attributed to a possibility of excited state energy migration from lower order aggregates to higher order aggregates. Lifetime as well as relative amplitude of all three states were recoverd isothermally. The dacay profiles of as prepared and recovered **OPV-C** films were similar as shown in Figure 4.16.

OPVC	As prepared (ns)	Sheared (ns)	Recovered (ns)
535 nm	0.3 (60%) 0.8 (37%) 2.8 (3%)	0.04(35%) 0.4 (44%) 1.6 (21%)	0.19 (48%) 0.8 (45%) 3.2 (7%)
570 nm	0.3 (49%) 0.79 (45%) 2.6 (6%)	0.06 (16%) 0.4 (55%) 1.6 (29%)	0.2 (32%) 0.8 (54%) 2.5 (14%)
620 nm	0.36 (51%) 1.2 (39%) 3.3 (10%)	0.25 (30%) 1.03 (56%) 2.9 (14%)	0.27 (39%) 1.0 (51%) 3.0 (10%)

Table 4.3. Lifetime of **OPV-C** film at different conditions (λ_{ex} = 440 nm).

An increase in the fluorescence lifetime was observed with an increase in collection wavelength, indicating a possible energy migration among **OPV-C** aggregates (Figure 4.16). Similar decay profiles were observed for recovered **OPV-C** sample. In order to prove the excited state energy migration among **OPV-**

C aggregates, we performed a time resolved emission in picosecond time scale.

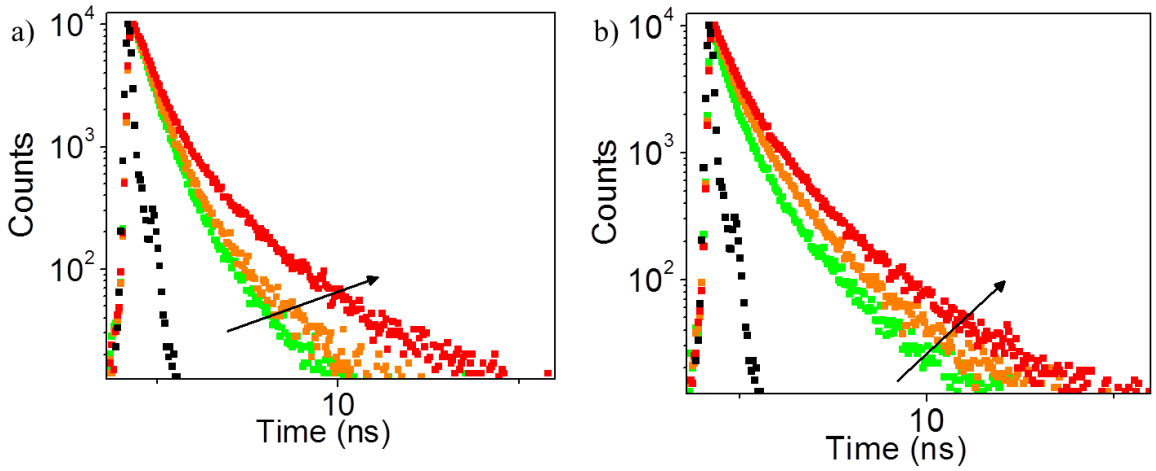

Figure 4.16. Lifetime decay profiles of (a) as prepared and (b) sheared **OPV-C** aggregates (λ_{ex} = 440 nm), emission collected at 535 nm (green), 570 nm (yellow), 620 nm (red) and prompt (black).

Thus, the observed fluorescence color change during mechanical stress can be explained on the basis of the formation of aggregates with different size and energy levels. **OPV-C** forms different type of aggregates as evident from emission as well as lifetime experiments. Upon exciting at 440 nm, the emission observed at 535, 570 and 620 nm with a tri-exponential lifetime can be considered as collective emission from aggregates of different size. Decay from lower order to higher order aggregates was observed in TRES analysis (Figure 4.17). After shearing, the emission band around 535 nm was dimished (lifetime 0.3 ns, 60% to 0.04, 35%) significantly with an increase in the band around 620 nm (lifetime 2.8 ns, 3% to 1.6 ns, 21%) which is ascribed to a mechanical perturbance of lower

order aggregates.

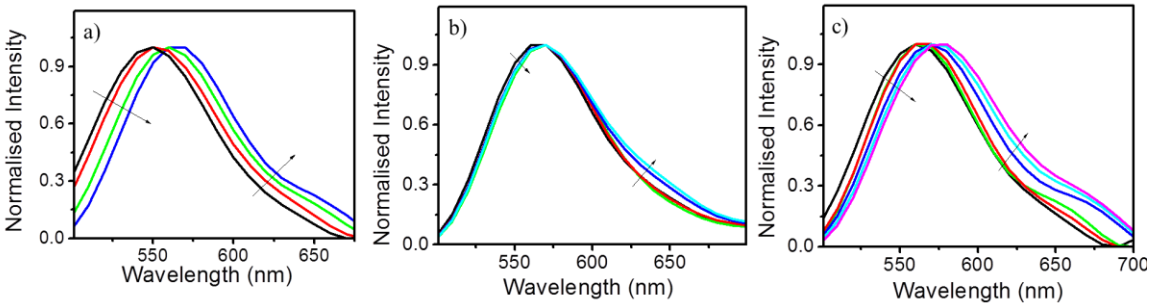

Figure 4.17. Time resolved emission spectra of (a) as prepared, (b) sheared and (c) recovered **OPV-C** aggregates (λ_{ex} = 440 nm).

Small changes observed in TRES analysis of sheared sample can be attributed to energy migration between higher order states. Upon recovery, the emission band at 535 nm (lifetime 0.19 ns, 48%) was increased rapidly and band around 620 nm (3.2 ns, 7%) decreased. Lifetime and TRES profiles were recovered as that of the initial film isothermally which can be ascribed to the recovery of the excited state energy migration path. Excitation spectra of all the three samples upon collecting the emission at different wavelengths of 535, 570 and 620 nm, overlap each other (Figure 4.18). Thus, an excitation of lower order aggregates and energy migration to higher order aggregates of **OPV-C** has been established here.

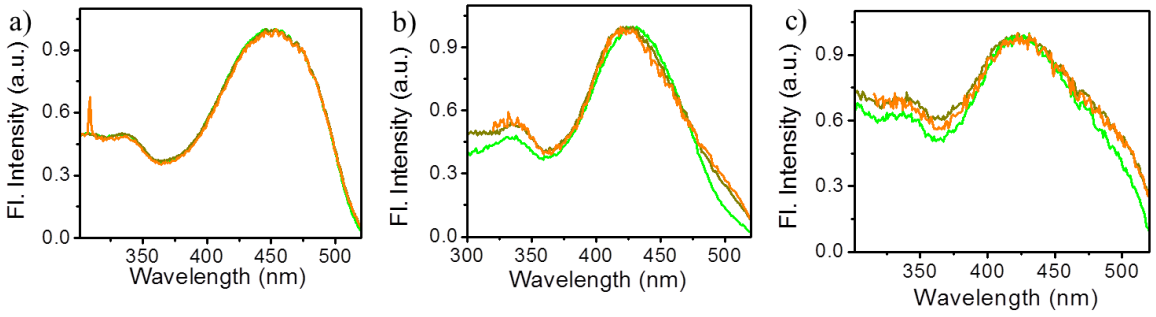

Figure 4.18. Excitation spectra of **OPV-C** (a) in $CHCl_3$ solution, (b) in *n*-decane gel and (c) xerogel.

4.3.6. Role of supramolecular chirality in understanding the re-organization process

A film state CD spectrum on quartz plate was measured in order to check the stimuli responsive nature of the **OPV-C** aggregates. After shearing, the CD signal of the aggregates became weak (Figure 4.19a) which suggest a dislocation of chromophores. However, no recovery in CD signal was observed, which indicates that the re-organization process lead to a condensed state which is different from the initial one. Heating or annealing process had less effect on the CD signal intensity (Figure 4.19a;inset). A complete recovery of the CD signal was observed only by solvent treatment of the film (Figure 4.19b), indicating a helical re-organization of the chromophore. The re-organization of the chromophore into the helical stack has been further proved with a time dependent FT-IR measurements as shown in Figure 4.19c. Hydrogen bonded N-H stretching peak (3300 cm^{-1}) of **OPV-C** upon shearing splits into two peaks (3300 cm^{-1} and 3420 cm^{-1}). With

time, a recovery of the peak around 3300 cm^{-1} with a subsequent reduction of the peak 3420 cm^{-1} was observed. FE-SEM analysis of samples before and after shearing revealed that the fibrous network has been converted to ill-defined structures (Figure 4.19d). Recovery process never reproduced the fibrous structures.

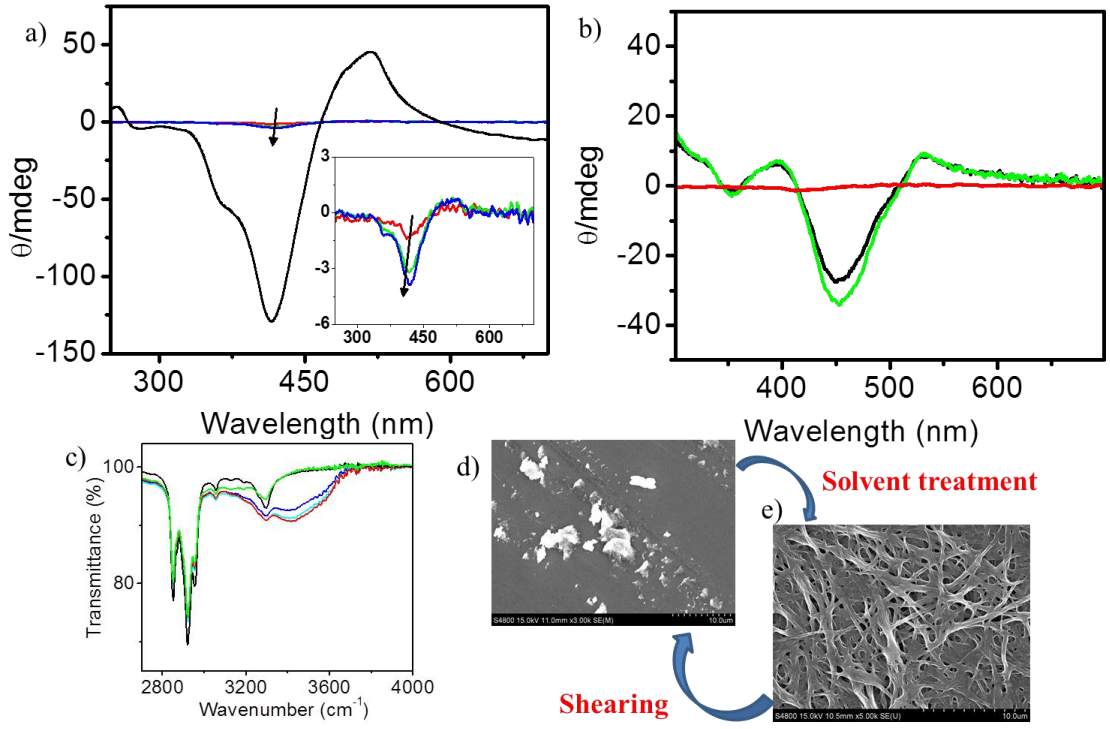

Figure 4.19. (a) CD spectra of as prepared (black), sheared (red) and annealed (at 110 °C, green – 30 min and blue - 60 min) **OPV-C** film. (b) CD spectra of as prepared (black), sheared (red) and recovered (green – with solvent treatment) **OPV-C** films. (c) FT-IR spectra of as prepared (black), sheared (red) and self-recovered (blue -30 min, cyan - 60 min and green - 12 hour) **OPV-C** film. FE-SEM image of (d) sheared **OPV-C** film and (e) recovered (with solvent).

The disruption and rearrangement of the chromophore packing were observed from the X-ray diffraction spectra as shown in Figure 4.20. The decrease in the intensity after shearing the film indicates a possible dissociation of **OPV-C** aggregates. Thermal treatment further decreases the intensity of the diffraction peaks which revealed a probable thermally induced disruption of **OPV-C** aggregates. However, the fluorescence remain the same even after the thermal treatment. Solvent treatement of the xerogel film helped to retain the diffraction peak similar to the initial state. The d-spacing value at 3.56 Å (corresponding to π-π stacking) showed more response when compared to the other peaks (Figure 4.20b).

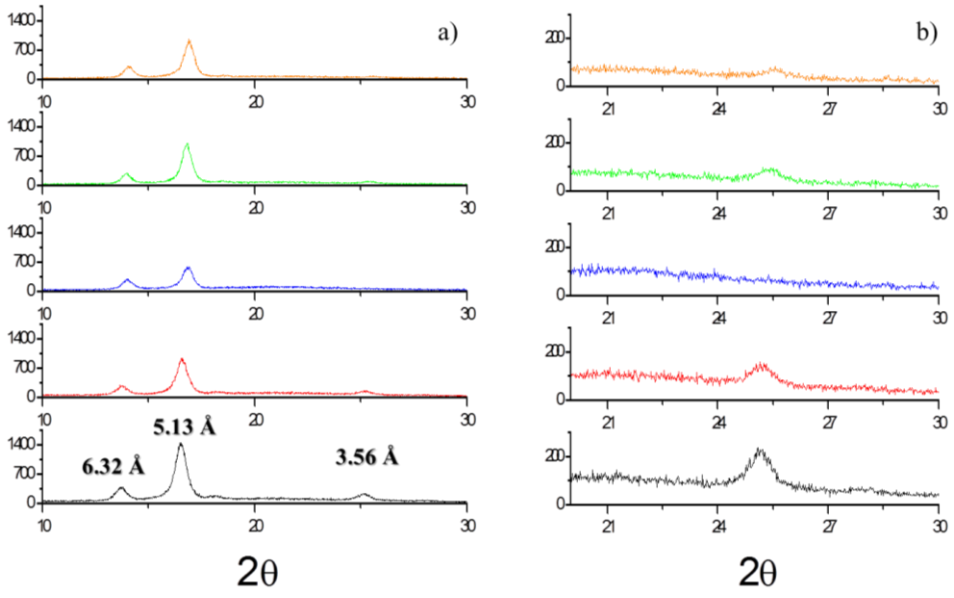

Figure 4.20. (a) X-ray diffraction pattern and (b) zoomed region of 2θ between 20-30° of a xerogel of **OPV-C** from *n*-decane (black), sheared (red), annealed at 140 °C for 1 h (blue), solvent recovered xerogel (green) and rescratched (orange).

Differential scanning calorimetry (DSC) of the as prepared **OPV-C** powder showed a melting transition around 160 ℃. At 120 ℃, recrystalization occurred followed by a phase transition around 80 ℃. The xerogel derived from *n*-decane showed an exothermic transition around 140 ℃ (Figure 4.21a) indicating that the initialy formed structure transformed into a more favourable one before melting to an isotropic state. Such structural reformation after themal annealing was further studied with CD. It has been observed that after annealing at 110 ℃ for 30 min the CD signal reduced significantly and further completely disappeared after keeping the same sample at 140 ℃ for 30 min (Figure 4.21b).

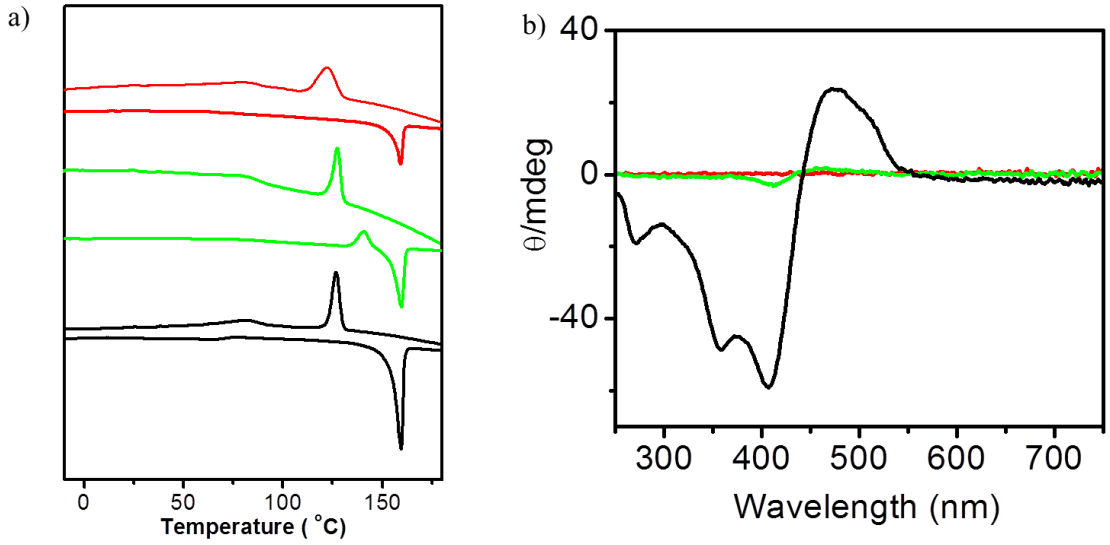

Figure 4.21. (a) DSC spectra of **OPV-C**, as prepared powder (black), xerogel (green) and sheared (red). (b) CD spectra of xerogel, as prepared (black), annealed at 110 °C for 30 min (green) and 140 °C for 30 min (red).

From the experiments described so far, we understood that temperature has a crucial role in the fluorescence recovery and re-organization process of **OPV-C** aggregates. To get a clear idea on the effect of temperature on fluorescence and CD of **OPV-C** aggregates, variable temperature measurements were carried out. Upon increasing the temperature of the **OPV-C** xerogel, coated on a quartz plate, the emission band around 620 nm was decreased as shown in Figure 4.22a. A broad spectrum was observed for the molten state at 200 ℃, which upon cooling gave back the fluorescence spectra corresponding to the aggregated **OPV-C** xerogel (Figure 4.22b) but with less features. This is clear from the normalized emission spectra of the initial and the recovered xerogel samples as shown in Figure 4.22c. A VT-CD measurement showed gradual decrease in the intensity which confirmed that the transformation occuring upon thermal annealing, which might be disrupting the existing helical structure (Figure 4.22d). Hence, it can be concluded that the effect of temperature on as prepared and sheared **OPV-C** aggregates is the same. Upon incresing the temperature, a disruption of the supramolecular organization of **OPV-C** occurs, which is evident from the VT-CD and the XRD studies. Further, increase in temperature lead to the formation of an isotropic solution state which upon cooling, resulted in a different state, recovering the fluorescence but failed to retain the CD.

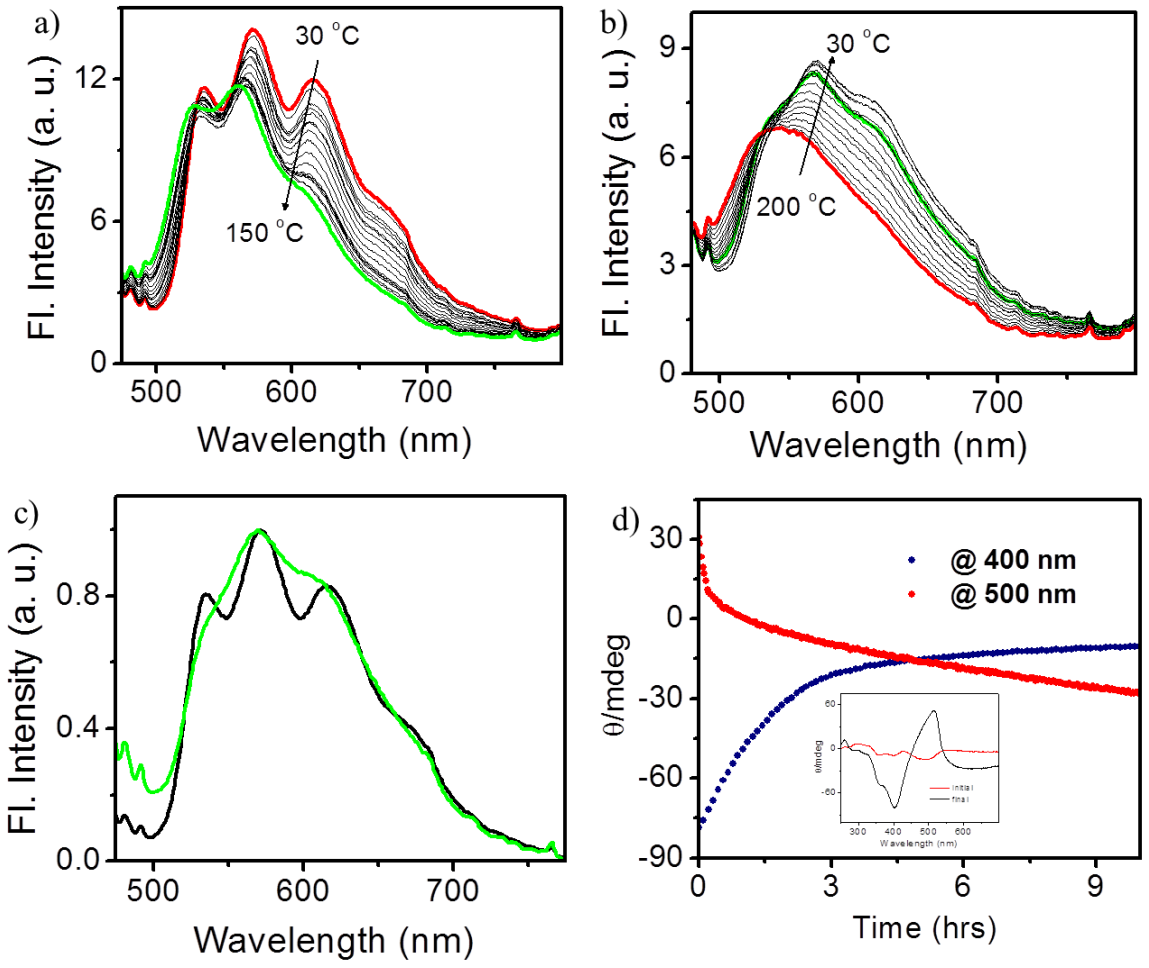

Figure 4.22. Variable temperature fluorescence spectra of **OPV-C** xerogel by changing the temperature (a) from 30 °C to 150 °C (b) from 200 °C to 30 °C. (c) Normalised spectra at 30 °C before (black) and after (green) measurements. (d) VT-CD measurements of **OPV-C** xerogel monitored at 400 nm (blue) and 500 (red); inset CD spectra at 30 °C before (black) and after (red) measurements.

4.3.7 Mechanism of mechanochromism by OPV-C aggregates

Based on the above observations, the mechanism of the shearing induced fluorescence switching, the loss of chirality, the isothermal recovery of the initial

fluorescence and the solvent directed recovery of chirality are explained as depicted in Figure 4.23. The initial xerogel contains aggregates of different size with unequal HOMO-LUMO gap which facilitates energy migration from lower order to higher order aggregates. Upon shearing, the helical fibrillar network of **OPV-C** aggregates loses its character. The disappearance of chirality indicates the possible damage of aggregates irrespective of their size. Recovery of the initial fluorescence with silent CD *via* a thermal process indicates that the molecule reassembles back to a state which is different from the initial state. Such an intermediate state must contain a number of aggregates as evident from the lifetime studies, however, with a non-helical packing, as evident from the CD studies. A solvent mediated recovery of the CD and the fluorescence ensures the presence of such intermediate state. The increase in the amorphous character upon shearing and the recovery by solvent treatment can also be supported with XRD patterns. Annealing of the xerogel (either as prepared or sheared) further reduces the peak intensity of the XRD which reveals the phase transformation from a helical to a non-helical form. Such a transformation can be further supported with a DSC analysis where an exothermic peak appeared at 140 ℃.

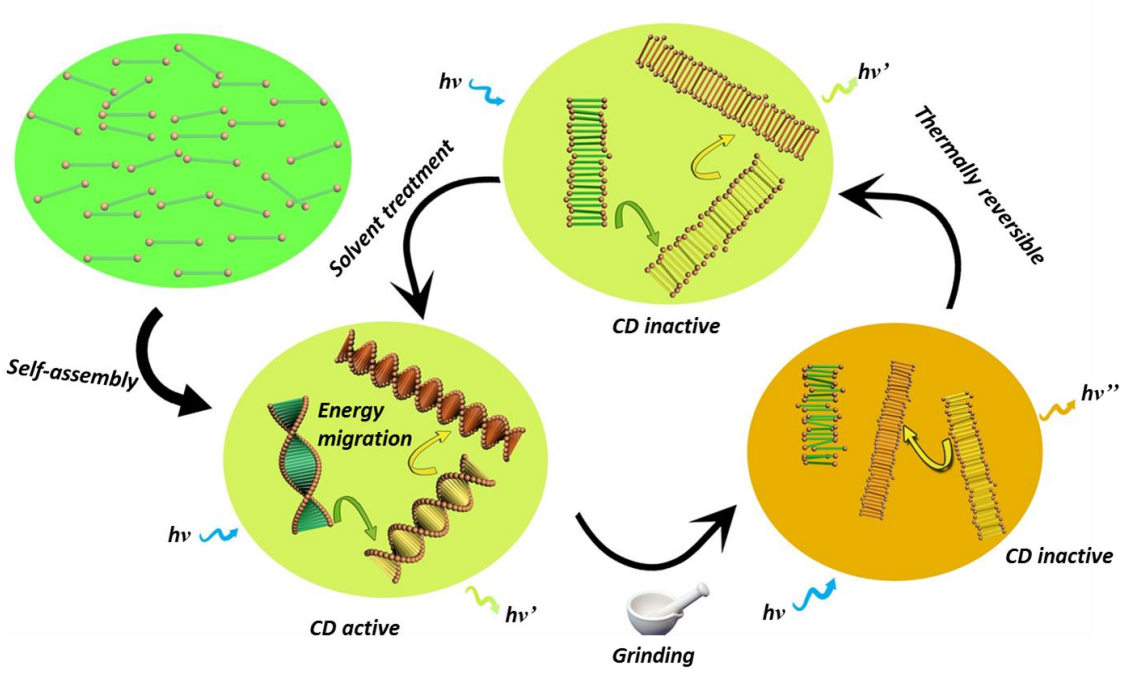

Figure 4.23. Possible pathways for the mechanochromic response by **OPV-C**.

4.4. Conclusions

In conclusion, we have synthesized a chiral **OPV-C** and an analogous achiral **OPV-A** derivatives. Aggregation and gelation properties of **OPV-A** is better when compared to those of **OPV-C** in *n*-decane. Both derivatives were fluorescent in solution as well as in the flim states. Fluorescence of **OPV-C** is found to be mechanoresponsive in the film/xerogel state and was isothermally reversible. The re-organization process was monitored by spectroscopic and photophysical studies which revealed that the size of aggregates plays a crucial role in mechanochromic behaviour. Thus, **OPV-C** is a versatile mechanochromic π-gelator which exhibits a mechanical stress induced fluorescence change and its recovery through thermal

and solvent induced molecular re-organization.

4.5. Experimental section

4.5.1. General

General information about experimental details is given in section 3.5, Chapter 3.

4.5.2. Synthesis and characterization

4.5.2.1. Synthesis of **OPV-A** (abbreviated as **OPV-BZ**) is described in the section 3.5, Chapter 3.

4.5.2.2. Synthesis of (2*E*,2'*E*)-3,3'-(4,4'-(1*E*,1'*E*)-2,2'-(2,5-bis(decyloxy)-1,4-phenylene)bis(ethene-2,1-diyl)bis(2,5-bis(dodecyloxy)-4,1-phenylene))bis(*N*-phenylacrylamide) (OPV-C).

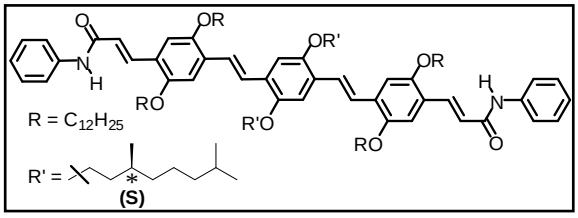

The **OPV** acid (150 mg, 0.09 mmol) and aniline (370 mg, 0.4 mmol) were stirred in dichloromethane (50 mL) in the presence of *N*,*N*'-diisopropylethylamine (70 µL, 0.4 mmol) at 0 ^{o}C and HATU (150 mg, 0.4 mmol) was added to the reaction mixture. Reaction was continued for 8 h at room temperature. The reaction mixture was extracted with dichloromethane and washed several times with water, dried over anhydrous sodium sulphate and the solvent was removed under reduced pressure. Purification by column chromatography (hexane/ $CHCl_3$, 3:7) over silica gel (230-400 mesh) resulted in yellowish orange solid in 70

% yield, mp: 152 ± 2℃; FT-IR (KBr): ν_{max}, 3302, 2920, 2845, 1664, 1598, 1530, 1506, 1464, 1442, 1420, 1390, 1343, 1261, 1206, 1094, 1013, 968, 850, 798, 760, 694, 505 cm^{-1}; ^{1}H NMR (500 MHz, $CDCl_3$) δ (ppm) 0.85-0.89(m, 18H, $-CH_3$), 1.25-1.7 (m, 150H, $-CH_2-$), 3.9-4.1 (m, 12H, $-OCH_2$), 6.6-6.7 (d, J = 27.1Hz, 2H, vinylic), 7.04-7.6(m,18H, aromatic), 7.95-8.0 (d, J = 15.54Hz, 2H, vinylic) ppm; ^{13}C NMR (125 MHz, $CDCl_3$) δ (ppm): 164.9, 145.5, 143.2, 140.9, 128.1, 127.6, 125.1, 121.2, 118.2, 116.4, 114.1, 68.7, 65.3, 38.8, 37.1, 36.5, 31.2, 29.6, 29.1, 28.3, 27.7, 25.3, 24.1, 22.2, 20.8, 14.2. MALDI-TOF MS: M_w = 1678.60, found: 1679.82.

4.5.3. Description of experimental techniques

Description of electronic spectral measurements, fluorescence lifetime measurements, scanning electron microscopy (SEM) and X-ray diffraction (XRD) is given in section 2.5, Chapter 2.

Description of gelation studies, gel melting temperature (T_{gel}) determination, transmission electron microscopy (TEM) and atomic force microscopy (AFM) is given in section 3.5, Chapter 3.

Rheology measurements: Rheology studies were performed using a modular compact rheometer Anton Paar MCR 150 Physica instrument.

Field emission-scanning electron microscopic measurements: Field Emission Scanning Electron Microscope (FE-SEM) images were obtained from S-4800,

Hitachi with an accelerating voltage of 10kV. Samples were prepared by drop casting solutions on a silicon wafer substrate. The samples were allowed to dry under vacuum conditions. Prior to the measurements, sample was coated with metallic platinum using sputtering method.

Differential scanning calorimetric Analysis: Differential scanning calorimetry was performed using a Perkin-Elmer Pyris 6 DSC instrument in sealed aluminum pans under nitrogen flow, at a heat/cooling rate of 10 °C/min.

Circular dichroism (CD) measurements: CD experiments were performed on JASCO 810 spectrometer using quartz cuvette of 1 cm (solution) and 1mm (gel) path length, equipped with peltier thermostatic cell holders, at various temperatures ($\Delta T = \pm 0.05$ K).

4.6. References

(1) (a) Wang, K. L. *Journal of Nanoscience and Nanotechnology* **2002**, *2*, 235; (b) Abraham, S.; Mallia, V. A.; Ratheesh, K. V.; Tamaoki, N.; Das, S. *J. Am. Chem. Soc.* **2006**, *128*, 7692; (c) Deshpande, P.; Pease, L. F.; Chen, L.; Chou, S. Y.; Russel, W. B. *Physical Review E* **2004**, *70*; (d) Yoon, S. J.; Chung, J. W.; Gierschner, J.; Kim, K. S.; Choi, M. G.; Kim, D.; Park, S. Y. *J. Am. Chem. Soc.* **2010**, *132*, 13675; (e) Ryadnov, M. G.; Woolfson, D. N. *J. Am. Chem. Soc.* **2005**, *127*, 12407; (f) Guerrero-Martinez, A.; Avila, D.; Martinez-Casado, F. J.; Ripmeester, J. A.; Enright, G. D.; De Cola, L.; Tardajos, G. *J. Phys. Chem. B* **2010**, *114*, 11489; (g) Breit, B.; Seiche, W. *Pure Appl. Chem.* **2006**, *78*, 249; (h)

Vicidomini, G.; Zwier, J. M.; Bianchini, P.; Cella, F.; Ronzitti, E.; Krol, S.; Szellas, T.; Brakenhoff, G. F.; Diaspro, A. *Multiphoton Microscopy in the Biomedical Sciences VII* **2007**, *6442*, 44224; (i) Zhang, X.; Li, B.; Chen, Z. H.; Chen, Z. N. *J. Mater. Chem.* **2012**, *22*, 11427; (j) Bu, L. Y.; Sun, M. X.; Zhang, D. T.; Liu, W.; Wang, Y. L.; Zheng, M.; Xue, S. F.; Yang, W. J. *J. Mater. Chem. C* **2013**, *1*, 2028; (k) Nishiuchi, T.; Tanaka, K.; Kuwatani, Y.; Sung, J.; Nishinaga, T.; Kim, D.; Iyoda, M. *Chem. -Eur. J.* **2013**, *19*, 4110.

(2) Chi, Z.; Zhang, X.; Xu, B.; Zhou, X.; Ma, C.; Zhang, Y.; Liu, S.; Xu, J. *Chem. Soc. Rev.* **2012**, *41*, 3878.

(3) Mizoshita, N.; Tani, T.; Inagaki, S. *Adv. Mater.* **2012**, *24*, 3350.

(4) Dong, Y. J.; Xu, B.; Zhang, J. B.; Tan, X.; Wang, L. J.; Chen, J. L.; Lv, H. G.; Wen, S. P.; Li, B.; Ye, L.; Zou, B.; Tian, W. J. *Angew. Chem. Int. Ed.* **2012**, *51*, 10782.

(5) Wang, Y. L.; Liu, W.; Bu, L. Y.; Li, J. F.; Zheng, M.; Zhang, D. T.; Sun, M. X.; Tao, Y.; Xue, S. F.; Yang, W. J. *J. Mater. Chem. C* **2013**, *1*, 856.

(6) (a) Kunzelman, J.; Kinami, M.; Crenshaw, B. R.; Protasiewicz, J. D.; Weder, C. *Adv. Mater.* **2008**, *20*, 119; (b) Dou, C. D.; Chen, D.; Iqbal, J.; Yuan, Y.; Zhang, H. Y.; Wang, Y. *Langmuir* **2011**, *27*, 6323; (c) An, B. K.; Gierschner, J.; Park, S. Y. *Acc. Chem. Res.* **2012**, *45*, 544; (d) Gupta, R.; Thomas, R.; Kulkarni, G. U. *J. Mater. Chem.* **2012**, *22*, 19139; (e) Zhang, G. Q.; Lu, J. W.; Sabat, M.; Fraser, C. L. *J. Am. Chem. Soc.* **2010**, *132*, 2160; (f) Liu, T. D.; Chien, A. D.; Lu, J. W.; Zhang, G. Q.; Fraser, C. L. *J. Mater. Chem.* **2011**, *21*, 8401; (g) Nguyen, N. D.; Zhang, G. Q.; Lu, J. W.; Sherman, A. E.; Fraser, C. L. *J. Mater. Chem.* **2011**, *21*, 8409; (h) Zhang, G. Q.; Singer, J. P.; Kooi, S. E.; Evans, R. E.; Thomas, E. L.; Fraser, C. L. *J. Mater. Chem.* **2011**, *21*, 8295.

(7) (a) Sagara, Y.; Mutai, T.; Yoshikawa, I.; Araki, K. *J. Am. Chem. Soc.* **2007**, *129*, 1520; (b) Sase, M.; Yamaguchi, S.; Sagara, Y.; Yoshikawa, I.; Mutai, T.; Araki, K. *J. Mater. Chem.* **2011**, *21*, 8347.

(8) (a) Ajayaghosh, A.; Praveen, V. K. *Acc. Chem. Res.* **2007**, *40*, 644; (b) Ajayaghosh, A.; Praveen, V. K.; Vijayakumar, C.; George, S. J. *Angew. Chem. Int. Ed.* **2007**, *46*, 6260; (c) Babu, S. S.; Praveen, V. K.; Prasanthkumar, S.; Ajayaghosh, A. *Chem.-Eur. J.* **2008**, *14*, 9577; (d) Babu, S. S.; Mahesh, S.; Kartha, K. K.; Ajayaghosh, A. *Chem.-Asian. J.* **2009**, *4*, 824; (e) Ajayaghosh, A.; George, S. J. *J. Am. Chem. Soc.* **2001**, *123*, 5148.

(9) (a) Ajayaghosh, A.; Varghese, R.; George, S. J.; Vijayakumar, C. *Angew. Chem. Int. Ed.* **2006**, *45*, 1141; (b) Ajayaghosh, A.; Vijayakumar, C.; Varghese, R.; George, S. J. *Angew. Chem. Int. Ed.* **2006**, *45*, 456; (c) George, S. J.; Ajayaghosh, A.; Jonkheijm, P.; Schenning, A. P. H. J.; Meijer, E. W. *Angew. Chem. Int. Ed.* **2004**, *43*, 3422.

(10) (a) Ajayaghosh, A.; Varghese, R.; Mahesh, S.; Praveen, V. K. *Angew. Chem. Int. Ed.* **2006**, *45*, 7729; (b) Ajayaghosh, A.; Varghese, R.; Praveen, V. K.; Mahesh, S. *Angew. Chem. Int. Ed.* **2006**, *45*, 3261.

(11) (a) Gopal, A.; Hifsudheen, M.; Furumi, S.; Takeuchi, M.; Ajayaghosh, A. *Angew. Chem. Int. Ed.* **2012**, *51*, 10505; (b) Rajaganesh, R.; Gopal, A.; Das, T. M.; Ajayaghosh, A. *Org. Lett.* **2012**, *14*, 748; (c) Kartha, K. K.; Mukhopadhyay, R. D.; Ajayaghosh, A. *Chimia* **2013**, *67*, 51; (d) Mahesh, S.; Gopal, A.; Thirumalai, R.; Ajayaghosh, A. *J. Am. Chem. Soc.* **2012**, *134*, 7227.

(12) (a) Korevaar, P. A.; George, S. J.; Markvoort, A. J.; Smulders, M. M. J.; Hilbers, P. A. J.; Schenning, A. P. H. J.; De Greef, T. F. A.; Meijer, E. W. *Nature* **2012**, *481*, 492; (b)

Gillissen, M. A. J.; Hoeben, T. T.; Spiering, A. J. H.; Vekemans, J. A. J. M.; Palmans, A. R. A.; Meijer, E. W. *Isr. J. Chem.* **2011**, *51*, 1118.

(13) Zhegang, H.; Seong-Kyun, K.; Myongsoo, L. *J. Mater. Chem.* **2011**, *21*.

(14) (a) Ajayaghosh, A.; Praveen, V. K.; Srinivasan, S.; Varghese, R. *Adv. Mater.* **2007**, *19*, 411; (b) George, S. J.; Ajayaghosh, A. *Chem. Eur. J.* **2005**, *11*, 3217.

(15) Rosch, U.; Yao, S.; Wortmann, R.; Wurthner, F. *Angew. Chem. Int. Ed.* **2006**, *45*, 7026.

(16) Yamaguchi, S.; Yoshikawa, I.; Mutai, T.; Araki, K. *J. Mater. Chem.* **2012**, *22*, 20065.

Papers Presented at Conferences (Posters/Oral)

1. Indo-French Workshop on 'Self-assembled Hybrid Systems: Advanced Materials for the Future' at Travancore Heritage, Trivandrum, Kerala, India during March 2-4, 2011 (**Oral Presentation**)
2. Eighth JNC research conference on chemistry of materials at Vivanta by TAJ, Kovalam, Kerala, India during September 30 - October 02, 2012 (**Best Poster Award**)
3. 15^{th} CRSI-NSC & 7^{th} CRSI-RSC Symposium at Banaras Hindu University, Varanasi, India during January 31 and February 1-3, 2013 (**Poster Presentation**)
4. NANO INDIA 2013 conference held at CSIR-NIIST, Trivandrum, Kerala, India during Feb 19-20, 2013 (**Poster Presentation**)

List of Publications

1. Solvent-Directed Self-Assembly of π Gelators to Hierarchical Macroporous Structures and Aligned Fiber Bundles

   S. S. Babu, S. Mahesh, **K. K. Kartha** and A. Ajayaghosh, *Chem. Asian J.* **2009**, *4*, 824.

2. Excited State Processes in Linear π-System-Based Organogels

   S. S. Babu, **K. K. Kartha** and A. Ajayaghosh, *J. Phys. Chem. Lett.* **2010**, *1*, 3413.

3. Excitation energy migration in oligo(*p*-phenylenevinylene) based organogels: structure-property relationship and FRET efficiency

   C. Vijayakumar, V. K. Praveen, **K. K. Kartha** and A. Ajayaghosh, *Phys. Chem. Chem. Phys.* **2011**, *13*, 4942.

4. Attogram Sensing of Trinitrotoluene with a Self-Assembled Molecular Gelator

   K. K. Kartha, S. S. Babu, S. Srinivasan and A. Ajayaghosh, *J. Am. Chem. Soc.* **2012**, *134*, 4834.

5. Supramolecular Gels and Functional Materials Research in India

   K. K. Kartha, R. D. Mukhopadhyay and A. Ajayaghosh, *Chimia*, **2013**, *67*, 47.

6. An Unprecedented Role of Supramolecular Chirality in the Design of a Mechanochromic Chiral π-Gelator.

   K. K. Kartha, S. Vishnu and A. Ajayaghosh (To be communicated)

7. Multi-Stimuli Driven Gelation and Morphological Transformation of an Oligo(*p*-phenylenevinylene) Derived Organogelator

   K. K. Kartha, S. Vishnu and A. Ajayaghosh (To be communicated)

8. Self-assembled Fluorescent Nanostructures for the Detection of Trinitrotoluene Vapor: A Quantitative Approach

   K. K. Kartha, S. Ogi, C. Vijayakumar, M. Takeuchi and A. Ajayaghosh (To be communicated)